Doctoral Dissertation

Study on development and application of reverse electrodialysis (RED) process from lab scale to pilot scale

ラボ及びパイロットスケールにおける

逆電気透析プロセスの開発と応用

に関する研究

March 2020

Soroush Mehdizadeh

Graduate School of Sciences and Technology for Innovation,
Yamaguchi University

Table of Content

Chapter 1

Introduction

1.1 Climate change and air pollution

Increasing the world energy demand following by enhancing the usage of fossil fuel has expanded the air pollution and global warming which well known as two major problems to human and animal health as well as political stability [1]. Combustion of fossil fuel not only has the major effect on air pollution, but also is the reason of 70-75% of all CO_2 emission which known as one of the main greenhouse gas [2]. World temperature affect significantly by the percentage and the amount of CO_2 in the atmosphere. The standard percentage of carbon dioxide in the atmosphere is only 0.04% [3]. The CO_2 percentage less than 0.04% would make the world too cool while the CO_2 excess more than 0.04% leads to make the world undesirably hot.

The world temperature affects by the balance between received and reflect radiation from the sun. The world need to radiate as much as energy that received back into the space in order to stay in a suitable range of temperature. In this regard, the greenhouse gases absorb low-frequency reflect from the world and lead to increasing the temperature. If the atmosphere just consisted of only oxygen and nitrogen, which in reality is up to 99% in atmosphere, then in average, around 288 watts would be absorb by each square meter of the earth's surface. The equilibrium temperature of the atmosphere would be -6 °C if all this 288 watts remit which is too cool for mankind [4]. Therefore, a tiny amount of greenhouse gases leaded to increasing the world temperature into an appropriate amount for mankind. Unfortunately, during the Industrial Revolution the excess of CO_2 gas more than standard made the world warmer than standard which is still continue. In addition to air pollution that mainly caused by the fossil fuel combustion and is the sixth-leading

reason of death, the global warming could lead to very serious problems [5]. The global warming enhances disease, tropical storm, heat stress, increases the sea level [1].

1.2 Renewable energy

In recent years, we have seen a growing concern on greenhouse emission and its impact on climate change [6]. Developing renewable and sustainable energy conversion technology is well known as an important strategy against global warming or even reduce its growing speed since it has less or non-greenhouse gas emission during energy production. Different applicable renewable energy technologies that proposed for addressing the climate change and air pollution mentioned briefly in below.

1.2.1 Solar energy

One of the application of solar energy is Solar photovoltaics (PVs). PVs rows of cells contain a special material that convert the radiation of sun into direct current (DC) electricity. This technology has the largest physical resources which is solar radiation and have attracted lots of attention in last few years [7]. In addition, concentrated solar power (CSP) technology using mirrors to focus sunlight and heat a fluid in a collector at high temperature is an another application of solar energy. The heated fluid flow from the collector to a different types of heat engines where the heat is converted to electricity. However, the problem of using solar energy is that the weather and climate have significant impact on its performance. The energy production at night as well as in cloudy weather significantly decrease which make the power generation unstable. In addition, solar energy needs large footprints and special location which should be mainly sunny. All of these

problems together with the high cost of solar cell and operation cost made the solar energy expensive.

1.2.2 Wind

The wind power is generated using wind turbine that convert the kinetic energy of the wind into electricity. Using an appropriate gearbox in order to turns the slow rotation of turbine into faster that convert the mechanical energy into electricity by a generator. The average of power density that can produce using wind power is 1.2 W/m^2 in average considering different area with various wind speed. In addition to the significant impact of wind power on environmental views and ecosystem, there are two other important barriers in the implementation of large-scale wind power. First, understanding the intermittency of wind and second the difficulty in identifying good wind locations [8].

1.2.3 Geothermal

The hot water and steam below the earth's surface can be extract known as geothermal energy. The hot water and steamed that extract from the earth can be historically used to provide heat for building, industrial, and domestic water as well as using in electricity generation in geothermal power plant. However, the application of applying the geothermal energy is not possible everywhere. In addition, the extraction and utilization of this huge quantity of heat needs some instruments in order to transfer the heat toward accessible depth beneath the Earth's surface [9].

1.2.4 Hydroelectric

Water drop from high to low height due to gravity can be generate electricity by turning a turbine and generator. This energy can produce by water falling from dams, some is produced by water flowing down rivers. Since 2005, the hydroelectric power was the world largest (17.4%) installed renewable source of electricity [1]. However, the power density is low and around 0.03 W/m^2. In addition, the main impact of the hydroelectric power plant is on environmental and ecosystem. It also has a significant effect on mankind living place, and underground water reservoir.

1.2.5 Tidal

The rise and fall of the water in ocean surface the gravity interaction between the earth, moon, and the sun cause swing current which known as tides. A tidal turbine is almost same with a wind turbine with a rotor that turns with its interaction during the ebb and flow of a tide and a generator in a tidal turbine which converts kinetic energy to electrical energy [1]. However, the application of tidal energy is in ocean which is hard place for installation of tidal power plant as well as corrosion of instrument by seawater. In addition, the cost of maintaining this energy instrument would be high.

1.2.6 Nuclear

The heat that generate during nuclear fission, when Uranium for example splits into two atoms and releases energy use as source for electricity production while older plants burn fossil fuel in this regard [10]. Nuclear power plant controls the generated energy from enriched uranium among nuclear fission in order to make high pressure steam from water following by electricity production. Although nuclear power has huge potential of energy

production, but any accident in that can make a disaster. In details, the core of nuclear reactor works in harsh condition for materials due to the combination of high temperature, high stress, and a chemically aggressive coolant as well as intense radiation fluxes [11]. For example, in Japan, as a result of earthquake on March 11, 2011, following by tsunami, the Dai-ichi nuclear power plant causing loss of power and hence disruption of controls and failed cooling system shortly after the earthquake [12]. Vending of gases following by hydrogen explosion and the fire in spent fuel pond of unit 4 resulted in the primary atmospheric releases of Fukushima radionuclide contaminants.

1.2.7 Salinity gradient energy (SGE)

The most available sources of renewable energy have mentioned above. Despite their high theoretical potential for energy production, all of them have some either limitation on actual power generation or environmental impact. Salinity gradient energy (SGE) is well known as another renewable source of energy that proposed by *Pattle* in 1950s [13]. SGE is defined as the electrochemical potential between two solutions with different salinities that can be extract for practical energy generation [14,15]. In this regard, the river mouth where the river reach to the sea has a huge potential to capture the SGE. In fact, if the mixing of river water with seawater toke place partly reversibly, work can be obtained using their mixing. Theoretically, about 0.4-0.5 kWh of energy can be potentially obtained by mixing each cubic meter of seawater with each cubic meter of river water calculated by Gibbs free energy of mixing that will explain in next section [14,16]. In other definition, this energy is equivalent with the hydroelectric power that generated by flowing down of one cubic meter water from 175 m height [17]. Estimation based on considering the total major rivers flow in the world showed that the magnificent 2TW of SGE can be

obtained as an actual energy [18,19]. In comparison with other source of renewable energy, SGE is in the same range with wave or geothermal while it is 100 times higher than tidal energy [20]. In addition, SGE is always available which leads to have stable energy as well as it applicable in different areas. It is worth noting that, Japan has a tremendous potential in obtaining its energy demand using different technologies based on SGE because there are a lot of rivers that flow into the ocean.

1.2.7.1 Gibbs free energy of mixing

Theoretically, the available SGE that can be calculated using Gibbs free energy of mixing ($\Delta_{mix}G$) as mentioned. In this regard, if we assume an ideal dilute solution ($\Delta_{mix}H = 0$), the Gibbs free energy of mixing can be defined as follow:

$$\Delta_{mix}G = \Delta G_b - (\Delta G_c + \Delta G_d) \quad [1]$$

$$\Delta_{mix}G = -(n_c + n_d)T\Delta_{mix}s_b - (-n_cT\Delta_{mix}s_c - n_dT\Delta_{mix}s_d) \quad [2]$$

where n and T refers to the amount of moles and temperature, respectively. Subscribes c, d, and b refers to the concentrate salt solution, diluted salt solution, and resulting brackish salt solution, respectively. $\Delta_{mix}s$ represented the molar entropy of mixing (J/mol.K) to the total molar entropy of the corresponding electrolyte solution defined as follow:

$$\Delta_{mix}s = -R\sum_i x_i ln x_i \quad [3]$$

where R is the universal gas constant (8.314 J/mol.K). In the case of just NaCl solved in water, x is the mole fraction of component i (i = Na, Cl, H_2O). Considering above equations, the theoretical available amount of energy from mixing of both 1m^3 of seawater and river water at 293 K is 1.4 MJ. Generally, there are two promising processes in order to convert

the SGE into applicable energy known as pressure retarded osmosis (PRO) and reverse electrodialysis (RED) that explain in the following sections. Since the main target of this focus on RED process, PRO process describe briefly.

1.3 Pressure retarded osmosis (PRO)

In PRO process, two solutions with different salinities are brought into contact while a semi-permeable membrane placed in between. This type of membrane is permeable to solvent (i.e. water) while retains solute (i.e. dissolved salt) [21,22]. The chemical potential difference called osmosis pressure causes the transport of water from dilute solution into concentrate solution to reach the equilibrium. If hydrostatic pressure is applied to the concentrate solution side, the water transport will partly retarded. The water transport from the low-pressure diluted solution to the high pressure concentrate solution results in increasing the pressure of the transport water. Consequently, this pressurized volume of transported water can be used to generate the electric power using a turbine. However, the energy loss due to converting the hydrostatic potential to electrical energy using turbine and generator could be significant. In addition, brine would be needed as high concentrate solution in PRO process to have sufficient efficiency, while the most available salt solution in the World is seawater which has much lower salinity than brine.

1.4 Reverse electrodialysis (RED)

The application of RED process to convert the SGE into electricity was firstly introduced in the early 1950's using a small stack with the maximum electromotive force of 3.1 Volts [13,17]. Then the RED process developed more in the late 1970's by Weinstein

and Leitz [23] and later Lacey in 1980 [24]. Even today, the RED process developed in such a way that combined with other hybrid systems such as seawater desalination [25], PRO [21], and microbial fuel cell [26].

In RED system, concentrate and dilute solutions flow alternatively among cation and anion exchange membranes (CEMs and AEMs) that are stacked between cathode and anode as shown in Figure 1 [14,27,28]. Non-conductive spacers usually place between ion exchange membranes (IEMs) in order to keep distance between them as well as improve the solution and ion attribution in feed compartments [29]. Feed solutions flow between IEMs while ions migrate from high into low salinity solution across the IEMs because of SGE. In this regard, cations and anions transport through CEMs and AEMs, respectively. The potential over each IEMs located between sea and river water is around 80 mV called membrane potential. The sum of the potential difference over all the IEMs in the RED stack is the electric potential difference of RED stack. At the electrodes redox reactions occur to convert the electrochemical potential into electricity. In lab-scale and short term experiments, Ag/AgCl is usually recognized as electrodes while Pt is appropriate in pilot-scale and long term experiments. Therefore, electrons migrate from anode to cathode through an external electrical circuit and consequently can power an external load or energy consumer such as light bulb. All of the RED stack parts include IEMs, spacers, electrode system, and the theory of RED process is described in following sections.

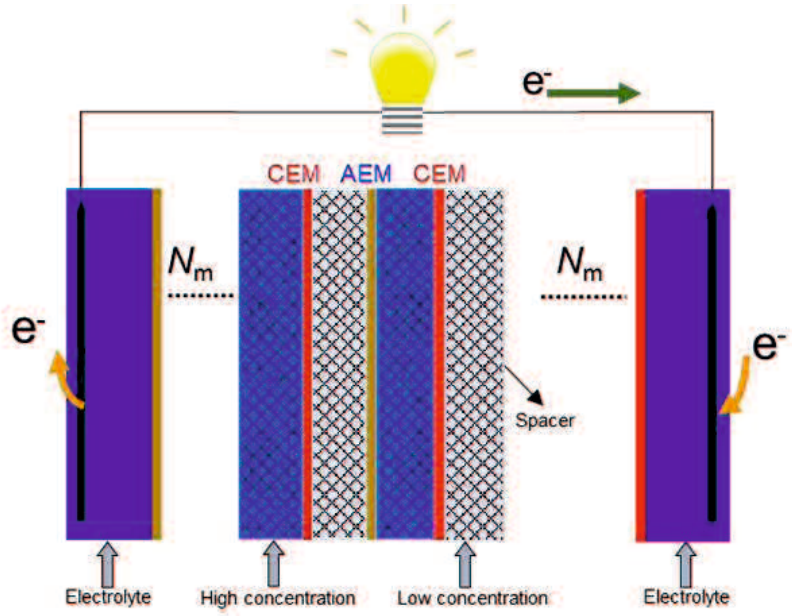

Figure 1. A simple schematic representation of a RED stack including ion exchange membranes, integrated spacers, and electrodes.

1.4.1 Ion exchange membranes (IEMs)

CEMs and AEMs have selectivity through cations and anions due to their functional charge group which are negative charged group for CEMs and positive charged group for AEMs. The most common negative charge groups are sulfonic acid ($-SO_3^-$), carboxylic acid ($-COO^-$), phosphoryl ($-PO_3^{2-}$), and phosphonic acid ($-PO_3H^-$) that allow the passage of cations and rejects anions through CEMs [30]. On the other hand, the most common positive charge functional groups that applied in AEMs are ammonium ($-NH_3^+$), secondary amine ($-NRH_2^+$), tertiary amine ($-NR_2H^+$), quaternary amine ($-NR_3^+$) that have selectivity for anions. An IEM can be either homogeneous or heterogeneous depends on the manufacture method and its own physical structure [31]. In homogenous IEMs type, the membrane bulk is uniformly charged, while the membrane bulk in heterogeneous IEMs

contain non-uniform charge distribution a well [30]. CMX and AMX are well known as two standard cation and anion exchange membrane, respectively, shown as figure 2.

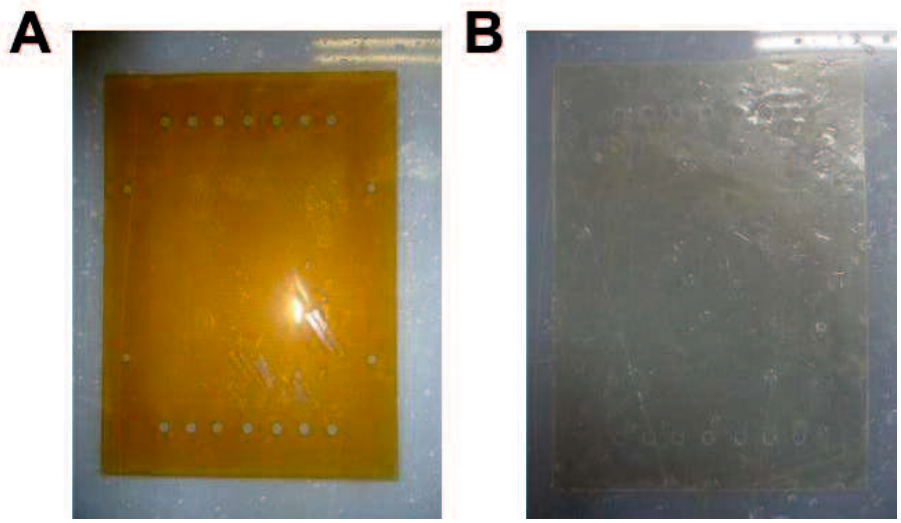

Figure 2. Lab-scale size of IEMS. A: CMX as cation exchange membrane, B: AMX as anion exchange membrane.

The most important parameters of an IEM that have significant effect on the performance and power output of RED process are membrane permselectivity and resistance. Other parameters such as ion exchange capacity, water content of membrane, and charge density have also effect on the RED performance due to their effect on both membrane permselectivity and resistance. For instance, high water content of membrane lead to losing the mechanical structure of an IEM following by reducing the permselectivity with the positive effect on membrane conductivity [27,32]. Water content of an IEM can be experimentally determined by measuring membrane swelling degree as follow:

$$SD = \frac{m_{wet} - m_{dry}}{m_{dry}} \times 100 \quad [4]$$

where m_{wet} and m_{dry} correspond to the IEM weight in wet and dry condition, respectively.

The number of fixed charged group in an IEM bulk can be identified by measuring an ion exchange capacity (IEC) of membrane that defined by the milli-equivalents (meq) of charged groups per gram of dry membrane [33]. The IEC is generally measured using determining the amount of counter-ions (e.g., cations for CEMs and anions for AEMs) after turning CEMs into saturated H^+ form and AEMs into saturated Cl^- form [33]. High IEC leads to increasing the membrane permselectivity while a high SD may decrease the effect of IEC and adversely affect the permselectivity [27,32]. So, there is a trade-off between IEC and SD on permselectivity of an IEM. In fact, permselectivity is defined as the ability of IEMs to selectively transport counter ions. The permselectivity of a perfect IEM should be 1 which means that co-ions (e.g., cations for AEMs and anions for CEMs) are fully prevented from migration through membrane bulk. However in real case, the transportation of co-ions are unavoidable, resulting the permselectivity less than 1 for an IEM. The permselectivity is defined as the ratio of measured membrane potential (E_{meas}) under a given concentration gradient and the corresponding theoretical electromotive force (E_{emf}) calculated by Nernst equation as follow [33,34]:

$$E_{emf} = \frac{RT}{ZF} ln \frac{\alpha_H}{\alpha_L} \quad [5]$$

$$Permselectivity = \frac{E_{meas}}{E_{emf}} \times 100\% \quad [6]$$

where *N, R,* and *T* are the number of membrane cells, the gas constant (J/mol.K) and the temperature (K), respectively. *Z* is the valence of the counter-ion (-) of an IEM, *F* is the Faraday constant (96485 C/mol), and *a* is the activity of the solution. Subscripts *H* and *L* refer to the high and low salinity solution, respectively.

Membrane resistance is defined as the resist of an against ionic current transportation. Membrane resistance has one of the major contribution on the RED stack internal resistance. Higher membrane resistance increases the voltage drop across the RED stack and consequently decreases the power output. Membrane resistance is usually measured in salt solution in both direct current (DC) or alternative current (AC) mood. The difference between the membrane resistance measurement is DC or AC mood is that the effect of concentration polarization, boundary layer, and double layer is more considerable in AC condition. During the measurement, the voltage drops across the membrane under different current density. Then the membrane resistance is calculated as the slope of current-voltage (I-V) curve.

1.4.2 Spacers

Spacer are used in RED stack in order to support IEMs, improving the solution and ions distribution, and making the flow channel [35]. Figure 3 shows two lab-scale spacers for high and low concentrate compartments with the gasket to prevent the solution leakage. Increasing the feed solution mixing, minimize the concentration polarization by reducing the non-ohmic resistance, while at the same time, non-conductive spacers cover the membrane area and occupy the feed channel volume resulting in higher ohmic resistance [29,36]. More importantly, spacer-filled channel has one of the major impact on pumping energy loss due increasing the pressure drop across the channel [16,37] which mainly depend on spacer geometry and materials [36]. In addition, the spacer thickness plays an important role in the power output performance of RED process because it has directly effect on the resistance of solution compartments. In fact, the low concentration compartment has been well recognized as the major part in RED stack internal resistance

[24,33,38]. The comprehensive study about the effect of spacer on RED stack resistance represent in chapter 2.

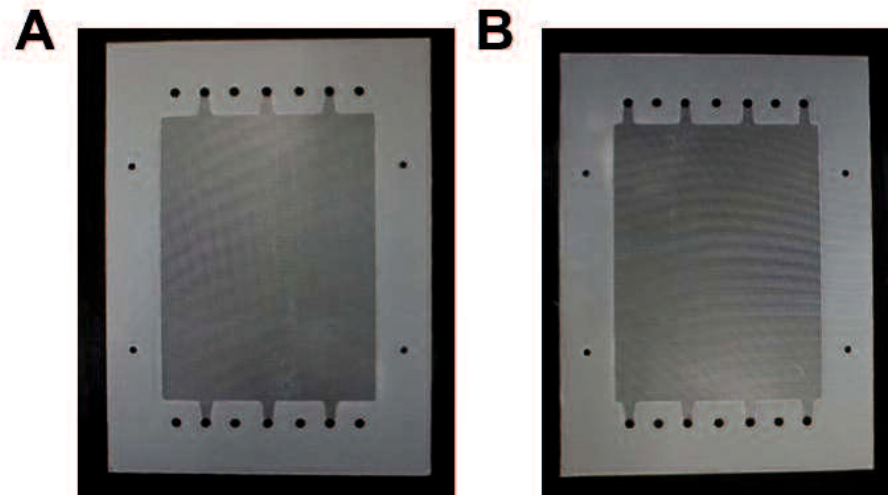

Figure 3. Lab-scale spacers that use in RED stack. A: spacer for high concentrate compartment, B: spacer for low concentrate compartment

1.4.3 Electrode and electrolyte system

The electrode compartment filled with electrolyte convert the ionic current into electric current through the redox reaction. The electrode system that usually used in RED process categorized into with and without opposite electrode reaction [39]. Applying electrode system without opposite reactions usually together with gas formation such as H_2, O_2, and Cl_2 because of water splitting. The voltage losses in this type of electrode system is usually high because of gas production and needed for special gas collection apparatuses for toxic and explosive gas [24,40,41]. On the other hand, electrode system with opposite reaction are used to improve the performance since there is no net chemical reaction occur during power generation [39]. This type of electrode also consist of reactive electrodes like Ag/AgCl, Cu/$CuSO_4$ and inert type electrodes such as titanium mesh coated

by Ru-Ir and graphite [41,42]. It is worth noting that the reactive electrodes need to change the feed solution and electric current direction periodical, while the inert electrode does not need these issues. In order to make sense for reader, figure 4 shows the Ag/AgCl reactive electrodes in lab-scale size. In addition, the redox reaction that occur when Ag/AgCl are electrodes are shown as follow:

$$Cathode: AgCl + e \rightarrow Ag + Cl^{-} \quad [7]$$

$$Anode: Ag \rightarrow AgCl + e \quad [8]$$

However, in the case of inert type electrodes such as Pt with Na2SO4 solution as electrolyte, the redox reaction take place as follow:

$$Cathode: 2H_2O + 2e \rightarrow H_2 + 2OH^{-}\ ,\ OH^{-} + Na^{+} \rightarrow NaOH \quad [9]$$

$$Anode: 2H_2O \rightarrow 4H^{+} + O_2 + 4e\ ,\ H^{+} + SO_4^{2-} \rightarrow H_2SO_4 \quad [10]$$

The lab-scale RED stack is shown as figure 5 after assembling all parts as well as endplates and pumps for feed solutions.

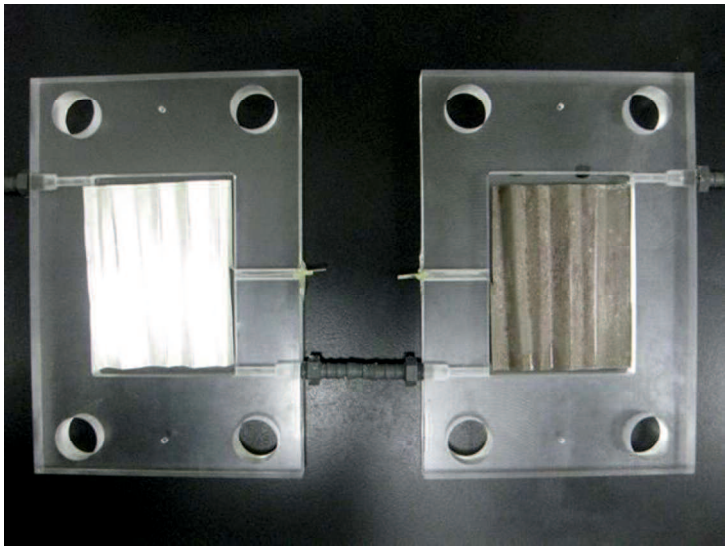

Figure 4. Lab-scale Ag/AgCl electrodes that use in lab scale RED stack

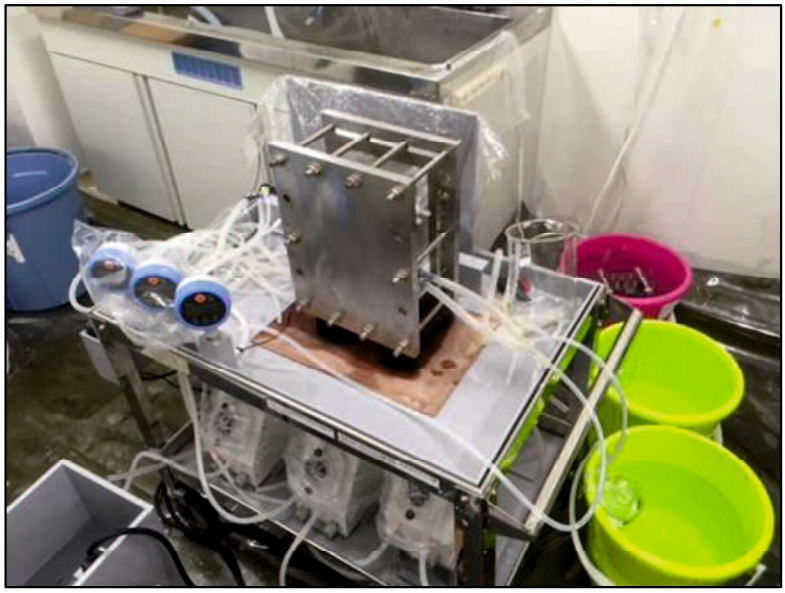

Figure 5. A lab-scale RED stack

1.4.4 Theory

The theoretical potential over a RED stack in open circuit condition, E_{ocv}, (e.g., zero current) when feeding by high and low concentrate aqueous monovalent ion solutions (e.g. NaCl) can be calculated using Nernst equation as follow [24,43]:

$$E_{OCV} = 2N\alpha \frac{R.T}{Z.F} \ln \frac{a_H}{a_L} \quad [11]$$

where, α is the permselectivity of the membrane (-). *N, R,* and *T* are the number of membrane cells, the gas constant (J/mol.K) and the temperature (K), respectively. *Z* is the valence of the counter-ion (-) of an IEM, *F* is the Faraday constant (96485 C/mol), and *a* is the activity of the solution. Subscripts *H* and *L* refer to the concentrated and dilute compartments, respectively. It is worth noting that the Nernst equation derived by considering molar flux from diffusion, M_d, and molar flux from electrophoretic effect, M_e, at zero current as follow:

$$M_d = -D\frac{dC}{dx} \quad [12]$$

$$M_e = -\mu C\frac{d\psi}{dx} \quad [13]$$

where D, C, and x are diffusion coefficient, concentration of specific ion, and distance across the membrane, respectively. In addition, μ is ion mobility and ψ is local potential. The total molar flux of a specific ion such as Na, M_{Na}, is equal to the accumulation of molar flux due to diffusion and electrophoretic effect. By converting the molar flux into electric current, the final equation can be derived as follow:

$$I = M_{Na^+}zF = -zF\left(D\frac{dC}{dx} + \mu C\frac{d\psi}{dx}\right) \quad [14]$$

considering the Eintein's relationship for ion mobility and integration from both sides of equation at $I=0$, the following equation can be obtain:

$$Einstein'srelationship \ \mu = \frac{DxF}{RT} \quad [15]$$

$$\psi_{inside} - \psi_{outside} = -\frac{RT}{zF}ln\frac{[Na^+]_H}{[Na^+]_L} \quad [16]$$

$$V_m = -\frac{RT}{zF}ln\frac{[C]_H}{[C]_L} \quad [17]$$

The generated power due to the drop of RED stack potential as well as an external load resistance shows as follow:

$$W = I \times E_{stack} = I^2 \times R_{load} = \frac{E_{OCV}^2 R_{load}}{(R_{stack}+R_{load})^2} \quad [18]$$

where I is current (A), E_{stack} is stack voltage, R_{load} is load resistance (Ω), and R_{stack} represent the stack resistance (Ω). The stack resistance is sum of the membranes, solution compartments, and electrode resistance shown by equation 6.

$$R_{stack} = \frac{N}{A}\left(\frac{t_{com,L}}{k_L} + \frac{t_{com,H}}{k_H} + R_{CEM} + R_{AEM}\right) + R_{el} \quad [19]$$

where A is membrane effective area (m^2). t_{com} is compartment thickness (m) and k is the conductivity of compartments ($S.m^{-1}$) of the RED stack. Subscript L and H means low and high concentrate compartments, respectively. In addition, R_{CEM} and R_{AEM} are the resistance of cation and anion exchange membranes ($\Omega.m^2$), respectively. R_{el} is the ohmic resistance of both electrodes and their compartments. The maximum power output of the RED stack can be obtained when the R_{load} is equal to the stack resistance [23,44,45] and simplified as follow:

$$P_{max} = \frac{E_{ocv}^2}{4R_{stack}} \quad [20]$$

Consequently, the power density, P_{gross}, can be expressed as follow:

$$P_{gross} = \frac{P_{max}}{2.N.A} \quad [21]$$

The performance of the RED process can be measured in two different ways called current-voltage (I-V) or constant current (CC) conditions. In the case of I-V measurement condition, the current increase from zero until the voltage decrease from maximum (OCV) to zero (e.g., shortcut current). In this regard, the slope of I-V curve represent as RED stack resistance and the maximum power usually happens when the stack voltage become half of OCV. In the case of CC measurement condition, the RED performance and power output

measure in a constant current while the voltage record. This type of measurement usually take place in order to investigate on power production stability.

1.5 Literature review

The first attempt of actually converting the SGE into electricity was performed by *Pattle* in 1954 to get 0.2 W/m^2 using a 47 pairs RED stack with 8 cm^2 of each membrane area and using seawater and river water as feed solutions [13]. More than two decades later in 1976, *Weintein* and *Leitz* developed a theoretical model of IEM that stacked in RED process [23]. Before 2000, although the theoretical studies showed the significant potential of RED process for energy production compare with other energy sources, but the practical investigation reported low power density (0.4 W/m^2) and energy conversion (1.8-11 %) [40,46–48]. The first study on the fouling in RED was also performed among this early phase in 1986 [49]. Study and research on RED process grow up rapidly in early 2000 because of increasing the cost of fossil fuel [50]. During this time different studies carried out on different effective aspects on RED process such as operation condition, stack configuration, and the role of IEMs on the power generation performance [15,16,33,38,51–54]. These attempt on improving the RED performance and design leaded to increasing the power density of RED process to 0.93 W/m^2 using seawater and river water as feed solutions [16,54].

Remarkable progress on RED process have been achieved in last decade from 2010 especially in developing membrane for RED process [55–58]. In this regard, *Guler* et al. reported the power density of 1.27 W/m^2 using the first tailor-made IEM that prepared for RED [59]. In addition, improving the spacer design, using ion conductive spacers, and

using ion exchange resin instead of non-conductive spacer increased the power density around 4 times [56,60–62]. Fortunately, in last decade, the pilot-scale of RED process has also been design and progressed in Netherlands and Italy [45,63].

1.5.1 Effect of feed solution on RED performance

The feed solution properties, specially solution conductivity, is one of the most effective parameter on the electromotive driving force and internal resistance of RED stack. For example, the low concentrate solution in RED process has the major contribution in the internal resistance of RED stack which is around 45% when seawater and river water are feed solution [15,16,64–67]. Although seawater and river water are the most common reported feed solution for RED process [28,68,69], but different alternative feed solutions have also applied instead. Alternative feed solutions that proposed instead of seawater include brine from seawater desalination plant, high salinity solution from dead sea, and model high concentration solution to use in close-loop osmotic heat engine [26,36,73,43,51,65–67,70–72]. On the other hand, the alterative feed solution instead of river water was limited into such as brackish water and treated wastewater [18,26,43,66,74].

Having higher salinity gradient between high and low concentrate feed solutions would reasonably lead to increasing the power output of RED process. Increasing the salinity gradient can be achieved by increasing or decreasing the high salinity or low salinity feed solutions, respectively. In this regards, by increasing the salinity of high concentrate feed solution from 0.5 M to 5.0 M can the salinity ratio can be increased ten times [22]. In this regard, *Daniilidis* et al. reported the significant power density of 6.7 W/m^2 using 0.01 M and 5 M NaCl feed solutions, while at the same time the

permselectivity of IEMs decreased because of the concentration of high salinity solution and so limited the power generation [71].

The effect of the multivalent ions that presence in natural feed solution on the performance of RED process is an another topic that studied many times [65,75–77]. In this regard, the presence of multivalent ions in feed solutions leaded to increasing the membrane resistance and so decreasing the RED power density [78]. In addition, the uphill transport of multivalent ions opposite of their concentration gradient in solution from low into high concentrate side lead to decreasing the RED stack voltage and power density as well [76,79]. For example, performing the RED performance measurement using natural feed solutions contain multivalent ions showed around 50% power reduction compare with the same measurement using model feed solutions [28]. Using monovalent selective membrane recommended in order to diminish the effect of multivalent ions on RED process performance [78,79]. Using monovalent selective membrane can reduce the uphill transport as well as decreasing the effect of multivalent ions on membrane resistance.

1.5.2 Effect of feed flow rate and temperature on RED performance

Changing the feed flow rate in RED process has multi-effect in different parameters. Increasing the feed solution leads to improving the ionic and solution mixing, reducing the non-ohmic resistance, increasing the electromotive force, enhancing the pumping energy, and decreasing the effect of changing the conductivity of low concentrate compartment during ion transport [16,38,53,69,80–82]. Hence, an optimum flow velocity should be identify for maximizing the net power density which reported on the range of 1 cm/s in lab-scale RED process [67].

The temperature of feed solutions has effect on solution conductivity and electromotive force [67,72]. In addition, the effect of temperature need to be consider, since the feed temperature would change because of climate change and season [15,38,71,83]. In this regard, Mei et al. showed the significant enhance in RED power performance at 60 °C [83].

1.5.3 Fouling in RED process

Using natural feed solutions for RED process would increase the fouling on both membrane and spacers which lead to decreasing the RED power performance because of increasing the resistance [28,84]. Type of membranes and their fixed charge group have effect on the type and rate of fouling. For example, the fouling type on negatively charge CEMs is mainly scaling, while positively charged AEMs are more sensitive to organic fouling and biofouling [28,85]. In addition to membrane, spacers are also sensitive to fouling formation specially biofouling type [62]. In order to reduce the impact of spacers on fouling, using profiled membranes have proposed instead of non-conductive spacers. In this regard, *Vermaas* el al. reported 20% increasing in power density when using profiled membranes compare with RED stack with membrane and non-conductive spacers [28]. In addition, the place of fouling whether in high concentrate compartment or low concentrate compartment can have different impact on power density. *Kingsbury* et al. showed that the effect of natural organic matter as foulants presence in low concentrate compartment was high than that in high concentrate compartment [84]. In chapter 5 of this study, we represent a comprehensive study on the effect of fouling and decreasing its impact on RED performance.

1.5.4 RED pilot-scale

Pilot scale testing of the RED process is an essential step for scaling up the RED process from lab scale into commercial. Until now, there are a few studies on RED pilot plant in Netherlands, Italy [45,63], South Korea [86], and Japan (our study). The first pilot scale RED performance measurement performed in Afsluitdijk, Netherlands using seawater and fresh water as feed solutions, but the operational data is not available to the public. In 2016, *Tedesco* et al. reported the experimental data of a pilot-scale RED stack located in the south of Italy, consisted of 125 cell pairs (44 × 44 cm^2) using natural and model brackish water (0.03 M NaCl) and saturated brine (4-5 M NaCl) as the feed solutions [45]. They reported the power out of 40 W when using natural feed solution, while the power output increased around 60% into 65W under the condition of using model feed solutions. They scaled up their pilot plant by adding to more RED units which consist of 500 cell pairs (44 × 44 cm^2) each. The maximum power output using natural and model feed solutions reported 330 W and 700 W, respectively [63]. In other study, *Nam* et al. reported the data of one of the biggest RED pilot-scale plant with 1000 cell pair and 250 m^2 total membrane area using municipal wastewater effluent (1.3-5.7 mS/cm) and seawater as feed solutions [86]. They reported the maximum power of 95.8 W at a velocity of 1.5 cm/s feed flow velocity. Our study on developing and investigation the RED pilot-scale plant represent in chapters 3 and 6.

1.6 Aim and outline of this study

The main purpose of studying in different type of renewable source of energy include RED process is to finally commercialize the process and produce actual energy

especially in Japan due to lack of natural energy sources. Compare with other renewable source of energy, RED using salinity gradient is counted as one of the new process that need more investigation and practical study in order to scale up into commercial level. Although in last two decades different studies have performed on improving and investigation of RED process, but there are still many unknown effective parameters in both lab and pilot scale of RED process. It would be very difficult and risky that commercialized the RED process without having comprehensive knowledge on different phenomena that govern on this process. Operating the RED process in pilot scale would be one of most important and necessary step before commercializing this process. The main target of this study is to develop, design, and operate one of the biggest pilot-scale RED plant with the maximum power density production of 1.5 W/m^2 which is the highest amount among other RED studies in pilot-scale. This would be a big step in order to start commercializing RED process specially in Japan. This thesis consists of 5 experimental chapters (Chapter 2～6) except introduction and summary (Chapter 1 and 7). The respective experimental chapters focused on the important research topics such as to improve **"RED stack design" (Chapter 2)**, to optimize the **"RED operation condition" (Chapter 3)**, to find out suitable **"RED applications" (Chapter 4)**, and to find out suitable **"pre-treatment method for RED" (Chapter 5)**, and to estimate **"scale-up of RED stack" (Chapter 6)** using high number of stacked IEMs with large effective membrane area, respectively.

In this regard, in **Chapter 2** the effect of spacer on the RED stack internal resistance based on spacer geometry has investigated. Therefore, a numerical modeling based on spacer geometry properties such as porosity, area fraction, and volume fraction has

developed in order to reflect the effect of spacer on RED stack non-ohmic resistance. For the first time, the both effect of spacer on solution compartment and membrane presented in this study. Considering this numerical modeling could be helpful in order to design novel spacers to minimize the effect of spacer on RED stack internal resistance without performing experiment which are time and cost consuming. The best spacer proposed to utilize for RED pilot-scale.

In **Chapter 3**, The effect of feed solution temperature has investigated on a pilot-scale RED stack power generation performance. The main feed solutions that considered for RED process are known as seawater and river water. However, the temperature of both seawater and river water depend on climate condition. Since the most appropriate location to apply RED process would be close to the sea, more comprehensive investigation was needed on the effect of feed solution temperature on pilot-scale RED performance. The result of this chapter has consider in order to find the best location for set upping the pilot-scale RED stack.

Although seawater and river water have mainly considered as an appropriate feed solution for RED process, but it is notable that river waters are mainly used for human demand such as farming and drinking. Therefore, it's necessary to find other suitable and high potential feed solutions for RED process. In this regard, In **Chapter 4**, a typical salt production plant in Japan with different discharge solutions considered as one of the high potential place for energy harvesting using RED process. This salt plant equipped with evaporation and ED system and contains 5 main discharge solutions with different salinity. Since these solutions are already passed many filtration steps, there is no need to apply special pre-filtration steps for RED process which is cost consuming. In this study, both

standard and one side monovalent selective membranes have investigated to find the best and appropriate types of membrane if natural feed solutions used in RED process. The results of this chapter helped us to find the best membranes combination in pilot-scale RED plant.

In **Chapter 5**, a wastewater center of Japan has considered as another high potential place for applying RED process. This center is located close to the sea and consequently the seawater is available as one of the feed solution for RED. In this center, municipal wastewater first treat using active carbon sludge and then purge into the sea. We investigate the possibility of using municipal wastewater that purge into the in order to use as low concentrate solution in RED process. In this regard, the effect of both physical and chemical pretreatment of municipal wastewater investigated on the performance of RED process. The results of this chapter considered in order to find the best pre-treatment procedure for pilot-scale RED plant.

In **Chapter 6**, a seawater desalination company in Okinawa has considered as another high potential placed to perform the RED process for energy production. Increasing the salinity gradient through the feed solutions in RED process is an effective way to increase the power generation. In this regards, the high concentrated seawater known as RO brine would be an appropriate alternative to seawater because of high salinity. RO brine from seawater desalination plant is usually purged into the sea while it passed many filtration stages and appropriate to use as RED feed solution. The research question and topic of each chapter has shown in table 1.

Table 1. Topics and outline of thesis

Chapter	Research question	Topic
2	How is the effect of spacer geometry on RED stack internal resistance?	Effect of spacer geometry on membrane and solution compartment resistances in reverse electrodialysis
3	What is the response of pilot-scale RED stack on changing the feed solutions temperature?	The effect of feed solution temperature on the power output performance of a pilot-scale reverse electrodialysis (RED) system with different intermediate distance
4	How much is the potential of salt production plant to apply RED process and what is the best membrane combination?	Evaluation of energy harvesting from discharged solutions in a salt production plant by reverse electrodialysis (RED)
5	What is the best pretreatment procedure to use municipal wastewater as a feed solution for RED process?	Reverse electrodialysis for power generation using seawater/municipal wastewater: Effect of coagulation pre-treatment
6	How much is the potential of seawater desalination plant in order to use RO brine as feed solution in RED process?	Power generation performance of a 299 cell pair pilot-scale RED stack with high gross power density

1.7 References

[1] M.Z. Jacobson, Review of solutions to global warming, air pollution, and energy security, Energy Environ. Sci. 2 (2009) 148–173. doi:10.1039/b809990c.

[2] M. Hoel, S. Kverndokk, Depletion of fossil fuels and the impacts of global warming, Resour. Energy Econ. 18 (1996) 115–136. doi:10.1016/0928-7655(96)00005-X.

[3] H.W. Sinn, Public policies against global warming: A supply side approach, Int. Tax Public Financ. 15 (2008) 360–394. doi:10.1007/s10797-008-9082-z.

[4] D. Archer, Fate of fossil fuel CO_2 in geologic time, J. Geophys. Res. C Ocean. 110 (2005) 1–6. doi:10.1029/2004JC002625.

[5] G.H. Brundtland, Reducing risks to health, promoting healthy life, J. Am. Med. Assoc. 288 (2002) 1974. doi:10.1001/jama.288.16.1974.

[6] A. Zecca, L. Chiari, Fossil-fuel constraints on global warming, Energy Policy. 38 (2010) 1–3. doi:10.1016/j.enpol.2009.06.068.

[7] M. Oliver, T. Jackson, The market for solar photovoltaics, Energy Policy. 27 (1999) 371–385. doi:10.1016/S0301-4215(99)00038-5.

[8] C.L. Archer, M.Z. Jacobson, Evaluation of global wind power, J. Geophys. Res. D Atmos. 110 (2005) 1–20. doi:10.1029/2004JD005462.

[9] E. Barbier, Geothermal energy technology and current status: An overview, Renew. Sustain. Energy Rev. 6 (2002) 3–65. doi:10.1016/S1364-0321(02)00002-3.

[10] R. Lamb, How Nuclear Power Works Introduction to How Nuclear Power Works Nuclear Fission: The Heart of the Reactor, (2011) 1–7.

[11] S.J. Zinkle, G.S. Was, Materials challenges in nuclear energy, Acta Mater. 61 (2013) 735–758. doi:10.1016/j.actamat.2012.11.004.

[12] K. Buesseler, M. Aoyama, M. Fukasawa, Impacts of the Fukushima nuclear power plants on marine radioactivity, Environ. Sci. Technol. 45 (2011) 9931–9935. doi:10.1021/es202816c.

[13] R.E. Pattle, Production of electric power by mixing fresh and salt water in the hydroelectric pile, Nature. 174.4431 (1954) 660.

[14] D.A. Vermaas, E. Guler, M. Saakes, K. Nijmeijer, Theoretical power density from salinity gradients using reverse electrodialysis, Energy Procedia. 20 (2012) 170–184. doi:10.1016/j.egypro.2012.03.018.

[15] E. Brauns, Salinity gradient power by reverse electrodialysis: Effect of model parameters on electrical power output, Desalination. 237 (2009) 378–391. doi:10.1016/j.desal.2008.10.003.

[16] J. Veerman, M. Saakes, S.J. Metz, G.J. Harmsen, Reverse electrodialysis: Performance of a stack with 50 cells on the mixing of sea and river water, J. Memb. Sci. 327 (2009) 136–144. doi:10.1016/j.memsci.2008.11.015.

[17] G.Z. Ramon, B.J. Feinberg, E.M.V. Hoek, Membrane-based production of salinity-gradient power, Energy Environ. Sci. 4 (2011) 4423–4434. doi:10.1039/c1ee01913a.

[18] B.E. Logan, M. Elimelech, U. States, Membrane-based processes for sustainable power generation using water, (2012). doi:10.1038/nature11477.

[19] Y. Mei, C.Y. Tang, Recent developments and future perspectives of reverse electrodialysis technology: A review, Desalination. 425 (2018) 156–174. doi:10.1016/j.desal.2017.10.021.

[20] J.D. Isaacs, W.R. Schmitt, Ocean energy: Forms and Prospects, Science (80) 207 (1980) 265–273.

[21] A. Achilli, T.Y. Cath, A.E. Childress, Power generation with pressure retarded osmosis: An experimental and theoretical investigation, J. Memb. Sci. 343 (2009) 42–52. doi:10.1016/j.memsci.2009.07.006.

[22] J.W. Post, J. Veerman, H.V.M. Hamelers, G.J.W. Euverink, S.J. Metz, K. Nymeijer, C.J.N. Buisman, Salinity-gradient power: Evaluation of pressure-retarded osmosis and reverse electrodialysis, 288 (2007) 218–230. doi:10.1016/j.memsci.2006.11.018.

[23] J.N. Weinstein, F.B. Leitz, Electric power from differences in salinity: The dialytic battery, Science (80) 191 (1976) 557–559. doi:10.1126/science.191.4227.557.

[24] R.E. Lacey, Energy by reverse electrodialysis, Ocean Eng. 7 (1980) 1–47. doi:10.1016/0029-8018(80)90030-X.

[25] E. Brauns, Towards a worldwide sustainable and simultaneous large-scale production of renewable energy and potable water through salinity gradient power

by combining reversed electrodialysis and solar power?, Desalination. 219 (2008) 312–323. doi:10.1016/j.desal.2007.04.056.

[26] R.D. Cusick, Y. Kim, B.E. Logan, Energy Capture from Thermolytic Solutions Supp Info, Science (80) 335 (2012) 1474–1477. doi:10.1126/science.1219330.

[27] E. Güler, R. Elizen, D.A. Vermaas, M. Saakes, K. Nijmeijer, Performance-determining membrane properties in reverse electrodialysis, J. Memb. Sci. 446 (2013) 266–276. doi:10.1016/j.memsci.2013.06.045.

[28] D.A. Vermaas, D. Kunteng, M. Saakes, K. Nijmeijer, Fouling in reverse electrodialysis under natural conditions, Water Res. 47 (2013) 1289–1298. doi:10.1016/j.watres.2012.11.053.

[29] S. Mehdizadeh, M. Yasukawa, T. Abo, Y. Kakihana, M. Higa, Effect of spacer geometry on membrane and solution compartment resistances in reverse electrodialysis, J. Memb. Sci. 572 (2019) 271–280. doi:10.1016/j.memsci.2018.09.051.

[30] T. Xu, Ion exchange membranes: State of their development and perspective, J. Memb. Sci. 263 (2005) 1–29. doi:10.1016/j.memsci.2005.05.002.

[31] M.Y. Kariduraganavar, R.K. Nagarale, A.A. Kittur, S.S. Kulkarni, Ion-exchange membranes: Preparative methods for electrodialysis and fuel cell applications, Desalination. 197 (2006) 225–246. doi:10.1016/j.desal.2006.01.019.

[32] J.G. Hong, B. Zhang, S. Glabman, N. Uzal, X. Dou, H. Zhang, X. Wei, Y. Chen, Potential ion exchange membranes and system performance in reverse

electrodialysis for power generation: A review, J. Memb. Sci. 486 (2015) 71–88. doi:10.1016/j.memsci.2015.02.039.

[33] P. Długołecki, K. Nymeijer, S. Metz, M. Wessling, Current status of ion exchange membranes for power generation from salinity gradients, J. Memb. Sci. 319 (2008) 214–222. doi:10.1016/j.memsci.2008.03.037.

[34] G.M. Geise, M.A. Hickner, B.E. Logan, Ionic resistance and permselectivity tradeoffs in anion exchange membranes, ACS Appl. Mater. Interfaces. 5 (2013) 10294–10301. doi:10.1021/am403207w.

[35] D.A. Vermaas, M. Saakes, K. Nijmeijer, Enhanced mixing in the diffusive boundary layer for energy generation in reverse electrodialysis, J. Memb. Sci. 453 (2014) 312–319. doi:10.1016/j.memsci.2013.11.005.

[36] J.W. Post, H.V.M. Hamelers, C.J.N. Buisman, Energy recovery from controlled mixing salt and fresh water with a reverse electrodialysis system, Environ. Sci. Technol. 42 (2008) 5785–5790. doi:10.1021/es8004317.

[37] D.A. Vermaas, M. Saakes, K. Nijmeijer, Doubled power density from salinity gradients at reduced intermembrane distance, Environ. Sci. Technol. 45 (2011) 7089–7095. doi:10.1021/es2012758.

[38] P. Długołęcki, A. Gambier, K. Nijmeijer, M. Wessling, Practical potential of reverse electrodialysis as process for sustainable energy generation, Environ. Sci. Technol. 43 (2009) 6888–6894. doi:10.1021/es9009635.

[39] J. Veerman, M. Saakes, S.J. Metz, G.J. Harmsen, Reverse electrodialysis:

Evaluation of suitable electrode systems, J. Appl. Electrochem. 40 (2010) 1461–1474. doi:10.1007/s10800-010-0124-8.

[40] A. R, Electric power produced from two solutions of unequal salinity by reverse electrodilysis, Indian J. Chem. 31 (1992).

[41] O. Scialdone, C. Guarisco, S. Grispo, A.D. Angelo, A. Galia, Investigation of electrode material - Redox couple systems for reverse electrodialysis processes. Part I: Iron redox couples, J. Electroanal. Chem. 681 (2012) 66–75. doi:10.1016/j.jelechem.2012.05.017.

[42] O.S. Burheim, F. Seland, J.G. Pharoah, S. Kjelstrup, Improved electrode systems for reverse electro-dialysis and electro-dialysis, Desalination. 285 (2012) 147–152. doi:10.1016/j.desal.2011.09.048.

[43] X. Zhu, W. He, B.E. Logan, Influence of solution concentration and salt types on the performance of reverse electrodialysis cells, J. Memb. Sci. 494 (2015) 154–160. doi:10.1016/j.memsci.2015.07.053.

[44] F. Suda, T. Matsuo, D. Ushioda, Transient changes in the power output from the concentration difference cell (dialytic battery) between seawater and river water, Energy. 32 (2007) 165–173. doi:10.1016/j.energy.2006.04.005.

[45] M. Tedesco, C. Scalici, D. Vaccari, A. Cipollina, A. Tamburini, G. Micale, Performance of the first reverse electrodialysis pilot plant for power production from saline waters and concentrated brines, J. Memb. Sci. 500 (2016) 33–45. doi:10.1016/j.memsci.2015.10.057.

[46] H. Ohya, Dialytic battery convertible free energy of mixing of sea water and river water, in: Organ. by Korean Inst Chem. Eng., 1983: pp. 451–456.

[47] F.E. Kivait, Energy recovery from saline water by means of electrochemical cells, Science (80). 194 (1976) 719–720. doi:10.1126/science.194.4266.719.

[48] G.L. Wick, Power from salinity gradients, Energy. 3 (1978) 95–100. doi:10.1016/0360-5442(78)90059-2.

[49] Ratkje, S. Kjelstrup, H. Torleif, F. Liv, Effect of biofilm formation on salinity power plant output on labratory scale, AIChE Symp. Ser., 1986: pp. 39–44.

[50] A. Achilli, A.E. Childress, Pressure retarded osmosis: From the vision of Sidney Loeb to the first prototype installation - Review, Desalination. 261 (2010) 205–211. doi:10.1016/j.desal.2010.06.017.

[51] M. Turek, B. Bandura, P. Dydo, Power production from coal-mine brine utilizing reversed electrodialysis, Desalination. 221 (2008) 462–466. doi:10.1016/j.desal.2007.01.106.

[52] J. Veerman, J.W. Post, M. Saakes, S.J. Metz, G.J. Harmsen, Reducing power losses caused by ionic shortcut currents in reverse electrodialysis stacks by a validated model, J. Memb. Sci. 310 (2008) 418–430. doi:10.1016/j.memsci.2007.11.032.

[53] M. Turek, B. Bandura, Renewable energy by reverse electrodialysis, Desalination. 205 (2007) 67–74. doi:10.1016/j.desal.2006.04.041.

[54] J. Veerman, R.M. de Jong, M. Saakes, S.J. Metz, G.J. Harmsen, Reverse

electrodialysis: Comparison of six commercial membrane pairs on the thermodynamic efficiency and power density, J. Memb. Sci. 343 (2009) 7–15. doi:10.1016/j.memsci.2009.05.047.

[55] D.H. Cho, K.H. Lee, Y.M. Kim, S.H. Park, W.H. Lee, S.M. Lee, Y.M. Lee, Effect of cationic groups in poly (arylene ether sulfone) membranes on reverse electrodialysis performance, Chem. Commun. 53 (2017) 2323–2326. doi:10.1039/c6cc08440k.

[56] H.K. Kim, M.S. Lee, S.Y. Lee, Y.W. Choi, N.J. Jeong, C.S. Kim, High power density of reverse electrodialysis with pore-filling ion exchange membranes and a high-open-area spacer, J. Mater. Chem. A. 3 (2015) 16302–16306. doi:10.1039/c5ta03571f.

[57] J.Y. Lee, J.H. Kim, J.H. Lee, S. Kim, S.H. Moon, Morphologically aligned cation-exchange membranes by a pulsed electric field for reverse electrodialysis, Environ. Sci. Technol. 49 (2015) 8872–8877. doi:10.1021/acs.est.5b01151.

[58] J.G. Hong, Y. Chen, Nanocomposite reverse electrodialysis (RED) ion-exchange membranes for salinity gradient power generation, J. Memb. Sci. 460 (2014) 139–147. doi:10.1016/j.memsci.2014.02.027.

[59] E. Guler, Y. Zhang, M. Saakes, K. Nijmeijer, Tailor-made anion-exchange membranes for salinity gradient power generation using reverse electrodialysis, ChemSusChem. 5 (2012) 2262–2270. doi:10.1002/cssc.201200298.

[60] B. Zhang, H. Gao, Y. Chen, Enhanced ionic conductivity and power generation using ion-exchange resin beads in a reverse-electrodialysis stack, Environ. Sci.

Technol. 49 (2015) 14717–14724. doi:10.1021/acs.est.5b03864.

[61] E. Güler, R. Elizen, M. Saakes, K. Nijmeijer, Micro-structured membranes for electricity generation by reverse electrodialysis, J. Memb. Sci. 458 (2014) 136–148. doi:10.1016/j.memsci.2014.01.060.

[62] D.A. Vermaas, M. Saakes, K. Nijmeijer, Power generation using profiled membranes in reverse electrodialysis, J. Memb. Sci. 385–386 (2011) 234–242. doi:10.1016/j.memsci.2011.09.043.

[63] M. Tedesco, A. Cipollina, A. Tamburini, G. Micale, Towards 1 kW power production in a reverse electrodialysis pilot plant with saline waters and concentrated brines, J. Memb. Sci. 522 (2017) 226–236. doi:10.1016/j.memsci.2016.09.015.

[64] J.Y. Nam, R.D. Cusick, Y. Kim, B.E. Logan, Hydrogen generation in microbial reverse-electrodialysis electrolysis cells using a heat-regenerated salt solution, Environ. Sci. Technol. 46 (2012) 5240–5246. doi:10.1021/es300228m.

[65] R.A. Tufa, E. Curcio, W. Van Baak, J. Veerman, S. Grasman, E. Fontananova, G. Di Profio, Potential of brackish water and brine for energy generation by salinity gradient power-reverse electrodialysis (SGP-RE), RSC Adv. 4 (2014) 42617–42623. doi:10.1039/c4ra05968a.

[66] X. Luo, X. Cao, Y. Mo, K. Xiao, X. Zhang, P. Liang, X. Huang, Power generation by coupling reverse electrodialysis and ammonium bicarbonate: Implication for recovery of waste heat, Electrochem. Commun. 19 (2012) 25–28. doi:10.1016/j.elecom.2012.03.004.

[67] M. Tedesco, E. Brauns, A. Cipollina, G. Micale, P. Modica, G. Russo, J. Helsen, Reverse electrodialysis with saline waters and concentrated brines: A laboratory investigation towards technology scale-up, J. Memb. Sci. 492 (2015) 9–20. doi:10.1016/j.memsci.2015.05.020.

[68] N.Y. Yip, D.A. Vermaas, K. Nijmeijer, M. Elimelech, Thermodynamic, energy efficiency, and power density analysis of reverse electrodialysis power generation with natural salinity gradients, Environ. Sci. Technol. 48 (2014) 4925–4936. doi:10.1021/es5005413.

[69] J. Veerman, M. Saakes, S.J. Metz, G.J. Harmsen, Electrical power from sea and river water by reverse electrodialysis: A first step from the laboratory to a real power plant, Environ. Sci. Technol. 44 (2010) 9207–9212. doi:10.1021/es1009345.

[70] K. Kwon, J. Han, B.H. Park, Y. Shin, D. Kim, Brine recovery using reverse electrodialysis in membrane-based desalination processes, Desalination. 362 (2015) 1–10. doi:10.1016/j.desal.2015.01.047.

[71] A. Daniilidis, D.A. Vermaas, R. Herber, K. Nijmeijer, Experimentally obtainable energy from mixing river water, seawater or brines with reverse electrodialysis, Renew. Energy. 64 (2014) 123–131. doi:10.1016/j.renene.2013.11.001.

[72] M. Tedesco, A. Cipollina, A. Tamburini, G. Micale, J. Helsen, M. Papapetrou, REAPower: use of desalination brine for power production through reverse electrodialysis, Desalin. Water Treat. 53 (2015) 3161–3169. doi:10.1080/19443994.2014.934102.

[73] A. Emdadi, P. Gikas, M. Farazaki, Y. Emami, Salinity gradient energy potential at the hyper saline Urmia Lake - ZarrinehRud River system in Iran, Renew. Energy. 86 (2016) 154–162. doi:10.1016/j.renene.2015.08.015.

[74] W. Li, W.B. Krantz, E.R. Cornelissen, J.W. Post, A.R.D. Verliefde, C.Y. Tang, A novel hybrid process of reverse electrodialysis and reverse osmosis for low energy seawater desalination and brine management, Appl. Energy. 104 (2013) 592–602. doi:10.1016/j.apenergy.2012.11.064.

[75] A.H. Avci, P. Sarkar, R.A. Tufa, D. Messana, P. Argurio, E. Fontananova, G. Di Profio, E. Curcio, Effect of Mg^{2+} ions on energy generation by Reverse Electrodialysis, J. Memb. Sci. 520 (2016) 499–506. doi:10.1016/j.memsci.2016.08.007.

[76] D.A. Vermaas, J. Veerman, M. Saakes, K. Nijmeijer, Influence of multivalent ions on renewable energy generation in reverse electrodialysis, Energy Environ. Sci. 7 (2014) 1434–1445. doi:10.1039/c3ee43501f.

[77] J.G. Hong, W. Zhang, J. Luo, Y. Chen, Modeling of power generation from the mixing of simulated saline and freshwater with a reverse electrodialysis system: The effect of monovalent and multivalent ions, Appl. Energy. 110 (2013) 244–251. doi:10.1016/j.apenergy.2013.04.015.

[78] J.W. Post, H.V.M. Hamelers, C.J.N. Buisman, Influence of multivalent ions on power production from mixing salt and fresh water with a reverse electrodialysis system, J. Memb. Sci. 330 (2009) 65–72. doi:10.1016/j.memsci.2008.12.042.

[79] E. Güler, W. van Baak, M. Saakes, K. Nijmeijer, Monovalent-ion-selective

membranes for reverse electrodialysis, J. Memb. Sci. 455 (2014) 254–270. doi:10.1016/j.memsci.2013.12.054.

[80] L. Gurreri, A. Tamburini, A. Cipollina, G. Micale, M. Ciofalo, CFD prediction of concentration polarization phenomena in spacer-filled channels for reverse electrodialysis, J. Memb. Sci. 468 (2014) 133–148. doi:10.1016/j.memsci.2014.05.058.

[81] R.A. Tufa, E. Curcio, E. Brauns, W. van Baak, E. Fontananova, G. Di Profio, Membrane Distillation and Reverse Electrodialysis for Near-Zero Liquid Discharge and low energy seawater desalination, J. Memb. Sci. 496 (2015) 325–333. doi:10.1016/j.memsci.2015.09.008.

[82] X. Zhu, W. He, B.E. Logan, Reducing pumping energy by using different flow rates of high and low concentration solutions in reverse electrodialysis cells, J. Memb. Sci. 486 (2015) 215–221. doi:10.1016/j.memsci.2015.03.035.

[83] Y. Mei, C.Y. Tang, Co-locating reverse electrodialysis with reverse osmosis desalination: Synergies and implications, J. Memb. Sci. 539 (2017) 305–312. doi:10.1016/j.memsci.2017.06.014.

[84] R.S. Kingsbury, F. Liu, S. Zhu, C. Boggs, M.D. Armstrong, D.F. Call, O. Coronell, Impact of natural organic matter and inorganic solutes on energy recovery from five real salinity gradients using reverse electrodialysis, J. Memb. Sci. 541 (2017) 621–632. doi:10.1016/j.memsci.2017.07.038.

[85] M. Vaselbehagh, H. Karkhanechi, R. Takagi, H. Matsuyama, Biofouling phenomena on anion exchange membranes under the reverse electrodialysis process,

J. Memb. Sci. 530 (2017) 232–239. doi:10.1016/j.memsci.2017.02.036.

[86] J. Nam, K. Hwang, H. Kim, H. Jeong, H. Kim, E. Jwa, S. Yang, J. Choi, C. Kim, J. Han, N. Jeong, Assessing the behavior of the feed-water constituents of a pilot-scale 1000-cell-pair reverse electrodialysis with seawater and municipal wastewater effl uent, Water Res. 148 (2019) 261–271. doi:10.1016/j.watres.2018.10.054.

Chapter 2

Effect of spacer geometry on membrane and solution compartment resistances in reverse electrodialysis

2.1 Introduction

The world energy demand has been increased due to raising the world population in last decades [1]. In addition, global warming and environmental pollution have become a further important reason for developing the renewable and feasible energy conversion technologies [2]. Salinity gradient power (SGP) has become as one of the sustainable and clean energy sources among different type of renewable energy such as solar, wind, geothermal and biomass [3]. SGP is an available energy that can be produced by a mixing of two solutions with different salinity (*e.g.*, a combination of seawater and river water) due to difference in electrochemical potential [4]. It is estimated that 2.4 – 2.6 TW power could be produced by mixing all available discharged river water with seawater, based on Gibbs free energy of mixing [5].

Reverse electrodialysis (RED), a membrane-based process, has become one of promising procedures for the SGP capturing. In RED process, concentrate and dilute solutions flow alternatively between cation-exchange membrane (CEM) and anion-exchange membrane (AEM) which are permeable for cations and anions, respectively. Consequently, cations and anions diffuse from the concentrate to the dilute solution compartment through CEM and AEM, respectively, and these ion passages in opposite direction can be converted into an electric power by redox reaction at suitable electrodes.

In RED stack, spacers play an important role to keep distance between membranes and improve ions distribution in solution compartment due to their mesh grid state [6]. In addition to the RED case, spacers are also used for the most membrane-based processes as spacer-filled channel (*e.g.,* electrodialysis (ED), spiral-wound (SW) module

in reverse osmosis (RO) and so on). In these applications, spacer geometry such as filaments thickness, distance and angles have always been considered as important effective factors on the process performance such as pressure drop, mass transfer, and resistance [6–8]. Accordingly, different aspects of spacer have been considered in RED process principally during previous years [9]. Since the RED process generally consists of the spacer filled channel like ED process, the effect of spacer geometry on the RED process performance including pressure drop, mass transfer and resistance should be also concerned. There are some studies that especially focus on the effect of spacer geometry on RED performances such as pressure drop [10,11]. However, since the main purpose in RED process is electrical power production and the internal resistance of RED stack should be minimized to achieve high power density [12], the investigation about the effect of spacer geometry on the RED stack resistance has usually become superior to pressure drop. The internal resistance of RED stack contains ohmic and non-ohmic (*e.g.*, concentration polarization, change of bulk solution concentration) resistances [13]. The ohmic regime of cell pair resistance (R_{CP}) in RED stack mainly consists of sum of membrane and solution compartment resistances. Therefore, the single cell pair resistance of RED stack without considering the spacer shadow effect can be simply written as follows [3]:

$$R_{cp} = R_{sea} + R_{river} + R_{AEM} + R_{CEM} \quad [1]$$

where R_{sea} and R_{river} are the resistance of seawater and river water compartments, respectively. In addition, R_{AEM} and R_{CEM} are AEM and CEM resistances, respectively. Moreover, it is expected that the presence of spacers between membranes must increase both the membrane and solution compartment resistances due to covering the membrane effective area and make ionic transport in tortuous ways, respectively. These are often

called as spacer shadow effects on membrane and solution compartment, respectively. Therefore, Eq. (1) should be converted by considering the shadow effects as follows [12,13]:

$$R_{cp} = \beta_{sol}(R_{sea} + R_{river}) + \beta_{mem}(R_{AEM} + R_{CEM}) \quad [2]$$

where β_{sol} and β_{mem} are coefficients to express the spacer shadow effects on solution compartments and on membrane, respectively.

So far, there are a few studies on the spacers shadow effects (both β_{sol} and β_{mem}) in RED stack [6,14–16]. *Vermaas et al*. investigated the β_{sol} using spacers with 60, 100 and 485 μm thicknesses without considering the β_{mem}, and indicated that the β_{sol} of spacer with 485 μm thickness in RED stack was almost 5 and 3 times higher than those with 60 and 100 μm thicknesses, respectively [14]. Moreover, since RED stack resistance has an inverse proportional effect on the RED gross power output, the β_{sol} with 320 μm thickness caused the 72 % diminution of RED gross power [15]. Therefore, their results clearly suggested that the spacer shadow effects has a large impact on the resultant RED performance.

In addition to the experimental evaluation for identifying the spacer shadow effect as well as the ohmic resistance, a simple predictive way for estimating both β_{sol} and β_{mem} are also required since the experimental approach is time-consuming. Post *et al*. firstly investigated both β_{sol} and β_{mem} separately, and searched suitable dimensional parameters of the spacers correlating with only β_{sol} [6]. Consequently, they proposed a good correlation between the inverse squared of porosity of the spacer ($1/\varepsilon^2$) and β_{sol}. More recently, *Wagholikar et al*. proposed that a mean shadow factor, β_{mean}, based on both area and

volume fractions of the spacer filaments would be more suitable to estimate the β_{sol} from the experimental data using 4 types of spacers with relatively high porosity range [17]. Because the β_{mean} is defined as the average of area and volume shadow factor, their careful consideration of the effect of both area fraction and volume fraction on the compartment resistance based on ion passage in tortuous way outside the spacer is more suitable for any spacers than those from only porosity. However, because the experimental data is still few, the further analysis is still required to prove their proposals. In addition, a suitable parameter of the spacer for estimating the β_{mem} has not been proposed yet, although it also might have a notable effect when using low porous spacers.

Therefore, in this study, the shadow effect of 16 types of spacers having a wide range of thickness and porosity have been experimentally investigated to identify the shadow effects on the membrane and solution compartment separately. Moreover, the relationship between spacer geometry and the shadow effects of them have been systematically evaluated by using the spacer geometries such as filaments diameter, distance and angle, and the spacer properties such as porosity, area fraction, volume fraction and their combinations. We also evaluated the contribution of the respective shadow effects on their total resistance in RED stack.

2.2 Theory

2.2.1 Spacer geometry and properties

According to previous works [17–19], the spacer geometries such as filaments diameter, distance and angle with each other of 16 types were measured. After then, the spacer properties such as porosity, volume fraction, area fraction, volume shadow factor,

mean shadow factor and so on were calculated from the geometries. Here, we further concerned that vertical and horizontal filaments have different diameters and distances with each other to obtain higher accurate calculation results than the previous literatures [17–19]. Fig. 1 shows an illustration of spacer with the length (L), width (W), its angle (θ) and the filaments diameter (D_W and D_L) as the spacer geometries, where the green area shows a repeatable unit of the spacer used for the geometry properties calculation. In RED, ion passage direction is perpendicular to the spacer. Table 1 presents the equations for calculating the spacer properties under an assumption that filament has a round shape. In this table, t_{sp} is the spacer thickness. Here, the measured angles between filaments in all spacers were with 5º variation from right angle (90 ± 5º), and therefore, we assumed the effect of angels on filament area and volume per unit cell can be negligible that made the respective equations more simplified.

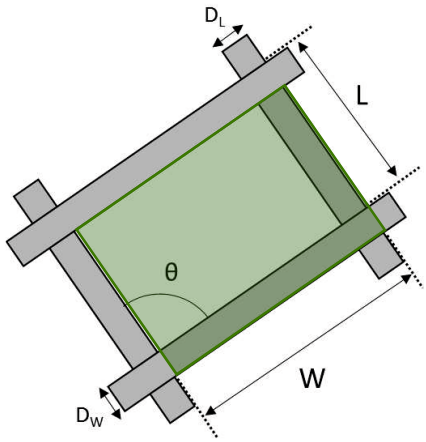

Figure 1. Scheme of net spacer geometry for geometry calculation

Table 1. Spacer geometry calculation equation for a unit cell

Spacer properties	Equation
Filaments area per unit cell (mm^2)	$a_f = (D_W.W + D_L(L - D_W))$
Unit cell area (mm^2)	$a_t = W.L.\sin\theta$
Fiber area fraction	$A' = {}^{a_f}/_{a_t}$
Area shadow effect	$\beta_{area} = {}^{1}/_{(1-A')}$
Filament volume of each unit cell (mm^3)	$v_f = \frac{\pi(D_W^2.W + D_L^2.L)}{4}$
Unit cell volume (mm^3)	$v_t = a_t t_{sp}$
Porosity (ε)	$\varepsilon = 1 - \frac{\pi D_W^2.W + \pi D_L^2.L}{4t_{sp}.l.\mathrm{W}.\sin\theta}$
Fiber volume fraction	$v' = {}^{v_f}/_{v_t}$
Volume shadow factor	$\beta_{vol} = 1/(1-v')$
Mean shadow factor	$\beta_{mean} = (\beta_a + \beta_v)/2$

2.2.2 Spacer shadow effect on RED cell pair resistance

In the absence of spacer, the theoretical ohmic resistance of each cell pair in RED stack can be simply expressed by using solution compartment resistance and membrane resistance as follows [20]:

$$R_{cp} = \left(\frac{t_{com,d}}{k_d} + \frac{t_{com,c}}{k_c}\right) + R_{CEM} + R_{AEM} \quad [3]$$

where t_{com} is compartment thickness and k is the conductivity of compartments of the RED stack. Subscript d and c means dilute and concentrate compartments, respectively.

In the presence of spacer with the non-conductive material, since the spacer occupies the feed solution compartments volumes in addition to covering the membrane effective area, it would increase the RED cell resistance. Thus, *Post et al*. proposed a parameter, β, to express the part of membrane area masked by the spacer, and $1/\varepsilon^2$ to reflect the tortuous ion transport in solution compartments as follows [6]:

$$R_{cp} = \frac{1}{\varepsilon^2}\left(\frac{t_{com,d}}{k_d} + \frac{t_{com,c}}{k_c}\right) + \frac{R_{CEM}}{1-\beta} + \frac{R_{AEM}}{1-\beta} \quad [4]$$

On the other hands, *Wagholikar et al*. also proposed β_m to express the spacer shadow effect on solution compartments without considering those on membrane as follows [17]:

$$R_{cp} = \beta_m\left(\frac{t_{com,d}}{k_d} + \frac{t_{com,c}}{k_c}\right) + R_{CEM} + R_{AEM} \quad [5]$$

Both two latter models need to be modified by more comprehensive study. Applying inverse squared of porosity in post *et al.* model has proposed for a few number of spacers with high range of porosity. In addition, *Wagholikar et al.* model just considers the spacer shadow effect in solution compartment by studying on a few spacers. In fact, the spacer shadow effect on both membrane and solution compartment are mainly related to the spacer geometry. The relationship between spacer geometry with β_{sol} and β_{mem} from Eq. 2 which proposed as factors to express the spacer shadow effects on solution compartment and membrane resistance, respectively, have been determined in this study. Four steps experiments which are described in the following section have identified to find the relationship between spacer geometry and spacer shadow effect on both membrane and solution compartment in RED stack.

2.3 Experimental

2.3.1 Materials and chemicals

NaCl solution with 0.508 M concentration was made with 99.5 % NaCl (NACALAI TESQUE, Inc. Japan) and deionized water purified with ion exchange resin cartridge (YA-053, ORGANO, Japan). 16 types of woven spacers have been purchased from ASTOM Corporation and SEFAR, and were abbreviated as spacers A-P. Neosepta CMX and AMX were obtained from ASTOM Corporation, Japan. Before use, these membranes were immersed in deionized water and 0.508 M NaCl solution for 24 h, respectively.

2.3.2 Spacer geometry measurement

Spacer geometries of the 16 types such as filaments diameter (D_W, D_L), angels (θ) and distance (W, L) were characterized by using an optical microscopic (Model-VHX-1000, KEYENCE, Japan) according to a previous literature [17]. The spacers thickness (t_{sp}) were measured by using a thickness meter (Code No. 156-101-10, MITUTOYO Company, CHINA). After then, these obtained parameters were used to calculate the spacers properties such as porosity (ε), area fraction (A'), mean shadow effect (β_m) and so on.

2.3.3 Resistance measurements

A self-made acrylic cell with two parallel Pt electrode was used to measure the cell resistance with different spacers and membrane as shown in Fig. 2. The effective area for membrane and spacer resistance measurement was 1 cm^2. Spacers, CMX and AMX were cut in a circle shape with 1.9 cm diameter, and set at the acrylic cell. Two plastic washers

were also equipped at both sides of the membrane and spacer to prevent the solution leakage. 0.508 M NaCl solution was purged inside the apparatus between electrodes connecting with a LCR meter (Model: AD-5827, A&D Company, TAIWAN) to measure solution and sample resistances, and the apparatus was then immersed in water bath at 24±0.1 °C. The solution and membrane resistances with/without spacers were measured with an alternative current (AC) of 10 kHz frequency to prevent the effect of concentration polarization on the measured resistance values.

To separately investigate the spacers shadow effects on membrane and solution compartment, four-step experiments have been performed as shown in Fig. 2(A)-(C). Firstly, we measured the bulk solution resistance between the electrodes without spacer, R_b, and the resistance with both the bulk solution and membrane (CMX or AMX) between the electrodes, R_{b+m}. The membrane resistances, R_m, of CMX and AMX were then obtained by subtracting the R_b from R_{b+m} as follows:

$$(R_m)_i = (R_{b+m})_i - R_b \quad [6]$$

where the subscribe i refers to membrane type. In the next, each spacer was set at the cell with solution, and the resistance of the solution compartment with the spacer and also the thickness same as spacers in addition to the bulk solution, R_{b+s}, were then measured. After then, according to the same way in R_m measurement, we calculated the compartment resistance of the solution with spacer, R_s, by subtracting the R_b from R_{b+s} as follows:

$$R_s = R_{b+s} - R_b \quad [7]$$

At the final step, each spacer set in the cell with the membrane to totally measure the solution compartment with spacer, membrane, and bulk solution resistance, R'_{b+s+m},

where the superscript (′) means the resistance including the shadow effect of the spacer on the membrane. After then, the compartment resistance of solution with spacer including the shadow effect on the membrane, R'_s, was calculated as follows:

$$(R_s')_i = (R'_{b+s+m})_i - (R_m)_i - R_b \quad [8]$$

Due to the presence of shadow effect on membrane, the values of $(R_s')_i$ should be higher than R_s. Here, this difference between $(R_s')_i$ and R_s was define as a resistance of spacer shadow effect on membrane, $(R_{sh})_i$, as shown in Eq. 9. In addition, to express the amount of spacer shadow effect on the membrane, the resistance ratio of $(R_{sh})_i$ to R_m, $RR_{(sh/m)i}$ was also defined as follows:

$$(R_{sh})_i = (R'_s)_i - R_s \quad [9]$$

$$RR(sh/m)_i = \frac{(R_{sh})_i}{(R_m)_i} \quad [10]$$

Moreover, because both side of the membrane is covered by the spacer in RED stack, the total spacer shadow effect on membrane is two times higher than that on one side of the membrane. Therefore, the spacer shadow effect on membrane in RED stack, β_{mem}, can be described under an assumption that the membranes have a symmetric structure, same surface morphology at the both side as follows:

$$(\beta_m)_i = 1 + 2RR(sh/m)_i \quad [11]$$

On the other hands, as shown in Eq. 5, the β_{sol} can be expressed by using R_s and the solution compartment resistance ($R_{sol(com)}$) with the distance, t_{com}, and conductivity, k, as follows [17]:

$$\beta_{sol} = \frac{R_s}{R_{sol(com)}} = R_s \frac{k}{h} \quad [12]$$

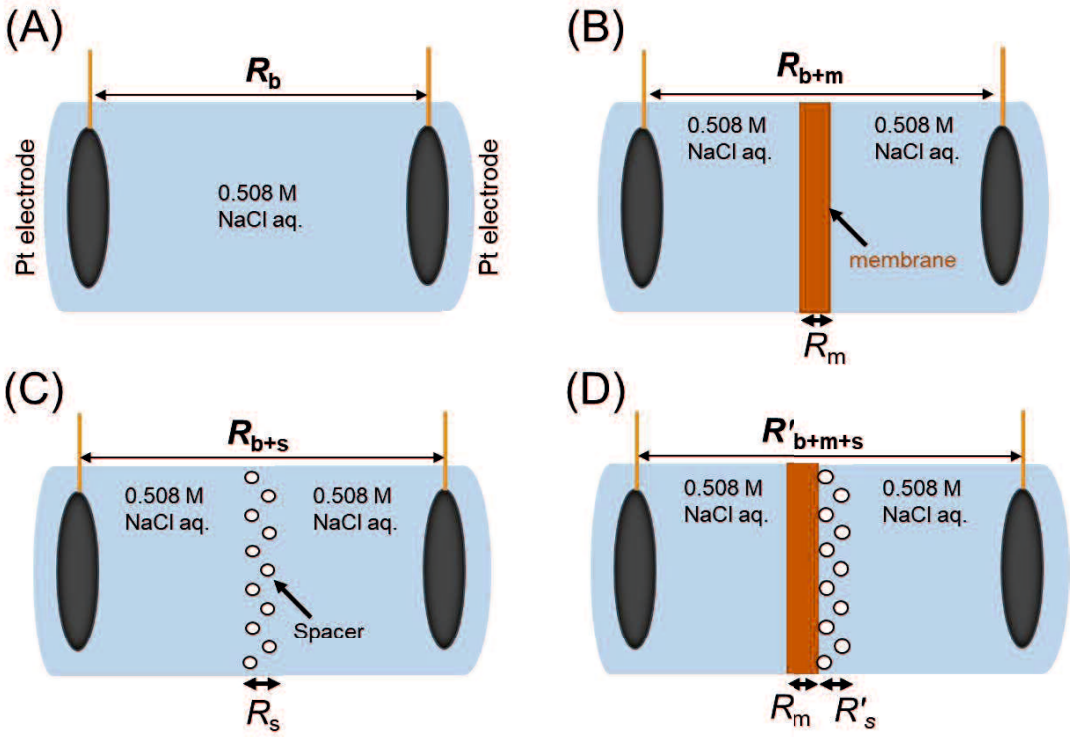

Figure 2. Resistance measurements (A) bulk solution without membrane and spacer, (B) with membrane, (C) with spacer, (D) with both membrane and spacer. By setting membrane and/or spacers the distance between electrodes increase same as the thickness of them in cell.

2.4 Result and discussion

2.4.1 Spacer geometry

Optical microscopic views of the spacers with a same magnification are shown in Fig. 3. The high magnified views with all the obtained parameters of the spacers is also shown in Appendix A (Tables A1 and A2). The calculated geometric properties of the spacer are presented in Table 2 and Fig. 4. The thickness and porosity of the 16 spacers were from 0.100 mm to 0.564 mm and in 56–85 %, respectively, and the porosities of them

were independent of their thickness as shown in Fig. 4(A). Type-A and B have almost same and thinner thickness (about 100 μm), but different in the porosity (A: 84.4%, B: 66.1%). Type-C, D, E, F, G and H have almost similar thickness (180-240 μm) with different porosity in a wide range (56.6 ~ 83.6%), and the other types have different and thicker thickness (317-564 mm) with different porosity (67-80%). The average fiber diameters (= $(D_W + D_L)/2$) of the spacers were about a half of the total spacer thickness (t_{sp}), and the fiber area fractions (A') were from 0.288 to 0.670 with an inverse relation to the porosity as shown in Fig. 4(B). In all spacers except the type-K, the fibers were knitted alternatively.

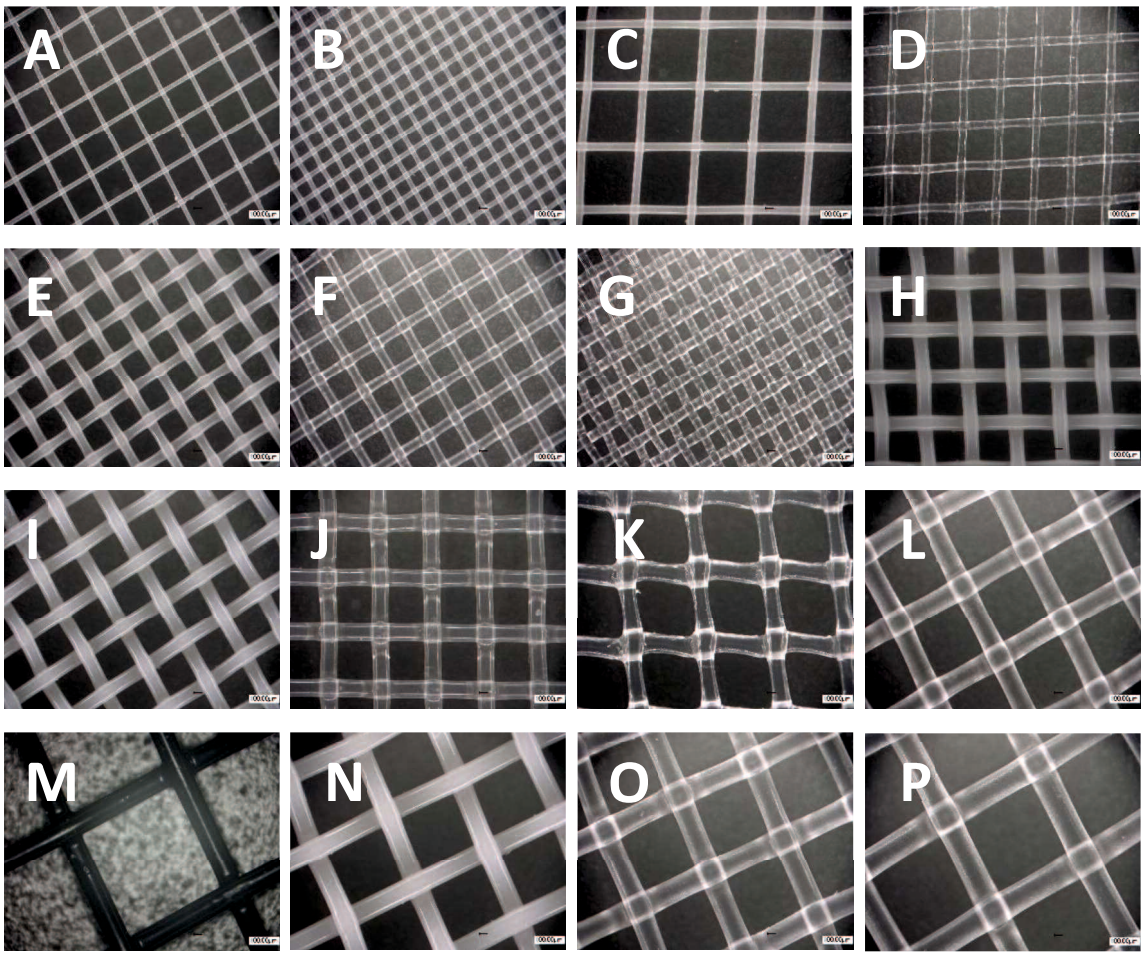

Figure. 3. Optical micrographs of spacers from A to P.

Table 2. Geometries and properties of 16 type spacers used in this study.

Spacer type	t_{sp} (mm)	D_W (mm)	D_L (mm)	W (mm)	L (mm)	Θ (°)
Type-A	0.100	0.064	0.063	0.411	0.405	90
Type-B	0.104	0.069	0.069	0.215	0.209	90
Type-C	0.180	0.115	0.115	0.690	0.722	84
Type-D	0.184	0.105	0.112	0.469	0.461	85
Type-E	0.199	0.138	0.138	0.409	0.411	90
Type-F	0.210	0.131	0.131	0.400	0.423	90
Type-G	0.231	0.115	0.132	0.333	0.253	90
Type-H	0.240	0.190	0.190	0.544	0.545	90
Type-I	0.317	0.189	0.189	0.547	0.548	90
Type-J	0.357	0.213	0.213	0.653	0.646	90
Type-K	0.375	0.231	0.212	0.874	0.843	94
Type-L	0.445	0.269	0.274	0.900	0.927	90
Type-M	0.467	0.300	0.300	1.620	1.570	90
Type-N	0.482	0.271	0.276	0.976	0.908	90
Type-O	0.498	0.293	0.291	0.980	0.961	90
Type-P	0.564	0.337	0.337	1.274	1.272	90

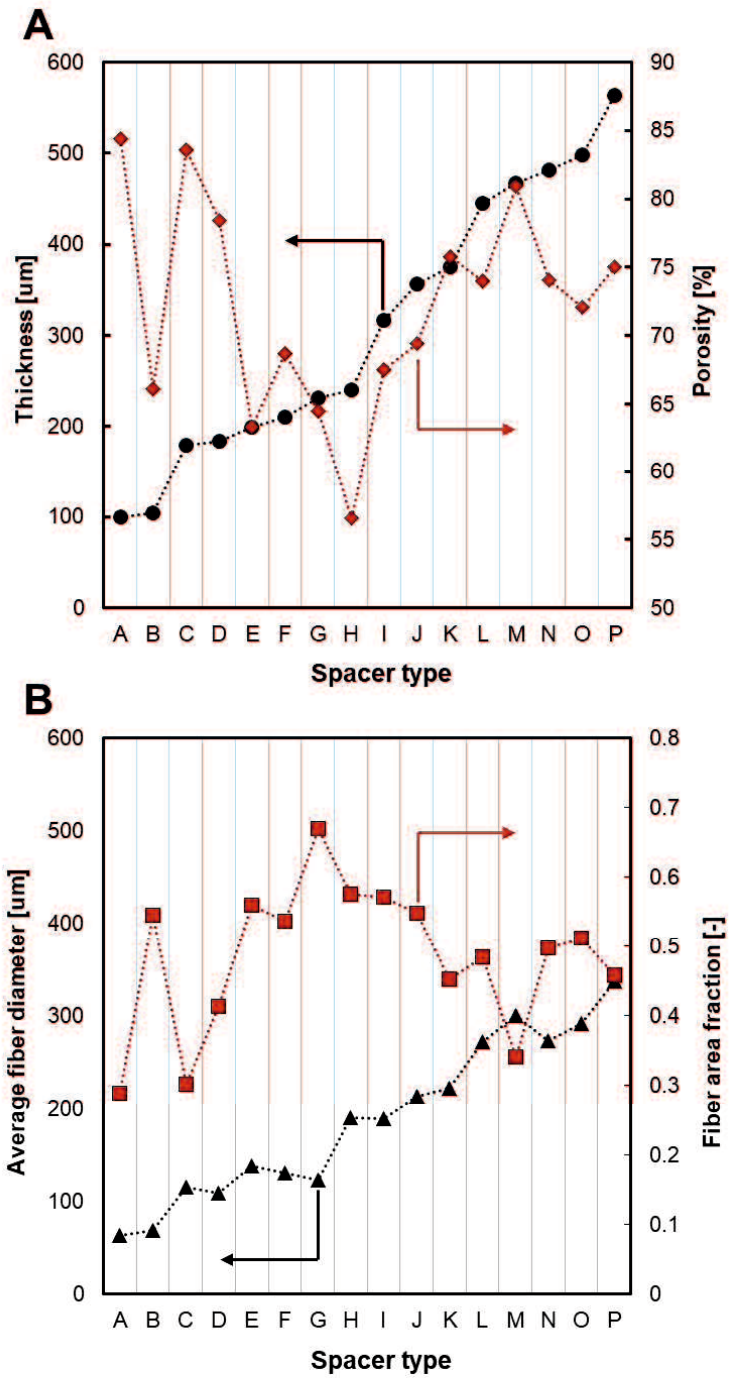

Figure. 4. The relationship between (A) spacer thickness and porosity, (B) fiber diameter and fiber area fraction.

2.4.2 Resistance measurements

From the $(R_m)_i$ measurement, we obtained the membrane intrinsic resistances of CMX, $(R_m)_{CMX}$, and AMX, $(R_m)_{AMX}$, of 2.33 Ω.cm^2 and 2.46 Ω.cm^2, respectively. Table 3 represents the obtained R_s and $(R'_s)_{CMX}$ which are resistance of the solution compartment in the presence of spacer without/with the shadow effect on the one side of the membrane (CMX), respectively. This difference between $(R'_s)_{CMX}$ and R_s ($(R'_s)_{CMX} > R_s$) indicated the existence of the shadow effect on the membrane. The R_s increased from type-A to type-P mainly due to increasing of the spacer thickness and also partially due to the spacer dimensions because R_s of type-B was about two times higher than that of type-A despite of almost same thickness, and type-E also showed higher R_s than that of type-F despite of thinner thickness of the spacer. Therefore, these results clearly supported that the shadow effect on the solution compartment depends on the spacer geometries. On the other hands, the obtained $(R_{sh})_{CMX}$ of the spacers were from 2.4~8.9% in the $(R_m)_{CMX}$, and also increased with the order from the type-A to type-P similar to the R_s. However, $(R_{sh})_{CMX}$ was also affected by the other spacer geometries as well as spacer thickness because the $(R_{sh})_{CMX}$ were not in the spacer thickness order. To figure out suitable parameter to express both shadow effects, those on solution compartment and membrane will be discussed in the following section 4.3 and 4.4, respectively.

Table 3. The obtained resistances in this study.

Spacer type	R_s, (Ωcm^2)	$(R'_s)_{CMX}$, (Ωcm^2)	$(R_{sh})_{CMX}$, (Ωcm^2)	$RR_{(sh/m)CMX}$ (-)
A	0.28	0.34	0.06	0.024
B	0.42	0.51	0.09	0.037
C	0.54	0.65	0.11	0.045
D	0.55	0.65	0.10	0.041
E	0.85	1.01	0.16	0.065
F	0.68	0.80	0.12	0.049
G	1.02	1.20	0.18	0.073
H	1.13	1.33	0.20	0.081
I	1.22	1.39	0.17	0.069
J	1.28	1.46	0.18	0.073
K	1.26	1.40	0.14	0.057
L	1.44	1.60	0.16	0.065
M	1.32	1.48	0.16	0.065
N	1.61	1.78	0.17	0.069
O	1.61	1.82	0.21	0.085
P	2.06	2.28	0.22	0.089

2.4.3 Spacer shadow effect on solution compartment

Here, to discuss the shadow effect on the solution compartment, we compared the obtained resistance of solution compartment with spacer (R_s) to those without spacer ($R_{sol(com)}$) as shown in Fig. 5. The $R_{sol(com)}$ was calculated from the solution conductivity (κ) and compartment thickness (t_{com}) same with the spacer thickness ($t_{com} = t_{sp}$). The dotted line shows the calculated $R_{sol(com)}$, and therefore, linearly increased with increasing the t_{com}. The difference between R_s and $R_{sol(com)}$ indicated the presence of spacer shadow effect on the solution compartment. To discuss the effect of spacer geometries on the spacer shadow

effect on the solution compartment, β_{sol} was calculated as an independent parameter of the thickness by using Eq. 12. To express the β_{sol} using spacer geometric characters and properties, at first, we attempted the usage of inverse squared of the porosity ($1/\varepsilon^2$) according to the previous work [6] as shown in Fig. 6(A). The dotted and solid lines here are linear approximation along the obtained experimental data and linear line with a slope of 1, respectively. Therefore, difference the dotted and solid lines indicates the usage of $1/\varepsilon^2$ is not appropriate. When the $1/\varepsilon^2$ was relatively lower than about 1.8 ($\varepsilon > 75\%$), the difference between dotted and solid lines was relatively low, and therefore, the $1/\varepsilon^2$ would be suitable to estimate the spacer shadow effect on the solution compartment. However, those difference clearly increased by increasing $1/\varepsilon^2$ higher than 1.8 ($\varepsilon < 75\%$) with the maximum error of 27.8%. Therefore, the $1/\varepsilon^2$ cannot represent perfectly the shadow effect on solution especially in the case of spacer with lower porosity. To express the shadow effect under a wide range of spacer geometries, we next attempted a mean shadow factor consisting of both area and volume fractions [17,21] instead of $1/\varepsilon^2$ as shown in Fig. 6(B). The obtained β_{sol} and those from a previous literature [17,21] were plotted as a function of mean shadow factor, β_{mean}. In the previous literature [17,21], they investigated the β_{sol} using only 4 spacers with relatively high porosity (> 79%). In Fig. 6(B), there was a good correlation between β_{sol} and the β_{mean} with the slope of 1 under a wide range of porosity (56-85%) of the spacers. Therefore, considering 16 types of spacers under a wide range in both porosity and thickness clearly supported that the β_{mean} is an appropriate parameter to predict the β_{sol} with appropriate accuracy, because the average errors in Fig. 6(B) using β_{mean} (6.3%) was less than those in Fig. 6(A) using $1/\varepsilon^2$ (13.7%).

The spacer shadow effect on solution compartment must be mainly due to ion passage in the tortuous way outside the spacer. Theoretically, difficulty of this ion passage can be expressed by using porosity, tortuosity and thickness, if we assumed the spacer is uniform and symmetric me [22]. However, it is difficult to express the tortuosity directly from the spacer geometry. In addition, if the spacer has non-uniform and asymmetric shape, the porosity of the whole spacer will be more meaningless. In this case, spacer area fraction may be more suitable parameter than the porosity to express the spacer shadow effect. From Fig. 6, it seems that in the case of applying high porous spacer, the effect of filaments area fraction on compartment shadow effect is negligible compared with filaments volume fraction. This is because small filaments do not have effective barrier properties on ion transportation. In this case, applying spacers porosity to predict the shadow effect on solution compartment seems to be valid. On the other hands, low porous spacers have filaments with higher area fraction which will increase the barrier effect of filaments area against ion transportation as well as tortuosity. Therefore, in the case of low porosity, that means high value of $1/\varepsilon^2$ in Fig. 6, the prediction from $1/\varepsilon^2$ was not suitable because of lack of consideration about tortuosity as mentioned above. In this case, the area fraction mainly should be considered to express the shadow effect. Therefore, the careful consideration of both area and volume fraction of spacer filaments is important for prediction of spacer shadow effect when using the wide variety of the spacer geometry. In addition, we have already tried to correlate the shadow effect the area and volume fraction individually instead of β_{mean} as shown in the supporting information. However, we could not find a good correlation between them in all range.

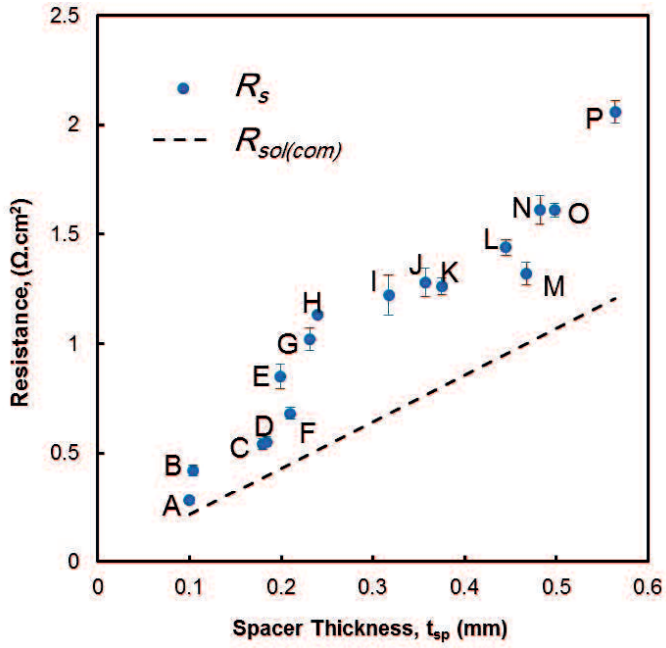

Figure. 5. Relationship between spacer thickness, t_{sp}, and resistance of solution compartment with and without spacer (R_s and $R_{sol(com)}$, respectively).

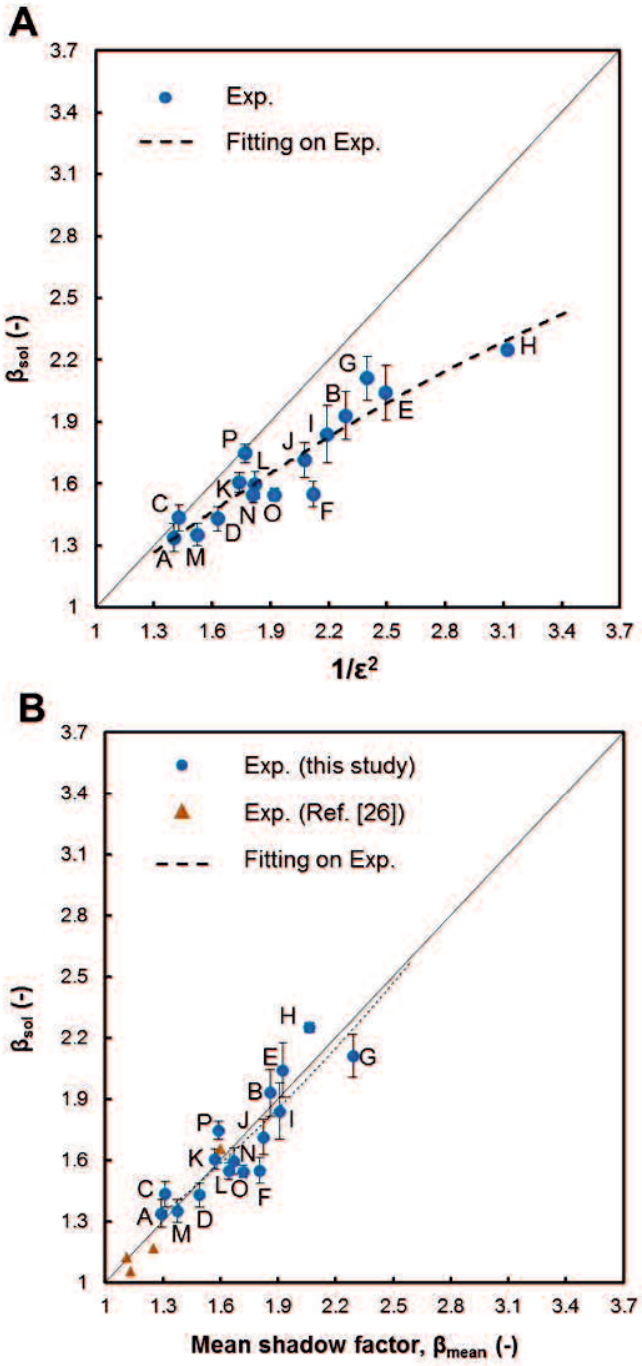

Figure. 6. Relationship between β_{sol} and (A) inverse square of porosity, $1/\varepsilon^2$, (B) mean shadow factor.

2.4.4 Spacer shadow effect on membrane

The solution compartment resistances with/without the spacer shadow effect on CMX, $(R'_s)_{CMX}$ and R_s, respectively, were shown in Fig. 7. Higher value of the $(R'_s)_{CMX}$ than those of R_s is due to presence of the spacer shadow effect on membrane which is almost 4-10 % of the resistance of CMX membrane. To discuss the effect of spacer geometries on the shadow effect on membrane, the difference between $(R'_s)_{CMX}$ and R_s was calculated as $(R_{(sh)})_{CMX}$, and the resistance ratio of $(R_{sh})_{CMX}$ to R_m, $RR_{(sh/m)CMX}$ was then obtained. Actually, the difference between $(R'_s)_{CMX}$ and R_s would be due to the fraction of membrane area covered by spacer filaments which would be affected by the spacer dimensions such as spacer mesh area fraction (A'), filaments diameter (D) and so on. Therefore, the average of horizontal and vertical filament diameters (D_{ave}) and their combinational parameters (A' D_{ave}, $\beta_a D_{ave}$ and $\beta_{mean} D_{ave}$) were firstly selected as an estimable parameters for the $RR_{(sh/m)CMX}$. Since the degree of the shadow effect on membrane must depend on the types of membrane especially of the thickness, the dimensional unit was still remained unlike the dimensionless parameters such as β_{mean} and $1/\varepsilon^2$ for estimating β_{sol}. For example, if the membrane has thicker thickness, the R_m become dominant, and therefore, the $RR_{(sh/m)i}$ must be decreased, whereas, the $RR_{(sh/m)i}$ will be increased when using a thinner membrane due to lower R_m. Thus, at least, a dimensional parameter relating to the membrane thickness is still hidden in the denominator of the proposed parameters. This is reason that the proposed parameters had the unit of length. The relationship between the selected parameters with $RR_{(sh/m)CMX}$ was shown in Fig. 8. As expected, all selected parameters had a proportional relationship with $RR_{(sh/m)CMX}$. The linear slope in Fig. 8 would depend on the types of membrane (R_m and thickness) due to

the same reason as mentioned above. However, a careful analysis and consideration are needed for the further discussion because in real case, the asymmetry, surface morphology and softness would be also effectible in addition to the thickness, in the future. The linear relationship and their approximation allowed to estimate the $RR_{(sh/m)CMX}$. The calculated results for all 16 spacers were shown in Fig. 9. The $RR_{(sh/m)CMX}$ estimated from the proposed parameters (D_{ave}, $A'D_{ave}$, $\beta_a D_{ave}$ and $\beta_{mean} D_{ave}$) agreed within the average deviation errors of 24.3%, 20.9%, 19.2% and 19.8%, respectively, with the experimental results in all 16 spacers. Therefore, since both side of membrane will be covered by spacers, we obtained the following equation for predicting β_{mem} which is applicable for all types of membranes as follows:

$$\beta_m = 1 + \frac{2(\beta_a D_{ave})}{\alpha_i} \quad [13]$$

where α_i (m) is dimensional coefficient related to the membrane thickness to express the degree of shadow effect on membrane as mentioned above. In this case, the α_i is equal to the inverse of the slope in Fig. 8.

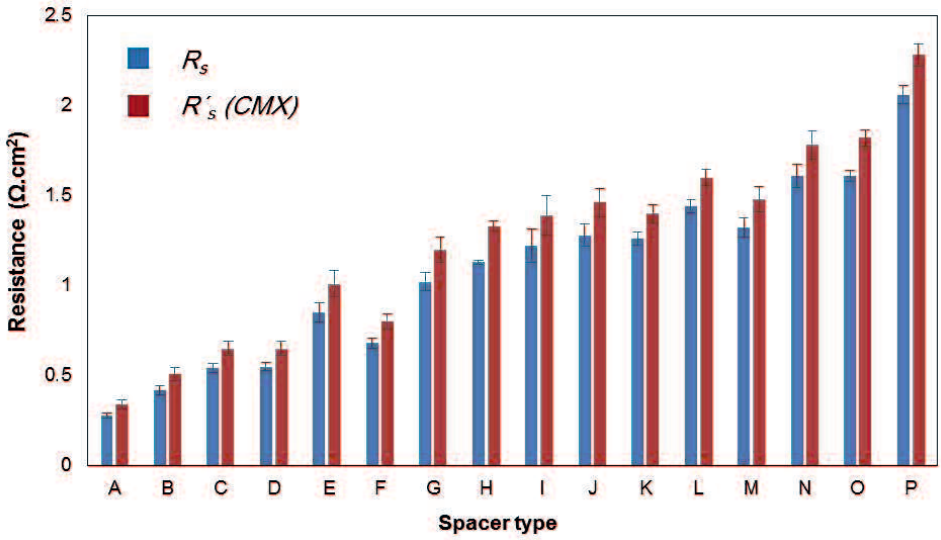

Figure. 7. Solution compartment resistance in the presence of spacer with/without shadow effect on membrane.

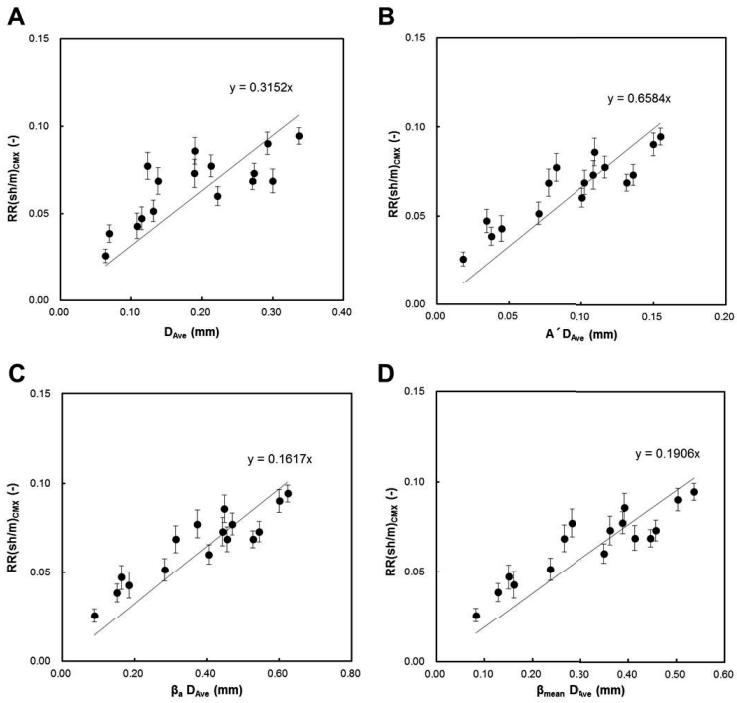

Figure 8. The obtained $RR_{(sh/m)CMX}$ as a function of (A) D_{ave}, (B)A' D_{ave},(C) $\beta_a D_{ave}$ and (D) $\beta_{mean} D_{ave}$.

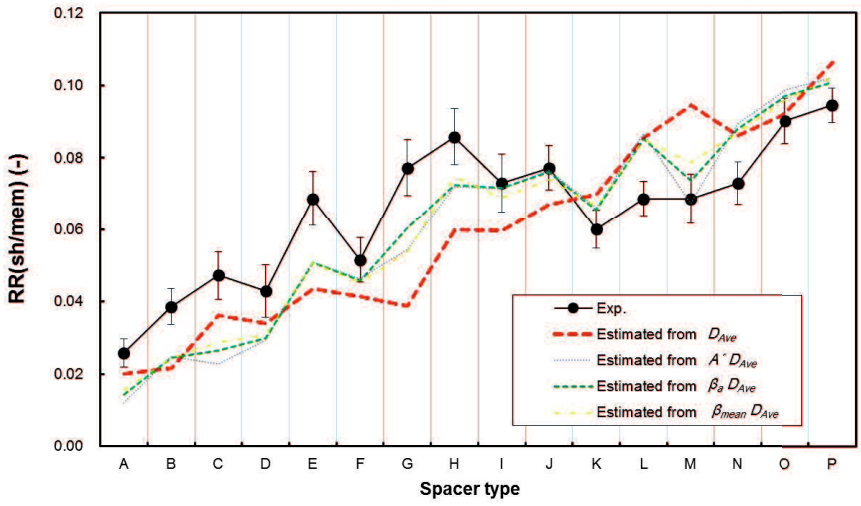

Figure 9. (A) the obtained $RR_{(sh/m)CMX}$, and those estimated from relationship of (B) D_{ave}, (B)A' D_{ave},(C) $\beta_a D_{ave}$ and (D) $\beta_{mean} D_{ave}$.

2.4.5 Contribution of Spacer shadow effects on RED stack resistance

Systematical investigation about the shadow effects of the spacer on the both membrane and solution compartment enabled us to predict the RED performance more quantitatively. The cell pair resistance, R_{cp}, including both shadow effects was given in this study as follows:

$$R_{cp} = \boldsymbol{\beta_{mean}} \left(\frac{t_{com,d}}{k_d} + \frac{t_{com,c}}{k_c} \right) + \left(1 + \frac{2(\beta_a D_{ave})}{\alpha_i}\right)(R_{CEM} + R_{AEM}) \quad [14]$$

This new empirical equation is applicable to estimate the RED cell pair resistance including spacer shadow effects with varying spacer geometry. Therefore, we also analyzed their resistance contribution in the total RED cell including river water and seawater compartments with spacers, anion- and cation-exchange membranes. The estimated results with varying types of spacers are shown in Fig. 10. Membranes used here were AMX and CMX, and the conductivities of seawater and river water were assumed to

be 46.8 mS/cm and 2.29 mS/cm, respectively, according to the previous literatures [23–25]. We also assumed that α_{AMX} and α_{CEM} in Eq. 14 were same for simplicity since they almost have the same thickness and resistance. The membrane resistance, solution conductivity, and spacer properties were obtained experimental data shown in section 3.4, section 3.3 and Table 2, respectively. The main and largest contribution in the RED cell pair resistance was the resistance of river water compartment and the shadow effect on both compartments with the degree of 34.1-58.4 % and 12.4-46.1 %, respectively, as shown in Fig. 10. The amount of spacer shadow effect on membrane seems to be similar to seawater compartment resistance which are not significant (less than 3%) in comparison with each cell resistance. In addition, the contribution of shadow effect on membrane can be decreased by using spacers thinner than gasket since the contact area and resulting shadow effect on the membrane must depend on the difference of the thickness between spacer and gasket. If the thickness of spacer become thinner than gasket, the contact area and resulting shadow effect decrease. In this study, we estimated the spacer shadow effect on membrane with making the resistance measurement cell tight using spacer and gasket with same thicknesses. Therefore, the estimated value would be higher than those in real case. Consequently, to enhance the RED power output, reduction of R_s is most important by considering the β_{sol} of the spacer.

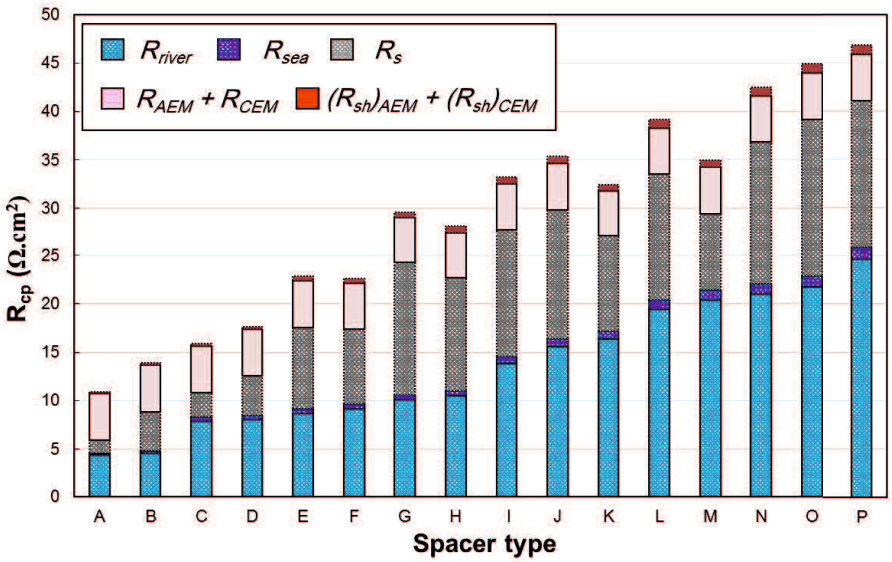

Figure 10. Contribution of the resistances in a RED cell with the respective spacers and membrane (CMX and AMX).

2.5 Conclusion

The resistance of the RED cell is significantly influenced by spacers within the solution compartment, called as spacer shadow effect. In this work, we investigate the effect of spacer geometry on the spacer shadow effect on both membrane and solution compartments resistances, separately, and proposed simple equation to express them using the spacer geometry. Applying 16 types of different spacers with a wide variety of porosity (56-84 %) and thickness (0.100-0.564 mm) indicates that the spacer shadow effect on membrane and solution can be separately expressed by using the spacer geometry, even for low porous spacer. For spacer shadow effect on solution, mean shadow factor consisting of both area and volume fractions are appropriate to express them than $1/\varepsilon^2$ which just depends on volume fraction. This new finding enables to estimate the RED stack resistance

with varying spacer dimensional characteristics more quantitatively. The precise estimation of a RED stack with varying spacer type proposes that increasing resistances due to the presence of spacer are 13.7-48.1% of the total RED cell pair resistance. Therefore, in the RED stack, the results showed that the porosity has dominant effect in the case of higher porous spacer, whereas the effect of area fraction would increase besides that of porosity when using lower porous spacer.

The proposed empirical equation is also promising to be useful for not only estimating the respective resistance in RED stack, but also designing suitable spacer geometry for enhancing RED performance.

2.6 Acknowledgements

This work was supported by JSPS KAKENHI Grant Number JP16H01796 and was partially supported by Subsidy for Research of Energy Infrastructure with Advanced Technology (Okinawa, Japan).

2.7 Nomenclature

Nomenclature	
A'	Filaments area fraction in unit cell (mm^2)
h	Thickness of solution compartment (μm)
k	Solution conductivity (mS/cm)
R_{AEM}	Resistance of AEM (Ωcm^2)
R_b	Resistance of solution bulk in resistance measurement cell (Ω)
R_{b+s}	Solution bulk and spacer resistance (Ω)
R_{b+m}	Bulk solution and membrane resistance (Ω)
R'_{b+s+m}	Resistance of solution bulk, spacer, and membrane include shadow effect of spacer on membrane (Ω)
R_{CEM}	Resistance of CEM (Ωcm^2)
R_{cp}	RED cell pair resistance (Ω)
R_m	Membrane resistance (Ωcm^2)
R_{river}	Resistance of river water compartment in RED stack (Ω)
R_s	Spacer resistance consist of solution compartment resistance with the thickness same as spacer as well as spacer shadow effect on solution compartment (Ω)
R'_s	Spacer resistance include shadow effect on membrane resistance (Ω)
R_{sea}	Resistance of river water compartment in RED stack (Ω)
R_{sh}	The amount of spacer shadow effect on membrane (Ω)
$RR(sh/m)$	Ration of spacer shadow effect on solution to membrane resistance (-)
t_{com}	Solution compartment thickness (μm)
v'	Filaments volume fraction (-)
v_f	Filaments volume of each cell (mm^3)
v_t	Unit cell volume (mm^3)
a_f	Filaments area per unit cell (mm^2)
a_t	Unit cell area (mm^2)
β_{area}	Area shadow effect of spacer (-)
β_{mean}	Spacer mean shadow factor consist of the average of volume and area shadow factor (-)
β_{mem}	Spacer shadow effect on membrane (-)
β_{sol}	Shadow effect of spacer in solution compartments (-)
β_{vol}	Spacer volume shadow factor (-)
ε	Spacer porosity (-)

2.8 References

[1] H. Kim, Y.E. Kim, N.J. Jeong, K.S. Hwang, J.H. Han, J.Y. Nam, E. Jwa, S.C. Nam, S.Y. Park, Y. Il Yoon, C.S. Kim, Innovative reverse-electrodialysis power generation system for carbon capture and utilization, J. CO_2 Util. 20 (2017) 312–317. doi:10.1016/j.jcou.2017.05.025.

[2] J.G. Hong, B. Zhang, S. Glabman, N. Uzal, X. Dou, H. Zhang, X. Wei, Y. Chen, Potential ion exchange membranes and system performance in reverse electrodialysis for power generation: A review, J. Memb. Sci. 486 (2015) 71–88. doi:10.1016/j.memsci.2015.02.039.

[3] J.G. Hong, W. Zhang, J. Luo, Y. Chen, Modeling of power generation from the mixing of simulated saline and freshwater with a reverse electrodialysis system: The effect of monovalent and multivalent ions, Appl. Energy. 110 (2013) 244–251. doi:10.1016/j.apenergy.2013.04.015.

[4] M. Tedesco, C. Scalici, D. Vaccari, A. Cipollina, A. Tamburini, G. Micale, Performance of the first reverse electrodialysis pilot plant for power production from saline waters and concentrated brines, J. Memb. Sci. 500 (2016) 33–45. doi:10.1016/j.memsci.2015.10.057.

[5] J.N. Weinstein, F.B. Leitz, Electric power from differences in salinity: the dialytic battery., Science. 191 (1976) 557–559. doi:10.1126/science.191.4227.557.

[6] J.W. Post, H.V.M. Hamelers, C.J.N. Buisman, Energy recovery from controlled mixing salt and fresh water with a reverse electrodialysis system, Environ. Sci. Technol. 42 (2008) 5785–5790. doi:10.1021/es8004317.

[7] D.A. Vermaas, M. Saakes, K. Nijmeijer, Enhanced mixing in the diffusive boundary layer for energy generation in reverse electrodialysis, J. Memb. Sci. 453 (2014) 312–319. doi:10.1016/j.memsci.2013.11.005.

[8] D.A. Vermaas, M. Saakes, K. Nijmeijer, Doubled Power Density from Salinity Gradients at Reduced Intermembrane Distance, (2011) 7089–7095.

[9] Y. Mei, C.Y. Tang, Recent developments and future perspectives of reverse electrodialysis technology: A review, Desalination. 425 (2017) 156–174. doi:10.1016/j.desal.2017.10.021.

[10] L. Gurreri, A. Tamburini, A. Cipollina, G. Micale, M. Ciofalo, CFD prediction of concentration polarization phenomena in spacer-filled channels for reverse electrodialysis, J. Memb. Sci. 468 (2014) 133–148. doi:10.1016/j.memsci.2014.05.058.

[11] L. Gurreri, A. Tamburini, A. Cipollina, G. Micale, M. Ciofalo, Flow and mass transfer in spacer-filled channels for reverse electrodialysis: a CFD parametrical study, J. Memb. Sci. 497 (2016) 300–317. doi:10.1016/j.memsci.2015.09.006.

[12] D.A. Vermaas, M. Saakes, K. Nijmeijer, Power generation using profiled membranes in reverse electrodialysis, J. Memb. Sci. 385–386 (2011) 234–242. doi:10.1016/j.memsci.2011.09.043.

[13] J. Moreno, E. Slouwerhof, D.A. Vermaas, M. Saakes, K. Nijmeijer, The Breathing Cell: Cyclic Intermembrane Distance Variation in Reverse Electrodialysis, Environ. Sci. Technol. 50 (2016) 11386–11393. doi:10.1021/acs.est.6b02668.

[14] D.A. Vermaas, M. Saakes, K. Nijmeijer, Doubled power density from salinity gradients at reduced intermembrane distance, Environ. Sci. Technol. 45 (2011) 7089–7095. doi:10.1021/es2012758.

[15] P. Długołęcki, J. Dabrowska, K. Nijmeijer, M. Wessling, Ion conductive spacers for increased power generation in reverse electrodialysis, J. Memb. Sci. 347 (2010) 101–107. doi:10.1016/j.memsci.2009.10.011.

[16] P. Długołe, A. Gambier, M. Wessling, Practical Potential of Reverse Electrodialysis As Process for Sustainable Energy Generation, 43 (2009) 6888–6894.

[17] V. V. Wagholikar, H. Zhuang, Y. Jiao, N.E. Moe, H. Ramanan, L.M. Goh, J. Barber, K.S. Lee, H.P. Lee, J.Y.H. Fuh, Modeling cell pair resistance and spacer shadow factors in electro-separation processes, J. Memb. Sci. 543 (2017) 151–162. doi:10.1016/j.memsci.2017.08.054.

[18] J. Balster, D.F. Stamatialis, M. Wessling, Towards spacer free electrodialysis, J. Memb. Sci. 341 (2009) 131–138. doi:10.1016/j.memsci.2009.05.048.

[19] A. Siddiqui, S. Lehmann, V. Haaksman, J. Ogier, C. Schellenberg, M.C.M. van Loosdrecht, J.C. Kruithof, J.S. Vrouwenvelder, Porosity of spacer-filled channels in spiral-wound membrane systems: Quantification methods and impact on hydraulic characterization, Water Res. 119 (2017) 304–311. doi:10.1016/j.watres.2017.04.034.

[20] H.J. Lee, F. Sarfert, H. Strathmann, S.H. Moon, Designing of an electrodialysis desalination plant, Desalination. 142 (2002) 267–286. doi:10.1016/S0011-9164(02)00208-4.

[21] J. Veerman, M. Saakes, S.J. Metz, G.J. Harmsen, Reverse electrodialysis: Performance of a stack with 50 cells on the mixing of sea and river water, J. Memb. Sci. 327 (2009) 136–144. doi:10.1016/j.memsci.2008.11.015.

[22] M. Yasukawa, S. Mishima, Y. Tanaka, T. Takahashi, H. Matsuyama, Thin-film composite forward osmosis membrane with high water flux and high pressure resistance using a thicker void-free polyketone porous support, Desalination. 402 (2017) 1–9. doi:10.1016/j.desal.2016.09.017.

[23] A. Daniilidis, D.A. Vermaas, R. Herber, K. Nijmeijer, Experimentally obtainable energy from mixing river water, seawater or brines with reverse electrodialysis, Renew. Energy. 64 (2014) 123–131. doi:10.1016/j.renene.2013.11.001.

[24] B. Zhang, H. Gao, Y. Chen, Enhanced Ionic Conductivity and Power Generation Using Ion-Exchange Resin Beads in a Reverse-Electrodialysis Stack, Environ. Sci. Technol. 49 (2015) 14717–14724. doi:10.1021/acs.est.5b03864.

[25] T. Rijnaarts, E. Huerta, W. van Baak, K. Nijmeijer, Effect of Divalent Cations on RED Performance and Cation Exchange Membrane Selection to Enhance Power Densities, Environ. Sci. Technol. (2017) acs.est.7b03858. doi:10.1021/acs.est.7b03858.

2.9 Supplementary information

2.9.1 Appendix A. Spacer geometry measurement

Different spacer (16 types) geometry includes filaments diameter, distance, and angles with each other have been measured by using an optical microscope. Upside views of all spacers with high magnitude and more details are shown in Fig. A1-A16. In addition, spacer geometry calculation include volume and area properties are also shown in Table A1, A2 for spacers types A-H and I-P with more details, respectively. All the spacers geometry properties that calculated in this study are present in this table which would be useful for more investigation.

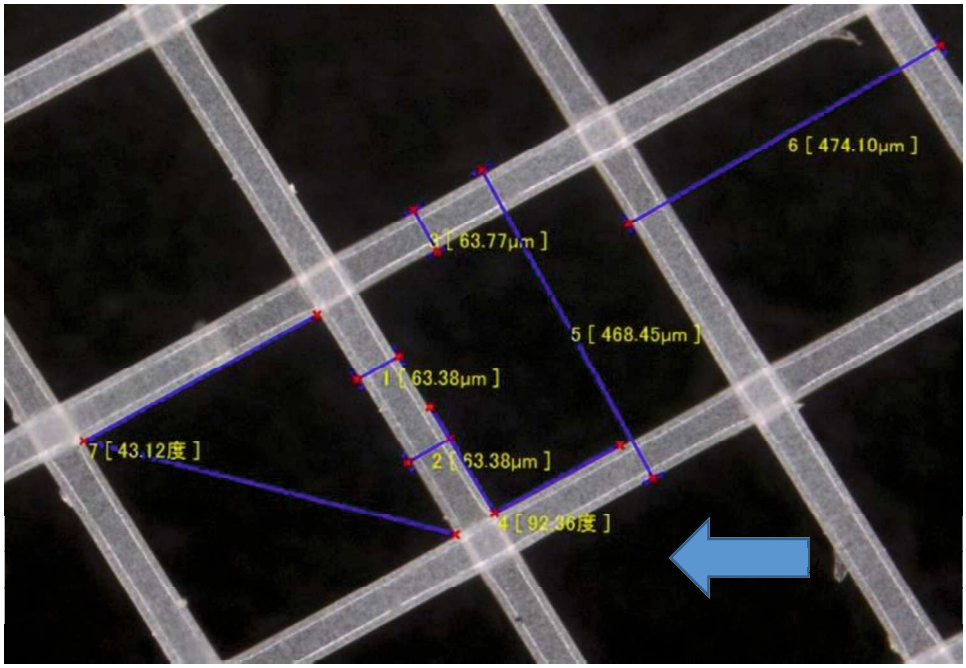

Figure A1. Upside view of spacer type A

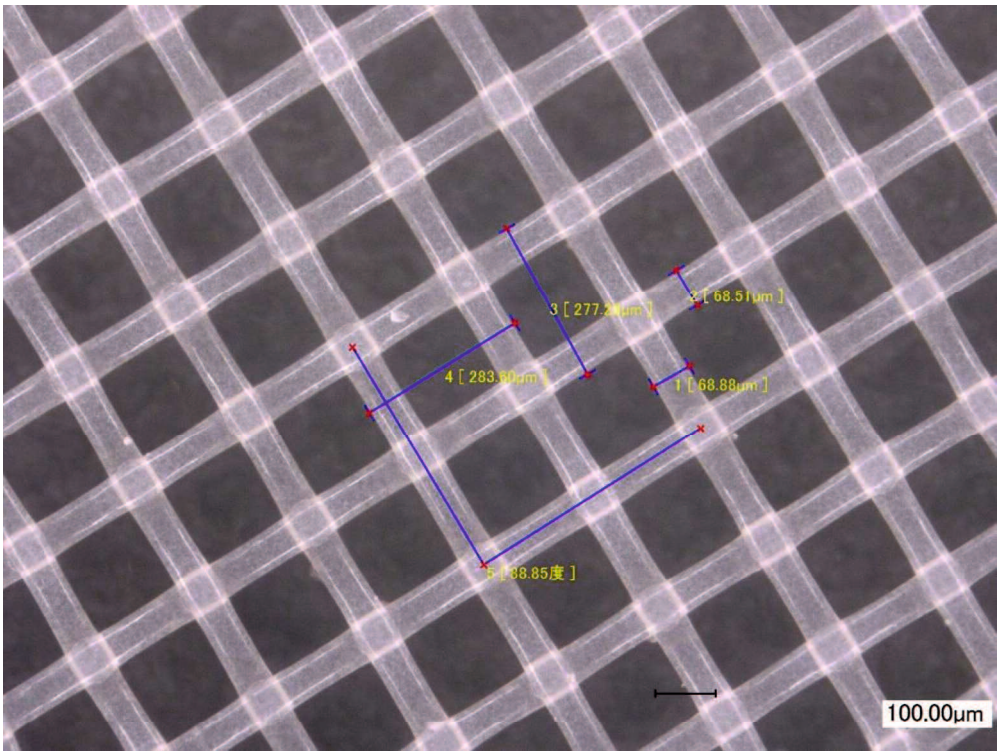

Figure A2. Upside view of spacer type B

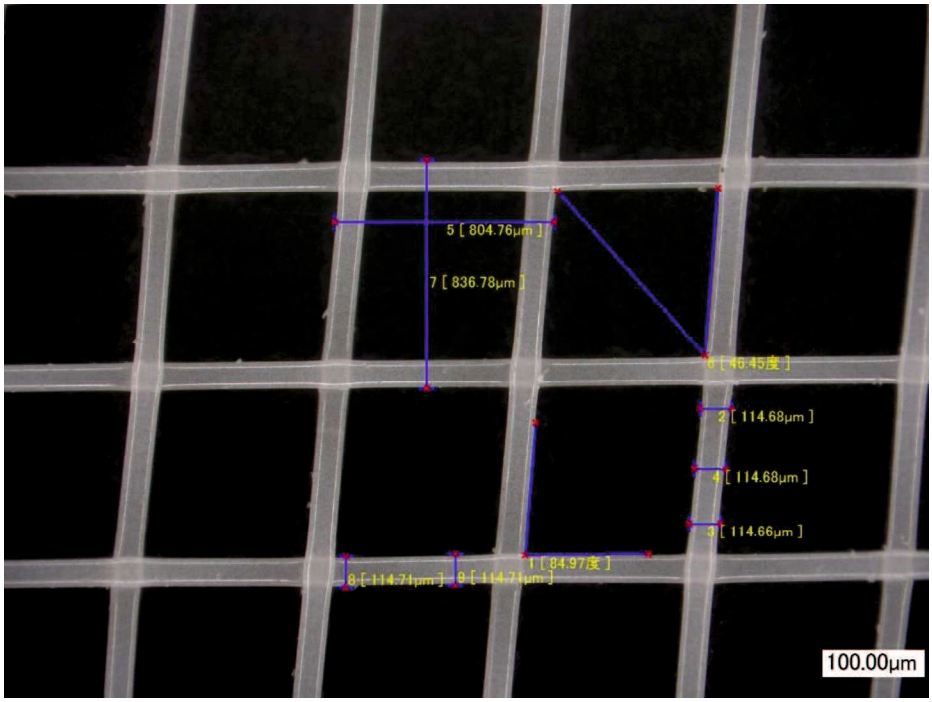

Figure A3. Upside view of spacer type C

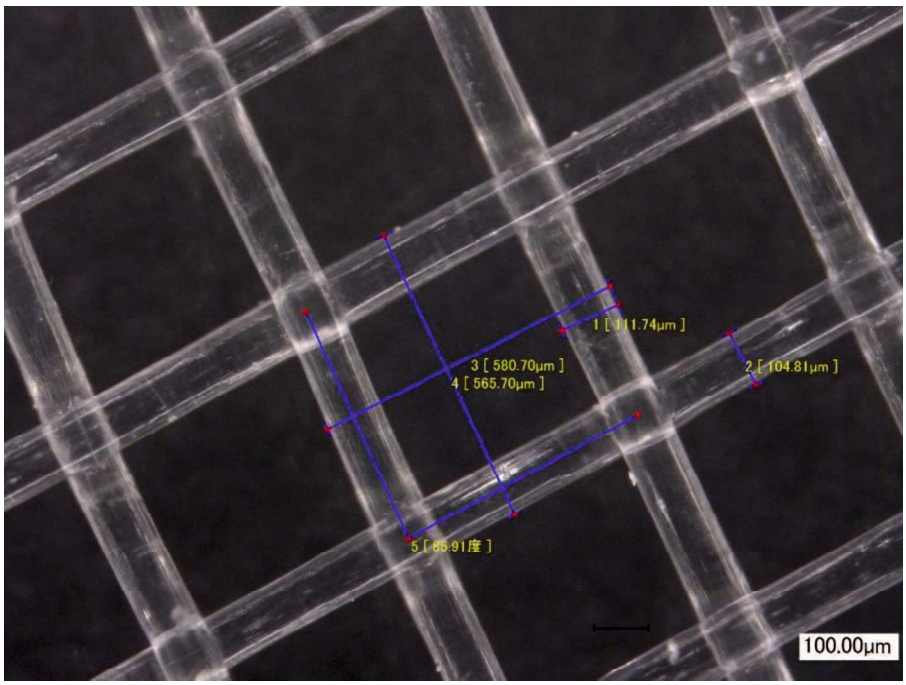

Figure A4. Upside view of spacer type D

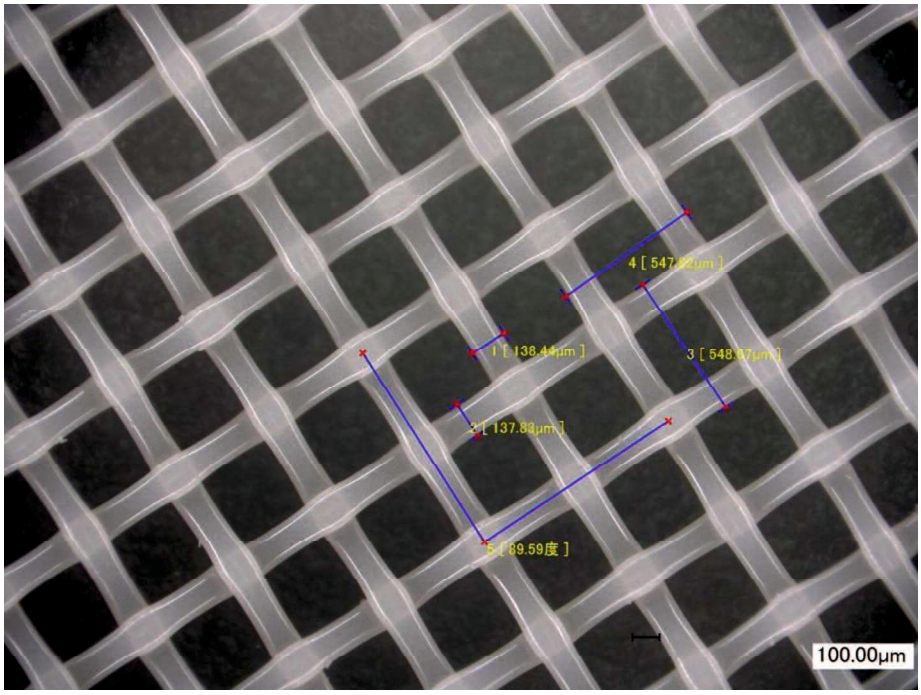

Figure A5. Upside view of spacer type E

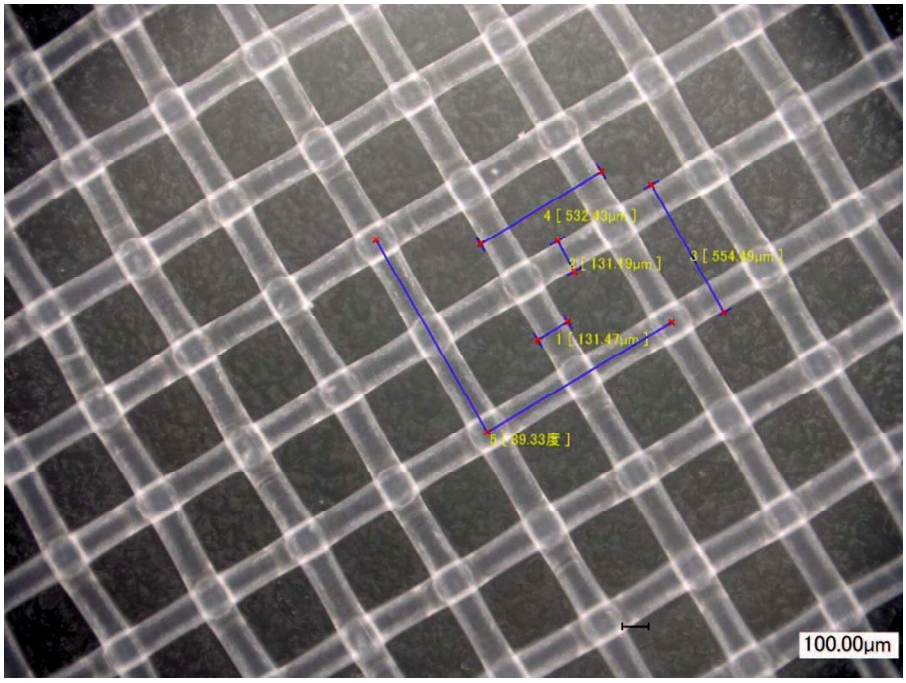

Figure A6. Upside view of spacer type F

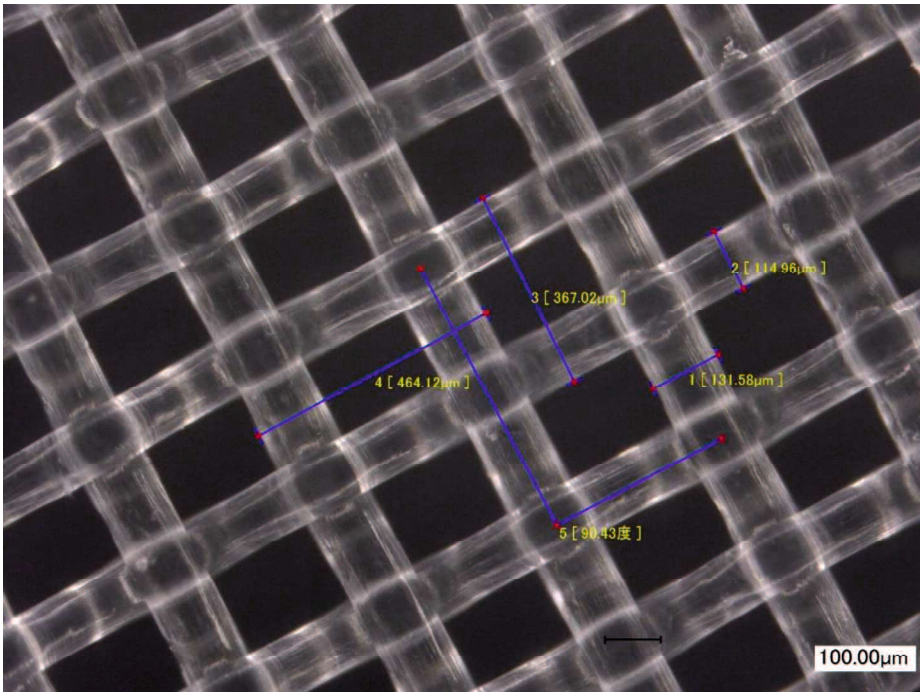

Figure A7. Upside view of spacer type G

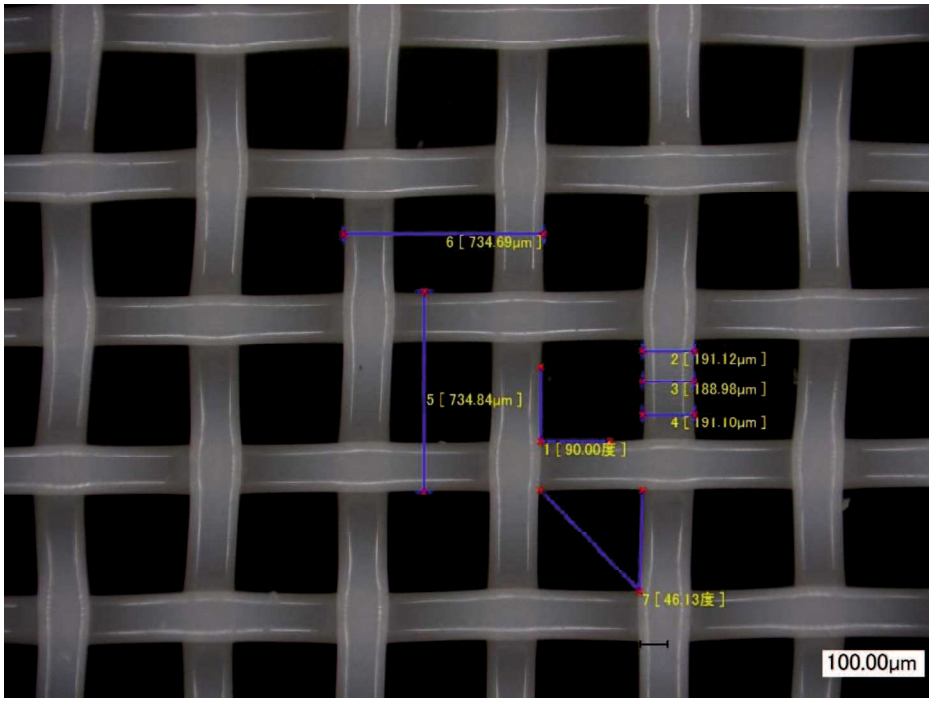

Figure A8. Upside view of spacer type H

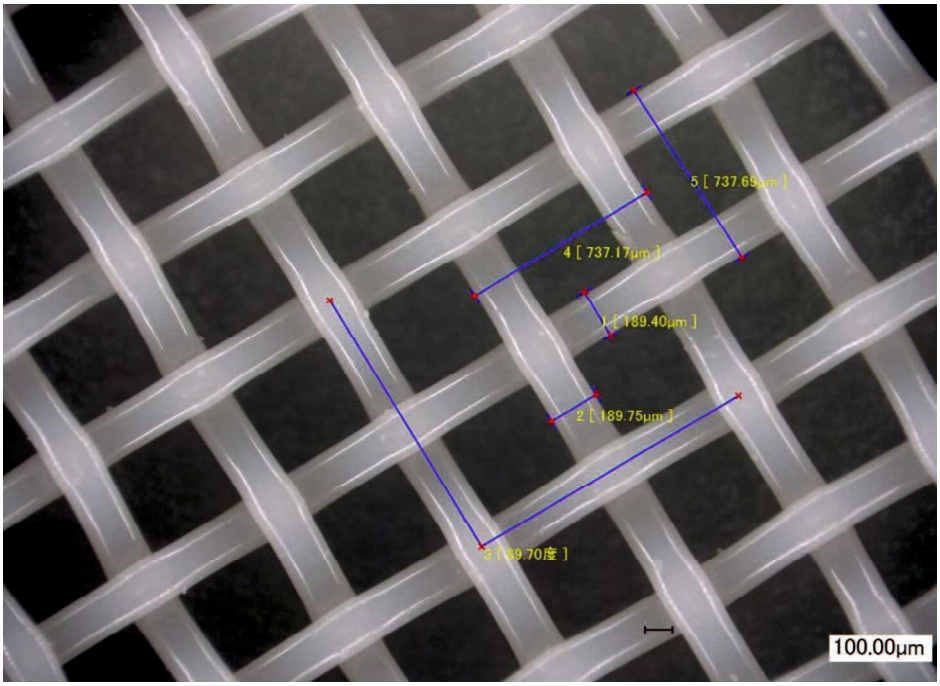

Figure A9. Upside view of spacer type I

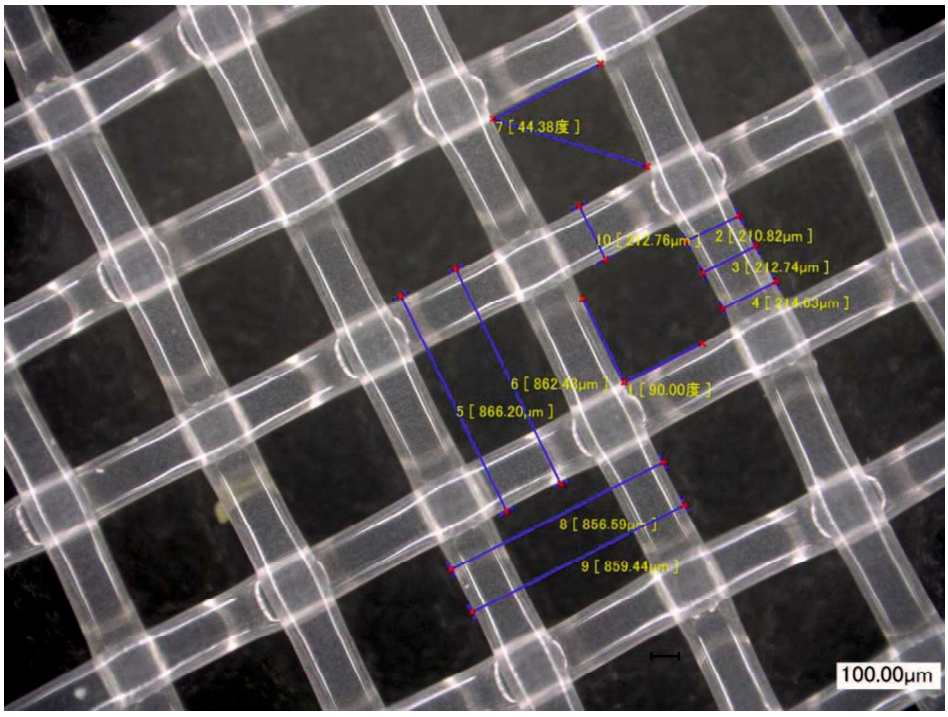

Figure A10. Upside view of spacer type J

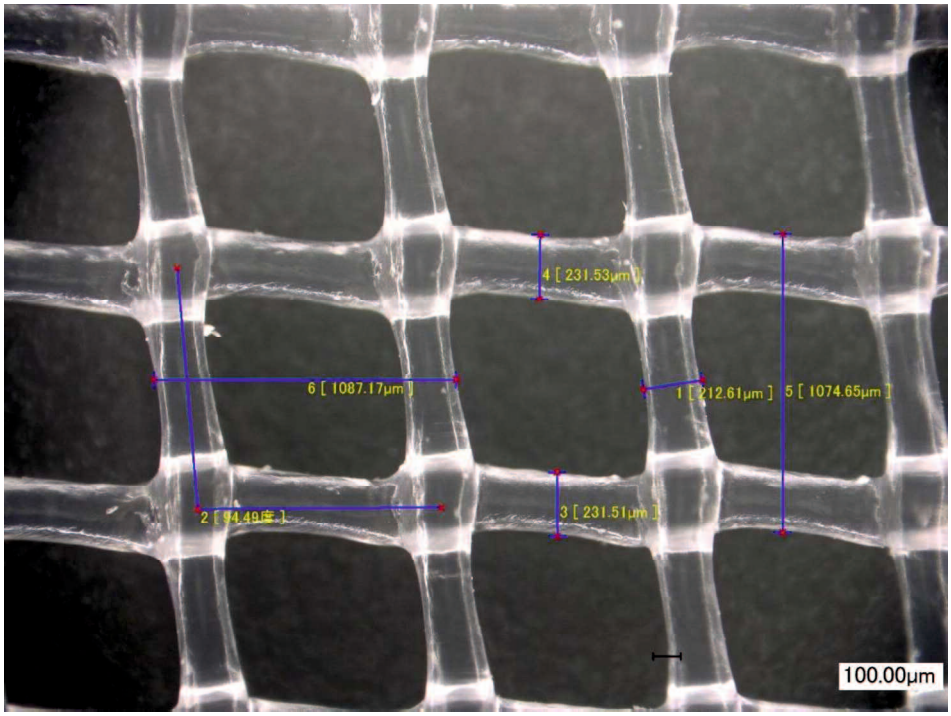

Figure A11. Upside view of spacer type K

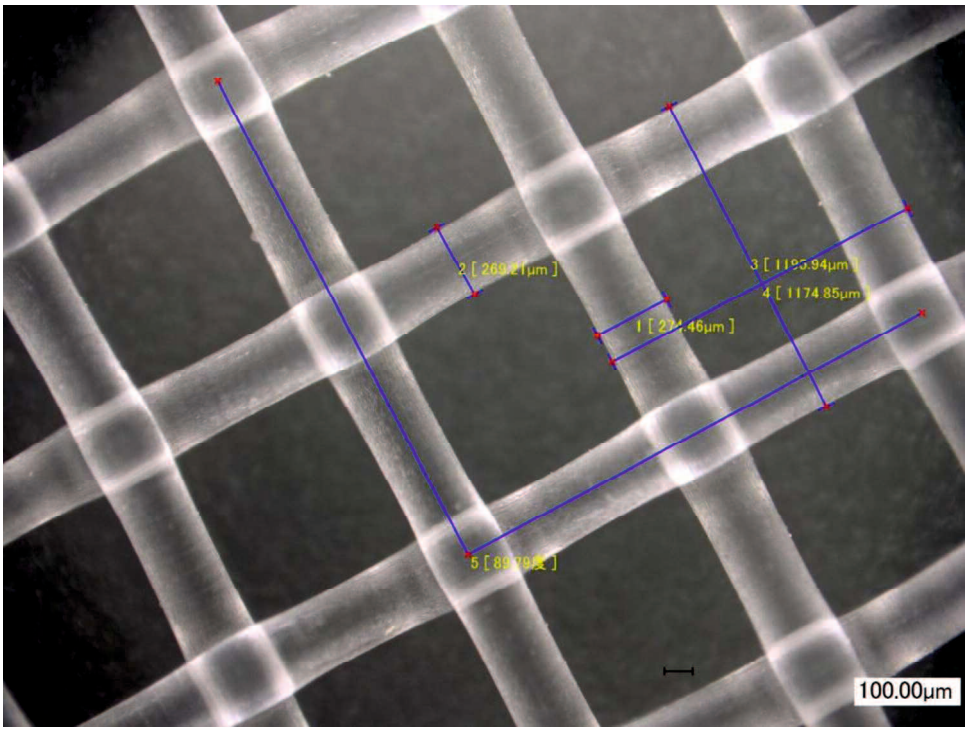

Figure A12. Upside view of spacer type L

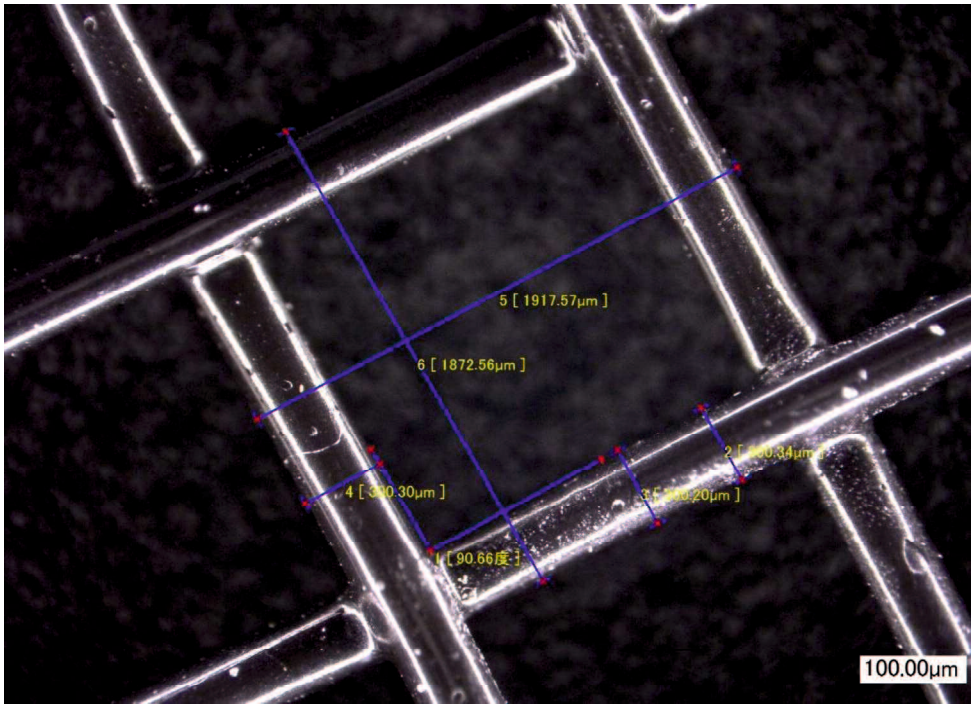

Figure A13. Upside view of spacer type M

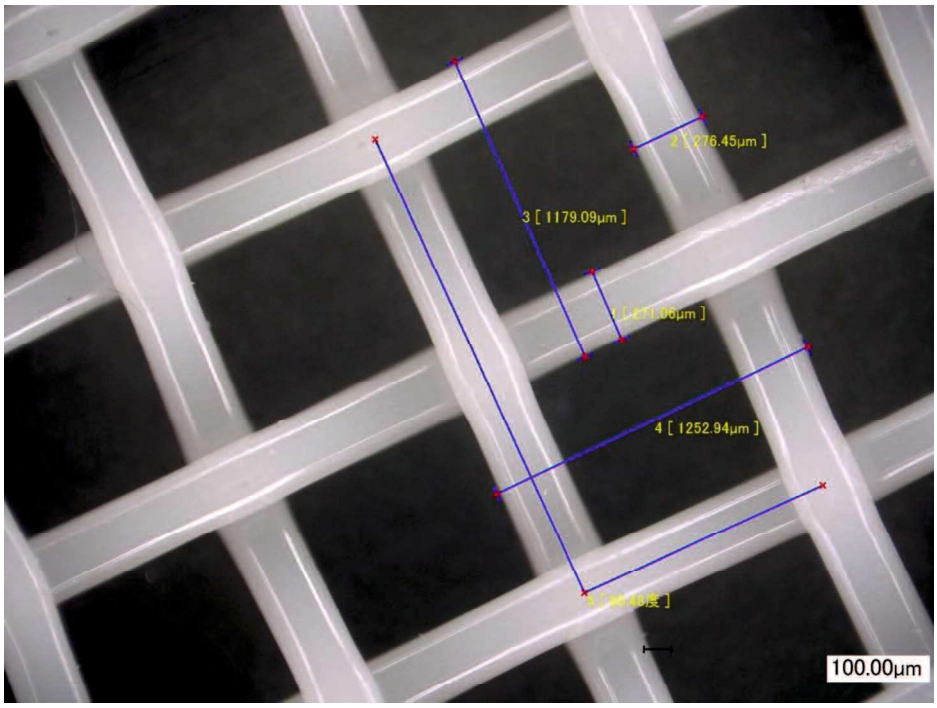

Figure A14. Upside view of spacer type N

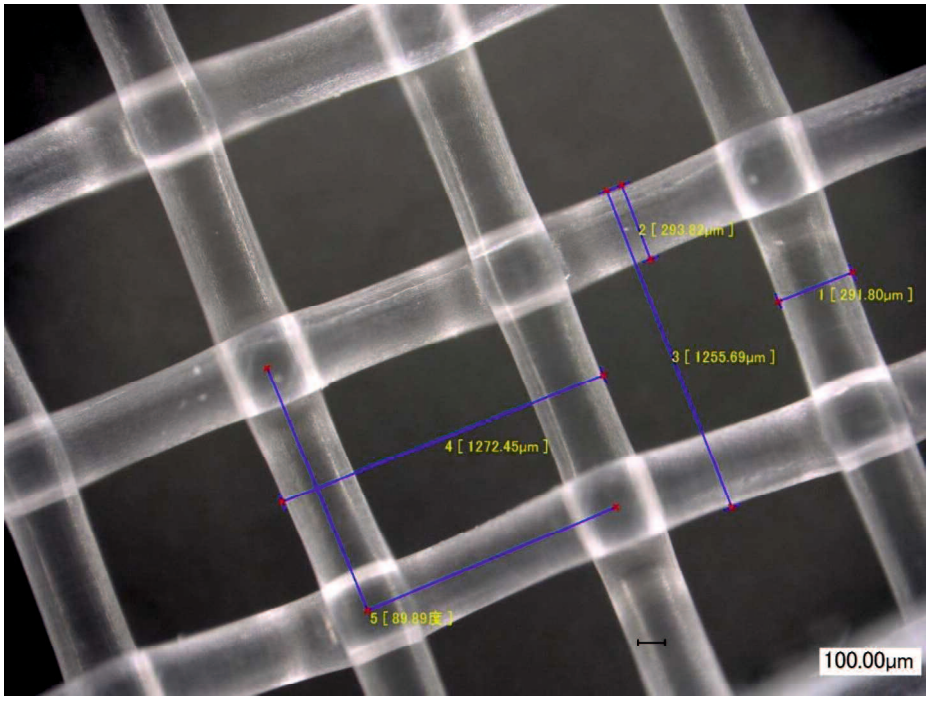

Figure A15. Upside view of spacer type O

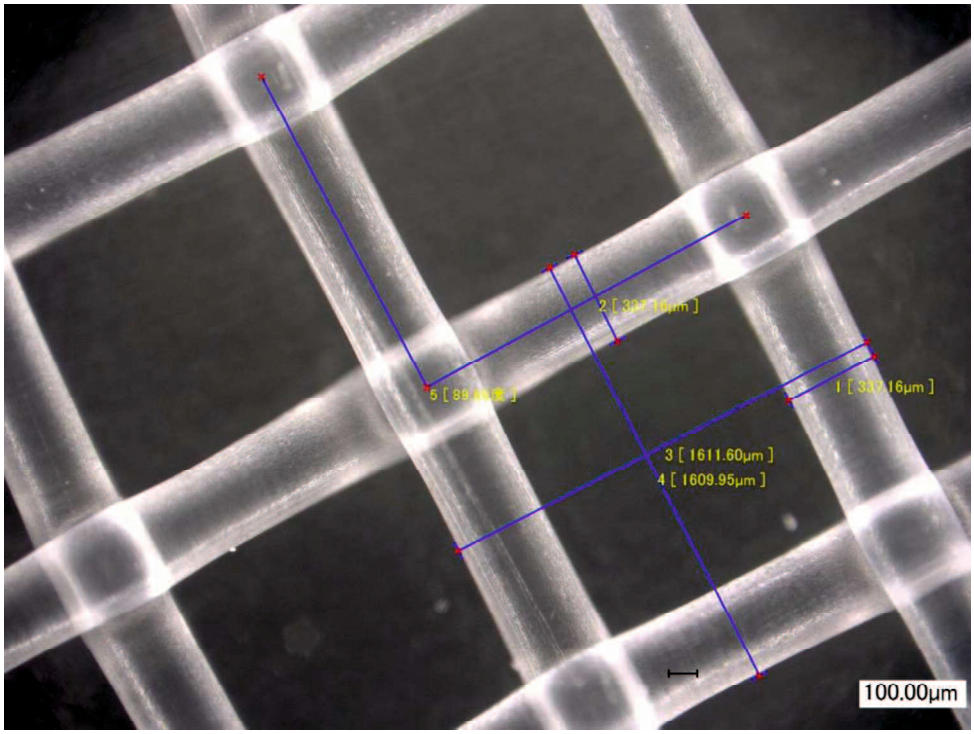

Figure A16. Upside view of spacer type P

Table A1. The properties of spacers types A-H due to geometric observation [17].

Spacer properties	A	B	C	D	E	F	G	H
Mesh Thickness, t_{sp} (mm)	0.1	0.104	0.18	0.184	0.199	0.21	0.231	0.24
Horizontal Fiber diameter, D_W (mm)	0.064	0.069	0.1147	0.105	0.1378	0.131	0.115	0.19
Vertical fiber diameter, D_L (mm)	0.063	0.069	0.1146	0.112	0.138	0.131	0.132	0.19
Mesh width, W (mm)	0.411	0.215	0.69	0.469	0.409	0.400	0.333	0.544
Mesh length, L (mm)	0.405	0.209	0.722	0.461	0.411	0.423	0.253	0.545
Filament angle, θ	90	90	84	85	90	90	90	90
Porosity, ε (%)	0.844	0.661	0.836	0.784	0.633	0.687	0.645	0.566
Fiber area per unit cell, $a_f = (D_W.W + D_L(L - D_W))$ (mm^2)	0.0478	0.0245	0.149	0.089	0.0943	0.091	0.056	0.171
Unit cell area, $a_t = W.L.\sin\theta$ (mm^2)	0.166	0.0449	0.495	0.215	0.168	0.169	0.084	0.297
Area fraction,	0.288	0.545	0.301	0.413	0.56	0.536	0.67	0.576

$A' = {}^{a_f}/_{a_t}$								
Area shadow factor,	1.404	2.199	1.43	1.704	2.273	2.16	3.03	2.36
$\beta_a = {}^{1}/_{(1-A')}$								
Fiber volume per unit cell,	0.0026	0.0016	0.0146	0.008	0.0122	0.011	0.006	0.030
				6			9	9
$v_f = \frac{\pi(D_W^2.W+D_L^2.L)}{4}$ (mm^3)								
Unit cell volume,	0.0166	0.0047	0.0891	0.039	0.0335	0.036	0.019	0.071
$v_t = a_t t_{sp}$ (mm^3)								
Volume fraction,	0.156	0.339	0.164	0.216	0.367	0.313	0.354	0.434
$v' = {}^{v_f}/_{v_t}$								
Volume Shadow factor,	1.184	1.513	1.196	1.276	1.58	1.46	1.55	1.77
$\beta_v = 1/(1-v')$								
Mean Shadow Factor,	1.294	1.86	1.313	1.489	1.93	1.81	2.29	2.06
$\beta_m = (\beta_a + \beta_v)/2$								

Table A2. The properties of spacers type I-P due to geometric observation

Spacer properties	I	J	K	L	M	N	O	P
Mesh Thickness, t_{sp} (mm)	0.317	0.357	0.375	0.445	0.467	0.482	0.498	0.564
Horizontal Fiber diameter, D_W (mm)	0.189	0.213	0.231	0.269	0.300	0.271	0.293	0.337
Vertical fiber diameter, D_L (mm)	0.189	0.213	0.212	0.274	0.300	0.276	0.291	0.337
Mesh width, W (mm)	0.547	0.653	0.874	0.900	1.62	0.976	0.98	1.274
Mesh length, L (mm)	0.548	0.646	0.843	0.927	1.57	0908	0.961	1.272
Filament angle, θ	90	90	94	90	90	90	90	90
Porosity, ε (%)	0.675	0.694	0.758	0.74	0.809	0.7407	0.721	0.75
Fiber area per unit cell, $a_f = (D_W.W + D_L(L - D_W))$ (mm^2)	0.172	0.231	0.332	0.405	0.868	0.441	0.483	0.745
Unit cell area, $a_t = W.L.\sin\theta$ (mm^2)	0.300	0.422	0.735	0.835	2.54	0.886	0943	1.622
Area fraction, $A' = {}^{a_f}/_{a_t}$	0.572	0.548	0.452	0.485	0.341	0.497	0.512	0.459
Area shadow factor,	2.34	2.209	1.83	1.94	1.517	1.988	2.049	1.85

$\beta_a = {}^{1}/_{(1-A')}$								
Fiber volume per unit cell, $v_f = \frac{\pi(D_W^2.W+D_L^2.L)}{4}$ (mm^3)	0.31	0.046	0.067	0.095	0.225	0.110	0.13	0227
Unit cell volume, $v_t = a_t t_{sp}$ (mm^3)	0.095	0.15	0.276	0.371	1.18	0.427	0.469	0.915
Volume fraction, $v' = {}^{v_f}/_{v_t}$	0.324	0.306	0.242	0.257	0.190	0.259	0.278	0.248
Volume Shadow factor, $\beta_v = 1/(1-v')$	1.48	1.44	1.319	1.346	1.23	1.349	1.385	1.33
Mean Shadow Factor, $\beta_m = (\beta_a + \beta_v)/2$	1.9	1.83	1.57	1.64	1.38	1.67	1.717	1.59

2.9.2 Appendix B. Correlation of mean shadow factor with other parameters

The relationship between spacer shadow effect on solution compartment with volume and area shadow factor of spacer are shown in Fig. B1 (A and B), respectively. However, there were not good agreements between them. Therefore, prediction of the spacer shadow effect on solution compartment from the volume and area shadow factor

individually are not appropriate. As a results, the spacer shadow effect on solution compartment could be represent by using mean shadow factor as shown in Fig 6(B).

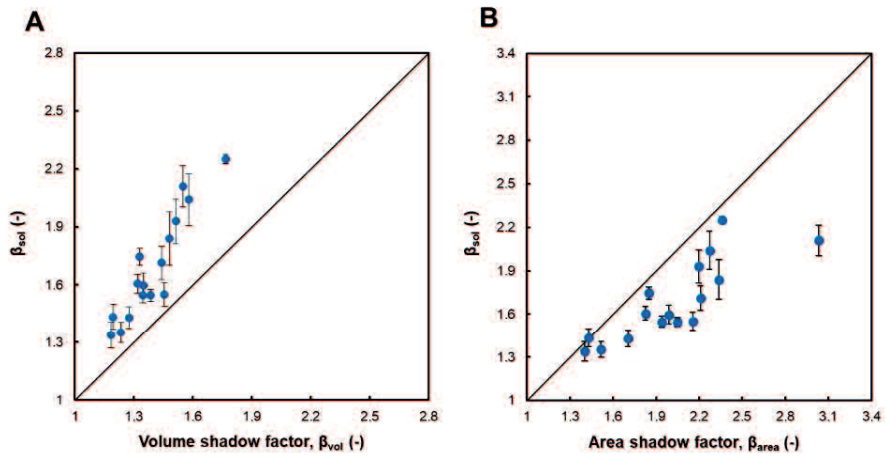

Figure B1. Relationship between β_{sol} and (A) volume shadow factor, (B) area shadow factor.

Chapter 3

The Effect of Feed Solution Temperature on the Power Output Performance of a Pilot-Scale Reverse Electrodialysis (RED) System with Different Intermediate Distance

3.1 Introduction

The ever increasing energy demand worldwide and environmental issues such as CO_2 emissions have led to an increased focus on renewable energy sources such as wind, sun and hydro power [1,2] Among all of the renewable sources used for energy production, salinity gradient energy (SGE) is known to be one of the most readily available and appropriate. SGE is defined as the electrochemical potential between two solutions with different concentrations, especially salt concentration. Theoretically it has been estimated using the Gibbs free energy that 1.7 MJ of power may be generated when mixing 1 m^3 of river water and a large amount of seawater. Therefore, when considering the large amount of river water discharged into seawater during the course of a year, a magnificent amount of power (1.4–2.6 TW) can be theoretically generated [3–5]. Reverse electrodialysis is known as a promising membrane-based process, which can directly convert SGE into an electrical current and energy [6–17].

In RED, cation exchange membranes (CEMs) as well as anion exchange membranes (AEMs) are alternatively stacked beside one another, while high and low concentration solutions flow between them, as shown in Fig. 1 [18–22]. Integrated porous spacers are located between the membranes in order to maintain the distance between the membranes as well as playing an effective role in the solution and ion distribution. Subsequently, cations and anions are transported from the high concentration side into the low concentration side and are converted into electric current via a redox reaction using an electrode and electrolyte at both ends of the RED stack.

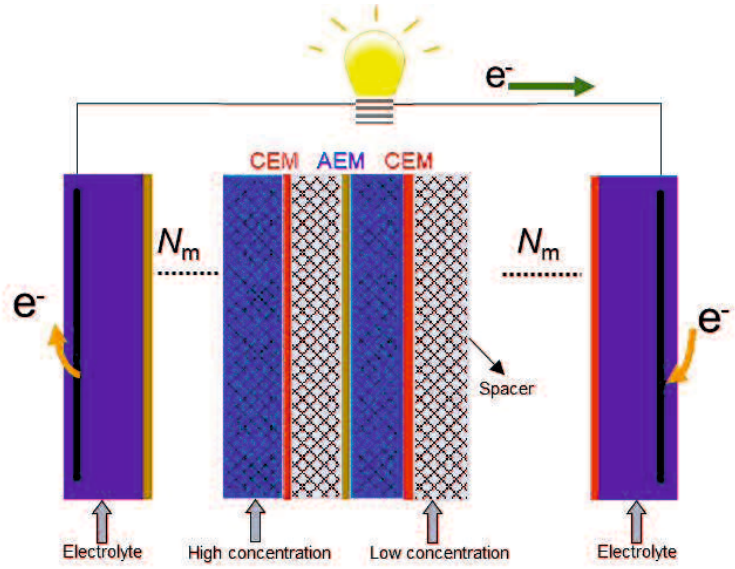

Figure 1. A simple schematic representation of a RED stack including ion exchange membranes, integrated spacers, and electrodes.

Reasonably, seawater and river water have been mainly considered as the feed solutions in the RED process because they are readily available. In this case, a RED power density has been varied by modifying and optimizing different parameters in the RED stack such the membrane, spacer, and operating conditions [23–26]. Among all of the operating conditions, temperature may be one of the more effective factors, which has been given less attention and could have a significant effect on RED performance [27]. Since the seaside is one of the most appropriate places for locating a RED process, the climate (temperature) of the applied solution and area will be important. Among the different areas in the world as well as the different seasons, the temperature of feed solution may be significantly different. Increasing the temperature will lead to an increase in the solution conductivity and a decrease in the respective resistance [28]. Therefore, since the solution resistance is one of the key parameters in the RED stack resistance, temperature may have a considerable effect on the RED process performance. Although, some studies have been

performed to investigate the effect of temperature on the RED process performance, there are no comprehensive studies on how a pilot-scale RED process may be affected by changing the temperature. For instance, *Benneker et al.* showed an ~40% increase in the RED power density can be achieved by increasing the feed temperature from 20 to 40 °C using a 4 cell pair RED stack [27]. In the case of a pilot-scale RED stack, the residence time of the feed solutions in the flow channels will be higher due to the dimensions of the stack [29–31] and therefore, the effect of temperature may be different. In addition, the final purpose of RED is to commercialize the process, so studying the RED process behavior on a pilot-scale will be more appropriate.

In this study, the effect of temperature on the individual feed solutions and membrane resistance were considered in order to discover the most effective parameter in the RED stack. In addition, we have investigated the effect of the temperature of the feed solutions on the power output of a pilot-scale RED system equipped with 200 and 600 μm spacers using model seawater and river water as the feed solutions. The flow rate of the feed solutions were also changed as well as the temperature to investigate their combined effects on the RED power output.

3.2 Experimental

3.2.1 Membrane and solution resistance

Neosepta® CMX and AMX (ASTOM Co., Japan) membranes, and the solution resistance at different temperatures were investigated using a handmade acrylic cell consisting of two parts separated by a membrane with an effective area of 1 cm^2 according to our previous report [32]. The specific properties of CMX and AMX are shown in Table

1 [33]. The sample solution was prepared using NaCl (model seawater) with a conductivity of 49 mS/cm at 25 °C. Briefly, the sample solution was purged inside the cell and the cell was then immersed in a water bath at temperatures ranging from 10 to 35 °C to measure the solution bulk resistance without a membrane, R_{bulk}. In addition, the ion conductivity of the solution at different temperatures was also measured using a conductivity meter (ES-51, HORIBA. Ltd. JAPAN). Subsequently, the same procedure was performed in the presence of a sample membrane in order to measure the resistance including both the solution and membrane resistance, $R_{bulk+mem}$, at a particular temperature. An alternating current (AC) of 10 kHz frequency was applied to prevent an increase in the membrane resistance via the concentration polarization effect. The membrane resistance, R_{mem}, was then calculated from the difference between R_{bulk} and $R_{bulk+mem}$ as follows:

$$R_{mem} = R_{bulk+mem} - R_{bulk} \quad [1]$$

Table 2. Physicochemical characterization of the CMX and AMX membranes.

Membrane	Thickness (mm)	Water content (%)	Area resistance ($\Omega.cm^2$)	Permselectivity* (%)
Neosepta CMX	0.14 – 0.20	25–30	1.8–3.8	97
Neosepta AMX	0.12–0.18	25–30	2.0–3.5	95

* 0.1/0.001 M NaCl at 25 °C.

3.2.2 RED stack

The RED experiment was performed using a pilot-scale RED stack to investigate the effect of the feed solution temperature on the RED stack performance. A 200-cell-pair commercial electrodialysis stack (Acilyzer AC10-20, ASTOM Corp., Japan) containing commercially available ion exchange membranes (IEMs) (Neosepta® AMX and CMX)

with a total membrane effective area of 40 m^2 (20 cm × 50 cm) was used. Spacers with thicknesses of 200 and 600 μm, and porosity of 84 and 85%, respectively and integrated with a gasket to prevent leakage were used. In addition, Pt-coated titanium was used as the electrode and a 5 wt.% aqueous solution of Na_2SO_4 was used as the electrolyte to convert ion transportation into electric current.

3.2.3 RED experiment

RED tests were performed using model seawater (SW) (53 ±0.5 mS/cm NaCl aq.) and model river water (RW)/wastewater (1.3 ±0.5 mS/cm NaCl aq.) prepared using tap water and 99.5% NaCl purchased from NACALAI TESQUE, Inc. Japan. The temperature of both feed solutions (SW and RW) was increased from 10 to 35 °C. The temperature and conductivity of the feed solutions were measured using a MC-31P conductive meter (DKK-TOA Corp., Japan). Both SW and RW were fed into the RED stack using a magnet pump (MD-30RZ-N, IWAKI CO., Ltd.) at different flow rates (2–6 L/min). The flow rates of SW and RW were set at the same value in each experiment and the flow rate of the electrode solution was adjusted in order to maintain a low pressure difference between the feed solution compartments and the electrode solution. Therefore, the solution leakage from the feed solution compartments into the electrolyte and vice versa was negligible. Electrical performance measurements were then carried out using a PLZ 164W instrument (Kikusui electronics crop., Japan). Both the current (I) and voltage (V) were recorded in all the experiments using a data logging system (midi LOGGER GL200, GRAPHTEC Co., Japan) connected to a personal computer. *I-V* curve tests were performed from zero to a maximum current (until the stack voltage became zero) at a current changing rate of 0.4 mA/s. The OCV and maximum current were obtained considering the vertical

and horizontal axis intercepts of the *I-V* curve, respectively. The RED stack resistance was also obtained from the slope of the *I-V* curves using Ohm 's law as follows [34]:

$$E_{stack} = OCV - R_{stack}I \quad [2]$$

where, E_{stack} and R_{stack} are the voltage and resistance of the RED stack, respectively. The RED power output, P_{gross}, and power density, P_d, are then defined using the following equations [34]:

$$P_{gross} = E_{stack}.I \quad [3]$$

$$P_d = {}^{P_{gross}}/_{NA} \quad [4]$$

where, N and A are the number of cell pairs and the effective membrane area of each cell, respectively. The pumping energy, P_{pump}, was also calculated to consider the total net power output, P_{net}, of the RED system as follows:

$$P_{pump} = \frac{(\Delta P_{sea} Q_{sea} + \Delta P_{river} Q_{river})}{\eta_{pump}} \quad [5]$$

$$P_{net} = P_{gross} - P_{pump} \quad [6]$$

where ΔP is pressure drop within the stack, Q is the flow rate of the solution, and η_{pump} is the pumping efficiency which we assumed to be 0.85 in this study.

3.3 Results and discussion

3.3.1 The effect of temperature on the solution resistance

The effect of temperature on the solution conductivity is shown in Fig. 2. The original solution was prepared at an initial conductivity of 49 mS/cm at 25 °C and the

conductivity was then measured at different temperatures ranging from 15 to 35 °C. The solution conductivity can be considered as the parameter to show the effect of temperature on the solution resistance since the conductivity of a solution has an inverse relationship with the solution resistance (*1/R*). Increasing temperature enhances the ionic diffusion according the Nernst-Haskell equation because the viscosity of the solution decreases with increasing the temperature [35]. Therefore, ions can move easier upon increasing the temperature, resulting in an increase in the conductivity. Moreover, the conductivity increases almost linearly upon increasing the temperature, and this linear relationship allows one to express the temperature dependence of the solution conductivity using the conductivity at 25 °C as a standard value as follows:

$$K\ (T) = K\ (25\ °C)[1 + 0.022\ (T - 25)], (R^2 = 0.9998) \quad [7]$$

where K(T) and K(25 °C) are the solution conductivity [mS/cm] at temperature T [°C]) and 25 °C, respectively. When considering this equation, the solution conductivity linearly increases/decreases upon increasing/decreasing the feed solution temperature with a temperature coefficient of ~2.2%/°C at 25 °C.

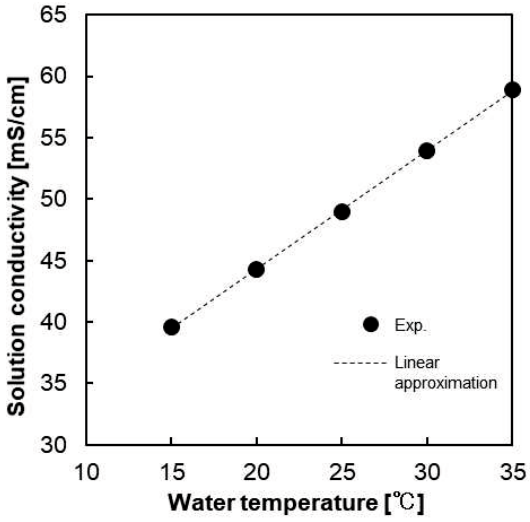

Figure 2. The relationship between the solution conductivity and water temperature.

3.3.2 The effect of temperature on the membrane resistance

Fig. 3(A) and (B) show the effect of the feed water temperature on the inverse of the membrane resistance ($1/R_m$) of CMX and AMX, respectively when changing the temperature from 10 to 35 °C. The ion conductivity of the membrane depends on both the ion mobility in the membrane and the ion concentration in the membrane. Donnan theory states when the ion concentration of the external solution is lower than the concentration of the fixed charged group inside the membrane, the concentration of the co-ion (ions with the same sign of charge to the fixed charged groups of membrane) is negligibly low inside the membrane and that of the counter-ions (ions with the opposite sign of charge to the fixed charged groups of membrane) is almost equal to the fixed charge groups concentration, which will be independent of the concentration of the external solution, indicating that the concentration of the counter-ions at the membrane/the external solution interface at the high concentration side is almost equal to that at the low concentration side

[36]. Therefore, we assumed that the effect of feed solution concentration in the low concentration compartment on the membrane resistance is negligible. In this case, the membrane conductivity (the inverse of the membrane resistance) also increased with increasing temperature because it also leads to an increase in ion mobility in the membrane as well as in the solution. Moreover, a clear linear relationship was obtained similar to that observed with the solution conductivity. Consequently, this linear relationship provides a linear empirical equation as follows:

$$K_m(T) = K_m(25\ ^\circ C)[1 + 0.027\ (T - 25)],\ (R^2 = 0.9800) \quad [8]$$

where $K_m(T)$ and K_m (25 °C) are the inverse resistance ($1/R_m$) of the CMX/AMX membrane at temperature T and 25 °C, respectively. It is worth noting that almost the same temperature coefficient (~2.7%/°C) was obtained for both CMX and AMX. Therefore, this simple approximation may be used as an empirical equation to predict the CMX/AMX resistance at different temperatures from 15 to 35 °C.

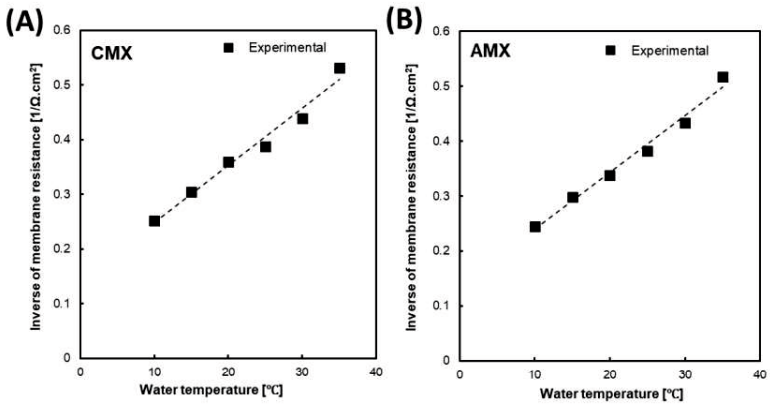

Figure 3. The effect of water temperature on the inverse values of the membrane resistance of CMX and AMX.

3.3.3 The effect of temperature on the RED performance

3.3.3.1 Open circuit voltage (OCV)

The OCV of the RED stack measured at feed flow rates (Q) of 1, 4, and 6 L/min, and at different temperatures and spacer thickness are shown in Fig. 4. The highest OCVs (31.33–33.87 V) were obtained at a feed flow rate of 6 L/min in both stacks with 200 and 600 μm spacers.

The salinity ratio between the high and low concentration compartments of the RED stack will decrease by osmotic water flow from the lower concentration side to the higher concentration side as well as co- and counter-ion diffusion from the higher to lower concentration sides during the OCV measurements, even at zero current [22]. Consequently, decreasing the salinity ratio on the membrane surface will lead to a decrease in the OCV of the RED stack. By increasing the feed flow rate, the residence time of the solution in the flow channels of the RED stack decreases, resulting in the feed solution being refreshed faster. This suppression of the decrease in the OCV was caused by water transport and ion diffusion, as-mentioned above. Therefore, in our pilot-scale RED stack, the OCV increased from 29.5 V to >33 V upon increasing the feed solution flow rate from 2 to 6 L/min using both types of spacer studied. In addition, the effect of the feed solution flow rate on the OCV value in the RED stack with a 200 μm spacer was slightly higher than that using a 600 μm spacer. Actually, even when using the same flow rate, the flow velocity between the membranes were different and slightly influenced the resulting OCV value.

In addition to the feed solution flow rate, the OCV of the RED stack was also affected by temperature. Theoretically, the RED stack OCV can be defined using Eq. (9), which is related to the temperature, ions valence, and concentration ratio as follows:

$$OCV = \frac{N_m \cdot \alpha \cdot R \cdot T_{ab}}{z \cdot F} \cdot \ln\left(\frac{C_H \gamma_H}{C_L \gamma_L}\right) \quad [9]$$

where R is the gas constant, T_{ab} is absolute temperature [K], N_m is the number of cell pairs, α is the average membrane permselectivity, z is the valence of the ions, F is the Faraday constant, and C and γ are the concentration and activity coefficient of NaCl, respectively. Subscripts H and L represent the high and low concentration sides, respectively. Therefore, upon increasing the temperature of the feed solution, the OCV will theoretically increase with a temperature dependence of ~0.35%/°C. However, Fig. 4 shows when using a low feed solution flow rate (Q = 2 L/min), the effect of temperature on the OCV of the RED stack disappeared (0.2 and 0.4%/°C for the 200 and 600 μm cases, respectively), meaning that the OCVs at 10 and 35 °C are almost identical, while the OCV increased with a temperature dependence >2%/°C at a flow rate of 6 L/min from 10 to 35 °C in both the 200 and 600 μm spacer cases. It seems that under low feed flow rate conditions, the dominant effect on the OCV will be due to the osmotic water flow as well as co- and counter-ion transportation as-mentioned above. However, upon increasing the feed flow rate, the effect of temperature on the stack OCV appears more clearly despite the presence of water and ion transportation. Empirical linear relationships between the RED stack OCV and feed solution temperature at different feed solution flow rates were also successfully obtained, as shown in Eq. 10–12 and Eq. 13–15 for the RED stack equipped with 200 and 600 μm spacers, respectively, in order to predict the stack OCV at different temperatures. At a flow rate of 6 L/min, 0.23%/°C and 0.26%/°C were obtained using the RED stack with 200 and

600 μm spacers, respectively, and these values were slightly less than the theoretical value (0.30%/°C) estimated using Eq. 9 because of the presence of water and ion transportation, as-mentioned above.

$$OCV\ (T) = OCV\ (25°C)[1 + 0.0002\ (T - 25)]\ \ (200\ \mu m\ at\ 2\ L/min, R^2 = 0.0067) \quad [10]$$

$$OCV\ (T) = OCV\ (25°C)[1 + 0.0015\ (T - 25)]\ \ (200\ \mu m\ at\ 4\ L/min, R^2 = 0.9742) \quad [11]$$

$$OCV\ (T) = OCV\ (25°C)[1 + 0.0023\ (T - 25)]\ \ (200\ \mu m\ at\ 6L/min, R^2 = 0.9807) \quad [12]$$

$$OCV\ (T) = OCV\ (25°C)[1 + 0.0004\ (T - 25)]\ \ (600\ \mu m\ at\ 2L/min, R^2 = 0.6334) \quad [13]$$

$$OCV\ (T) = OCV\ (25°C)[1 + 0.0021\ (T - 25)]\ \ (600\ \mu m\ at\ 4L/min, R^2 = 0.9129) \quad [14]$$

$$OCV\ (T) = OCV\ (25°C)[1 + 0.0026\ (T - 25)]\ \ (600\ \mu m\ at\ 6L/min, R^2 = 0.9922) \quad [15]$$

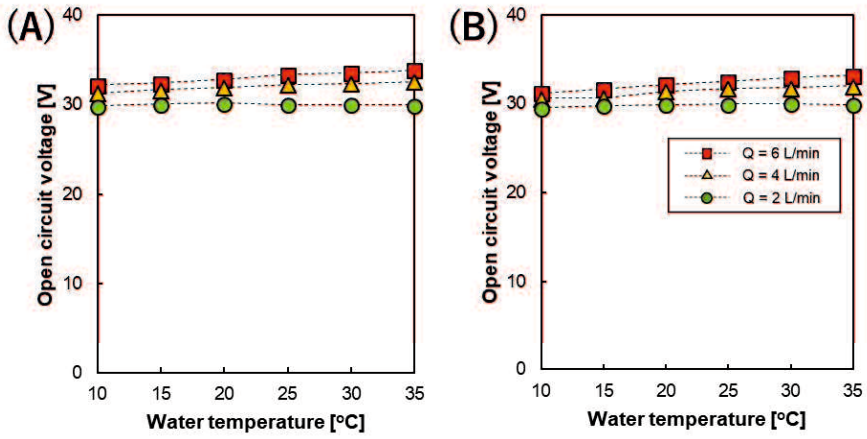

Figure. 4. The temperature dependence of the RED stack OCV at different feed solution flow rates using an intermediate distance in the stack of (A) 200 and (B) 600 μm, respectively.

3.3.3.2 RED stack power output

The maximum power output (gross power, P_{max}) of the RED stack was measured during *I-V* tests conducted at different flow rates and temperatures. Fig. 5(A) and (B) show the relationship between P_{max} with different feed solution flow rates and temperatures using the RED stack equipped with 200 and 600 μm spacers, respectively. All of the *I-V* and *I-P* curves are shown in the Supplementary Information. Similar to the stack OCV, the highest P_{max} (22.5–38.6 and 11.09–21.52 W using the RED stack with 200 and 600 μm spacers, respectively) was obtained at the higher feed solution flow rate of 6 L/min, while the lower P_{max} (15–20 and 10.47–17.28 W using the RED stack with 200 and 600 μm spacers, respectively) was obtained at the lower feed solution flow rate of 2 L/min [23,37]. The higher RED stack power output observed in the 200 μm was mainly attributed to the lower resistance of the solution compartment in the stack. Moreover, linear relationships were also obtained for all the flow rates studied, although their temperature dependence was different. As a result, their linear relationships provide empirical equations that can be used to predict the gross power of the stack at different temperatures as well as different flow rates as follows:

$$P_{max}\,(T) = P_{max}\,(25°C)[1 + 0.011\,(T - 25)]\;\;(200\;\mu m\;at\;2L/min, R^2 = 0.9739) \quad [16]$$

$$P_{max}\,(T) = P_{max}\,(25°C)[1 + 0.017\,(T - 25)]\;\;(200\;\mu m\;at\;4L/min, R^2 = 0.9962) \quad [17]$$

$$P_{max}\,(T) = P_{max}\,(25°C)[1 + 0.020\,(T - 25)]\;\;(200\;\mu m\;at\;6L/min, R^2 = 0.9988) \quad [18]$$

$$P_{max}\,(T) = P_{max}\,(25°C)[1 + 0.016\,(T - 25)]\;\;(600\;\mu m\;at\;2L/min, R^2 = 0.9883) \quad [19]$$

$$P_{max}\ (T) = P_{max}\ (25°C)[1 + 0.018\ (T - 25)]\ \ (600\ \mu m\ at\ 2L/min, R^2 = 0.9970) \quad [20]$$

$$P_{max}\ (T) = P_{max}\ (25°C)[1 + 0.019\ (T - 25)]\ \ (600\ \mu m\ at\ 6L/min, R^2 = 0.9973) \quad [21]$$

where P_{max}(T) is maximum power at temperature T and P_{max}(25 °C) is the maximum power at 25 °C. The effect of temperature on the power output was significantly higher when compared with the those observed for the OCV. In fact, maximum power output of RED stack is affected by both OCV and the stack resistance (R_{stack}) as follows [32]:

$$P_{max} = \frac{V_{OC}^2}{4R_{stack}} \quad [22]$$

Actually, R_{stack} contains ohmic (membrane, solution, and electrode system resistances) and non-ohmic (concentration polarization) regimes, which are affected by both the feed solution flow rate and temperature. Increasing the feed solution flow rate is helpful to reduce the concentration polarization layer on the membrane surface as well as increasing the ion distribution, which leads to a reduction in the stack non-ohmic resistance [38,39]. On the other hand, the membrane and solution resistance decrease upon increasing the temperature due to the increase in the ion mobility and solution conductivity, as-mentioned before. Therefore, upon increasing both the feed solution flow rate and temperature, the power output was increased due to the reduction in the stack resistance, as shown in Fig. 5. Moreover, when considering the effect of temperature on the solution and membrane resistance (Eq. 7 and 8), and the stack OCV (Eq. 10–15), the dominant parameters for the RED stack power output will be the solution and membrane resistance.

It is worth noting that increasing the feed solution flow rate (6 L/min) makes the power output of the RED stack become more dependent on temperature when compared to using a low feed solution flow rate (2 L/min). In fact, at a high feed solution flow rate, the

stack resistance is mainly dependent on the membrane and solution resistance, while the effect of concentration polarization becomes lower. Therefore, the effect of temperature on the RED stack power output is almost in the same range as the effect of temperature on the membrane and solution resistance (2–3%/°C) when using the higher feed solution flow rate. However, in the case of the lower feed solution flow rate, the dominant parameter in the RED stack resistance is the concentration polarization, which is almost independent of temperature. Hence, at a low feed solution flow rate, the dependence of the power output of the RED stack becomes less upon changing the temperature. In addition, changing the feed solution flow rate from 2 into 6 L/min was more effective on the RED stack power output when using the 200 μm spacers. In fact, increasing the feed solution flow rate on the RED stack with the 200 μm spacer has a significant effect on the flow velocity of the feed solution between the membranes, which leads to a significant decrease in the concentration polarization effect. However, when using the RED stack with the 600 μm spacers, changing the flow rate had a lower effect on the feed velocity and subsequently, the concentration polarization effect. Since the temperature dependence with different flow rates can only be obtained using the pilot-scale experiment, the obtained results are promising toward the design of a full-scale RED system in the future.

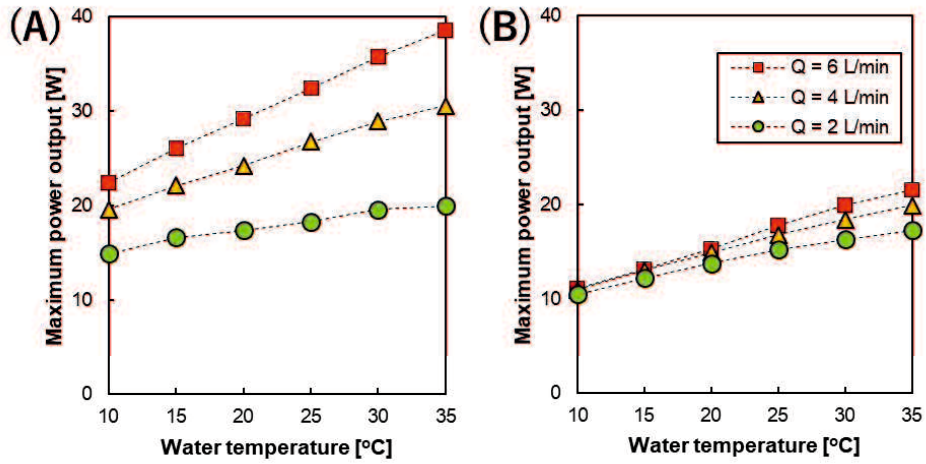

Figure. 5. The temperature dependence of the maximum power output of the RED stack with an intermediate distance of (A) 200 and (B) 600 μm at different feed solution flow rates.

3.3.3.3 Pumping energy and net power output

Fig. 6 shows the temperature dependence of the pumping energy at different feed solution flow rates calculated from the pressure drops using Eq. 5. Reasonably, the pumping energy using the 200 μm spacer was higher than that using the 600 μm spacer. This can be attributed to both the higher feed solution flow velocity and smaller intermediate distance. In addition, changing the feed solution flow rate has more of an effect on the feed velocity in the case of the RED stack with 200 μm spacers. Therefore, the difference between the pumping energy at different flow rates using the RED stack with 200 μm spacers was more prominent.

When increasing the water temperature from 10 to 35 °C, the pumping energy gradually decreased because the viscosity of the feed solutions decreased. The viscosity of water decreases from 1.30 to 0.719 cP upon increasing the temperature from 10 to 35 °C. Furthermore, the pumping energy significantly increases at high feed solution flow rates

and the smaller intermediate distance, as shown in Fig. 6(A). In this case, the effect of decreasing the solution viscosity became more prominent due to the higher flow velocity. Whereas, the pumping energy did not change significantly using the 600 μm spacers due to the lower feed flow velocity, as shown in Fig. 6(B).

The net power output of the RED stack was obtained by subtracting the pumping energy from gross power output, as shown in in Fig. 7. Interestingly, roughly linear relationships were still obtained under all the conditions studied although their slopes (temperature dependence) were different. The net power output of the RED stack equipped with 200 μm spacers showed steeper slopes upon increasing the temperature and the slopes rapidly changed depending on the flow rate used. On the other hand, the net power output of the RED stack with 600 μm spacers increased almost linearly with increasing temperature at all the feed solution flow rates studied and the temperature dependence of the slopes was less steep than those observed when using 200 μm spacers. In addition, when changing the flow rate, the change in the temperature dependence was less than that observed using the 200 μm spacers. Therefore, during pilot-scale operation, conditions such as the flow rate and stack conditions (intermediate distance between the membrane) strongly influence the temperature dependence of the resulting net power output. At the highest temperature (35 °C), the RED stack with 200 μm spacers and a feed solution flow rate of 4 L/min showed the highest net power output (~22.7 W (0.57 W/m^2)) among the all experimental conditions used in this study.

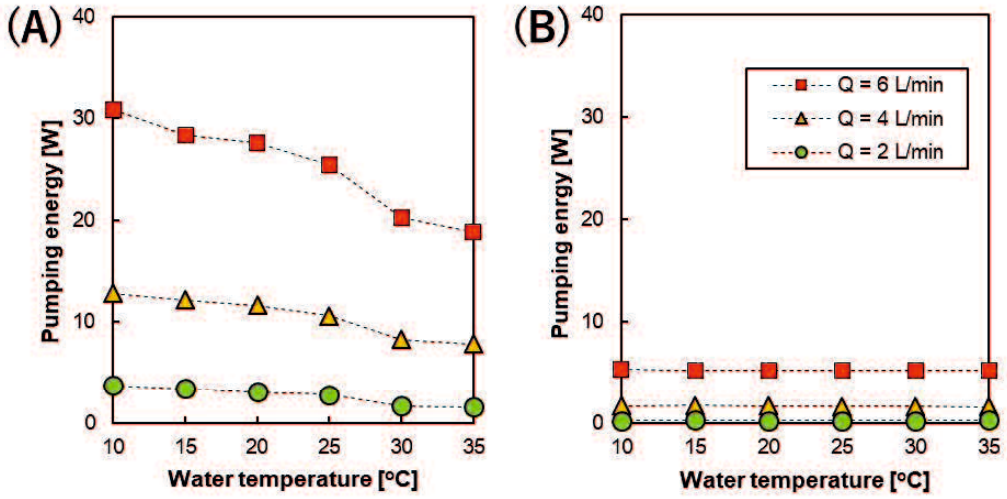

Figure. 6. The temperature dependence of the pumping energy calculated from the pressure drop of the stack with an intermediate distance of (A) 200 and (B) 600 μm at different feed solution flow rates.

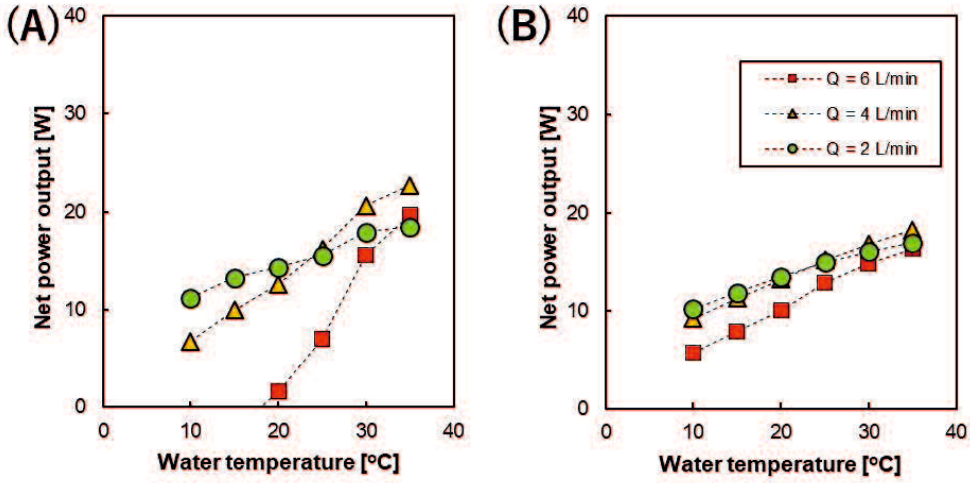

Figure. 7. The temperature dependence of the net power output of the RED stack with an intermediate distance of (A) 200 and (B) 600 μm at different flow rates.

3.4 Conclusions

The effects of temperature on the solution and membrane resistance, and subsequent power generation performance of two pilot-scale RED stacks (200 and 600 μm) have been presented in this study. Both the solution and membrane resistance show linear temperature dependences of ~2.2 and 2.7%/°C, respectively. On the other hand, the temperature dependence of the RED stack OCV was ~0.2%/°C, which was independent of the intermediate distance. However, the subsequent power output and its temperature dependence was influenced by experimental conditions such as the flow rate and intermediate distance with a temperature coefficient of 1.1–2.0%/°C, which approaches its predicted value of ~3%. Furthermore, the net power output was dramatically influenced by temperature, especially in the case of the higher performance RED stack (smaller intermediate distance and high flow rate conditions). On the other hand, the temperature dependence of the resulting net power became less when using the lower performance stack (larger intermediate distance and low flow rate conditions). These results are promising for the future design of a full-scale RED system and the selection of a suitable location considering water temperature.

3.5 References

[1] H. Kim, Y.E. Kim, N.J. Jeong, K.S. Hwang, J.H. Han, J.Y. Nam, E. Jwa, S.C. Nam, S.Y. Park, Y. Il Yoon, C.S. Kim, Innovative reverse-electrodialysis power generation system for carbon capture and utilization, J. CO2 Util. 20 (2017) 312–317. doi:10.1016/j.jcou.2017.05.025.

[2] R. Long, B. Li, Z. Liu, W. Liu, Hybrid membrane distillation-reverse electrodialysis electricity generation system to harvest low-grade thermal energy, J. Memb. Sci. 525 (2017) 107–115. doi:10.1016/j.memsci.2016.10.035.

[3] J.N. Weinstein, F.B. Leitz, Electric power from differences in salinity: The dialytic battery, Science. 191 (1976) 557–559. doi:10.1126/science.191.4227.557.

[4] L. Gurreri, A. Tamburini, A. Cipollina, G. Micale, M. Ciofalo, CFD prediction of concentration polarization phenomena in spacer-filled channels for reverse electrodialysis, J. Memb. Sci. 468 (2014) 133–148. doi:10.1016/j.memsci.2014.05.058.

[5] J.W. Post, H.V.M. Hamelers, C.J.N. Buisman, Energy recovery from controlled mixing salt and fresh water with a reverse electrodialysis system, Environ. Sci. Technol. 42 (2008) 5785–5790. doi:10.1021/es8004317.

[6] T. Rijnaarts, E. Huerta, W. van Baak, K. Nijmeijer, Effect of divalent cations on RED performance and cation exchange membrane selection to enhance power sensities, Environ. Sci. Technol. 51 (2017) 13028–13035. doi:10.1021/acs.est.7b03858.

[7] J. Moreno, V. Díez, M. Saakes, K. Nijmeijer, Mitigation of the effects of multivalent ion transport in reverse electrodialysis, J. Memb. Sci. 550 (2018) 155–162. doi:10.1016/j.memsci.2017.12.069.

[8] L. Gurreri, A. Tamburini, A. Cipollina, G. Micale, M. Ciofalo, Flow and mass transfer in spacer-filled channels for reverse electrodialysis: A CFD parametrical study, J. Memb. Sci. 497 (2016) 300–317. doi:10.1016/j.memsci.2015.09.006.

[9] D.A. Vermaas, D. Kunteng, M. Saakes, K. Nijmeijer, Fouling in reverse electrodialysis under natural conditions, Water Res. 47 (2012) 1289–1298. doi:10.1016/j.watres.2012.11.053.

[10] Z.Y. Guo, Z.Y. Ji, Y.G. Zhang, F.J. Yang, J. Liu, Y.Y. Zhao, J.S. Yuan, Effect of ions (K^+, Mg^{2+}, Ca^{2+} and SO_4^{2-}) and temperature on energy generation performance of reverse electrodialysis stack, Electrochim. Acta. 290 (2018) 282–290. doi:10.1016/j.electacta.2018.09.015.

[11] F. Liu, O. Coronell, D.F. Call, Electricity generation using continuously recirculated flow electrodes in reverse electrodialysis, J. Power Sources. 355 (2017) 206–210. doi:10.1016/j.jpowsour.2017.04.061.

[12] B. Zhang, H. Gao, Y. Chen, Enhanced ionic conductivity and power generation using ion-exchange resin beads in a reverse-electrodialysis stack, Environ. Sci. Technol. 49 (2015) 14717–14724. doi:10.1021/acs.est.5b03864.

[13] J.G. Hong, W. Zhang, J. Luo, Y. Chen, Modeling of power generation from the mixing of simulated saline and freshwater with a reverse electrodialysis system : The effect of

monovalent and multivalent ions, Appl. Energy. 110 (2013) 244–251. doi:10.1016/j.apenergy.2013.04.015.

[14] D.A. Vermaas, J. Veerman, M. Saakes, K. Nijmeijer, Influence of multivalent ions on renewable energy generation in reverse electrodialysis, Energy Environ. Sci. 7 (2014) 1434–1445. doi:10.1039/c3ee43501f.

[15] F. Giacalone, P. Catrini, A. Tamburini, A. Cipollina, A. Piacentino, G. Micale, Exergy analysis of reverse electrodialysis, Energy Convers. Manag. 164 (2018) 588–602. doi:10.1016/j.enconman.2018.03.014.

[16] X. Tong, B. Zhang, Y. Chen, Fouling resistant nanocomposite cation exchange membrane with enhanced power generation for reverse electrodialysis, J. Memb. Sci. 516 (2016) 162–171. doi:10.1016/j.memsci.2016.05.060.

[17] J. Moreno, N. De Hart, M. Saakes, K. Nijmeijer, CO_2 saturated water as two-phase flow for fouling control in reverse electrodialysis, Water Res. 125 (2017) 23–31. doi:10.1016/j.watres.2017.08.015.

[18] S. Pawlowski, J.G. Crespo, S. Velizarov, Pressure drop in reverse electrodialysis: Experimental and modeling studies for stacks with variable number of cell pairs, J. Memb. Sci. 462 (2014) 96–111. doi:10.1016/j.memsci.2014.03.020.

[19] B. Kang, H.J. Kim, D.K. Kim, Membrane electrode assembly for energy harvesting from salinity gradient by reverse electrodialysis, J. Memb. Sci. 550 (2018) 286–295. doi:10.1016/j.memsci.2018.01.006.

[20] J. Luque, D. Salvo, A. Cosenza, A. Tamburini, G. Micale, A. Cipollina, Long-run operation of a reverse electrodialysis system fed with wastewaters, J. Environ. Manage. 217 (2018) 871–887. doi:10.1016/j.jenvman.2018.03.110.

[21] N. Michal, R. Ashu, J. Hn, R. Kodým, E. Curcio, K. Bouzek, Hydrogen production from industrial wastewaters : An integrated reverse electrodialysis - water electrolysis energy system, J. Clean. Prod. 203 (2018) 418–426. doi:10.1016/j.jclepro.2018.08.269.

[22] S. Mehdizadeh, M. Yasukawa, M. Kuno, Y. Kawabata, M. Higa, Evaluation of energy harvesting from discharge solutions in a salt production plant by reverse electrodialysis (RED), Desalin. (n.d.).

[23] D.A. Vermaas, M. Saakes, K. Nijmeijer, Doubled power density from salinity gradients at reduced intermembrane distance, Environ. Sci. Technol. 45 (2011) 7089–7095. doi:10.1021/es2012758.

[24] M. Turek, B. Bandura, P. Dydo, Power production from coal-mine brine utilizing reversed electrodialysis, Desalination. 221 (2008) 462–466. doi:10.1016/j.desal.2007.01.106.

[25] M. Turek, B. Bandura, Renewable energy by reverse electrodialysis, Desalination. 205 (2007) 67–74. doi:10.1016/j.desal.2006.04.041.

[26] J. Veerman, M. Saakes, S.J. Metz, G.J. Harmsen, Reverse electrodialysis: Performance of a stack with 50 cells on the mixing of sea and river water, J. Memb. Sci. 327 (2009) 136–144. doi:10.1016/j.memsci.2008.11.015.

[27] A.M. Benneker, T. Rijnaarts, R.G.H. Lammertink, A. Wood, Effect of temperature gradients in (reverse) electrodialysis in the Ohmic regime, J. Memb. Sci. 548 (2018) 421–428. doi:10.1016/j.memsci.2017.11.029.

[28] R. Sauerheber, B. Heinz, Temperature Effects on Conductivity of Seawater and Physiologic Saline, Mechanism and Significance, Chem. Sci. J. 6 (2015) 4–8. doi:10.4172/2150-3494.1000109.

[29] J. Veerman, M. Saakes, S.J. Metz, H.G. Jan, Electrical power from sea and siver water by reverse electrodialysis : A first step from the laboratory to a real power plant, Environ. Sci. Technol. 44 (2010) 9207–9212.

[30] M. Tedesco, C. Scalici, D. Vaccari, A. Cipollina, A. Tamburini, G. Micale, Performance of the first reverse electrodialysis pilot plant for power production from saline waters and concentrated brines, J. Memb. Sci. 500 (2016) 33–45. doi:10.1016/j.memsci.2015.10.057.

[31] M. Tedesco, A. Cipollina, A. Tamburini, G. Micale, Towards 1 kW power production in a reverse electrodialysis pilot plant with saline waters and concentrated brines, J. Memb. Sci. 522 (2017) 226–236. doi:10.1016/j.memsci.2016.09.015.

[32] S. Mehdizadeh, M. Yasukawa, T. Abo, Y. Kakihana, M. Higa, Effect of spacer geometry on membrane and solution compartment resistances in reverse electrodialysis, J. Memb. Sci. 572 (2019) 271–280. doi:10.1016/j.memsci.2018.09.051.

[33] R.K. Nagarale, G.S. Gohil, V.K. Shahi, Recent developments on ion-exchange membranes and electro-membrane processes, Adv. Colloid Interface Sci. 119 (2006) 97–130. doi:10.1016/j.cis.2005.09.005.

[34] J. Nam, K. Hwang, H. Kim, H. Jeong, H. Kim, E. Jwa, S. Yang, J. Choi, C. Kim, J. Han, N. Jeong, Assessing the behavior of the feed-water constituents of a pilot-scale 1000-cell-pair reverse electrodialysis with seawater and municipal wastewater ef fl uent, Water Res. 148 (2019) 261–271. doi:10.1016/j.watres.2018.10.054.

[35] M. Shibuya, M. Yasukawa, T. Takahashi, T. Miyoshi, M. Higa, H. Matsuyama, Effect of operating conditions on osmotic-driven membrane performances of cellulose triacetate forward osmosis hollow fiber membrane, Desalination. 362 (2015) 34–42. doi:10.1016/j.desal.2015.01.031.

[36] M. Higa, A. Taniokab, K. Miyasakab, An experimental study of ion permeation in multicomponent ion systems as a function of membrane charge density, J. Memb. Sci. 64 (1991) 255–262.

[37] R. Long, B. Li, Z. Liu, W. Liu, Performance analysis of reverse electrodialysis stacks: channel geometry and flow rate optimization, Energy. 158 (2018) 427–436. doi:10.1016/j.energy.2018.06.067.

[38] D.A. Vermaas, M. Saakes, K. Nijmeijer, Enhanced mixing in the diffusive boundary layer for energy generation in reverse electrodialysis, J. Memb. Sci. 453 (2014) 312–319. doi:10.1016/j.memsci.2013.11.005.

[39] P. Długoł, D. Joanna, K. Nijmeijer, M. Wessling, Ion conductive spacers for increased power generation in reverse electrodialysis, J. Memb. Sci. 347 (2010) 101–107. doi:10.1016/j.memsci.2009.10.011.

3.6 Supplementary information

3.6.1 Appendix A

Figures A1 and A2 show the current-voltage (*I-V*) and current-power (*I-P*) relationships of the RED stack having different intermediate distance (200 and 600 μm, respectively) at 10-35° C with changing the flow rate. The y-intercept of I-V curve indicates the open circuit voltage (OCV) of the stack, and the maximum value of the power were subsequently used to evaluate the effect of water temperature on the resulting RED power output as shown in Figure 5.

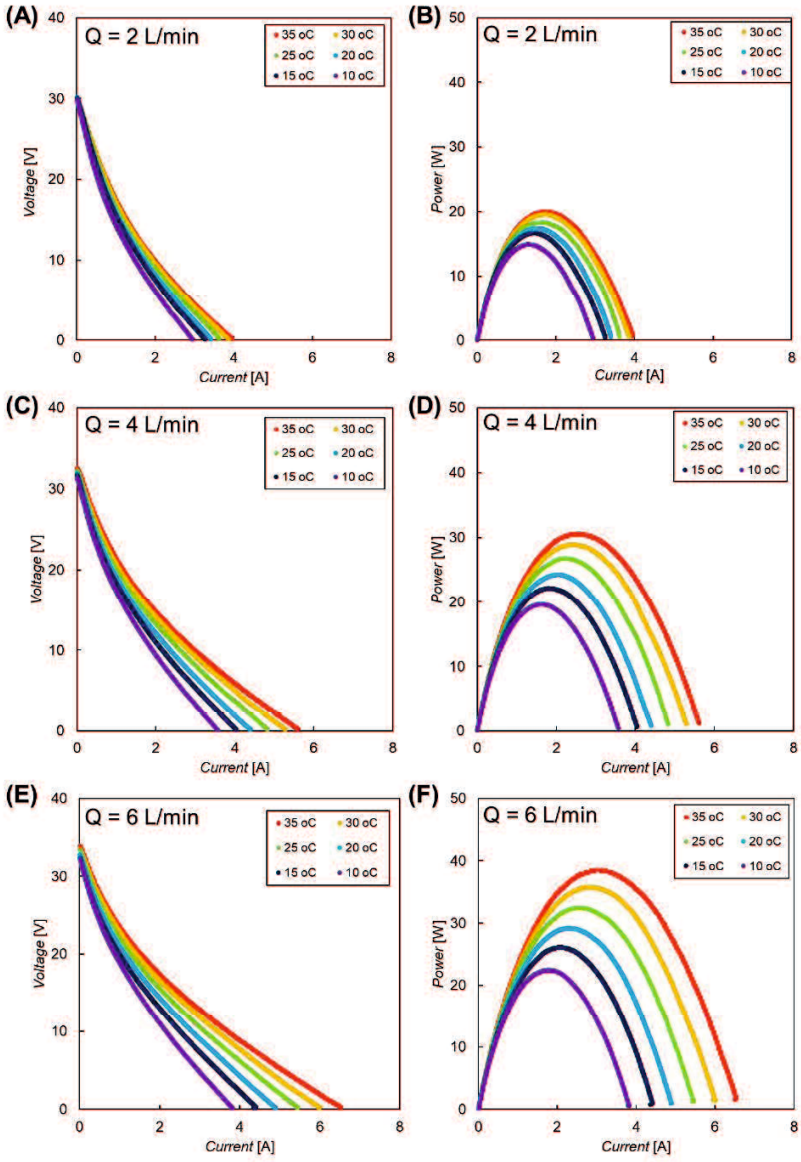

Figure A1. (A, C, E) current-voltage (*I-V*) and (B, D, F) current-power (*I-P*) relationships of the RED stack having the intermediate distance of 200 □m at 10-35°C with different flow rate, *Q*.

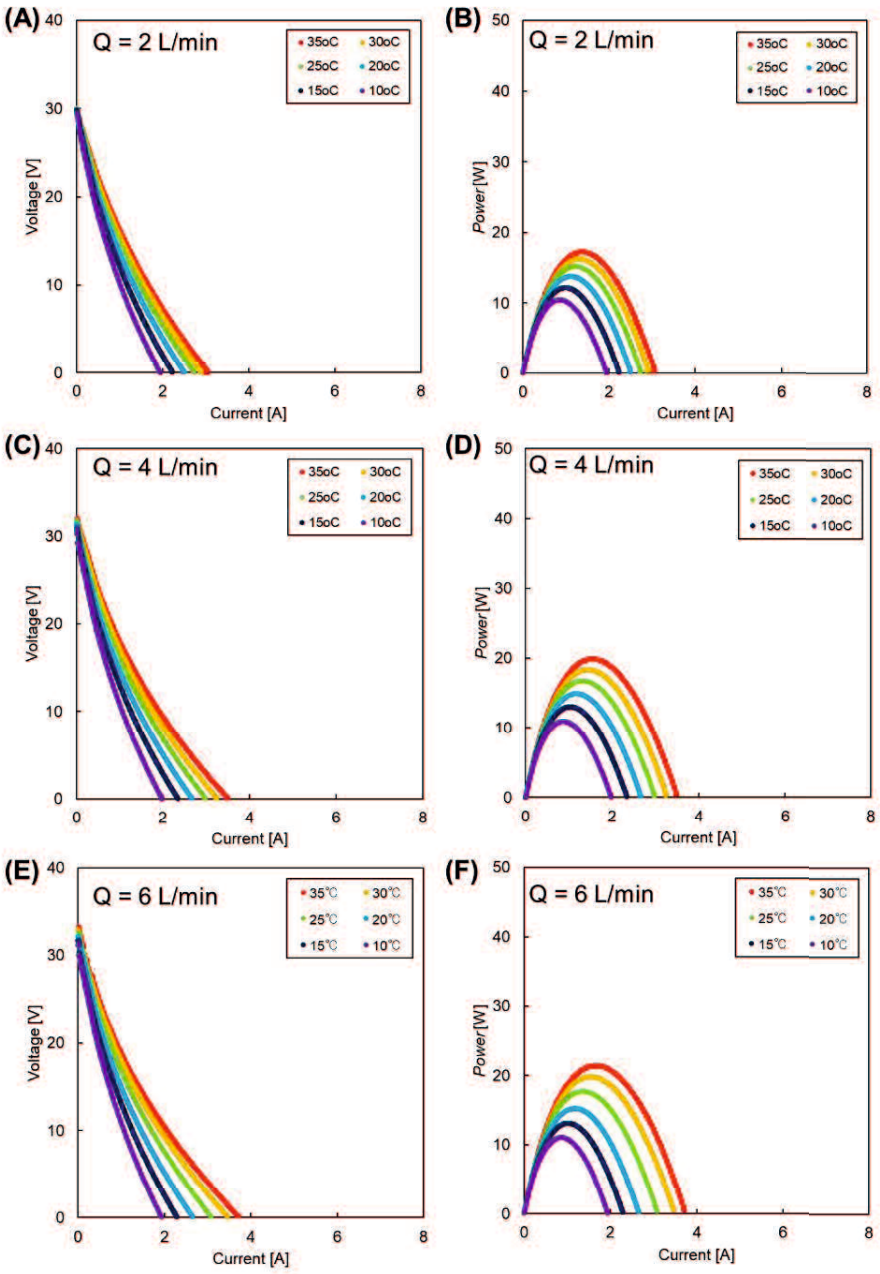

Figure A2. (A, C, E) current-voltage (*I-V*) and (B, D, F) current-power (*I-P*) relationships of the RED stack having the intermediate distance of 600 □m at 10-35°C with different flow rate, *Q*.

Chapter 4

Evaluation of energy harvesting from discharged solutions in a salt production plant by reverse electrodialysis (RED)

4.1 Introduction

Salinity gradient energy (SGE) is known as an electrochemical potential between two solutions with different concentrations and a process proposed by *Pattle* in 1954 [1]. It was theoretically estimated that the total world SPE can produce a total of 1.4 -2.6 TW by applying all discharge river water into the sea in the world [2,3] Membrane-based pressure retarded osmosis (PRO) and reverse electrodialysis (RED), which utilize semi-permeable membranes and ion exchange membranes (IEMs), respectively, are two promising processes among the technologies available for harvesting energy by SGE [2,4–8]. The RED process is typically favored over the PRO system, as a higher net power density is achieved by means of RED when compared to PRO and no moving parts for high pressures are required as seawater and river water act as the feed solutions [9–11].

In RED, concentrated and dilute solutions flow alternatively between anion and cation exchange membranes (AEMs and CEMs) which are selective for anions and cations, respectively, as shown in Fig. 1. Anions and cations are transported from high concentrate compartment (HCC) into low concentrate compartment (LCC) through AEM and CEM due to their concentration gradient, respectively [8]. The flux of anions and cations in the opposite direction can be converted into electric current by means of two suitable electrodes placed at the ends of a RED stack.

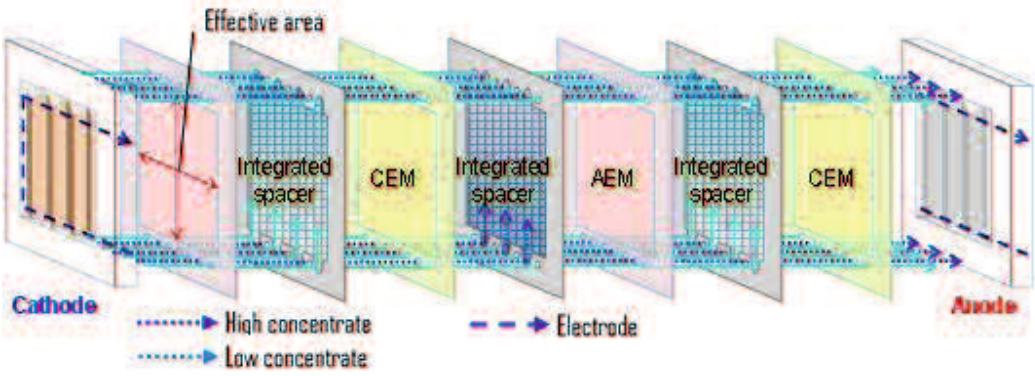

Figure. 1. Simple scheme of a RED stack includes IEMs, integrated spacers, and electrodes.

In many studies, artificial seawater (0.5 M NaCl) and river water (0.015 M NaCl) have been considered as feed solutions for the RED process [11]. In these studies, RED power density was increased from 0.46 to 1.05 W/m^2 by optimizing different factors in the RED stacks such as the membranes, spacers, and hydrodynamic conditions [11–14]. A power density of 2.20 W/m^2 was also achieved by applying a 60 µm spacer, however, this led to a significantly increased pressure drop, which consumed a high amount of energy used for pumping the feed solutions [11]. In addition, an investigation of a real case, natural seawater and river water, were applied as feed solutions for a RED process, where a significant reduction in power density compared with artificial feeds due to the presence of divalent ions (*e.g.* Mg^{2+}, Ca^{2+}, SO_4^{2-}) as well as NaCl was seen [15–18]. This was later determined to be from the transport of divalent ions against their concentration gradient when large amount of monovalent ions were present in HCC, [19,20] termed uphill transport, and effectively reduced the electrochemical potential [18]. In addition, multivalent ions have a large hydration radius; hence it increased membrane resistance. Therefore, applying monovalent ion selective membranes was proposed to improve the RED performance when divalent ions were present in RED feed solutions in comparison to standard membranes due to their barrier effect against divalent ions [18]. However, to

the best of our knowledge, the performance of the RED process by applying one-sided monovalent ion selective membranes in the presence of multivalent ions in feed solutions has not yet been investigated. Since ions are transported from HCC to LCC, monovalent selective properties on one-sided of the membrane should show better performance than on both sides of the membranes due to lower membrane resistance.

Moreover, the application of RED is not just limited to using seawater and river water as feed solutions. For instance, *Daniilidis et al*. reported getting a RED power density of 6.7 W/m^2 by utilization of river water (0.01 M NaCl) and brine (5 M NaCl) at 60 ºC [8]. Applying a brine with high concentration and a much greater salinity ratio between the RED feed solutions can increase the RED power density, but at the same time leads to decreased the permselectivity of the IEMs and the energy efficiency of the RED system. In addition, *Kingsbury et al*. have investigated the RED performance of five real salt solution pairs such as desalination brine, treated wastewater, saline wastewater, seawater, and river water [21]. They concluded that the natural organic materials have 43% impact on RED performance which is a greater effect than the multivalent ions, which may be directly related to the presence of a high amount of organic material in the feed solutions.

In addition, when considering all different types of applied feeds solutions used for the RED process, a salt production plant could be the most appropriate and have the highest potential for harvesting energy with the RED process. We have found the only a few studies have been performed to investigate the RED performance by utilizing different solutions available from salt production plants. In one case, *Tedesco et al*. have reported the experimental data of a RED pilot-scale with 125 cell pairs and a membrane with a 50 m^2 effective area which supplied a concentrated brine (equivalent to 4–5 M NaCl) from the

salt production plant basins and brackish water (equivalent to 0.03 M NaCl) from a shoreline well [22]. The power densities of 1.6 W/m^2 and 2.7 W/m^2 per cell pair were produced by applying natural solutions and artificial solutions, respectively. In addition, they also increased the scope of their project by scaling into 3 RED pilot plants with a total membrane effective area of 400 m^2 to achieve 1 KW of power production [23]. These plants produced 700 W and 330 W power using artificial and natural feed solutions, respectively.

Unlike the latter two studies, some of the salt production plants are based on membrane–thermal processes to reduce the unit costs [24]. In these types of salt production plants, seawater is initially concentrated with an electrodialysis (ED) process into a brine to reduce the required volume for the evaporation step which increases the production rate. Then brine was heated to produce distilled water and salt by means of an evaporation system. These types of salt production plants can be appropriate for RED systems due to the availability of different solutions with a variety salinity and ion compositions.

In this study, a typical salt production plant which is equipped with ED stacks and evaporators are comprehensively investigated for their potential to harvest energy by means of the RED process. Initially, different available solutions were sampled from the salt production plant to perform essential characterization such as ion composition, ion conductivity, membrane resistance, and membrane potential. The performance of RED was then compared between different solution combinations applying both standard and one-sided monovalent selective membranes to achieve the highest power density in feed solutions that contained multivalent ions. This is the first time that one-sided monovalent

selective membranes have been applied and evaluated in a RED process. Finally, the best membrane and solution combinations are proposed.

4.2 Experimental

4.2.1 Samples from salt production plant

The typical process of a salt production plant involves ED for pre-concentration of brine before evaporation as shown in Fig. 2. For simplicity, the other apparatuses such as the pretreatment system and the multiple effect evaporators are abbreviated. The *X* character is applied to express the magnitude ratio of volume flow rate in each stream, where the volume flow rate of bittern stream is *X* m^3/h as a reference. In this plant, seawater (E) flows into the ED system and split into concentrated (ED brine) and dilute solutions. Then, the ED brine (C) is pumped into an evaporator which produces distilled water (A), bittern (B), and salt by means of dryers. Thus, in the salt plant, all the different solutions abbreviated as A to E are accessible. These 5 types of solutions have the potential to be used for harvesting energy, especially since some of them are simply discarded. Ion conductivity of the solutions was measured by using a conductivity meter (ES-51, HORIBA. Ltd. JAPAN). Sample solutions B and C were diluted twice by adding pure water before measurement since their conductivities are higher than were measurable by our conductivity meter (< 200 mS/cm), then the conductivity was assumed to be double the value. Anion and cation compositions were evaluated by using ion chromatography (DIONEX, ICS-2000 for anions, and DIONEX, ICS-1500 for cations).

4.2.2 Membranes and chemicals

Standard IEMs (Neosepta® CMX and AMX) and one-sided monovalent selective IEMs (Neosepta® CIMS and ACS-8T) were obtained from ASTOM Corporation, Japan. Unless otherwise specified, 99.5% NaCl from NACALAI TESQUE, Inc. Japan and deionized water purified with ion exchange resin cartridge (YA-053, ORGANO, Japan) were used to prepare the NaCl solutions.

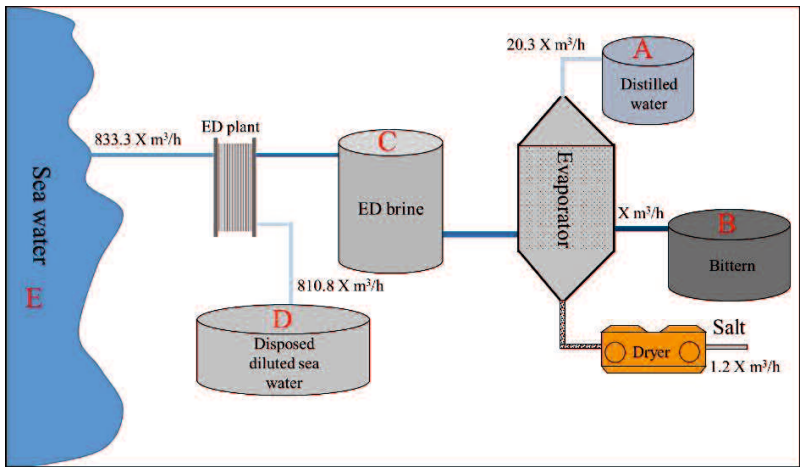

Figure 2. Simplified scheme of a typical salt production plant where ED and evaporators are used.

4.2.3 Membrane resistance measurement

For membrane resistance measurement, we initially used all solutions from A to E, to evaluate the effects of ion composition and concentration of the solutions on membrane resistance [7,25,26]. For standard comparison a solution of 0.5 M NaCl was used. According to our previous research, [27] membrane resistance was measured using a custom acrylic cell with two parallel Pt electrodes connected with a LCR meter (Model: AD-5827, A&D Company, TAIWAN) with an effective area of 1 cm^2. The sample solution was briefly purged inside the cell and the apparatus was then immersed in water bath at 24

± 0.1 °C to measure solution bulk resistances without membrane, R_{bulk}. After that, the same procedure was performed with a sample membrane to measure both the solution and membrane resistances, $R_{bulk+mem}$. An alternating current (AC) of 10 kHz frequency was applied to prevent an increase in the amount of membrane resistance from a concentration polarization effect. The membrane resistance, R_{mem}, was then calculated from the difference between R_{bulk} and $R_{bulk+mem}$ as follows [27]:

$$R_{mem} = R_{bulk+mem} - R_{bulk} \quad [1]$$

4.2.4 Membrane potential measurement

Membrane potential measurements were performed using samples A, B, D and E (excluding C) since the sample C was used as the evaporator feed. Solution A was preferably used as the low concentration solution for all combinations as it has the lowest salinity. The membrane potentials were measured using an acrylic plastic cell with two chambers separated by a sample membrane as shown in Fig. 3 according to the pervious literature [28]. The volume of each chamber and membrane effective area were 400 cm^3 and 2.54 cm^2, respectively. Chamber I and II of the cell were filled with low concentrate and high concentrate solutions, respectively. In total we measured 18 combinations of the membrane potential between the 3 solution combinations (A-B, A-D, and A-E) using 2 standard IEMs (AMX and CMX) and 2 one-sided monovalent IEMs with 2 membrane orientations (CIMS(L), CIMS(H), ACS-8T(H) and ACS-8T(L)). When using one-sided monovalent selective IEMs (CIMS and ACS-8T), its monovalent selective layer was tested facing both the HCC and LCC sides (abbreviated as (H) and (L), respectively) to

investigate the effect of membrane orientation on the membrane potential. Membrane potential between the solutions were measured by means of Ag/AgCl electrodes (TOAHS-205C) with salt bridges (3 N KCl) and a voltmeter (KT-2008, Kaise Corporation, Japan) at 25.0 ± 0.5 ºC.

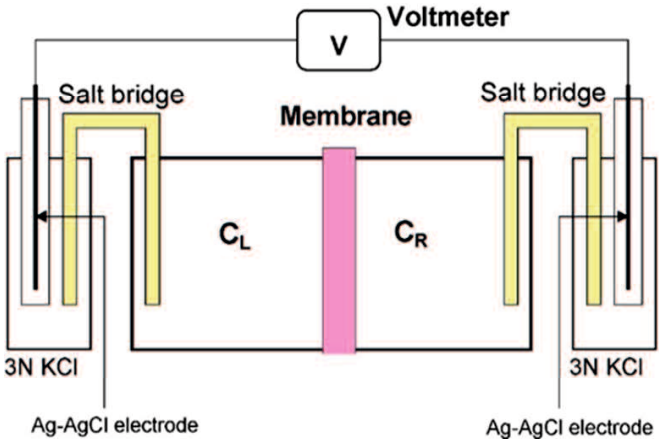

Figure 3. Membrane potential measurement apparatus.

4.2.5 RED stack

Three types of RED stacks consisting of 10 membrane pairs with an effective membrane area of 88 cm^2 (IEM: 11 cm × 8 cm) were used for the RED tests. Therefore, the total effective membrane area of the stack was 1760 cm^2. The first RED stack was equipped with CMX/AMX, and both the second and third stacks consisted of CIMS/ACS-8T with the monovalent selective layer facing towards the LCC and HCC, respectively. Woven spacers integrating gaskets of 200 μm were set between the IEMs to keep inter-membrane distance and prevent leakage in the all three stacks. Ag and AgCl were used as the cathode and anode electrodes, respectively, at each end of RED stack. As electrodes for RED, Ag and AgCl used less energy consumption because they do not produce any hydrogen and oxygen during the I-V tests, and are also safer in lab-scale experiments than

other electrodes such as Pt. An aqueous solution of 3 M NaCl was used as the electrode solution at both end of the RED stack. The flow rate of the solution was set at different values in each experiment in order to keep the pressure difference between the feed solutions compartments and the electrode solution at a minimum value. Therefore, the solution leakage from solution compartments into electrolyte and vice versa was negligible.

4.2.6 RED experiments

RED tests were performed using both real sample solutions from the salt production plant and an artificial solution for comparison. In the case of the artificial solution, we adjusted the ion conductivity of the NaCl solution to the same as the real sample solution. Both HCC and LCC were fed to the stack using a magnet pump (MD-30RZ-N, IWAKI CO., Ltd.) with a linear flow velocity of 1 cm/s because it has suggested that linear velocity higher than 1 cm/s was ideal to reduce the concentration polarization effect [29,30]. Three digital pressure gauges (KDM 30, KRONE Co., Ltd) were used to check the pressure drop at the HCC, LCC, and electrolyte compartments. Inlet and outlet solution conductivity as well as temperature (20–21 ºC) were also measured using a conductivity meter (MC-31P, DKK-TOA Corp., Japan).

The electrochemical performance of the RED stack such as open circuit voltage (OCV), maximum current, stack resistance, and maximum power density was evaluated using a potentiostat/galvanostat (HAB-151). The I-V curve tests were performed from zero to a maximum current (until the stack voltage became zero) with the current changing rate of 0.4 mA/s. Both the current and voltage values through I-V tests were recorded using a data logging system (midi LOGGER GL200, GRAPHTEC Co., Japan) connected to a personal computer. The OCV and maximum current were obtained from the vertical and

horizontal axis intercept of the I-V curve, respectively. The RED stack resistance was also obtained from the slop of I-V curves and Ohm 's law as follows [22]:

$$E_{stack} = OCV - R_{stack}I \quad [2]$$

where, E_{stack} and R_{stack} are voltage and resistance of the RED stack, respectively. The RED power output, P, and power density, P_d, are then defined by the two following equations [22]:

$$P = E_{stack}.I \quad [3]$$

$$P_d = {}^{P}/_{NA} \quad [4]$$

where, N and A are the number of cell pairs and the effective membrane area of each cell, respectively.

Theoretically, the power and power density reaches maximums (P_{max} and $P_{d,max}$, respectively) when the stack voltage was expressed as follows [22]:

$$P_{max} = \frac{OCV^2}{4.R} \quad (at\ V = \frac{OCV}{2}) \quad [5]$$

$$P_{d,max} = \frac{OCV^2}{4NAR} \quad [6]$$

4.3 Results and discussion

4.3.1 Sample solutions properties

The ion conductivity of the sample solutions (A-E) is shown in Fig. 4. The conductivity of the solution A (distilled water) is almost the same as that of tap water (about 0.2 mS/cm [31]). Among them, solution B (brine after evaporator) had the highest

conductivity of 332 mS/cm because it had the highest concentration of different salts containing K^+, Mg^{2+} and Ca^{2+} ions even after the NaCl precipitation process at the evaporator. Solution C (seawater brine after ED) reached approximately 6 times higher conductivity than solution E (seawater before ED). Solution D (diluted seawater after ED) had a conductivity of 38.1 mS/cm, which is about 78% of the conductivity of the seawater (E). Table 1 shows the ion composition and concentration of all the above-mentioned solutions. Solution C contains the highest percentage of the monovalent cations: Na^+ ion, 93.1%, and K^+ ion, 2.95% and the lowest percentage of bivalent cations: 2.62% Mg^{2+} and 1.31% Ca^{2+} compared to those of seawater (solution E: 86.44%, Na^+; 1.83%, K^+; 9.84%, Mg^{2+}; 1.88%, Ca^{2+}) due to selective enrichment of the monovalent cations by ED using monovalent selective CEMs. Similarly, solution C consists of a higher percentage of monovalent anions, Cl^-, and a lower percentage of the divalent anions, SO_4^{2-}, than those of seawater due to the use of monovalent selective AEMs. Conversely, the percentage of the monovalent ions, Na^+ and K^+ in solution D is lower than those in solution E, and that of the divalent ions are higher than those in solution E. A similar situation occurs for the anions of the same two solutions. As predicted, solution B includes the highest percentage of the divalent cations (55.0%, Mg^{2+}; 22.6%, Ca^{2+}) as most of the NaCl in solution C was precipitated during the evaporating process. The percentage of SO_4^{2-} and NO_3^- in all the solutions was low and did not vary significantly when compared to the divalent cations.

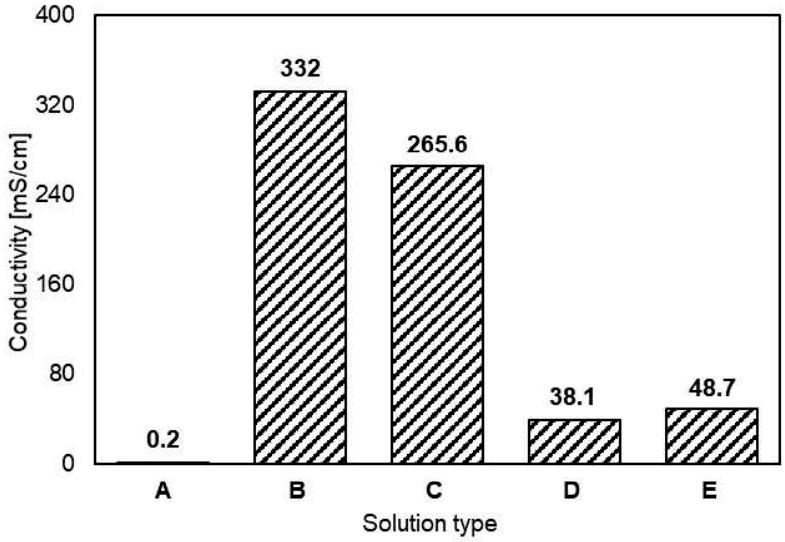

Figure 4. Ion conductivity of solutions A to E.

Table 1. Ion composition and concentration of solutions A to E.

Solution types	Cations				Anions		
	Na^+ (%)	K^+ (%)	Mg^{2+} (%)	Ca^{2+} (%)	Cl^- (%)	NO_3^- (%)	SO_4^{2-} (%)
A	82.90%	7.49%	9.10%	0.43%	98.46%	0.00%	1.53%
B	9.45%	12.93%	54.96%	22.63%	97.65%	2.34%	0.01%
C	93.11%	2.95%	2.62%	1.31%	99.91%	0.00%	0.09%
D	83.24%	1.64%	13.43%	1.69%	92.86%	0.00%	7.14%
E	86.44%	1.83%	9.84%	1.88%	95.10%	0.00%	4.89%

4.3.2 Membrane resistance

The measured resistance of IEMs in the different solutions is shown in Fig. 5. In the case of solution A, it was too difficult to obtain membrane resistance since solution A has such high resistance (much higher than the membrane resistance) due to its low conductivity that distinguishing an accurate value of the difference between R_{bulk} and $R_{bulk+mem}$ in Eq. (1) was not possible. In general, the membrane resistance increases with

increasing composition of divalent ions [18,32]. Therefore, as predicted, the resistance of the standard CEM, CMX, increased with increasing divalent cation concentration in the solutions [(divalent cations): 0.5 M NaCl (0.0%) < C (3.9%) < E (11.7%) < D (15.1%) << B (77.6%)]. In solution B, the resistances of CMX and CIMS reached approximately 34 $\Omega.cm^2$ and 48 $\Omega.cm^2$, respectively. Moreover, although the CIMS had the lowest resistance in the NaCl solution, the obtained resistance of CIMS in solutions B, D, and E, (excluding solution C, which has lowest divalent content), was higher than those of CMX due to the presence of a high concentration of divalent cations in the solutions. It is difficult for divalent cations to permeate through the selective layer on the CIMS because the groups with an opposite charge on the selective layer [18]; hence, the membrane resistance of CIMS using a solution containing high divalent content is higher than that of CMX. Since solution B has highest divalent cation composition of all the solutions, the resistance of both CMX and CIMS showed the highest values because the ionic mobility of the divalent ions with a high hydration radius is low in the CEMs.

In the case of the AEMs, it is almost the same situation as the CEMs: ACS-8T has lower membrane resistance than AMX in 0.5 M NaCl; however, the resistance of ACS-8T was higher than that of AMX in solutions B, D and E, excluding solution C. It also indicates that the resistance of the monovalent selective AEM was higher than that of the standard AEM in a solution with high divalent ion content. In addition, the effect of divalent anions on AEMs resistance was lower than that of divalent cations on CEMs resistance. The presence of SO_4^{2-} could leads to the formation of sodium and sulphate pairs ($NaSO_4^-$) which is a monovalent ionic species [16]. In the case of AEMs in solution B, although the amount of the divalent anions in the solution was negligible, AEMs showed

higher resistance compared with the membrane resistance in other solutions. In general, permselectivity of an IEM decreases with increasing salt concentration because co-ions, which have the same charge as the fixed charged groups in the IEM, are distributed in the IEM at high salt concentrations [33]. Therefore, because of the high concentration and the composition of divalent cations in solution B, more co-ion transport will occur and the transport has more effect on AEMs resistance.

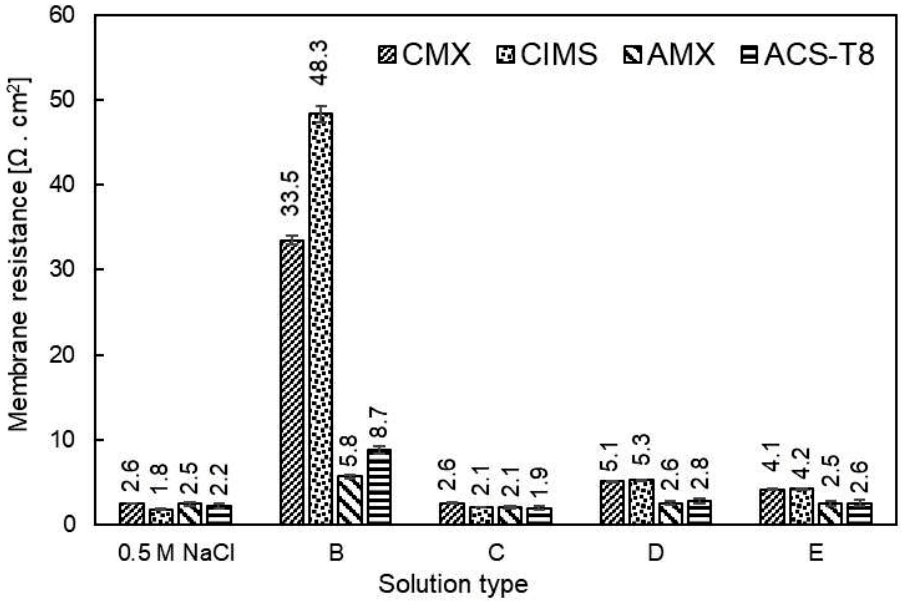

Figure 5. Different membranes resistances in 0.5 M NaCl for solutions B to E.

4.3.3 Membrane potential

The membranes potentials (E_m) of CEMs and AEMs using the different solution combinations are shown in Fig. 6A and Fig. 6B, respectively. Since solution C was utilized as a product stream for subsequent salt precipitation, the solution was not considered as a feed for the RED process. Here, the subscripts L and H refer to the side of the selective layer facing the low and high concentrate solutions, respectively.

The ion composition and conductivity of the low-concentration compartment is one of the most important factors, more so than the effect of ion concentration and composition of the high-concentration compartment for the resultant membrane potential due to the Donnan potential [15,32,34]. This would lead to increasing all the membrane potentials to between 110 mV to 130 mV which is two times higher than membrane potential between seawater and river water [32]. In addition, although solution B had almost 7.5 times higher conductivity than solutions D and E, the membrane potential of the A–B combination was slightly higher than the A-D and A-E combinations. In effect, around 70% of the total cations in solution B consisted of divalent cations which led to a decrease in the membrane potential by considering the membrane electrochemical potential equation as follows [7,35]:

$$E_m = \alpha \frac{R.T}{Z.F} \ln \frac{a_H}{a_L} \quad [7]$$

where, α is the permselectivity of the membrane (-). *R* and *T* are the gas constant (J/mol.K) and the temperature (K), respectively. *Z* is the valence of the counter-ion (-) of an IEM, *F* is the Faraday constant (96485 C/mol), and *a* is the activity of the solution. Subscripts *H* and *L* refer to the concentrated and dilute compartments, respectively. *M. Higa et al.* [34] compared the experimental data and the calculation of the Donnan potential in a single salt solution containing mono-, di-, and tri-valent cations. The potential depends both on concentration and the valence of the counter-ion in the solution. Therefore, if the solution contains only divalent ions, E_m becomes half of those of strictly monovalent ions because $Z = 2$. In a mixed solution containing mono- and di-valent cations, the Donnan potential depends on the ion composition. In a solution where the composition ratio of divalent cations to monovalent cations is less than unity, the potential is approximately equal to the

potential calculated by substituting Z = 2 into eq. (7), and in the case where the ratio is more than 100, the potential is approximately equal to the potential calculated by substituting Z = 1 into eq. (7) [34]. Therefore, the membrane potential in all the solutions, excluding C, in which the divalent ion composition is too low, will depend on the activity of the divalent ions. Moreover, high composition of divalent cations in solution B would also decrease the activity of the solution, resulting in a reduction of the membrane potential [22]. In addition, the presence of a high amount of divalent cations not only influence the CEMs potential, but also decrease the AEMs potential as well by decreasing the permselectivity of the membrane [17,32].

In all combinations, the obtained E_m of the monovalent selective IEMs [both (L) and (H)] were slightly higher than those of the standard IEMs because of the barrier property against divalent ions of the selective membrane even in the case where the selective layer is facing the lower concentrate (L). Therefore, membrane potential in eq. 7 can be expressed by a sum of the Donnan potentials and diffusion potentials as follows [35]:

$$E_m = \alpha \frac{R.T}{Z_{(H)}.F} \ln \frac{a_H}{a_{m(H)}} + E_{diff} - \alpha \frac{R.T}{Z_{(L)}.F} \ln \frac{a_{m(L)}}{a_L} \quad [8]$$

where, $a_{m(H)}$ and $a_{m(L)}$ are the activity within the membrane at the high and low concentration sides, respectively. Therefore, if $a_{m(H)} = a_{m(L)}$, $Z_{(H)} = Z_{(L)}$ and E_{diff} are negligible, Eq. 8 can be abbreviated as Eq. 7. When using monovalent selective IEMs, the values of $a_{m(H)}$ and $a_{m(L)}$ ($Z_{(H)}$ and $Z_{(L)}$, also) must be different due to the presence of the selective layer on one-side only. Generally, because of the order activity ratio between membrane bulk at both sides of the solution ($a_H < a_L < a_{m(H) \text{ or } (L)}$), the impact of the 3rd

term is higher than that of 1st term in Eq. 8. The Donnan potential of the low concentrate side is more affected by partitioning the ions within the monovalent selective layer. Therefore, the monovalent selective layer was more effective when it was facing the low concentrate side of the solution. Consequently, the membranes potential with (L) was surely higher than that with (H) when the solution includes the divalent ions.

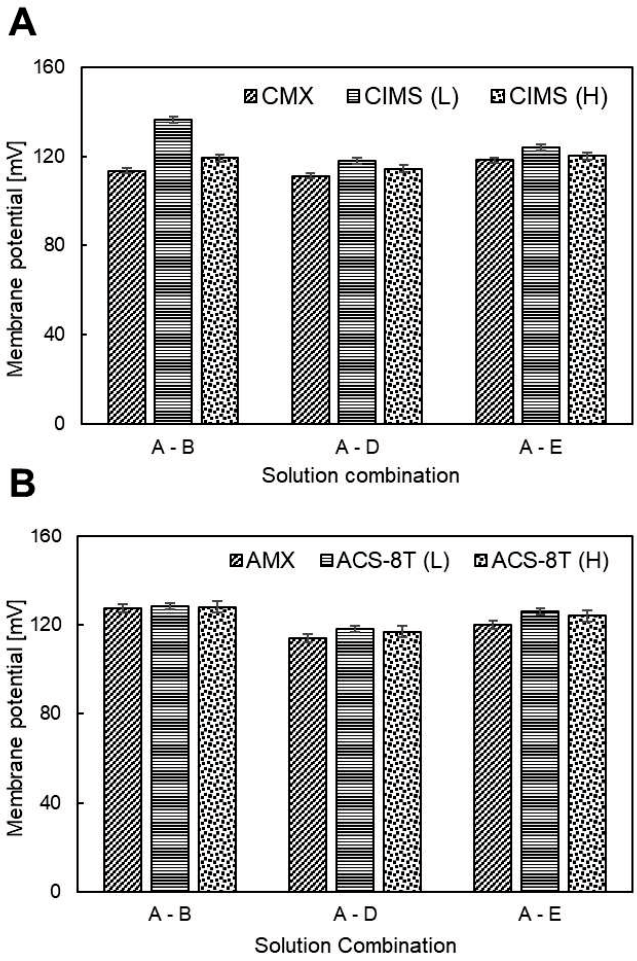

Figure 6. Different membranes potential, A) for all CEMs and B) for all AEMs, through the combination of solution A with B, D, and E. (Letters L and H refers to monovalent selective side facing the low and high concentrate compartment, respectively.)

4.3.4 RED stack performance

4.3.4.1 Open circuit voltage (OCV)

Since the amount of solution B in the salt production plant is quite low and concentration of divalent ions is relatively high, resulting in the high membrane resistance, solution B was not considered as the RED feed solution. Therefore, the highest membrane resistance was found in the A-B combination and the RED performance with the A-B combinations was much lower than those with combinations A-D and A-E as shown in the supplementary information.

The RED stack OCV using the A-D and A-E feed solution combinations is shown in Fig. 7. Considering the stack had 10 membranes cell pairs (20 membranes), the RED stack OCV using both the solutions was slightly lower than the potential that is 10 times the sum of each CEM and AEM in a single cell. The reasons in the difference were that the voltage drops at the interface between the electrode and the electrode solution and/or the potential drop caused by the ionic shortcut current [36] was not negligible in the stack.

A RED stack with CIMS / ACS-8T membranes was assembled with the selective layer facing the HCC and LCC as shown by the H and L letters, respectively. In addition, artificial NaCl solutions with the conductivity set to the same as solutions A, D, and E were also used to investigate the effect of divalent ions more clearly. Although the conductivity of solution E was almost 26% higher than that of solution D, the OCV with A-E (2.119 V) was just slightly higher (4%) than that of A-D (2.043 V). Since the conductivity of solution A was very low (0.2 mS/cm), the difference between the conductivity of solution E and D did not have a significant effect on the salinity ratio and the resulting stack OCV. In both

solution combinations, the stack OCV with artificial solutions was slightly higher than those with real solutions due to the presence of divalent ions in the real solution. According to the membrane potential measurements, the stack OCV with CIMS/ACS-8T was higher than that with CMX/AMX due to the presence of divalent ions in both solutions D and E. It is worth noting that the stack OCVs with A-D and A-E were almost 50% higher than double the reported stack OCV with 5 cell pairs using real seawater and river water previously reported [32]. This is due to the fact that LCC has a low conductivity and leads to a higher salinity ratio between HCC and LCC.

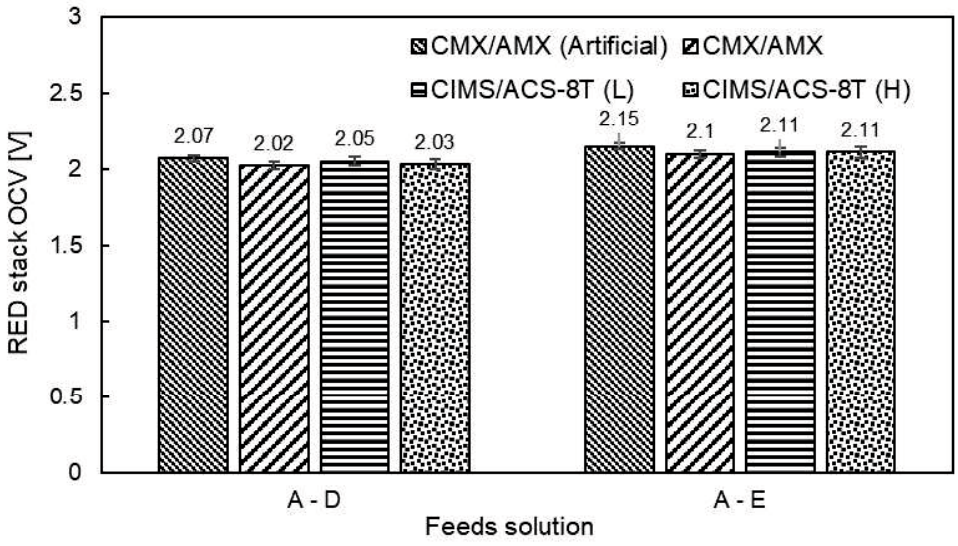

Figure 7. The open circuit voltage (OCV) of the RED stack.

4.3.4.2 Stack resistance

Fig. 8 shows the resistance of the RED stack, obtained from a slope of the I-V curve test, with A-D and A-E feed solution combinations using the differently assembled membranes. These resistance values also include membrane and solution compartment

resistances as well as electrodes and electrolyte solutions. The resistance of electrode and electrolytes were measured separately to investigate their magnitude on the RED stack resistance which was between 17–26% stack resistance. More information is reported in the supplementary information.

In Fig. 8, the average resistance through each cell of all the RED stacks was more than 2 times higher than those with the same conditions using seawater and river water as feed solutions reported in literature [8]. This is because of the dominant effect of LCC conductivity on RED stack resistance (LCC conductivity is too low). As expected, the lowest resistance was the RED stack with CMX/AMX using the artificial feed solutions (79 $\Omega.cm^2$ and 74 $\Omega.cm^2$ for A-D and A-E feed solutions combinations, respectively). Artificial feed solutions consisting of only NaCl with higher mobility in both the solutions and in the membranes gave the lowest resistance when compared to the feed solutions containing divalent ions.

The average of the stack resistances with CIMS/ACS-8T was ca. 20% higher than that with CMX/AMX. In addition, the RED stack in which the one-sided monovalent selective membrane with selective layer faced towards the LCC showed 16% and 13% higher resistance than that with the selective layer facing the HCC using the A-D and A-E feed solutions, respectively. During RED operation, both monovalent and divalent ions diffuse from HCC into LCC through the membrane in line with their concentration gradient. In the case of the membrane with the selective layer facing the LCC, first, both monovalent and divalent ions diffuse from HCC into the membrane bulk, followed by the monovalent ions passing from the membrane bulk into the LCC, however it is difficult for the divalent ions to pass through the selective layer. This will increase the divalent ion concentration

inside the membrane. The high concentration of the divalent ions with low mobility gives high membrane resistance on the RED stack. Although, in the case of the selective layer facing the HCC, the divalent ion accumulation due the barrier effect of the selective layer will not occur. Therefore, the stack resistance in a case of the selective layer facing the HCC has a lower stack resistance than when facing the LCC.

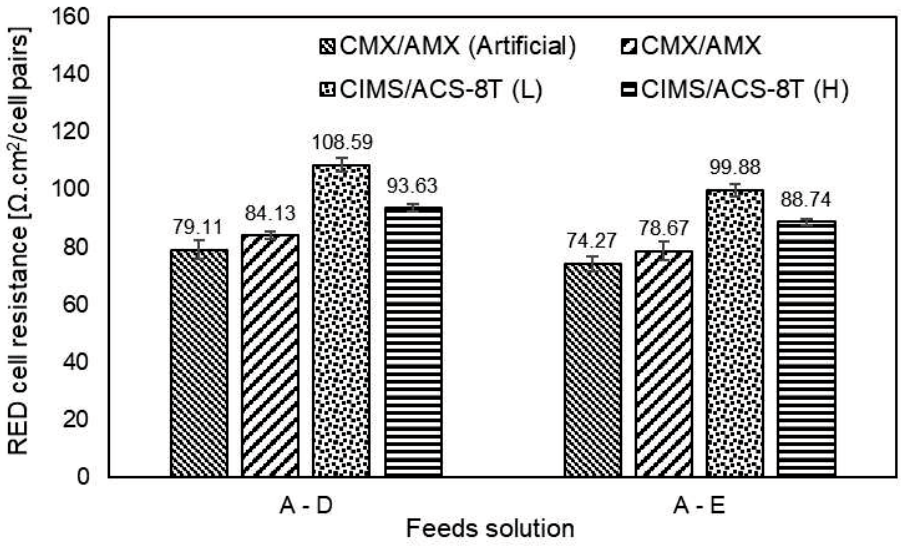

Figure 8. RED stack resistance with A-D and A-E feed solution combinations.

4.3.4.3 Power density

The power density-current curves for both the A-D and A-E feed solution combinations are shown in Fig. 9A and Fig. 9B, respectively. In addition, the I-V curve of all the RED tests are shown in the supplementary information. The maximum power density of the RED stack related to both stack OCV and stack resistance is calculated by Eq. 6. Therefore, the interaction effect of OCV and stack resistance are the main parameters that effect the power density. The highest power density was obtained when using the NaCl artificial solution with a value of 0.487 W/m^2 and 0.577 W/m^2 for A-D and A-E

combinations, respectively. The maximum power density of the RED stack, from high to low, was CMX/AMX, CIMS-ACS-8T(H) and CIMS-ASC-8T(L) in both the feed solution combinations. In all the membrane pairs for the RED stacks, the power density using the A-E solution combination was higher than when using the A-D solution combination. The RED stack OCV in all the membrane pairs in the former was higher than in the latter, where the RED stack resistance in all the membrane pairs in the former was lower than that in the latter. Therefore, this indicates that the both effect of the stack resistance and OCV using A-E leads to higher power output than when using the A-D feed solution combination. The power density of the stack with CIMS/ACS-8T(H) was almost the same as that with CMX/AMX in the A-D solution combination. However, the former was higher than the latter in the A-E solution combination. Finally, the lowest amount of power density was obtained when using CIMS/ACS-8T with the selective layer facing the LCC with a value of 0.368 W/cm^2 and 0.386 W/cm^2 for A-D and A-E feed solutions, respectively. This was due to the highest amount of RED stack resistance despite having the highest OCV.

As reported in literature, when applying real feed solutions (consisting of both monovalent and divalent ions) in both HCC and LCC, the RED power output was diminished to around 40–50% compared to the artificial solution [22] However, the difference between maximum power with the artificial and the real feed solutions by means of CMX/AMX was around 4–6% in this study. This is due to the dominant effect of ion composition and concentration of solution A on the RED power output. In both cases, when using the artificial or the real solution, the amount of divalent ions in solution A is negligible. This was an important reason to diminish the impact of divalent ions such as the uphill transport on the RED performance. Therefore, it is that the composition and

concentration of the low concentrate solution is one of the key factors to increase the RED performance.

In conclusions, the power output of a RED stack depends on both the stack resistance and the stack OCV. The monovalent selective layer of CIMS and ACS-8T gave a higher OCV than the standard IEMs. However, the layer also gives higher stack resistance. Due to this tradeoff, the RED stack with monovalent selective IEMs depends more strongly on the divalent ion composition in solution and the orientation of the IEMs in the stack than with standard IEMs.

In this study, we used monovalent selective CEMs developed for the ED process. The monovalent selective CEMs had a dense monovalent selective layer on one side of the membrane surface. However, based on these results, a monovalent selective CEM with a monovalent selective layer having both a high number of ion-exchange groups for high divalent cation barrier property, and low cross-linking density for low membrane resistance for divalent ions will give high power output to a RED stack.

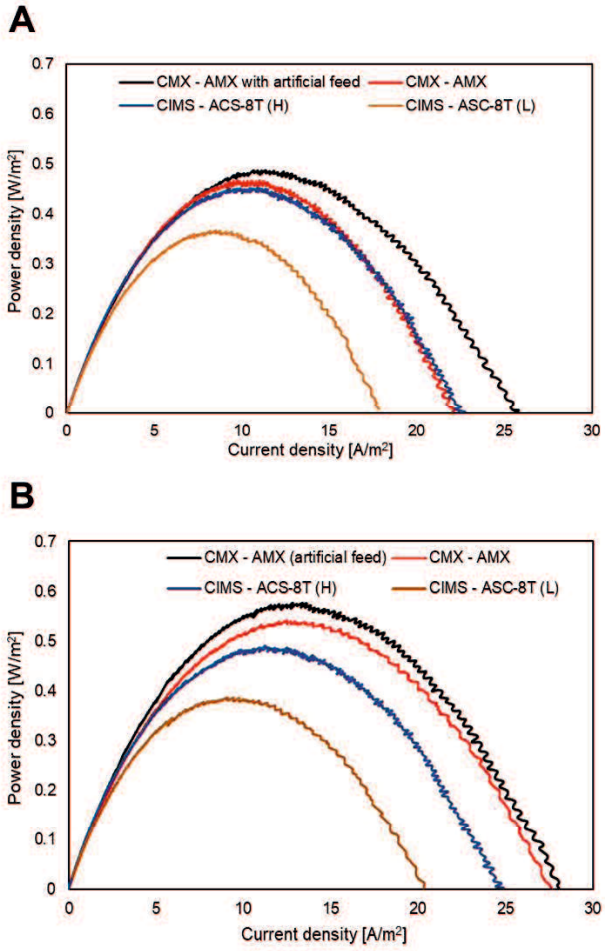

Figure 9. The relationship between power density and current density for A) feed solution combination of A-D and B) feed solution combination of A-E. (For interpretation of the references to color in this figure, refer to the web version of this article.)

4.4 Conclusion

RED is a promising process that can produce energy by mixing two solutions with different salinity. In previous studies, seawater and river water were primarily considered as feeds solutions for a RED process. However, salt production plants are an appropriate location due to the presence of the discharged solution with different salinities. In this study,

solutions from a typical salt production plant were evaluated for RED-based energy harvesting. Since this salt plant consists of ED and evaporation systems, five different solutions were available and investigated to find the best solution combination for the RED process. In addition, the performance of standard membranes (CMX/AMX) was compared with one-sided monovalent selective membranes (CIMS/ACS-8T). Since the ion transportation in the RED process is from HCC into LCC, applying one-sided monovalent selective membranes was more helpful than membranes with monovalent selective layer at both sides, ultimately resulting in higher resistance. The obtained membrane potential was almost 2 times greater than the membrane potential between seawater and river water. In addition, CIMS/ACS-8T with a selective side in the low concentrate side showed slightly higher membrane potential. The presence of divalent ions showed a significant effect on membrane potential. The feed solution combinations of A-E and A-D showed better RED performance among all the feed combinations. The OCV of the RED process with these feed solutions were almost 2 times higher than the OCV of the RED process using seawater and river water. However, the obtained power density was 40% lower than the RED process with seawater and river water due to the high resistance of the LCC. The RED performance of the one-sided monovalent selective membrane with the selective layer facing towards the HCC was almost the same as with CMX/AMX, while those facing the LCC showed almost 30% lower performance. Monovalent selective CEMs developed for the ED process were used in this study. The monovalent selective layer of the CEMs with high dense structure gives high membrane resistance in a case of using salt solutions with divalent ions. Therefore, monovalent selective CEMs with looser monovalent selective layer will be suitable for RED systems to get high power output.

4.5 Acknowledgements

This work was supported by JSPS KAKENHI Grant Number JP16H01796, Salt Science Research Foundation (SSRF) No 1813, and was partially supported by Subsidy for Research of Energy Infrastructure with Advanced Technology (Okinawa, Japan).

4.6 References

[1] R.E. Pattle, Production of electric power by mixing fresh and salt water in the hydroelectric pile, Nature. 174.4431 (1954) 660.

[2] B. Zhang, H. Gao, Y. Chen, Enhanced ionic conductivity and power generation using ion-exchange resin beads in a reverse-electrodialysis stack, Environ. Sci. Technol. 49 (2015) 14717–14724. doi:10.1021/acs.est.5b03864.

[3] M. Vaselbehagh, H. Karkhanechi, R. Takagi, H. Matsuyama, Biofouling phenomena on anion exchange membranes under the reverse electrodialysis process, J. Memb. Sci. 530 (2017) 232–239. doi:10.1016/j.memsci.2017.02.036.

[4] J.G. Hong, B. Zhang, S. Glabman, N. Uzal, X. Dou, H. Zhang, X. Wei, Y. Chen, Potential ion exchange membranes and system performance in reverse electrodialysis for power generation: a review, J. Memb. Sci. 486 (2015) 71–88. doi:10.1016/j.memsci.2015.02.039.

[5] R. Long, Z. Kuang, Z. Liu, W. Liu, Temperature regulated reverse electrodialysis in charged nanopores, J. Memb. Sci. 561 (2018) 1–9. doi:10.1016/j.memsci.2018.05.026.

[6] B. Kang, H.J. Kim, D.K. Kim, Membrane electrode assembly for energy harvesting from salinity gradient by reverse electrodialysis, J. Memb. Sci. 550 (2018) 286–295. doi:10.1016/j.memsci.2018.01.006.

[7] X. Zhu, W. He, B.E. Logan, Influence of solution concentration and salt types on the performance of reverse electrodialysis cells, J. Memb. Sci. 494 (2015) 154–160. doi:10.1016/j.memsci.2015.07.053.

[8] A. Daniilidis, D.A. Vermaas, R. Herber, K. Nijmeijer, Experimentally obtainable energy from mixing river water, seawater or brines with reverse electrodialysis, Renew. Energy 64 (2014) 123–131. doi:10.1016/j.renene.2013.11.001.

[9] J.W. Post, J. Veerman, H.V.M. Hamelers, G.J.W. Euverink, S.J. Metz, K. Nymeijer, C.J.N. Buisman, Salinity-gradient power : evaluation of pressure-retarded osmosis and reverse electrodialysis, 288 (2007) 218–230. doi:10.1016/j.memsci.2006.11.018.

[10] R. Long, B. Li, Z. Liu, W. Liu, Performance analysis of reverse electrodialysis stacks: channel geometry and flow rate optimization, Energy. 158 (2018) 427–436. doi:10.1016/j.energy.2018.06.067.

[11] D.A. Vermaas, M. Saakes, K. Nijmeijer, Doubled power density from salinity gradients at reduced intermembrane distance, Environ. Sci. Technol. 45 (2011) 7089–7095. doi:10.1021/es2012758.

[12] M. Turek, B. Bandura, Renewable energy by reverse electrodialysis, Desalination. 205 (2007) 67–74. doi:10.1016/j.desal.2006.04.041.

[13] M. Turek, B. Bandura, P. Dydo, Power production from coal-mine brine utilizing reversed electrodialysis, Desalination. 221 (2008) 462–466. doi:10.1016/j.desal.2007.01.106.

[14] J. Veerman, M. Saakes, S.J. Metz, G.J. Harmsen, Reverse electrodialysis: performance of a stack with 50 cells on the mixing of sea and river water, J. Memb. Sci. 327 (2009) 136–144. doi:10.1016/j.memsci.2008.11.015.

[15] J.W. Post, H.V.M. Hamelers, C.J.N. Buisman, Influence of multivalent ions on power production from mixing salt and fresh water with a reverse electrodialysis system, J. Memb. Sci. 330 (2009) 65–72. doi:10.1016/j.memsci.2008.12.042.

[16] D.A. Vermaas, J. Veerman, M. Saakes, K. Nijmeijer, Influence of multivalent ions on renewable energy generation in reverse electrodialysis, Energy Environ. Sci. 7 (2014) 1434–1445. doi:10.1039/C3EE43501F.

[17] A.H. Avci, P. Sarkar, R.A. Tufa, D. Messana, P. Argurio, E. Fontananova, G. Di Profio, E. Curcio, Effect of Mg^{2+}ions on energy generation by reverse electrodialysis, J. Memb. Sci. 520 (2016) 499–506. doi:10.1016/j.memsci.2016.08.007.

[18] T. Rijnaarts, E. Huerta, W. Van Baak, K. Nijmeijer, Effect of divalent cations on RED performance and cation exchange membrane selection to enhance power densities, Environ. Sci. Technol. 51 (2017) 13028–13035. doi:10.1021/acs.est.7b03858.

[19] M. Higa, T. Yamakawa, Design and preparation of a novel temperature-responsive ionic gel. 2. concentration modulation of specific ions in response to temperature changes, (2005) 11373–11378. doi:10.1021/jp0502499.

[20] M. Higa, A. Tanioka, K. Miyasaka, Simulation of the transport of ions against their concentration gradient across charged membranes, J. Memb. Sci. 37 (1988) 251–266.

[21] R.S. Kingsbury, F. Liu, S. Zhu, C. Boggs, M.D. Armstrong, D.F. Call, O. Coronell, Impact of natural organic matter and inorganic solutes on energy recovery from five real salinity gradients using reverse electrodialysis, J. Memb. Sci. 541 (2017) 621–632. doi:10.1016/j.memsci.2017.07.038.

[22] M. Tedesco, C. Scalici, D. Vaccari, A. Cipollina, A. Tamburini, G. Micale, Performance of the first reverse electrodialysis pilot plant for power production from saline waters and concentrated brines, J. Memb. Sci. 500 (2016) 33–45. doi:10.1016/j.memsci.2015.10.057.

[23] M. Tedesco, A. Cipollina, A. Tamburini, G. Micale, Towards 1 kW power production in a reverse electrodialysis pilot plant with saline waters and concentrated brines, J. Memb. Sci. 522 (2017) 226–236. doi:10.1016/j.memsci.2016.09.015.

[24] M. Turek, Dual-purpose desalination-salt production electrodialysis, Desalination. 153 (2003) 377–381. doi:10.1016/S0011-9164(02)01131-1.

[25] G.M. Geise, A.J. Curtis, M.C. Hatzell, M.A. Hickner, B.E. Logan, Salt concentration differences alter membrane resistance in reverse electrodialysis stacks, Environ. Sci. Technol. Lett. 1 (2013) 36–39. doi:10.1021/ez4000719.

[26] P. Długołecki, P. Ogonowski, S.J. Metz, M. Saakes, K. Nijmeijer, M. Wessling, On the resistances of membrane, diffusion boundary layer and double layer in ion exchange membrane transport, J. Memb. Sci. 349 (2010) 369–379. doi:10.1016/j.memsci.2009.11.069.

[27] S. Mehdizadeh, M. Yasukawa, T. Abo, Y. Kakihana, M. Higa, Effect of spacer geometry on membrane and solution compartment resistances in reverse electrodialysis, J. Membr. Sci. (2019) 271-280. doi:10.1016/j.memsci.2018.09.051.

[28] M. Higa, D. Masuda, E. Kobayashi, M. Nishimura, Y. Sugio, T. Kusudou, N. Fujiwara, Charge mosaic membranes prepared from laminated structures of PVA-based charged layers. 1. preparation and transport properties of charged mosaic membranes, J. Memb. Sci. 310 (2008) 466–473. doi:10.1016/j.memsci.2007.11.024.

[29] P. Długołecki, J. Dabrowska, K. Nijmeijer, M. Wessling, Ion conductive spacers for increased power generation in reverse electrodialysis, J. Memb. Sci. 347 (2010) 101–107. doi:10.1016/j.memsci.2009.10.011.

[30] P. Długołe, A. Gambier, M. Wessling, Practical potential of reverse electrodialysis ss process for sustainable energy generation, Environ. Sci. Technol. 43 (2009) 6888–6894.

[31] J.S. Park, J.H. Song, K.H. Yeon, S.H. Moon, Removal of hardness ions from tap water using electromembrane processes, Desalination. 202 (2007) 1–8. doi:10.1016/j.desal.2005.12.031.

[32] J. Moreno, V. Díez, M. Saakes, K. Nijmeijer, Mitigation of the effects of multivalent ion transport in reverse electrodialysis, J. Memb. Sci. 550 (2018) 155–162. doi:10.1016/j.memsci.2017.12.069.

[33] M. Higa, A. Tanioka, K. Miyasaka, An experimental study of ion permeation in multicomponent ion systems as a function of membrane charge density, J. Memb. Sci. 64 (1991) 255–262.

[34] M. Higa, A. Tanioka, A. Kira, A novel measurement method of Donnan potential at an interface between a charged membrane and mixed salt solution, J. Memb. Sci. 140 (1998) 213–220.

[35] R.E. Lacey, Energy by reverse electrodialysis, Ocean Eng. 7 (1980) 1–47. doi:10.1016/0029-8018(80)90030-X.

[36] J.W. Post, H.V.M. Hamelers, C.J.N. Buisman, Energy recovery from controlled mixing salt and fresh water with a reverse electrodialysis system, Environ. Sci. Technol. 42 (2008) 5785–5790. doi:10.1021/es8004317.

4.7 Supplementary information

4.7.1 Appendix A. Theoretical calculation of RED performance

Theoretical calculation of RED performance using A–B, A–D, and A–E feeds solution combinations was performed using the basic measured information such as membrane potential, membrane resistance, and conductivity of the solutions. Since each RED stack contains 10 cell pairs, the stack OCV was calculated by considering 10 times each individual membrane's potential through each feed solution combination. Each solution compartment resistance was calculated using the ratio of compartment thickness into solution conductivity ($^{h}/_{k}$). Since it wasn't possible to measure the membrane resistance in solution type A due to its low conductivity, all the membrane resistances were calculated using highly concentrated solutions (B, D, and E). The stack resistance as well as the maximum power density were calculated using the following equations:

$$R_{stack} = N_{cells}(^{h}/_{k_H} + ^{h}/_{k_L} + R_{AEM} + R_{CEM}) \quad [A1]$$

$$P_{d,max} = \frac{OCV^2}{4AR_{stack}} \quad [A2]$$

where, h is each compartment thickness, k_H is the conductivity of the highly concentrated solution, and k_L is the conductivity of low concentrated solution. The main purpose was to calculate the theoretical maximum power output of the RED stack with the same condition of this study. Fig. A1 and Fig. A2 show the theoretical RED cell resistance and maximum power output, respectively. Although the conductivity of solution type B is too high, the calculated RED performance using A–B solution combination is lower than those with the two other solution combinations. This is due to the presence of a high

concentration of divalent ions in solution type B which increased the resistance of applied IEMs. Therefore, just A–D and A–E solution combinations were applied for experimental RED test measurements.

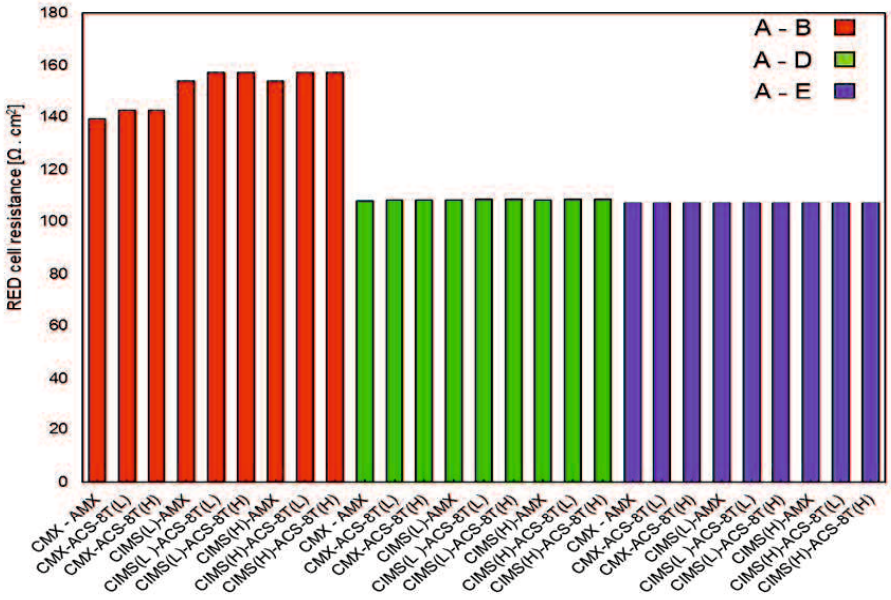

Figure A1. Theoretical RED cell resistance for A–B, A–D, and A–E feed solution combinations.

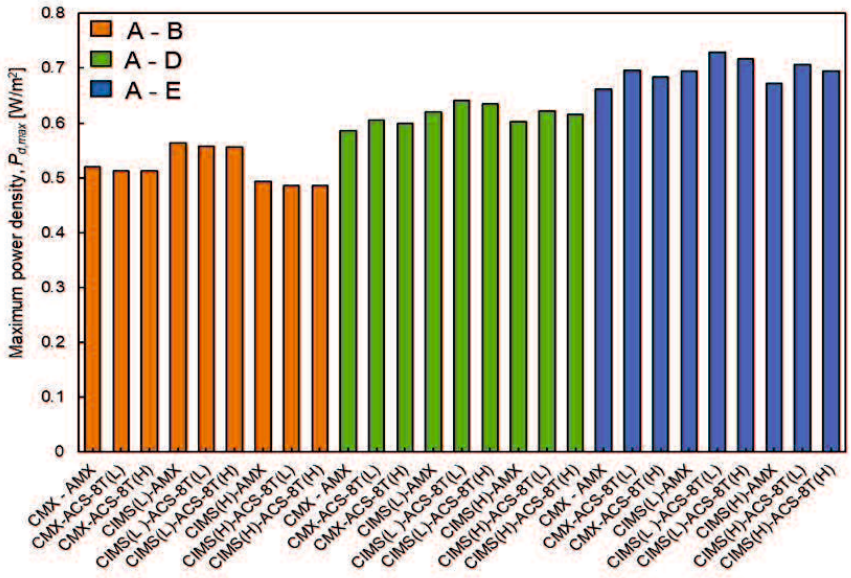

Figure A2. Theoretical Maximum power output of RED using A–B, A–D, and A–E feed solution combinations.

4.8 Appendix B. I-V curve of RED tests

All of the I-V curves of A-D and A-E solution combinations with different membranes and orientations are shown in Fig. B1 and Fig. B2, respectively. As mentioned previously, the RED stack resistance can be obtained be the slope of I-V curve. In addition, the OCV of the RED stack can be identified when the current is zero.

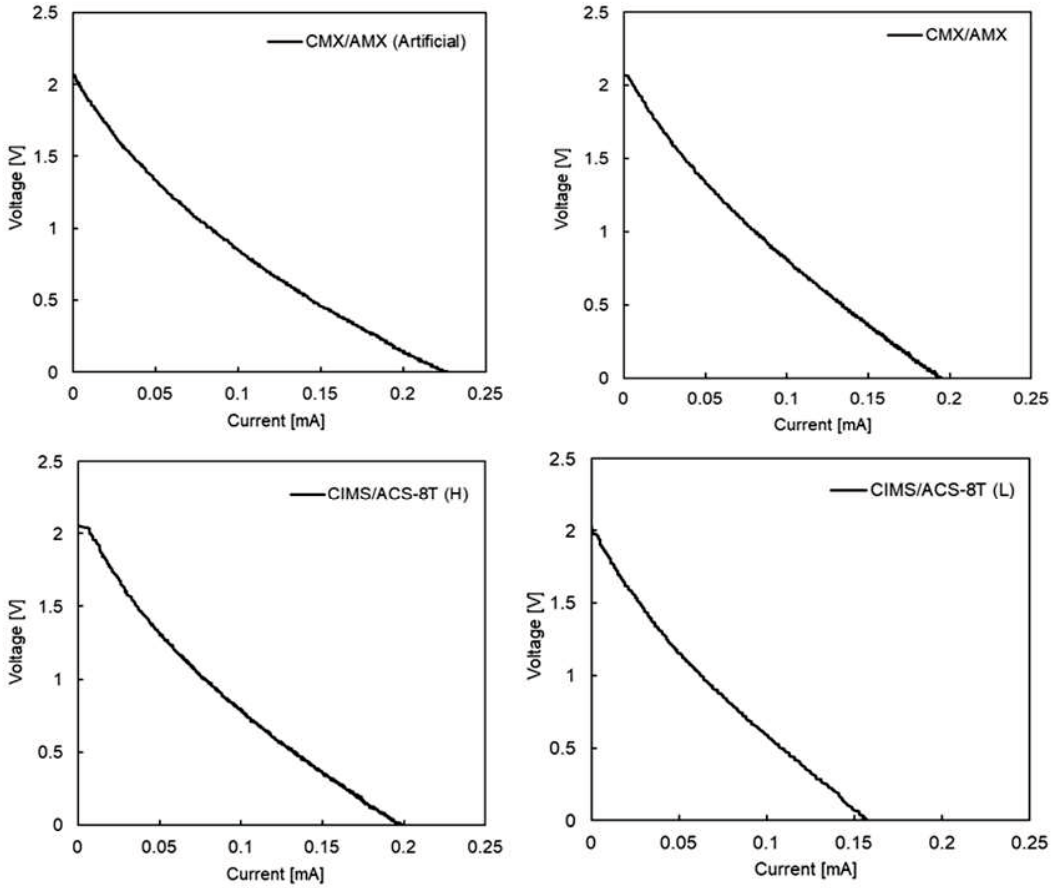

Figure B1. The I-V curve of the A-D feed solution combination with different membranes and orientations.

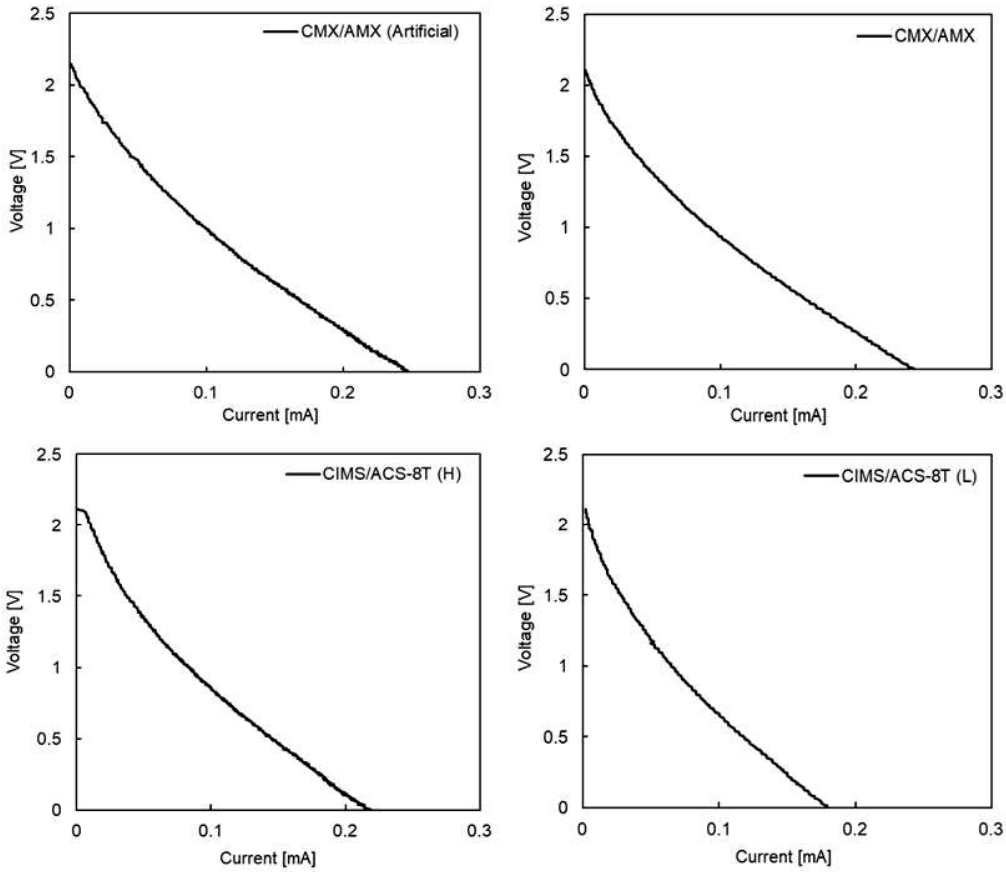

Figure B2. The I-V curve of the A-E feed solution combination with different membranes and orientations.

4.9 Appendix C. Electrode and electrolyte resistance of the RED stack

The resistance of electrode and electrolyte of RED stack was measured by applying different voltages and measuring current through the electrode and electrolyte solutions without membranes and feed solution compartments. The resistance was obtained by measuring the slope of I-V curve. Fig. C1 shows the I-V curve of the electrode and electrolyte solution applied in the RED experiments.

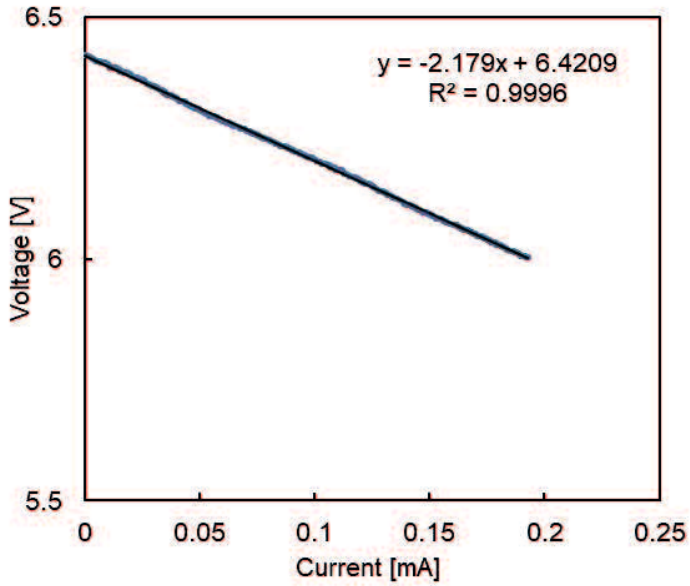

Figure C1. The I-V curve through the electrode and electrolyte solution applied in the RED experiments.

Chapter 5

Reverse electrodialysis for power generation using seawater/municipal wastewater: Effect of coagulation pre-treatment

5.1 Introduction

Reverse electrodialysis (RED) is a major emerging processes for the production of electrical power from the salinity gradient energy (SGE) generated on the mixing of two solutions with different salinities [1–4]. In RED, the high and low salinity solutions flow alternatively between stacked anion and cation exchange membranes (AEMs and CEMs) with inter-membrane porous gaskets integrating spacers. The anions and cations then migrate from the high salinity compartment (HSC) into the low salinity compartment (LSC) through the AEMs and CEMs, respectively, because of the concentration gradient between the two solutions. Consequently, the cation and anion transport in opposing directions results in an external electric current by redox reactions at suitable electrodes connected to an external load.

Seawater and river water are abundant resources and are considered the most common and promising aqueous solutions for RED because of their huge energy potential [5]. The current SGE potential calculated from the amount of river water discharged into the sea has been estimated as 2000 TWh per year, which is around 10% of the world's energy demand [6,7]. However, the implementation of RED using sea and river water requires improved RED power generation performance, and many studies, mostly using NaCl solutions as model solutions, have been carried out. In contrast, more recent studies have addressed more practical issues using real solutions to investigate the effects of divalent ions in seawater [8,9], membrane fouling [10,11], and the effect of natural organic materials (NOM) [12]. When using real water samples, the performance reduction caused by divalent ions and NOMs must be controlled to achieve stable power generation, for

example, by preventing fouling, but these are still challenging issues. For instance, *Vermaas* et al. reported a three-fold increase in the pressure drop, as well as 60% reduction in power output, of the RED process after 25-days operation using real seawater and river water as the feed solutions [11]. They showed that clay minerals and organic fouling affect the AEMs, whereas scaling by calcium phosphate was more dominant on CEMs. Having a comprehensive understanding about the fouling phenomena, as well as finding a way to overcome this issue, could be more challenging and important when other types of solutions except seawater and river water are used for the RED process.

In addition to the combination of seawater and river water, other real sample solutions have been proposed as RED feeds, such as reverse osmosis (RO) brine/river water [2,13] and the salty solutions discharged from salt production plants [14]. In any cases, the most concerning issue in the RED feed solution is the low concentration solution, which is often river water. River water is also used for human demands such as drinking water and agricultural irrigation, and, in the case of mixing seawater and river water, the environmental impact on the ecosystem at the mixing point (the brackish water region) must be considered. Thus, the use of municipal wastewater instead of river water would be more appropriate if the wastewater treatment (WWT) plant is located near the sea. In Japan, fortuitously, 17% of the municipal wastewater plants are located close to the sea [15].

When using municipal wastewater, adequate pre-treatment before RED is essential to remove the particles and natural organic materials (NOM) that would cause membrane fouling and performance reduction of the subsequent RED process. For example, Kingsbury et al. reported a 13–77% reduction in RED power output over a short operating time, and the reduction in the power output was dependent on the NOM concentration in

the feed solutions [12]. Therefore, finding an efficient pre-treatment method, either chemical or physical, to remove or decrease the particle and NOM concentrations is urgently required. Chemical coagulation combined with filtration are two primary waste and WWT processes. These methods are used to settle particles and remove the NOMs [16–19]. Charge neutralization is the most common and effective way to precipitate NOMs, but this is challenging because NOMs are highly negatively charged and have a wide range of molecular weights [20]. Polyaluminum chloride (PAC) is the most common coagulant and can successfully treat water and wastewater with different chemical and biological properties [21]. PAC can be prepared by the partial hydrolysis of acidic aluminum chloride solutions in a reactor, thus yielding cationic aluminum species that interact electrostatically with anionic NOMs, thus forming insoluble charge-neutral products [20,22]. Therefore, the coagulation of NOMs in wastewater using PAC before the RED process seems to be an effective way to improve the RED performance and decrease fouling by NOMs. However, the effect of residual Al and its composite salts in the treated wastewater on the RED performance remains unclear and has not been investigated significantly. This is surprising because aluminum is associated with various problems such as increased turbidity, reduced hydraulic capacity, solid–liquid separation, and Alzheimer's disease [16]. Therefore, the identification of the optimum dosage on PAC for coagulation is crucial from a number of different viewpoints.

In this study, we investigated the effect of different PAC dosages on the membrane properties, such as membrane resistance and potential. Then, the coagulation process was carried out using real wastewater samples obtained from municipal WWT plant with the aim of achieving the maximum NOM removal. Finally, the effect of the

coagulation of wastewater (NOM removal) was investigated by measuring the RED performance using treated and non-treated feed solutions to identify the optimum method for enhancing the power output while minimizing fouling.

5.2 Experimental

5.2.1 Sample solutions and materials

Real seawater and municipal wastewater samples were obtained from Tokuyama Bay and the Tokuyama Eastern wastewater plant, respectively, in the city of Shunan, Yamaguchi Prefecture, Japan. The municipal wastewater had been treated by the standard activated sludge method and sampled after strainer filtration before the addition of chloride. The seawater was directly sampled from Tokuyama Bay near the wastewater plant. The conductivities of these solutions were measured using a conductivity meter (ES-51, Horiba Ltd., Japan). In addition, model seawater and municipal wastewater were prepared based on the conductivity of the natural solutions using tap water with 99.5% NaCl from Nacalai Tesque, Inc., Japan. A solution of 10.0–11.0% PAC provided from Takasugi Pharmaceutical Co., Ltd., Japan was used as a coagulant. All reagents were of commercial grade and used as received unless otherwise mentioned.

5.2.2 Membrane resistance measurements

Membrane resistance measurements were performed using both model (NaCl) and real sample solutions having different PAC concentrations. As mentioned, PAC is often used as a coagulant in various types of wastewater treatments. In WWT plants, PAC is also sometimes added to improve the wastewater quality and ensure the quality of the

discharged wastewater. However, if the treated wastewater is used for RED, the dosage of PAC for must be controlled precisely because the addition of excess PAC would have a negative impact on the RED process. Therefore, model solutions containing NaCl with different dosages of PAC were used to assess the membrane performance. An acrylic cell with an effective area of 1 cm^2 capped with two Pt electrodes connected to an LCR meter (Model: AD-5827, A&D Company, Taiwan) was used to measure the membrane resistance using a method reported by us previously [23]. Two types of commercially available ion-exchange combination membranes, Neosepta® CMX/AMX (Astom Corporation, Japan) and Fumatech FKS/FAS (Fumatech BWT GmbH, Germany), were used. The specific properties of CMX/AMX and FKS/FAS [24] are listed in Table 1. Each membrane was first immersed in a solution of 0.5 M NaCl plus different doses of PAC (0 to 400 ppm) for 24 h. First, the sample solution was purged into the cell, and the apparatus was then immersed inside the water bath at 24 ± 0.1 °C to measure the solution bulk resistance, R_{bulk}. Then, the same procedure was performed using the membrane located inside the cell to measure the sum of the solution and membrane resistances, $R_{bulk+mem}$. The membrane resistance, R_{mem}, was then calculated from the difference between R_{bulk} and $R_{bulk+mem}$ as follows:

$$R_{mem} = R_{bulk+mem} - R_{bulk} \quad [1]$$

To reduce the effects of concentration polarization on the membrane resistance, the resistances were measured using an alternating current (AC) at 10 kHz frequency.

Table 1. Physicochemical characteristics of CMX/AMX and FKS/FAS membranes.

Membrane	Thickness (mm)	Ion exchange capacity (meq/g)	Specific area resistance (Ω cm^2)
Neosepta CMX	0.14–0.20	1.5–1.6	1.8–3.8
Neosepta AMX	0.12–0.18	1.4–1.42	2.0–3.5
Fumatech FKS	0.75–0.13	0.8–1.2	2.0–4.5
Fumatech FAS	0.75–0.13	1.0–1.4	2.0–3.0

5.2.3 Membrane potential measurements

As for the membrane resistance, the purpose of this measurement was to investigate the effect of the excess PAC in the wastewater after pre-treatment on the membrane potential. The membrane potential was measured using two acrylic plastic chambers separated by a membrane, as reported by us previously [14]. Chambers I and II were filled with high and low concentration solutions with volumes of 400 cm^3, and the chambers were separated by a membrane with an effective area of 2.54 cm^2. The membrane potential between the solutions was then measured using Ag/AgCl electrodes (TOAHS-205C) connected with salt bridges (3 N KCl) and attached to a voltmeter (KT-2008, Kaise Corporation, Japan) at 24 ± 0.1 °C. Each measurement was taken after 10 min to obtain stable values. In all experiments, the high concentration chamber was filled with NaCl-based model seawater with a conductivity of 48.6 mS cm^{-1}. In contrast, the low concentration chamber was filled with based model municipal wastewater having a conductivity of 0.5 mS cm^{-1}. This model solution comprised NaCl and different doses of

PAC, from 0 to 400 ppm that leads to increasing the model municipal wastewater conductivity.

5.2.4 Coagulation procedure

Coagulation was performed for real wastewater samples obtained from a wastewater plant using a jar tester (Tachometer Jar-Tester, Yamato Corporation, Japan) at 24 ± 0.1 °C. The sampled municipal wastewater was transferred into a 1-L beaker and mixed with stirrer at 200 rpm before the addition of PAC. After dosing with PAC, the sample solution was stirred rapidly at 200 rpm for 120 s and, then, slowly stirred at 60 rpm for 15 min. The sample was then aged for 20 min to allow further precipitation. Samples were collected from 2 cm bellow the solution surface.

The collected sample was then filtered using a 0.45-µm filtration membrane to remove more coagulant particles. Subsequently, the turbidity was measured using a portable turbidimeter (TN-100 Eutech Instruments Pte., Ltd.). The UV–vis absorption at 254 nm (UV_{254}) and total organic carbon (TOC) were measured using a UV-2550 device with 1-cm quartz cells (Shimadzu Corporation, Japan) and a Total Organic Carbon Analyzer (TOC-V_{CPN}, Shimadzu Corporation, Japan), respectively. TOC measurements were performed because NOM mainly consists of humic and fulvic acids [25,26]. Finally, the Al residue before and after coagulation was quantified using an atomic absorption spectrophotometer (AAS, AA-7000F, Shimadzu Corporation, Japan) equipped with a graphite furnace atomizer (GFA-7000), an autosampler (ASC-7000), and an atomizer changer (AAC-7000).

5.2.5 RED experiments

5.2.5.1 RED stack

A ten cell pair RED stack equipped with CMX/AMX was used for the RED performance measurements. Each membrane has an effective membrane area of 88 cm^2 (IEM: 11 cm × 8 cm). Therefore, the total membranes effective area was 1760 cm^2. Two-hundred-micrometer-thick gaskets and woven spacers were set between all membranes to prevent solution leakage and maintain the inter-membrane region, respectively. To reduce the energy consumption of the electrodes producing hydrogen and oxygen, Ag and AgCl were used as the cathode and anode, respectively, at each end of the RED stack. In both electrolyte compartments, 3.0 M NaCl aqueous solution was circulated. The flow rate of the electrolyte solution was set at different values, depending on the pressure of the feed solution, to minimize the pressure difference between the feed solution and electrolyte compartment. Therefore, the leakage from the feed solution to the electrolyte and vice versa was negligible.

Three types of solution combination including two types of model solution and one type of real sample were used as the RED feed solutions for a comprehensive study on the effect of PAC on the power generation performance. The first type of model feed solution was model seawater prepared from NaCl. This solution had a conductivity of 48.6 mS/cm. The aqueous model municipal wastewater was prepared from NaCl and had a conductivity of 0.5 mS/cm. In addition, different dosages of PAC, from 0 to 400 ppm, were added. Here, because the addition of PAC to the model municipal wastewater leads to an increase in its conductivity, a second type of model solution was prepared without PAC

but with the conductivity adjusted to be equal to those of the PAC-containing solutions. This allowed us to differentiate the effect of PAC itself on RED performance from the effects of the changes in conductivity induced by PAC. The second type of model solution were aqueous solutions comprising NaCl with a conductivity of 48.6 mS/cm or conductivities identical to the samples dosed with PAC. Finally, a third type of solution to mimic natural seawater and natural municipal wastewater before and after coagulation was also used.

5.2.5.2 RED performance measurement

The RED stack performance was monitored using the open circuit voltage (OCV), maximum current, maximum power density, and stack resistance, which were evaluated by current–voltage (*I-V*) tests using a potentiostat/galvanostat (HAB-151, Hokuto Denko Co., Japan). In the *I-V* tests, the current was changed from zero to the maximum current until the stack voltage became zero with a current step of 0.4 mA/s. Both high and low concentration feeds were fed to the RED stack using two magnetic pumps (MD-30RZ-N, Iwaki Co., Ltd.) with a linear flow velocity of 1 cm/s. This flow velocity has been reported to be an ideal value to reduce concentration polarization effects [14,27,28]. Three digital pressure gauges (KDM 30, Krone Co., Ltd) were used to evaluate the pressure drop in the HSC, LSC, and electrolyte compartments. The conductivities of both inlet and outlet solutions, as well as the temperature (23–24 °C), were also measured using a conductivity meter (MC-31P, DKK-TOA Corp., Japan).

The current and voltage during the *I-V* tests were recorded using a data logging system (midi LOGGER GL200, Graphtec Co., Japan) connected to a personal computer. The OCV and shortcut (maximum) current were obtained from the vertical and horizontal

axes intercepts of the *I-V* curves, respectively. The RED power output (P) and power density (P_d) were defined by multiplying the stack voltage and current and dividing this value by the total membrane effective area, as shown by equations (2) and (3) [12].

$$P = E_{stack}.I \quad [2]$$

$$P_d = {}^{P}/_{NA} \quad [3]$$

In equations (2) and (3), N and A are the number of cell pairs and the effective membrane area of each cell, respectively. In addition, the RED stack resistance was obtained from the gradient of the *I-V* curves.

5.3 Result and discussion

5.3.1 Effect of PAC on membrane resistance

The membrane resistances when immersed in the 0.5 M NaCl model solution with different PAC concentrations and that without PAC was measured to understand the impact of the PAC dose during wastewater treatment on the RED performance. Because the model solution is almost free of NOMs, all dissolved PAC in this solution would represent an excess of coagulant in a natural wastewater solution. Fig. 1 shows the resistances of the CMX/AMX, as well as FKS/FAS, membranes as a function of PAC concentration in the model 0.5 M NaCl solution. In both types of membranes, the effect of PAC on the AEMs was negligible, but a significant effect on the CEMs was noted. In fact, the CMX resistance increased more than 100% on increasing the PAC concentration from 0 to 400 ppm, reaching a maximum of 5.37 Ω cm^2. On the addition of PAC into the model solution, Al^{3+} undergoes hydrolysis, forming a variety of dissolved Al species such as

$Al(OH)^{2+}$, $Al_2(OH)_2^{4+}$, $Al_3(OH)_4^{5+}$, and $Al_{13}O_4(OH)_{24}^{7+}$, as well as Al hydroxide precipitates such as $Al(OH)_{3(am)}$ [22,26]. Therefore, the all Al hydrolyzed species tended to absorb on the CEM, which is negatively charged. Consequently, the presence of Al-based multivalent ions would cause an increase in the membrane resistance because of their lower mobility, larger hydrated radius, and strong interactions with the negatively charged CEM species [9,29]. In addition, the generation of $Al(OH)_{3(am)}$ resulted in an increase in the turbidity of the model solution as it precipitated on the membrane. This also resulted in an increase in the membrane resistance because of the reduction in the effective area of the membrane. The slight increase in the AEM resistance could also be due to the precipitation of $Al(OH)_{3(am)}$ on the surface.

On comparing the membrane types, we found that PAC affected FKS significantly, and the resistance was almost seven-times greater (13.37 $\Omega.cm^2$) than that of CMX on increasing the PAC concentration from 0 to 400 ppm. Initially, FKS showed a lower membrane resistance and, thus, higher RED power generation performance than that using CMX. However, we found that the Al species had more effect on the FKS membrane than the CMX membrane because of the higher charge density of FKS than that of CMX, as well as its greater thinness. Therefore, the results show that if the over dosing PAC is not negligible and accumulate in the CEM, the FKS membrane would not be preferable even though their good lower membrane resistance. We also made a preliminary test to see if the accumulated PAC could be physically removed (washed away) without using any chemical agents, and the results indicate that accumulation occurred with/on the CEM even at low PAC concentrations. Therefore, finding the optimum concentration of PAC for

natural municipal wastewater treatment is crucial to suppress the negative effects of excess PAC.

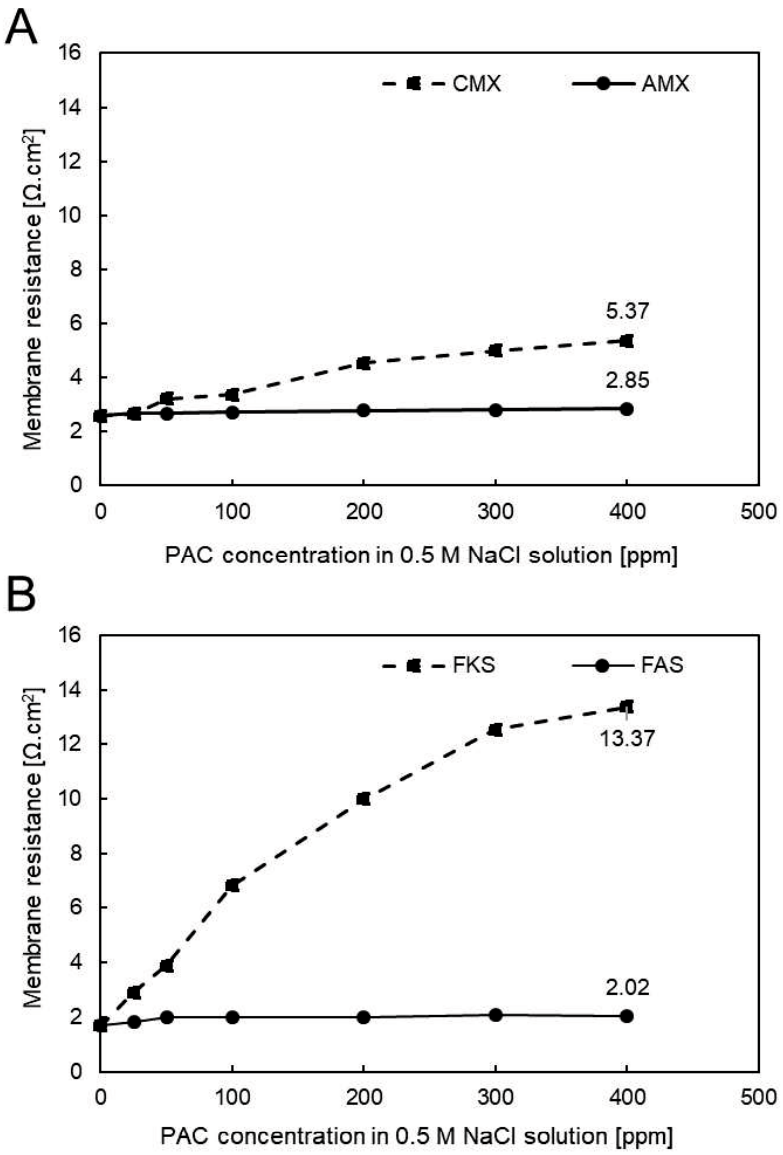

Figure 1. Membrane resistance as the function of PAC concentration in 0.5 M NaCl solution. A shows the results for the standard CMX/AMX membrane, and B shows the results for the thin FKS/FAS membrane.

5.3.2 Effect of PAC on membrane potential

To investigate the effect of PAC in wastewater on the membrane potential between the seawater and wastewater, we must understand the effect of PAC on the solution conductivity because the salinity ratio, which corresponds to the membrane potential, is proportionally related to the conductivity ratio between the high and low concentration solutions. Fig. 2 shows the effect of PAC on the wastewater conductivity, which increased from 0.5 to 1.6 mS/cm on increasing the PAC concentration from 0 to 400 ppm. An increase in the wastewater conductivity is intuitive because PAC forms charged Al species, chlorides, and other salts on hydrolysis. Therefore, the addition of PAC decreases the salinity ratio and the resulting membrane potential. In addition, the adsorption of PAC on the membrane reduces the membrane potential because it has the same effect as a multivalent ion.

The changes in wastewater conductivity on the introduction of PAC had a clear negative impact on the membrane potentials of both the CMX and AMX, as shown in Fig. 3. In the case of CMX, the potential decreased by about 15%, from 115 to 98 mV by increasing the PAC concentration from 0 to 400 ppm. The CMX potential changed on increasing the PAC concentration from 0 to 100 ppm (0.5 to 0.7 mS/cm), and this shift is consistent with the change in potential on increasing the PAC concentration from 100 to 400 ppm (0.7 to 1.6 mS/cm). Using the Nernst equation to calculate the theoretical membrane potential, we found that the effect of changing the LSC conductivity on the membrane potential would be more significant when using very low-conductivity LSC, and it becomes less effective when using a highly conductive LSC. This is consistent with the observed CMX potentials at different PAC concentrations.

In the case of AMX, the potential of AMX also showed the same decreasing trend on increasing the PAC concentration in the model LSC, as shown in Fig. 3B. However, generally the AMX potential was lower than that of CMX because of its different properties, such as lower permselectivity. In fact, the AMX potential decreased by 24%, from 105 to 80 mV, on increasing the PAC concentration to 400 ppm in the LSC. PAC can be represented as $AlCl_3$, so three Cl^- ions are dissolved for each Al^{3+} ion; thus, the addition of PAC should affect the membrane potential of the AMX to a greater extent than that of the CMX, as observed. Generally, Al species will absorb with negatively charged groups and, thus, would not adsorb on the AMX. Therefore, the observed decrease in the membrane potential was due to the change of salinity ratio because of the increase in the Cl^- ion concentration on the addition of PAC.

Although these results clearly indicate that PAC addition decreased both the membrane potential of the CMX and that of the AMX, the mechanism of this reduction is not clear from these results, especially in the case of CMX. Therefore, we also conducted the same experiment using model NaCl solution without PAC but with the same conductivity as in the above experiments.

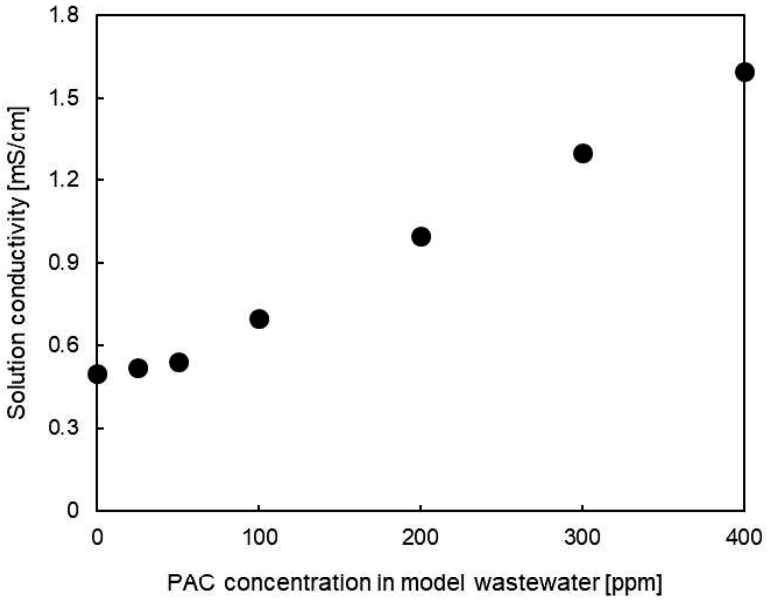

Figure 2. The effect of PAC concentration on model wastewater conductivity.

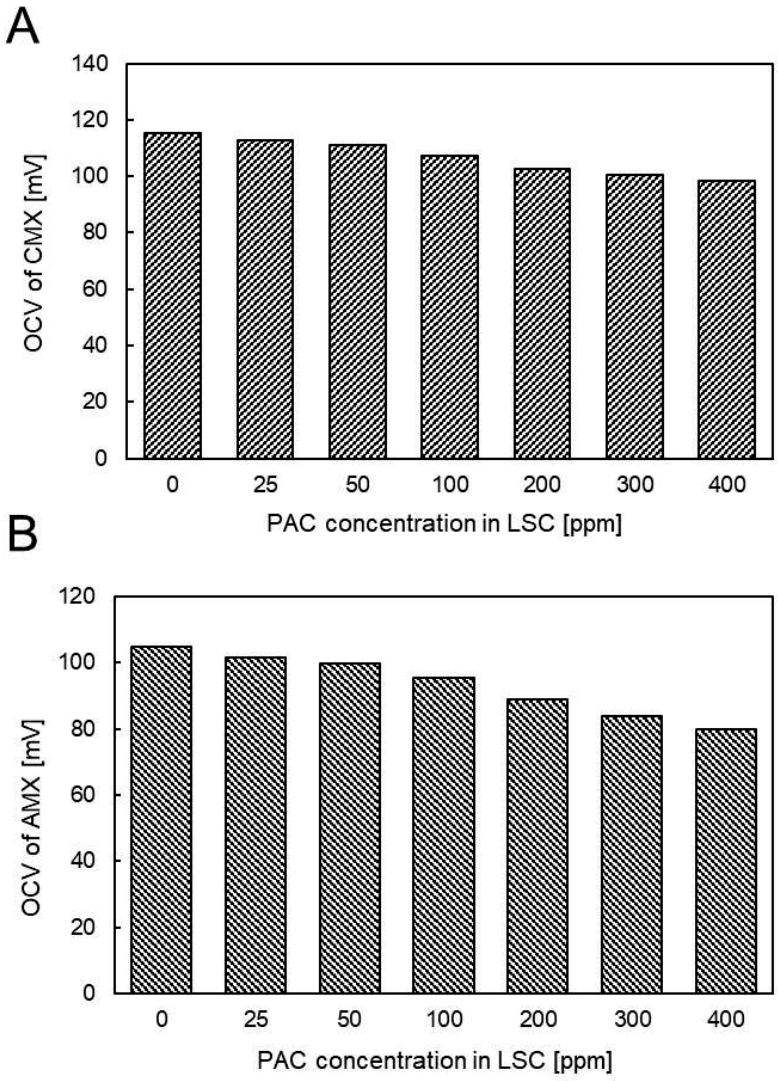

Figure 3. The effect of PAC concentration in the LSC on CMX and AMX OCVs.

5.3.3 Effect of PAC on RED performance using the model solution

The effect of PAC on the RED performance was also investigated using two types of model solution (NaCl with and without PAC) and real sample solutions. The HSCs used in all model tests were aqueous model seawater containing only NaCl. The two types of model wastewater had the same conductivity, which was achieved by adjusting the

amount of NaCl. Using these solutions, we investigated the effect of conductivity on the OCV reduction mechanism of the IEMs.

The OCVs of the RED stack using two types of model wastewaters as the LSC are shown in Fig. 4. The maximum OCV of the RED stack was 1.96 V when using model seawater and model wastewater having conductivities of 0.5 mS/cm. The OCV of the RED stack decreased by more than 18% on increasing the model wastewater conductivity and the PAC dosage to 1.6 mS/cm and 400 ppm, respectively. As shown in Fig. 4, the differences between the RED stack OCV using LSC with different conductivities and that with PAC was negligible. Therefore, the reduction in the OCV of the RED stack was due to the reduction in the salinity or conductivity ratio between the high and low concentrate compartments, as discussed in Section 4.2. This also suggests that PAC itself had no influence on the membrane potential of both CMX and AMX.

Fig. 5 shows the stack resistance values, which were calculated using the initial slopes of the *I-V* curves, when using the model solutions with and without PAC. We found that the stack resistance in the absence of PAC clearly decreased, almost halving on increasing the conductivity of LSC from 0.5 to 1.6 mS/cm because the conductivity of the LSC solution decreased. In contrast, in the case of those with PAC, interestingly, the stack resistance slightly increased and then decreased with increasing solution conductivity. In this case, although the LSC resistance decreased with increasing conductivity, the membrane resistance of the CMX also increased because of the presence of PAC, as discussed in Section 3.1. Therefore, the difference in the RED stack resistances with and without PAC is clearly due to the effect of PAC on the membrane resistance, as shown by

the black arrows in Fig. 5, and this difference increased with increasing PAC concentration, as expected.

In addition, the gross power density of the RED stack using same solution combinations are also shown in Fig. 6. The gross power density when using model wastewater without PAC slightly increased and then decreased on increasing the LSC conductivity. The maximum gross power density was obtained when using the model wastewater with its conductivity of 1.0 mS/cm. The membrane potential based on the salinity ratio and stack resistance (especially that of LCS because of its lower conductivity) are two important parameters for the resulting RED power output performance. Increasing the conductivity of LCS resulted in a decrease in the membrane potential but also a decrease in the stack resistance. Therefore, this competitive trade-off relationship provided the maximum gross power when the conductivity was 1.0 mS/cm.

On the other hand, when using model wastewater with PAC, the gross power output remarkably decreased with increasing PAC concentration. The reduction in the gross power density reached around 41% on increasing the PAC concentration to 400 ppm. Because the presence of PAC had no influence on the membrane potential, this performance reduction must be due to the increase in the membrane resistance of CMX, as mentioned in Section 4.1. The positively charged Al species, consequently, increased the membrane resistance, as has been reported for other multivalent ions [8,29–33]. For example, *Avci et al*. reported a 95% performance reduction in the presence of $MgCl_2$ in feed solutions compared with those containing only NaCl [9].

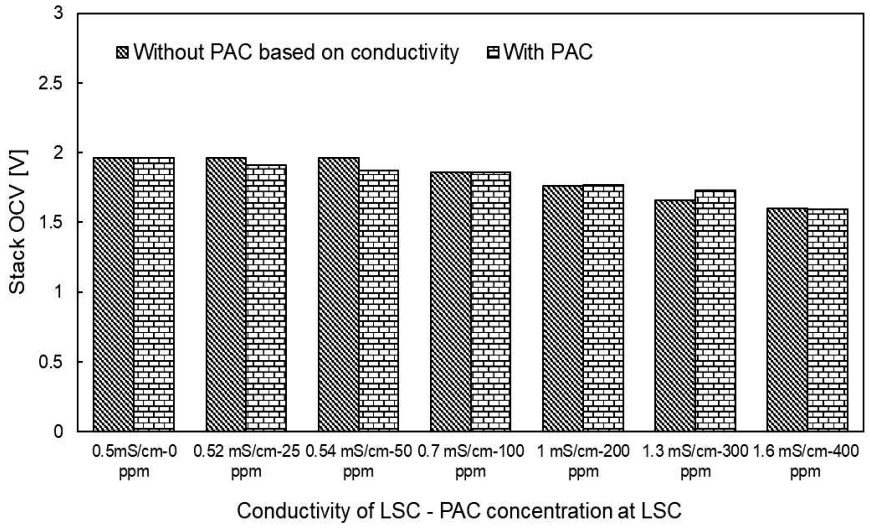

Figure 4. OCV of the RED stack using model seawater and wastewater with different conductivities without PAC and in the presence of PAC in the LSC.

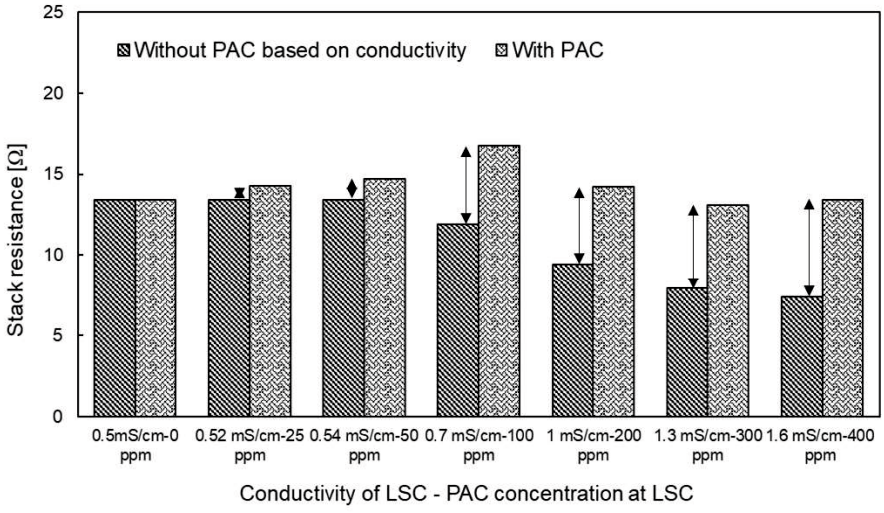

Figure 4. RED stack resistance using model seawater and wastewater with different conductivities without PAC and in the presence of PAC in the LSC.

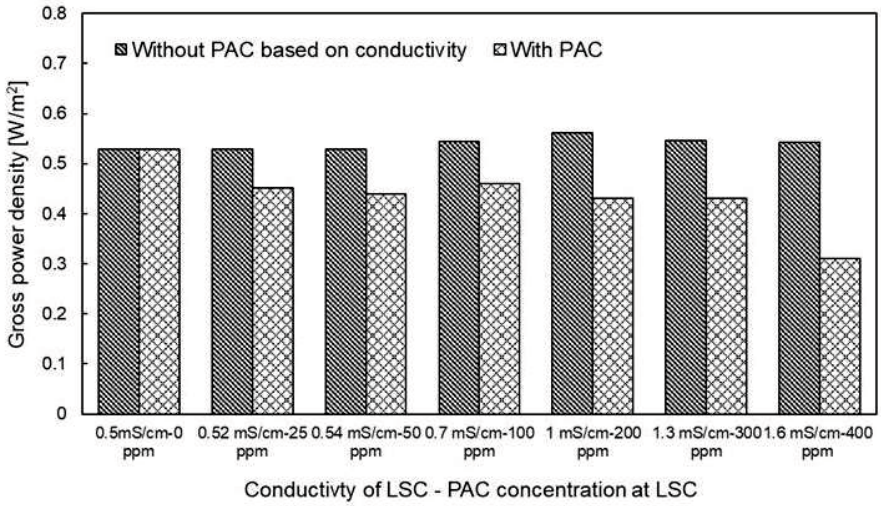

Figure 5. Gross power density of RED stack using model seawater and wastewater with different conductivities without PAC and in the presence of PAC in the LSC.

5.3.4 Natural wastewater coagulation treatment

The treatment of real municipal wastewater by adding PAC as a coagulant was assessed on the basis of turbidity, UV_{254} reduction, and TOC removal. TOC is the total organic matter content, and UV_{254} measurements indicate the presence of aromatic and hydrophobic compounds.

Fig. 7 shows the changes in turbidity, UV_{254}, and TOC in natural municipal wastewater using PAC at concentrations from 0 to 400 ppm. The natural municipal wastewater had already been treated by the standard activated sludge method in the WWT plant, and the turbidity, UV_{245}, and TOC removal were all significantly affected by the dosage of PAC. In all terms of these parameters, the removal properties increased sharply on the initial increase in the PAC dosage (< 10 ppm) but then slightly decreased when the

PAC dosage became higher than 10 ppm. At a dosage of 10 ppm PAC, the optimum removal efficiency of turbidity, UV_{245} and TOC of 63.6%, 70.3%, and 21.6% were achieved, respectively. In this regard, the exact values of the final turbidity, UV absorbance, and TOC concentration corresponding to the highest removal efficiency of PAC were 0.04 NTU, 0.058 Abs, and 5.14 ppm. These results indicate that the removal efficiency increased at both low and high coagulant dosages. Yang *et al*. reported turbidity, UV_{245}, and TOC removal efficiencies of 94.5%, 53.5% and 34.8%, respectively from Yellow River water [16]. In addition, Wang *et al.* investigated the application of PVA on water contaminated by oil-sand processing [34]. They reported maximum TOC and UV_{245} removal efficiencies of around 24% and 15%, respectively, which shows the good removal efficiency of our method.

The efficiency of Al-based coagulants largely depends on the presence of Al_a, Al_b and Al_c in these types of coagulants [35]. The apparent molecular weight of the three Al species increase as $Al_a < Al_b < Al_c$. In contrast with other Al-based coagulants which are mainly contain monomeric species (Al_a), PAC mainly consists of medium polymer species (Al_b) and colloidal or solid species (Al_c). The Al_b and Al_c content in PAC corresponds to the removal of turbidity, UV_{254}, and TOC because of their high charge neutralization ability, whereas monomeric Al_a is the most unstable species in raw water, immediately being hydrolyzed to form hydroxide before reacting with organic matter and decreasing the pH of the effluent. Increasing the PAC dosage resulted in uncontrolled hydrolysis until the pH reached a limiting value, which caused the further reduction in contaminant removal [36]. As shown in Fig. 8, the pH of effluents decreased rapidly at first, subsequently decreasing slightly from pH 6 on increasing the PAC dosage and reaching an

almost constant pH of 4. In fact, the optimum pH of the effluents for the maximum coagulation process performance with PAC is known to be 5.5–6.5 [16]. Therefore, the removal efficiency decreased on increasing the PAC concentration from 10 ppm because the effluent pH was lower than 5.5. Therefore, the increasing initial pH of natural wastewater is proposed as an effective way to improve the coagulation efficiency.

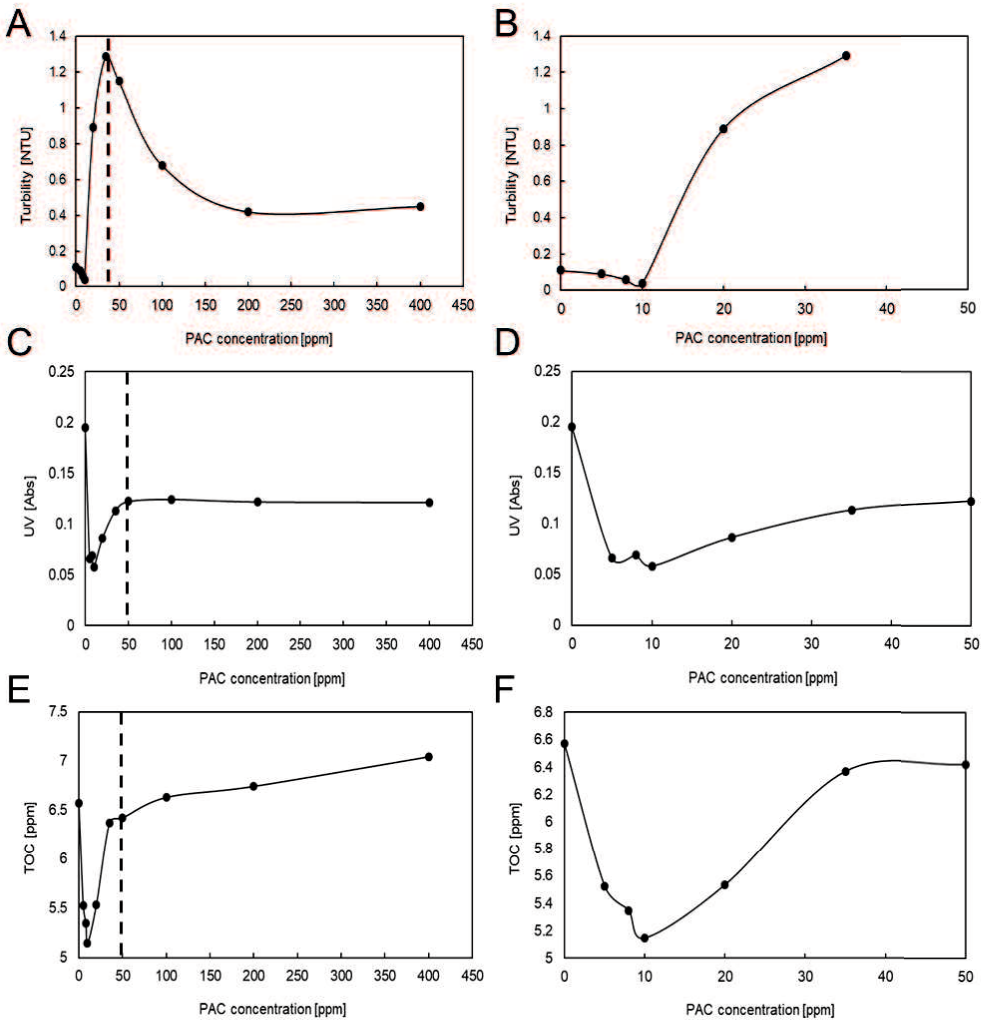

Figure 6. Turbidity of wastewater after coagulation over the whole range (A) and narrow range (B) of PAC concentrations, UV_{254} of wastewater after coagulation over the whole range (C) and

narrow range (D) of PAC concentrations, and TOC of treated wastewater after coagulation over the whole range (E) and a narrow range (F) of PAC concentrations.

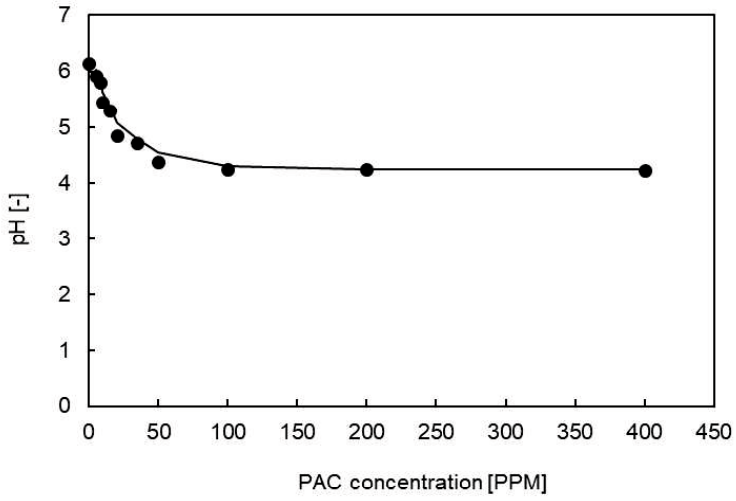

Figure 7. pH of treated wastewater after coagulation with PAC.

5.3.5 Effect of pH on the coagulation removal efficiency

Coagulation using PAC without initial pH control resulted in a moderate reduction in the turbidity, UV_{245}, and TOC (63.6%, 70.3%, and 21.6%, respectively). The negative impact of the NOM on the RED performance in both the short and long term [11,12] indicates that further removal before the RED process is required. As discussed in Section 3.4, the maximum NOM (TOC) removal efficiency of 22% was achieved using a dosage of 10 ppm PAC, and the TOC in the effluent fell to 5.15 mg/L, although this is still high. For instance, Yang *et al*. achieved an optimum organic compound removal of 32.7% from water from the Yellow River using PAC, and the final organic compound concentration reached 1.63 mg/L [16]. Therefore, greater removal of NOM is required to

minimize the negative effects on the RED performance. As mentioned, the reduction in the pH on adding PAC into real municipal wastewater is one of the key parameters affecting (and reducing) NOM coagulation. Therefore, the initial pH of the natural municipal wastewater was increased by adding different doses of NaOH before coagulation using PAC at concentrations of 10, 100, and 400 ppm. This wide PAC dosage range was selected to obtain a comprehensive understanding of the effect of changing the initial pH on the coagulation process.

Considering the PAC dosage, the initial pH was changed from 6 to 10 when using 10 ppm PAC, and it was changed from 7 to 12 when using 100 and 400 ppm PAC. The TOC removal efficiency as the function of different initial pH is shown in Fig. 9. In the case of 10 ppm PAC, the TOC removal efficiency significantly improved from 21.6% to 41.7% on increasing the pH from 6 to 7, but it slightly decreased at pH values greater than 7. When using 100 ppm PAC, the TOC removal efficiency was almost constant, even on increasing the pH from 7 to 9. However, the TOC suddenly increased to maximum value of 50.1% at pH 10. In addition, the use of 400 ppm of PAC also resulted in the maximum TOC removal efficiency of around 20% at a pH of 12. Among all the results, although the maximum TOC removal efficiency was achieved using 100 ppm PAC at a pH of 10 (50.1% removal), the optimum point of TOC removal was set to 10 ppm PAC and the pH to 7 (41.7% removal) for the RED process because the PAC and NaOH consumption in the coagulation process were less than those when using 100 ppm PAC.

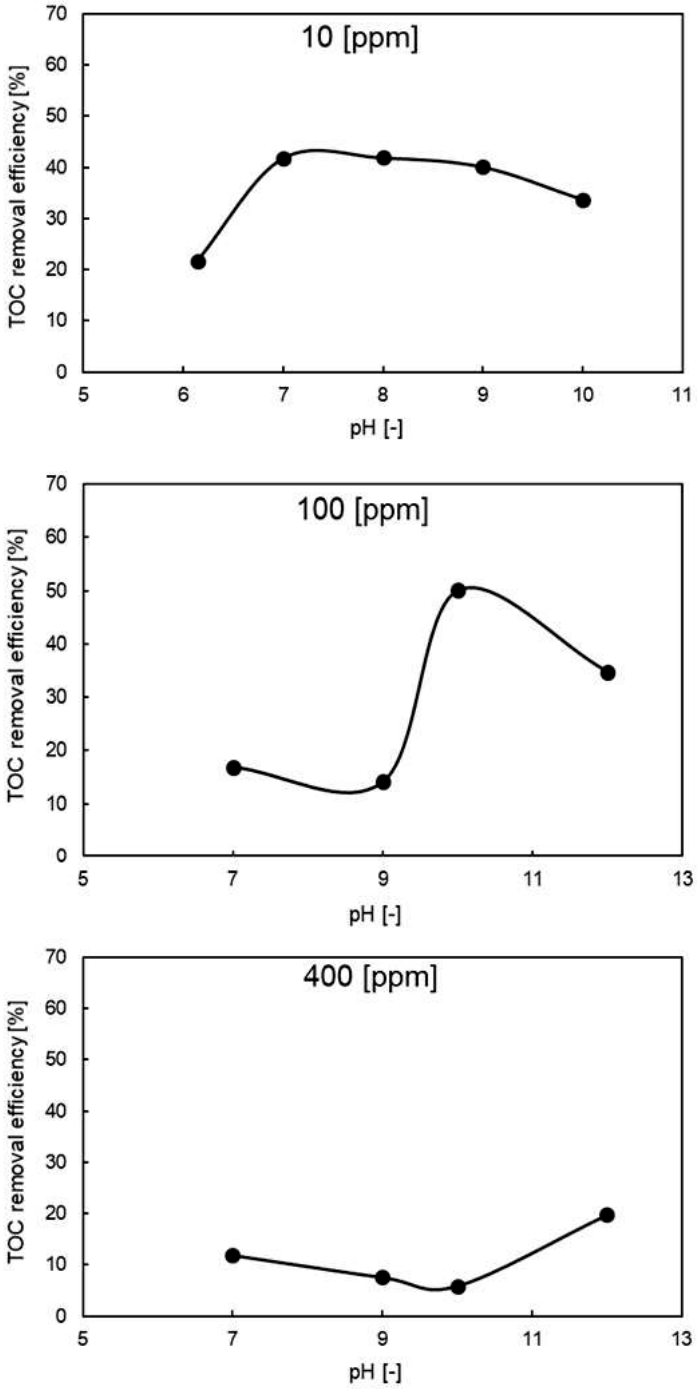

Figure 8. Effect of initial pH on TOC removal efficiency using 10, 100, and 400 ppm PAC.

5.3.6 RED performance using natural wastewater after coagulation

Different coagulation processes using PAC for real wastewater treatment and subsequent RED power generation were carried out to evaluate the overall process. The performance of the RED process was measured using real seawater and municipal wastewater samples before and after coagulation to identify the effect of natural wastewater coagulation on the RED performance. For this purpose, four types of LSC solutions, natural municipal wastewater (1) without filtration and coagulation, (2) just after filtration, (3) after coagulation with 10 ppm PAC at pH 7 followed by filtration, and (4) after coagulation with 100 ppm PAC at pH 10 followed by filtration, were used in the RED tests. The natural seawater was used just after filtering in all cases.

The OCVs of the RED stack when using the four natural feed solution combinations are shown in Fig. 10. The results of NaCl model case are also shown here for comparison. First, we could not show the result for type (1) because the LSC solution flow stopped after a short experimental time because of the accumulation of particles within the spacers; thus, it was not possible to measure the OCV and RED performance. In the other cases (type 2–4 and model for comparison), the resulting OCVs of the RED stack were comparable, except that of type 4, which was slightly lower. The negligible difference between the RED stack OCV when using type-2 and type-3 feed solutions is due to the similar concentration ratio in both cases through HSC and LSC. The use of 100 ppm of PAC led to a slight increase in the conductivity in the LSC because of the increase in Al residue in the municipal wastewater after coagulation, as well as the decrease in salinity ratio between the high and low concentration compartments and reduced OCV. In contrast, in the case of type-3, the PAC was almost completely consumed during the coagulation

process. In addition, the difference between the OCVs using real solutions and model solutions are negligible, even though multivalent ions are included in the real solutions. Thus, if the LSC concentration is quite low, the effect of multivalent ions on the OCV is less than that of the salinity ratio [14].

The gross power density, as well as resistance of the RED stack, when using the model feed solutions, as well as type-2–4 feed solutions is shown in Fig. 11. Reasonably, the highest maximum power with the lowest resistance was obtained when using model feed solutions because they contained only NaCl (monovalent ions) without organic compounds or particles. The maximum power was achieved when using feed solutions treated by coagulation with 100 ppm PAC at pH 10 (type 4), after coagulation with 10 ppm PAC at pH 7 (type 3), and after filtration alone (type 2). The difference between the power generated with the model and real solutions is mainly due to the effect of multivalent ions and NOM on the membrane resistance because the obtained OCVs are almost identical. Furthermore, among the natural feed solutions, the gross power density increased by 14% and 18% when using feed solution types 3 and 4, respectively, compared with that after filtration alone. Because all natural solutions contained divalent ions and the difference between them was the residual concentration of NOM, in the real solution samples, coagulation with the optimized PAC dosage improved the RED process performance because of the partial removal of NOM. This result is consistent with the results of other studies, which have shown the significant impact of NOM on RED performance [11,12].

Although the maximum gross power density of the RED process was obtained when using the type-4 feed solution, the difference in the RED performance using feed solution types 3 and 4 was negligible because these samples showed almost the same TOC

removal. In addition, although the RED stack OCV was higher when using feed solution type 3 than when using type 4, the stack resistance was also higher when using feed solution type 3, as shown in Fig. 11B. In fact, the higher conductivity of the LSC when using feed solution type 4 was due to the presence of more Al, as reflected by the stack resistance. On the basis of these results, the use of type-2 feed solution (coagulation of municipal wastewater with 10 ppm PAC at the pH of 7) is recommended because of the PAC, as well as NaOH, concentration required.

Using coagulation as the main pre-treatment step for RED feed solutions might also lead to a reduction in the total cost of the pre-treatment process; for example, direct filtration through sand [37] or a drum filter [38] has been proposed as a pre-treatment step for RED, and the coagulation step before filtration reduces the need to replace the filter and ensures higher water quality, promising a lower fouling propensity for RED stacks in long-term use. Therefore, although an excess amount of PAC reduces the RED performance because of the increase in CEM resistance, coagulation using PAC at the optimum dosage is a useful way to not only enhance the power generation performance but also ensure long-term stable operation.

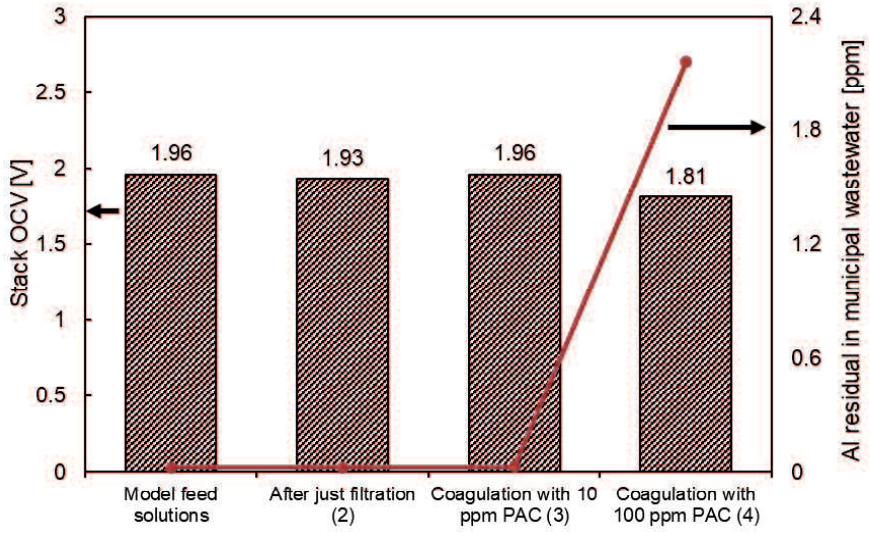

Figure 9. RED stack OCV using seawater as the HSC and both model and natural municipal wastewater before and after coagulation as the LSC (left-hand axis) and the Al residual concentration in the municipal wastewater (right-hand axis).

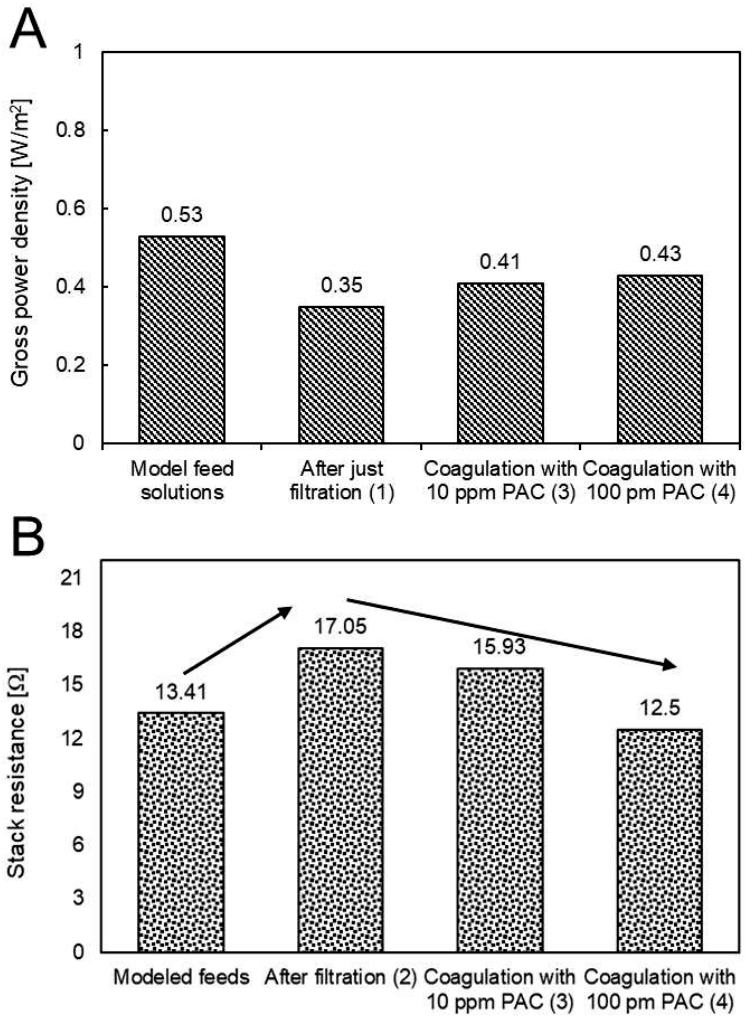

Figure 10. A: Gross power density. B: RED stack resistance of the RED process using seawater as HSC and both model and real municipal wastewater samples before and after coagulation.

5.4 Conclusion

In this study, coagulation using PAC was used as a pre-treatment step for RED power generation. Tests with municipal wastewater instead of river water, as well as NaCl-based model solutions, were carried out. Measurements of the membrane potential and membrane resistance in the presence of PAC in the model solution revealed that the PAC

residue in the wastewater after the coagulation process significantly reduces the RED performance by 40% because of the increased CEM resistance. In contrast, the OCVs and AEM resistance were not influenced by the presence of PAC, even at high concentrations of 400 ppm. Therefore, precise PAC dosing is crucial to ensure a low amount of PAC residue after coagulation before RED. PAC coagulation for real wastewater samples was also demonstrated and enabled the removal of 42% and 50% organic materials when the optimum PAC dosages of 10 ppm was used at pH 7 and 100 ppm at pH 10, respectively. Consequently, the RED tests using pre-treated wastewater revealed that the efficient removal of chemicals from the wastewater can enhance the RED power generation performance by about 20% because of the negligible amount of PAC residue in the wastewater after coagulation. In addition, because the coagulation-based pre-treatment improves the water quality, it is also a useful method to suppress membrane fouling of the RED stack and loading factor of the filtration-based pre-treatment. The accumulation of low concentrations of PAC into the CEM and subsequent RED performance also should be investigated over long-term use using natural municipal wastewater.

5.5 Acknowledgements

This work was supported by Sasakura Enviro-Science Foundation and JSPS KAKENHI Grant Number JP16H01796 and Salt Science Research Foundation (SSRF) No 1813.

5.6 References

[1] R.E. Lacey, Energy by reverse electrodialysis, Ocean Eng. 7 (1980) 1–47. doi:10.1016/0029-8018(80)90030-X.

[2] M. Tedesco, C. Scalici, D. Vaccari, A. Cipollina, A. Tamburini, G. Micale, Performance of the first reverse electrodialysis pilot plant for power production from saline waters and concentrated brines, J. Memb. Sci. 500 (2016) 33–45. doi:10.1016/j.memsci.2015.10.057.

[3] Y. Mei, C.Y. Tang, Recent developments and future perspectives of reverse electrodialysis technology: A review, Desalination. 425 (2017) 156–174. doi:10.1016/j.desal.2017.10.021.

[4] J.W. Post, C.H. Goeting, J. Valk, S. Goinga, J. Veerman, H.V.M. Hamelers, P.J.F.M. Hack, Towards implementation of reverse electrodialysis for power generation from salinity gradients, Desalin. Water Treat. 16 (2010) 182–193. doi:10.5004/dwt.2010.1093.

[5] A. Daniilidis, D.A. Vermaas, R. Herber, K. Nijmeijer, Experimentally obtainable energy from mixing river water, seawater or brines with reverse electrodialysis, Renew. Energy. 64 (2014) 123–131. doi:10.1016/j.renene.2013.11.001.

[6] J.W. Post, H.V.M. Hamelers, C.J.N. Buisman, Energy recovery from controlled mixing salt and fresh water with a reverse electrodialysis system, Environ. Sci. Technol. 42 (2008) 5785–5790. doi:10.1021/es8004317.

[7] R.A. Tufa, S. Pawlowski, J. Veerman, K. Bouzek, E. Fontananova, G. di Profio, S. Velizarov, J. Goulão Crespo, K. Nijmeijer, E. Curcio, Progress and prospects in reverse

electrodialysis for salinity gradient energy conversion and storage, Appl. Energy. 225 (2018) 290–331. doi:10.1016/j.apenergy.2018.04.111.

[8] Z.Y. Guo, Z.Y. Ji, Y.G. Zhang, F. J. Yang, J. Liu, Y.Y. Zhao, J.S. Yuan, Effect of ions (K^+, Mg^{2+}, Ca^{2+} and SO_4^{2-}) and temperature on energy generation performance of reverse electrodialysis stack, Electrochim. Acta. 290 (2018) 282–290. doi:10.1016/j.electacta.2018.09.015.

[9] A.H. Avci, P. Sarkar, R.A. Tufa, D. Messana, P. Argurio, E. Fontananova, G. Di Profio, E. Curcio, Effect of Mg^{2+} ions on energy generation by Reverse Electrodialysis, J. Memb. Sci. 520 (2016) 499–506. doi:10.1016/j.memsci.2016.08.007.

[10] X. Tong, B. Zhang, Y. Chen, Fouling resistant nanocomposite cation exchange membrane with enhanced power generation for reverse electrodialysis, J. Memb. Sci. 516 (2016) 162–171. doi:10.1016/j.memsci.2016.05.060.

[11] D.A. Vermaas, D. Kunteng, M. Saakes, K. Nijmeijer, Fouling in reverse electrodialysis under natural conditions, Water Res. 47 (2012) 1289–1298. doi:10.1016/j.watres.2012.11.053.

[12] R.S. Kingsbury, F. Liu, S. Zhu, C. Boggs, M.D. Armstrong, D.F. Call, O. Coronell, Impact of natural organic matter and inorganic solutes on energy recovery from five real salinity gradients using reverse electrodialysis, J. Memb. Sci. 541 (2017) 621–632. doi:10.1016/j.memsci.2017.07.038.

[13] M. Tedesco, A. Cipollina, A. Tamburini, G. Micale, Towards 1 kW power production in a reverse electrodialysis pilot plant with saline waters and concentrated brines, J. Memb. Sci. 522 (2017) 226–236. doi:10.1016/j.memsci.2016.09.015.

[14] S. Mehdizadeh, M. Yasukawa, M. Kuno, Y. Kawabata, M. Higa, Evaluation of energy harvesting from discharge solutions in a salt production plant by reverse electrodialysis (RED), Desalination. 467 (2019) 95–102. doi:10.1016/j.desal.2019.04.007.

[15] M. Higa, T. Watanabe, M. Yasukawa, N. Endo, Y. Kakihana, H. Futamura, K. Inoue, H. Miyake, J. Usui, A. Hayashi, M. Matsuhashi, Sustainable hydrogen production from seawater and sewage treated water using reverse electrodialysis technology, Water Pract. Technol. (2019). doi:10.2166/wpt.2019.048.

[16] Z. Yang, B. Gao, Q. Yue, Coagulation performance and residual aluminum speciation of $Al_2(SO_4)_3$ and polyaluminum chloride (PAC) in Yellow River water treatment, Chem. Eng. J. 165 (2010) 122–132. doi:10.1016/j.cej.2010.08.076.

[17] A. Zouboulis, G. Traskas, P. Samaras, Comparison of single and dual media filtration in a full-scale drinking water treatment plant, Desalination. 213 (2007) 334–342. doi:10.1016/j.desal.2006.02.102.

[18] M. Yan, D. Wang, J. Qu, J. Ni, C.W.K. Chow, Enhanced coagulation for high alkalinity and micro-polluted water: The third way through coagulant optimization, Water Res. 42 (2008) 2278–2286. doi:10.1016/j.watres.2007.12.006.

[19] M. Tomaszewska, S. Mozia, A.W. Morawski, Removal of organic matter by coagulation enhanced with adsorption on PAC, Desalination. 161 (2004) 79–87. doi:10.1016/S0011-9164(04)90042-2.

[20] M. Yan, D. Wang, J. Ni, J. Qu, C.W.K. Chow, H. Liu, Mechanism of natural organic matter removal by polyaluminum chloride: Effect of coagulant particle size and hydrolysis kinetics, Water Res. 42 (2008) 3361–3370. doi:10.1016/j.watres.2008.04.017.

[21] J.E. Van Benschoten, J.K. Edzwald, Chemical aspects of coagulation using aluminum salts I . Hydrolytic reactions of alum and ployaluminum chloride, Water Res. 24 (1990) 1519–1526.

[22] B.Y. Gao, Y.B. Chu, Q.Y. Yue, B.J. Wang, S.G. Wang, Characterization and coagulation of a polyaluminum chloride (PAC) coagulant with high Al_{13} content, J. Environ. Manage. 76 (2005) 143–147. doi:10.1016/j.jenvman.2004.12.006.

[23] S. Mehdizadeh, M. Yasukawa, T. Abo, Y. Kakihana, M. Higa, Effect of spacer geometry on membrane and solution compartment resistances in reverse electrodialysis, J. Memb. Sci. 572 (2019) 271–280. doi:10.1016/j.memsci.2018.09.051.

[24] S. Mehdizadeh, M. Yasukawa, T. Abo, M. Kuno, Y. Noguchi, M. Higa, The effect of feed solution temperature on the power output performance of a pilot-scale reverse electrodialysis (RED) system with different intermediate distance, Membranes (Basel). 9 (2019) 73. doi:10.3390/membranes9060073.

[25] M. Sillanpää, M.C. Ncibi, A. Matilainen, M. Vepsäläinen, Removal of natural organic matter in drinking water treatment by coagulation: A comprehensive review, Chemosphere. 190 (2018) 54–71. doi:10.1016/j.chemosphere.2017.09.113.

[26] T.K. Trinh, L.S. Kang, Response surface methodological approach to optimize the coagulation-flocculation process in drinking water treatment, Chem. Eng. Res. Des. 89 (2011) 1126–1135. doi:10.1016/j.cherd.2010.12.004.

[27] P. Długołecki, J. Dabrowska, K. Nijmeijer, M. Wessling, Ion conductive spacers for increased power generation in reverse electrodialysis, J. Memb. Sci. 347 (2010) 101–107. doi:10.1016/j.memsci.2009.10.011.

[28] P. Długołe, A. Gambier, M. Wessling, Practical potential of reverse electrodialysis process for sustainable energy generation, Environ. Sci. Technol. 43 (2009) 6888–6894.

[29] T. Rijnaarts, E. Huerta, W. van Baak, K. Nijmeijer, Effect of divalent cations on RED performance and cation exchange membrane selection to enhance power sensities, Environ. Sci. Technol. 51 (2017) 13028–13035. doi:10.1021/acs.est.7b03858.

[30] J.W. Post, H.V.M. Hamelers, C.J.N. Buisman, Influence of multivalent ions on power production from mixing salt and fresh water with a reverse electrodialysis system, J. Memb. Sci. 330 (2009) 65–72. doi:10.1016/j.memsci.2008.12.042.

[31] D.A. Vermaas, J. Veerman, M. Saakes, K. Nijmeijer, Influence of multivalent ions on renewable energy generation in reverse electrodialysis, Energy Environ. Sci. 7 (2014) 1434–1445. doi:10.1039/C3EE43501F.

[32] R.A. Tufa, E. Curcio, W. Van Baak, J. Veerman, S. Grasman, E. Fontananova, Potential of brackish water and brine for energy generation by salinity gradient power-reverse electrodialysis (SGP-RE), RSC Adv. 4 (2014) 42617–42623. doi:10.1039/c4ra05968a.

[33] J. Moreno, V. Díez, M. Saakes, K. Nijmeijer, Mitigation of the effects of multivalent ion transport in reverse electrodialysis, J. Memb. Sci. 550 (2018) 155–162. doi:10.1016/j.memsci.2017.12.069.

[34] C. Wang, A. Alpatova, K.N. McPhedran, M. Gamal El-Din, Coagulation/flocculation process with polyaluminum chloride for the remediation of oil sands process-affected water: Performance and mechanism study, J. Environ. Manage. 160 (2015) 254–262. doi:10.1016/j.jenvman.2015.06.025.

[35] M. Yan, D. Wang, J. Qu, W. He, C.W.K. Chow, Relative importance of hydrolyzed Al(III) species (Al_a, Al_b, and Al_c) during coagulation with polyaluminum chloride: A case study with the typical micro-polluted source waters, J. Colloid Interface Sci. 316 (2007) 482–489. doi:10.1016/j.jcis.2007.08.036.

[36] O.S. Amuda, I.A. Amoo, Coagulation/flocculation process and sludge conditioning in beverage industrial wastewater treatment, J. Hazard. Mater. 141 (2007) 778–783. doi:10.1016/j.jhazmat.2006.07.044.

[37] J.P. Van Der Hoek, D.O. Rijnbende, C.J.A. Lokin, P.A.C. Bonné, M.T. Loonen, J.A.M.H. Hofman, Electrodialysis as an alternative for reverse osmosis in an integrated membrane system, Desalination. 117 (1998) 159–172. doi:10.1016/S0011-9164(98)00086-1.

[38] A.M. Weiner, R.K. McGovern, J.H. Lienhard V, Increasing the power density and reducing the levelized cost of electricity of a reverse electrodialysis stack through blending, Desalination. 369 (2015) 140–148. doi:10.1016/j.desal.2015.04.031.

Chapter 6

Power generation performance of a 299 cell pair pilot-scale RED stack with high gross power density

6.1 Introduction

Increasing the world energy demand due to growing up the population leads to continuously use fossil fuels more [1–3]. On the other hand, rapid consumption of fossil fuel has made more attraction on renewable energy sources due to environmental concerns especially about CO_2 emission [2]. Among different renewable energy sources (e.g., solar, wind, wave, geothermal, and biomass), salinity gradient energy (SGE) has also been considered as one of the sustainable and clean energy resources [4] since *Pattel* et al. has firstly illustrated the SGE at 1954 as an electrochemical potential between two solutions with different salinities [5]. The global potential of the SGE estimated by considering all discharged river water (RW) into seawater (SW) are theoretically around 1.4-2.6 TW, and is sufficiently considerable amount compared with the modern world energy demand [6,7].

In last decade, to harvest the SGE, various processes have been introduced and improved owing to the progressing on membrane technology [8–11]. Membrane-based reverse electrodialysis (RED) where ion exchange membranes are used is one of the emerging processes [2,7,12–14] and would be an appropriate way for SGE capturing because the RED process can directly convert the SGE into available electricity [15]. In the RED, concentrate and dilute solutions flow alternatively between alternatively stacked anion and cation exchange membranes (AEMs and CEMs) [16]. The anions and cations transport in opposite direction from the concentrate into the dilute solution compartments through the AEMs and CEMs, respectively, and the electrochemical potential is generated between the electrode at the both terminal ends. The generated potential can be then converted into an electric current by redox reaction at the electrodes.

Towards implementation of the RED process, use of natural solutions (not artificial such as NaCl solution) at suitable place where sufficient amount of SGE can be potentially obtained has always been considered as most important issue, especially in last two decades [14]. As easily imagined, a combination of natural SW and RW is most promising choice due to their easy availability and its huge potential. Theoretically, significant amount of about 2.5 MJ energy can be released by mixing 1 m3 of RW with large amount of SW [17]. However, the actual obtained energy from natural SW and RW becomes much lower than those theoretically expected [18]. Recently, owing to the developments of stack structure (e.g. small intermediate distance) and IEMs (e.g. low membrane resistance), the RED power output using SW/RW has increased from 0.05 W/m2membrane to 1.02 W/m2membrane [19–22]. In addition, opportunities to access the wide variety of feeds having higher SGE also will provide higher power output performances. Hence, Daniilidis et al. demonstrated the RED power generation using brine (5 M NaCl) instead of SW as a concentrate feed solution. In this case, they successfully obtained the power density of 6.7 W/m2 with the intermembrane distance of 100 μm [18]. Different types of the natural solutions can be also used as the RED feeds, such as seawater brine, saline wastewater, treated wastewater, municipal wastewater and so on instead of SW and RW, respectively [23].

When using natural solution as the feeds, the presence of divalent ions (e.g. Mg^{2+}, Ca^{2+}, SO_4^{2-}) together with NaCl in natural feed solutions showed significant impact on RED performance [19,24,25]. For instance, the molar fraction of 10% $MgSO_4$ beside 90% NaCl in both RED feed solutions (SW and RW) represented around 29% to 50% diminishing of power density due to the uphill transport of divalent ions which leads to

decreasing the stack voltage as well as increasing the membrane resistance [26]. Therefore, applying monovalent selective membranes was proposed as a potentially useful choice to prevent divalent ions transport through the IEMs [27]. The impact of divalent ions on RED power density seemed much lower when using the monovalent selective IEMs as compared with the standard IEM case [28]. Therefore, it seems that the using one-side monovalent selective IEMs with its selective layer facing into low concentrate compartment (LCC) would be more helpful to prevent uphill transport. However, more considerations are still required because the monovalent selective IEMs would show higher resistance due to their rejection properties against the divalent ion transportation especially in the case that high percentage of the divalent ions is included in the feed.

Subsequent scaling up of the RED stack will be also one of the indispensable problems for enhancing the RED power output towards the full-scale commercialization. However, there are few researches on the power generation performance of a large-scale RED stack, especially using natural feed solutions. *Veerman* et al. investigated the effects of residence time and flow direction (co-current and counter-current) on the RED performance of a bench-scale stack (50 cell pairs and its total effective membrane area of 18.75 m2) composed of standard IEMs (not monovalent ion selective) using model NaCl solutions as feeds. Consequently, the maximum power density of around 0.63 W/m2 was obtained when using model SW and RW in co-current flow condition. Tedesco et al. reported the power generation performance of pilot-scale RED stacks (3 RED stacks and their total effective membrane are 400 m2) composed of standard IEMs using natural brine (5M) and brackish water (0.03 M NaCl) as well as their model solutions [29,30]. They consequently achieved the high power output of about 700 W and 330 W using model and

natural feed solutions, respectively. They also proposed that the much lower power output in natural case than the model case would be due to the effect of non-NaCl substance such as divalent ions in the feeds. Thus, their large-scale studies will be a helpful for increasing the RED power output. However, in order to design and optimize the full-scale RED stack, the further study is still required. In addition, a pilot-scale RED stack with monovalent selective IEMs has not been demonstrated yet when using natural solutions as feeds.

Co-locating of reverse osmosis (RO) SW desalination plant with RED process could be an interesting opportunity to recovery of energy for seawater desalination [31]. Using RO brine as concentrate feed solution instead of discharging into seawater (SW) would be useful strategy if low salinity wastewater (e.g. treated sewage, industrial wastewater and so on) is also available near the desalination plant. In present study, we evaluated the performance of the RED stack in a pilot-scale (299 cell pairs and 179.4 m2 membrane effective area). Both model and natural SW/RW as well as RO bine/RW feeds solutions combination have been applied for the performance comparison. Here, natural RW was used as model wastewater especially in RO brine case because co-locating of RW and seawater desalination is nonsense. In addition, this RED stack is equipped with one-side monovalent selective membranes with its selective layer facing into lower concentration compartment (LCC) to diminish the effect of uphill transport for the first time, especially in pilot scale. Both current – voltage (I-V) and constant current (CC) tests were performed under different feed flow rate conditions to evaluate the maximum power density in the steady state.

6.2 Case study

6.2.1 Seawater desalination plant

The Okinawa SW desalination plant was constructed in Chatan-town, Okinawa island, Japan, since early 1996 with approximately 12,000 m^2 land area as shown in Fig. 1. The Okinawa desalination adopted the RO method (spiral wound, polyamide membrane) with its recovery rate of about 40% to make fresh water from SW. The maximum capacity of fresh water production is about 40,000 m^3/day, and therefore, the flow rate of the discharged RO brine is then 60,000m^3/day (total maximum uptake of SW is therefore 100,000m^3/day). Here, there is also an opportunity to access RW from water purification plant in Chatan town neighbor to the desalination plant, and therefore, used as model wastewater and RW for RO brine and SW cases, respectively. Table 1 shows the ion composition of the RW, SW and RO brine preliminary measured by using ion chromatography. Divalent ion (Mg ions) composition for cation are 11%, 13% and 16% in SW, RO brine and RW, respectively. Those (SO_4 ions) for anion are 5%, 5% and 8 % in SW, RO brine and RW, respectively. Therefore, divalent ion composition in RW was slightly higher than those in SW and RO brine, potentially leading us to use the monovalent selective layer with its selective layer facing to RW.

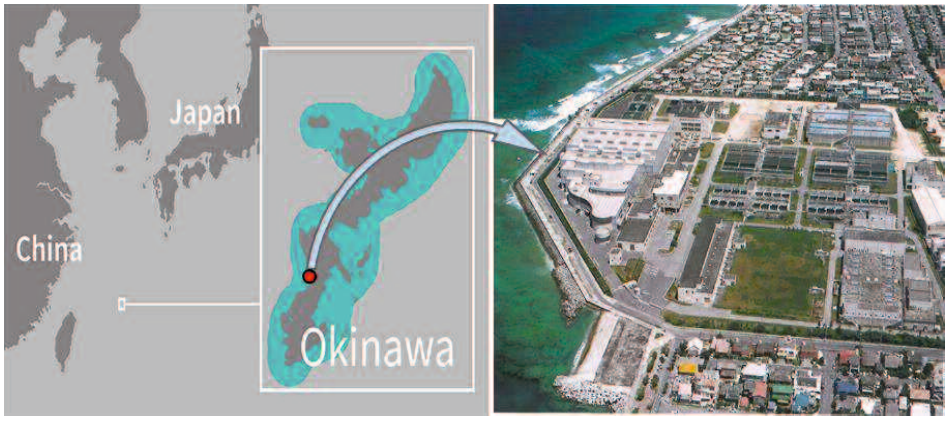

Figure 1. Water desalination plant of Okinawa islands in Chatan town, Japan [32]

Table 1. Ion composition of available solutions in the water desalination unit

Solution	Conductivity [mS/cm]	Na^+	K^+	Mg^{2+}	Ca^{2+}	NO_3^-	Cl^-	SO_4^{2-}
RW [mmol/dm^3]	0.2 ± 0.05	1.24	0.12	0.22	n.a.	0.58	2.82	0.27
SW [mmol/dm^3]	46 ± 1	459	9.70	52	n.a.	n.a.	536	27
RO brine [mmol/dm^3]	75 ± 1	1578	36.80	217	n.a.	n.a.	1660	85

6.2.2 RED pilot plant

6.2.2.1 Feed solution

Natural RW and SW as well as RO brine were used as low concentrate and high concentrate RED feed solutions, respectively, and were connected to the intake lines into RED pilot plant as shown in Fig. 2. Model feed solutions of NaCl aq. were prepared based on ion concentration (not conductivity) of the natural feed solutions. Therefore, the conductivities of the model RO brine (~ 1 mol/dm^3 NaCl) and model SW (~ 0.53 mol/dm^3

NaCl) were fixed to 90 ± 1 mS/cm and 50 ± 1 mS/cm, respectively. Natural RW was always used as the low concentrate feed even in model case. Since we need high temperature feed solutions to minimize the RED stack resistance, all experiments were performed during summer season (August) with the feed solutions temperature around 28-30 °C.

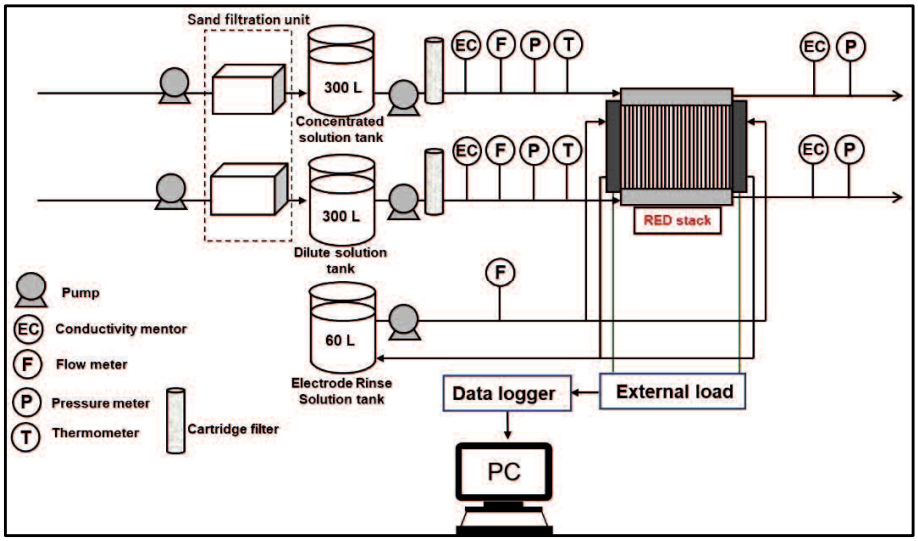

Figure 2. The layout of RED plant.

6.2.2.2 Pre-treatment

All the natural feed solutions were firstly fed into AF-4 type (ZEOLITE Co., Ltd., Japan) sand filtration as pretreatment with 1.26 m^3/h filtration capacity. After pretreatment, the solution were storage into the respective tanks (300 L) before use. In addition, the feeds solutions were also passed a cartridge filter with its effective pore size of 0.45 μm before the RED stack by using two feeding pump (CM1-3, GRUNDFOS Pump Co., Ltd., Japan).

6.2.2.3 A pilot-scale RED stack

A RED stack used in this study composed 299 cell pairs with its total effective membrane area of 179.4 m^2. One side monovalent selective IEMs, CIMS and ACS-8T

(ASTOM. Corp., Japan) as CEM and AEM, respectively, were stacked alternatively in the stack with its selective layer facing to the LCC. Table 2 shows the membrane properties of CIMS and ACS-8T which have measured after purchasing. Two Pt electrodes were used as cathode and anode at the two ends of the stack. Na_2SO_4 solution as the electrolyte solution with its conductivity of 50 ± 2 mS/cm was fed into the RED stack using a magnet drive pump (MX-70VM32, IWAKI CO., Ltd., Japan). The flow rate of the electrolyte solution was flexibly changed, depending on the flow rate of the feeds in order to keep the pressure difference in suitable value. 200 μm woven spacers were used to keep the distance between the membranes equipped with gasket to prevent leakage. The inlet flow rates of the feeds were measured using flow meters (FD-P20, KEYENCE CORPORATION, Japan). Pressure and temperature at the both inlet and outlet were measured using pressure meter (FHXI-200KP-02-V, OPTEX FA Co., Ltd, Japan) and temperature meter (V1-2000-R3/8CF-M3Y, NIHONDENSOKU Co., Ltd, Japan), respectively. The conductivity of both feeds at both inlet and outlet were measured using conductive meters (EC-430, SUNTEX Instruments Co., Ltd., Japan). All of the data were recorded in real time by using a multi-logger system (GT SoftGOT2000, Mitsubishi Electric Corporation, Japan) connecting with a personal computer.

Table 2. Properties IEMs used in this study.

Membrane	Type	Ion exchange capacity [meq/g]	Resistance [Ω.cm^2]	Water content [-]	Thickness [μm]
CIMS	One side monovalent selective	2.3	2.02	0.39	150
ACS-8T	One side monovalent selective	1.9	2.03	0.2-0.3	150

6.3 Experimental procedure

6.3.1 RED performance test

RED stack was tested under both current-voltage (I-V) and constant current (CC) condition under different feed flow rate conditions. Both I-V and CC conditions were set up using a multifunctional DC electronic load (PLZ664WA, KIKUSUI electronics corporation, Japan). In I-V test condition, the current gradually increased from zero by the sequence of 10 mA/s until the generated voltage becomes zero. Whereas, the CC tests were also performed by measuring the power output of the stack under constant current until the power become stable (for at least 30 min). Therefore, the CC test will provide a steady-stated power generation performance under equilibrium of the concentration profile within the pilot-scale RED stack.

6.3.2 Open circuit voltage (OCV)

The maximum voltage of the RED stack at zero current condition is known as open circuit voltage (OCV) which can show the electrochemical potential of the stack for the power production. The actual OCV of the RED stack during all RED tests at the different feed flow rates were also recorded. In addition to actual voltage, the theoretical OCV can be expressed by Nernst equation as follows:

$$OCV_{stack} = N_{cell}.\alpha\ \frac{R.T}{zF}\ln\frac{\gamma_H C_H}{\gamma_L C_L} \quad [1]$$

where N_{cell} and α are number of RED stack cell pairs and the average permselectivity of the CEM and AEM (-), respectively. R is gas constant (8.314 J/mol.K), T is temperature (K), F is Faraday constant (96485 C/mol), z is ionic valance (monovalent = 1, divalent =

2). γ and C are the average ion (Na^+ and Cl^-) activity coefficient (-) and ion concentration (mol/dm^3), respectively. Subscribes L and H refer to low and high concentrated solution, respectively. Here, in order to evaluate the reduction of the actual OCV, the theoretical OCV of the stack was calculated from the solution conditions at the both inlets and outlets under a simple assumption that all ions are NaCl. The detailed calculation methods were shown in supplementary information.

6.3.3 Stack resistance

The internal resistance of RED stack consists of ohmic and non-ohmic resistance (*e.g.*, concentration polarization, change of bulk solution concentration) [4]. The ohmic regime of the RED stack resistance, which called theoretical resistance, contains a sum of the solution compartment and membrane resistances as follows [4]:

$$R_{Ohmic} = N_{cells}(\beta_{sol}(R_H + R_L) + \beta_{mem}(R_{AEM} + R_{CEM})) \quad [2]$$

where N_{cell} is number of cell pairs. R_H and R_L are the resistance of high concentrate and low concentrate compartments, respectively. In addition, R_{AEM} is AEM resistance, R_{CEM} is CEM resistances, β_{sol} is spacer shadow effect on solution compartments, and β_{mem} is spacer shadow effect on membrane resistance [4].

The actual resistance of RED stack containing both ohmic and non-ohmic regime can be obtained from the slop of I-V curves and Ohm's law as follows:

$$E_{stack} = OCV - R_{stack}I \quad [3]$$

where E_{stack} and R_{stack} are voltage and resistance of the RED stack, respectively. However, this stack resistance is based on the lab-scale experiment and can be adopted under an

assumption that the salinity difference is constant. Therefore, although the slope of I-V curve in small-scale stack case mainly expressed the stack resistance, those in large-scale case may not be equal to the stack resistance because salt concentration change within the stack is not negligible unlike small-scale stack case, resulting in the reconsideration about the Eq (3). Therefore, here, we defined the slope of I-V curve in the pilot-scale stack as pseudo stack resistance in order to discuss the resulting stack performance.

6.3.4 Gross power output

The RED stack gross power output, P_{gross}, can be calculated by multiplying stack voltage (E_{stack}) into current (I) as shown in Eq. 4. In addition, the net power (P_{net}) can be calculated by subtraction the pumping energy due to hydraulic losses from P_{gross} as follows:

$$P_{gross} = E_{stack}.I \quad [4]$$

$$P_{net} = P_{gross} - \frac{\Delta p_L Q_L + \Delta p_H Q_H}{\eta_{pump}} \quad [5]$$

where Δp is pressure drop, Q is feed flow rate, and η_{pump} is the pump efficiency (assumed as 85%) Gross power and net power densities ($P_{d,gross}$ and $P_{d,net}$, respectively) can be then calculated by dividing P_{gross} and P_{net} to total membrane effective area (A_{total}) as follows:

$$P_{d,gross} = \frac{P_{gross}}{A_{total}} \quad [6]$$

$$P_{d,net} = \frac{P_{net}}{A_{total}} \quad [7]$$

6.3.5 Energy estimation

The extractive SGE when mixing two solutions with different salinity can be calculated from Gibbs free energy of mixing (SGE) from following equations [30]:

$$(SGE)_i = 2RT(Q_H C_{H,i} Ln\frac{\gamma_{H,i}C_{H,i}}{\gamma_{eq}C_{eq}} + Q_L C_{L,i} Ln\frac{\gamma_{L,i}C_{L,i}}{\gamma_{eq}C_{eq}}) \quad [8]$$

$$C_{eq} = \frac{Q_H C_{H,i} + Q_L C_{L,i}}{Q_H + Q_L} \quad [9]$$

where T (K) is the average temperature of feed solution and C_{eq} is the equilibrium concentration calculated from Eq. 9. Small asterisk, i, means the place (inlet or outlet of the stack). Then, the SGE consumed in the RED stack (ΔSGE_{RED}) can be calculated by subtracting the SGE at outlet (SGE_{out}) from SGE at inlet (SGE_{in}) as follows:

$$\Delta SGE_{RED} = SGE_{in} - SGE_{out} \quad [10]$$

Then, total energy efficiency (η_E) and energy conversion efficiency of the RED stack (η_{RED}) can be calculated as follows:

$$\eta_E = \frac{P_{gross}}{\Delta SGP_{in}} \quad [11]$$

$$\eta_{RED} = \frac{P_{gross}}{\Delta SGP_{RED}} \quad [12]$$

At the maximum power output condition, η_{RED} theoretically becomes 0.5 (= 50%) under a perfect RED process condition. To calculated the SGE and η of the system, we eliminated the divalent ion (we assumed only NaCl included) for simplicity. The calculation details are also shown in the supplemental information.

6.4 Results and discussion

6.4.1 Open circuit voltage (OCV)

Among all RED performance measurements using natural and model feed solutions, respective three numbers of the actual OCV were represented at different flow rate conditions as shown in Fig. 3. The theoretical OCVs calculated for both inlet and outlet conditions between high and low concentrated feed solutions under an assumption that only NaCl presence in feed solutions were also shown in order to compare with experimental data. Since the outlet solutions concentration depended on the flow rate, three numbers of OCV were calculated for outlet between outlet high and low concentrated solutions, whereas one OCV was calculated from the inlet condition. Here, for simplicity, the permselectivity of the membranes was assumed to be 1. The detailed data (The conductivity of the inlet and outlet at zero current condition as well as all OCVs) were also shown in supplemental information. Reasonably in all cases, the actual OCV were increased by increasing the feed flow rates due to increasing the salinity ratio between HCC and LCC even at zero current. The salinity ratio (electrochemical potential) between the high and low concentrate compartments must gradually decreases from the inlet to the outlet of the RED stack due to ion diffusion (ionic current in the stack) from higher to lower concentrate compartments even at the zero current condition. Actually, unfavorable ion diffusion from the higher to the lower concentrate compartments and/or unfavorable water permeation from lower to higher concentrate compartments, are also occurred, resulting in a reduction of OCV from the theoretical values. Therefore, increasing the feed flow rates can diminish the above effects by flushing the fresh solution.

At the highest feed flow rate conditions, the actual OCV of the RED stack using model and natural RO brine/RW as well as SW/RW feed solutions were around 60% and 65% of the theoretical OCV calculated from inlet condition, respectively. This OCV reduction in the actual would be due to ions diffusion as mentioned above. Lower OCV reduction in SW/RW case than RO brine/RW case would because of lower ion (and/or water) diffusions through the membranes because of lower salinity gradient between SW/RW compare with RO brine/RW. In addition, the permselectivity of the IEM also will decrease by increasing the concentration of the feed and leads to co-ions diffusion toward the membrane as well as counter-ions diffusion.

Interestingly, the resulting OCVs were almost same to the theoretical OCV calculated from the outlet condition in all cases. Closing the actual value of OCVs with theoretical outlet OCVs would represent that the above diffusions happened very fast at the begging of the stack when feed solutions flowed into the compartments, and the salinity ratio rapidly and exponentially decreased. Therefore, the electrochemical potential of the whole stack mainly depends on the outlet conditions. In addition, the difference between the OCVs using natural and model feed solutions was around 3% which was significantly lower among the literatures which was around 10-15% [19,23,26–28,33]. this would represent that, facing the monovalent selective layer of membranes into the low concentrate compartment can effectively decrease the uphill transport, and subsequently suppress the OCV reduction.

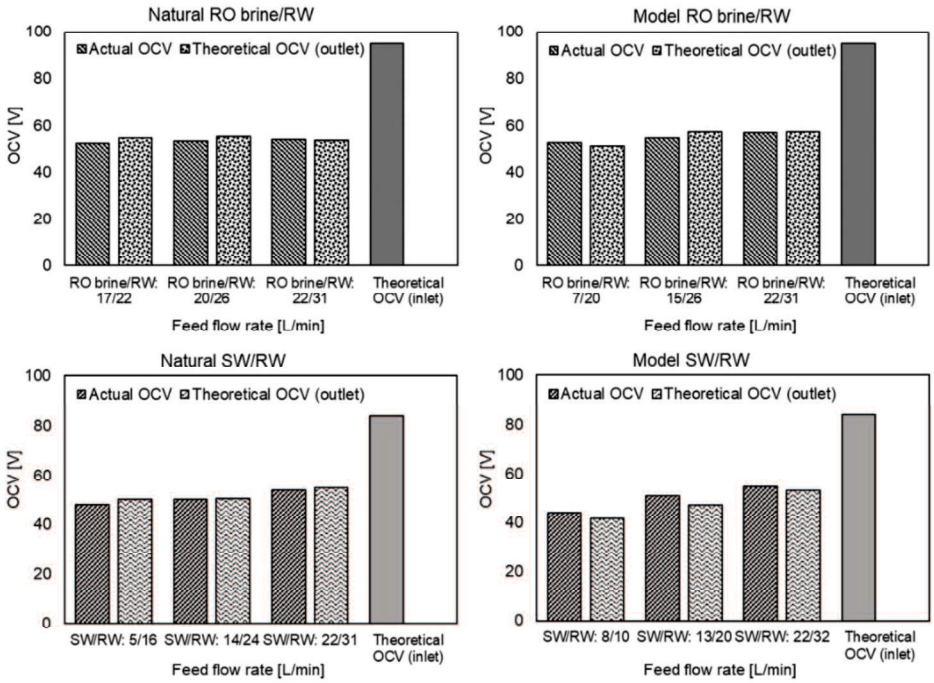

Figure 3. Actual and theoretical OCV using natural and model feed solution.

6.4.2 Stack resistance (Ω)

The pseudo stack resistances estimated from *I-V* curves when using model and natural feed solutions at three different flow rate conditions are shown in Fig. 4. The results indicated that the pseudo stack resistance decreased with increasing the feed flow rate. However, the ohmic resistance of the stack should be increased with increasing the flow rate due to the resistance of the LCC (a major resistance of the stack). In fact, the conductivity of LCC should become lower (higher resistance) by increasing the feed flow rate which leads to increasing the RED stack resistance. This results clearly indicated that the Eq. (3) cannot be directly adopted for the pilot-scale *I-V* data. Actually, because the concentration change within the stack is so large, both OCV and pseudo stack resistance in Eq. (3) will be changed, depending the operating conditions such as current and flow rates.

Therefore, at the lower flow rate condition, the OCV reduction was also influenced on the *I-V* curve and subsequently resulted in the increase of the pseudo stack resistance, especially much lower flow rate condition such as SW/RW = 5/16 case in Fig. 4. The increase of the non-ohmic resistance at the lower flow rate condition is also another potential reason to explain this increase of the pseudo stack resistance. In fact, the effect of concentration polarization as well as the effect of boundary layer on stack resistance would become more considerable at low feed flow rate. Consequently, in all cases, the pseudo stack resistance decreased with increasing the feed flow rate. In addition, since RO brine has higher conductivity than SW, the pseudo stack resistance in RO brine/RW case were about 35-45% lower than that in SW/RW case, respectively.

In order to compare this study with literature, *Tedesco et al*. performed the REAPower project by the RED pilot-scale with 194 m^2 membrane effective area using natural/model concentrated brine (215 mS/cm) and brackish water (0.7-6.5 mS/cm) feed solutions [29]. In the most similar case to our study using model concentrate brine and brackish water (3.5 mS/cm), the stack resistance of 2.3-2.7 Ω were reported at the highest feed flow velocity which was almost similar to our study using model RO brine/RW even with lower feed solutions conductivity. Moreover, in the case of using natural concentrate brine and brackish water (3.5 mS/cm) at highest feed flow rates the RED stack resistance reported with the value of 3.2-3.9 Ω which was also similar to the RED stack resistance in our study using natural RO brine/RW at the highest feed flow rates. Having the same range of the RED stack resistance in this study with even lower conductive feed solution compare with later literature would be due the applying one-side monovalent selective membrane that used in our study. As mentioned, multivalent ions can lead to increase the membrane

resistance due to their higher hydride radius than monovalent ions and their higher charge which make them attach stronger to membrane charged groups in the membrane bulk and so make ions transportation difficult. Therefore, applying monovalent selective membrane in this study seems to be effective in order to reduce the impact of multivalent ions (uphill transport) on the RED stack resistance.

The difference of the pseudo stack resistances using natural and model feed solution in this study were around 35-43 % due to two main reasons. First, the monovalent selective membranes are not perfect and couldn't reject 100 % multivalent ions. Second, the conductivity of model RO brine and SW was higher than those natural types since they made based on NaCl concentration. Therefore, the resistance of model RO brine and SW feed solution were lower than those natural solutions.

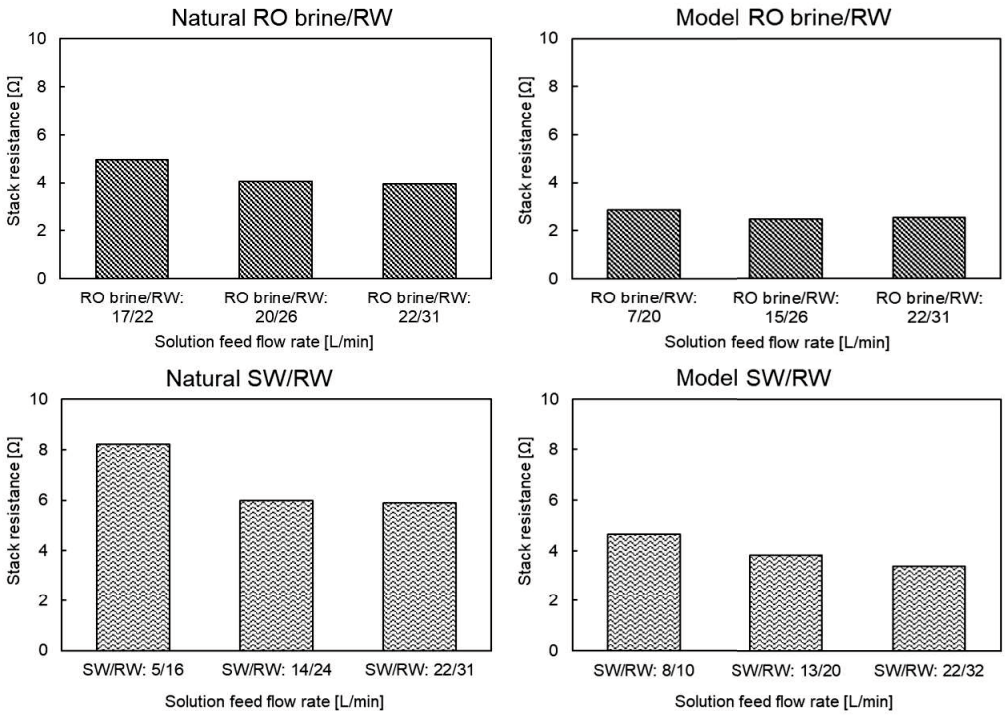

Figure 4. RED stack resistance using natural and model feed solution with different flow rate.

6.4.3 RED performance with natural RO brine and RW

Fig. 5(A) shows the maximum gross power output of the RED stack obtained at different feed flow rate through I-V test condition. Here, the RO brine flow rate was also increased simultaneously when increasing the RW flow rate in order to suppress the hydraulic pressure difference between the HCC and LCC since much excessive hydraulic pressure difference will lead the unfavorable membrane deformation and water leakage. The RW and RO brine flow velocities were increased from 1.25 to 1.73 cm/s (22-31 L/min) and 0.95 to 1.17 cm/s (17-21 L/min), respectively. The maximum respective flow rate conditions are due to the mechanical feeding limitation. The maximum power output increased from 124.42 W (0.69 W/m^2) to 173.2 W (0.96 W/m^2) by increasing the RW flow rate from 22 L/min into 31 L/min as well as increasing the RO brine. To the best of our knowledge, the gross power density of 0.96 W/m^2 is the highest in literatures demonstrating

the pilot-scale RED stack using any type of natural feed solutions (0.38-0.84 W/m^2) [29,30,34]. This would be due to applying one side monovalent selective membrane which applied for the first time in pilot-scale RED stack and significantly decreased the impact of uphill transport of divalent ions from low concentrate compartment into high concentrate compartment [24]. Actually, the concentration of divalent ions in low concentrate compartment is very low and so the selective layer could effectively play as a barrier wall against uphill transport ion divalent ions absorption on membrane surface.

The maximum net power output of the RED stack was then calculated by subtracting the pumping energy which related to the feed flow rates, pressure drop, and pump efficiency from gross power output as shown in Fig. 5(B). The all recorded pressure drops of the RED stack at different conditions are shown in supplementary information. Reasonably, the pumping energy consumption increased with increasing the feed flow rate; hence, although increasing flow rate allows the increase of the maximum power output, optimum flow rate condition must exist to get the maximum net power output of the RED system. In this case, although the pumping energy increased from 15 W into 27.96 W by increasing the feed flow rates, but the maximum net power of 143.64 W (0.80 W/cm^2) was still obtained at the highest feed flow rate condition. To the best of our knowledge, the obtained net power output of about 140 W is the highest value especially when using natural feed solution in a pilot scale compare with other literatures with about 75 W [29].

In addition, the RED tests in CC condition were also performed in order to estimate the steady stated power output performance under the current of about 6-7 as shown in Fig. 6. Here, due to the limitation of the feeding amount of the natural RO brine solution, just two feed flow rate conditions were adopted. the obtained power output in CC

mode was slightly lower than those in I-V mode. Therefore, especially in the case of large-stack, equilibrium of the concentration profile within the stack changing by the ionic current is important and influenced on the resulting power output of the stack. As such reason, lower reduction of the power output in CC mode at the higher flow rate condition (10.0%) was observed even at the higher current condition than those at lower flow rate condition (12.9%) as shown in Figs. 6(A) and (B). The difference through the RED stack performance in CC and I-V condition would have two more main reasons. First, although both natural feed solution passes two pre-treatment steps, but all organic materials and foulants could not perfectly removed from solution which has some impact on CC condition. Secondly, natural feed solution contains multivalent ions as well as monovalent ions which boosted the effect of concentration polarization on the membrane surface due to higher charge.

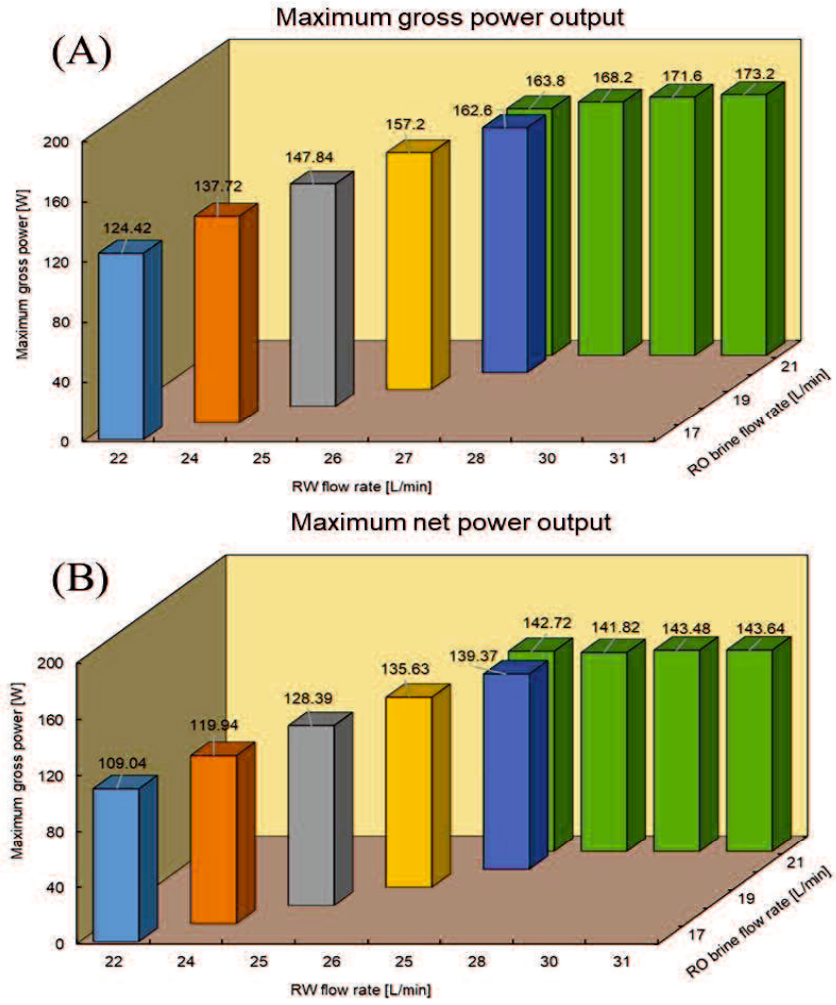

Figure 5. The RED stack performance using natural RO brine/RW feed solutions. A: the maximum gross power output, B: the maximum net power output

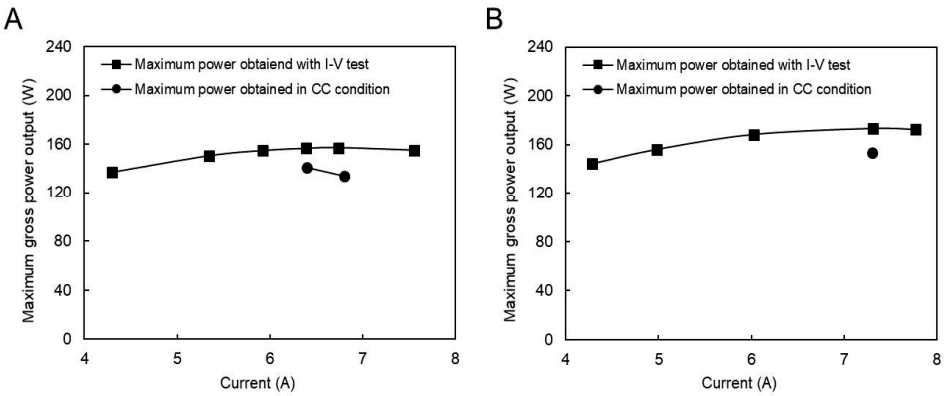

Figure 6. Constant current measurement with natural RO brine and RW feed solution, A: RO brine/RW; 26/20 (L/min), B: RO brine/RW; 31/22 (L/min).

6.4.4 RED performance with model RO brine and RW

RED tests with model RO brine and RW were also performed in order to investigate the effect of divalent ions on the performance of RED stack. Since this stack equipped with sand pre-filtration and cartridge filter, we assumed that most of the natural organic materials which has a significant effect on RED performance was removed from feed solutions [23]. In this case, except few tests at high feed flow rate to obtain the maximum amount of power output, most of the measurements were performed using low feed flow rates due to the limitation of the volume of model solution tank as shown in Fig. 7. As expected, the RED power output enhanced by increasing the feed low rate. For instance, the maximum power output increase 5.5 W by increasing 1 L/min of RW flow rate at constant RO brine flow rate. The maximum gross power density reached to 1.46 W/m^2 (263 W) which is a significant amount compare with other studies by considering the salinity ratio of feed solutions. For instance, *Tedesco et al*, reported the maximum gross power density of 1.65 W/m^2 using saline water (0.9 mS/cm) and concentrated brine (215

mS/cm) which has almost 1.4 times higher salinity ratio than our study. In addition, the maximum obtained power output using model RO brine and RW became around 35 % higher than same condition with the natural feed solutions. The impact of divalent ions in natural feed solution which increase the membrane resistance as well as higher conductivity of model RO brine (90 mS/cm) than natural RO brine (75 mS/cm) would be the main reasons for obtaining higher power output. The pumping energy increased from 3.7 W into 31 W by increasing the feed flow rate except for the highest feed flow rate (RO brine/RW: 22/31 L/min) which consumed 41.4 W for as the pumping energy. This later would be due to the significant increase in pressure drop of around 80 kPa at both high and low concentrate compartments. As mentioned, all of the pressure drop date has shown in supplementary information. Therefore, the maximum net power of 232.39 W (~1.29 W/m^2) was obtained using RO brine/RW: 15/26 L/min due to the trade-off between the effect of feed flow rate on gross power and pumping energy.

The RED test in CC condition was also performed in four different flow rate conditions as shown in Fig. 8. In this case, interestingly, the difference between the performances in I-V test and CC test became much smaller (0.5-3.0%). Therefore, the further reduction in CC test from I-V test when using natural solution is mainly due to the presence of divalent ions. In fact, the presence of divalent ions in natural feed solution could be multiplier factor in increasing the concentration polarization since they have higher charge and so their concentration and respective charge become higher around membrane surface. In addition, the presence of organic component in model feed solutions which prepared with tap water and NaCl is negligible compare with natural feed solution. In fact, the pre-treatment steps for natural feed solution cannot perfectly remove all organic

materials. Therefore, much less fouling phenomena during CC test using model feed solutions would be another important parameter that explain the less difference of RED performance with I-V and CC condition.

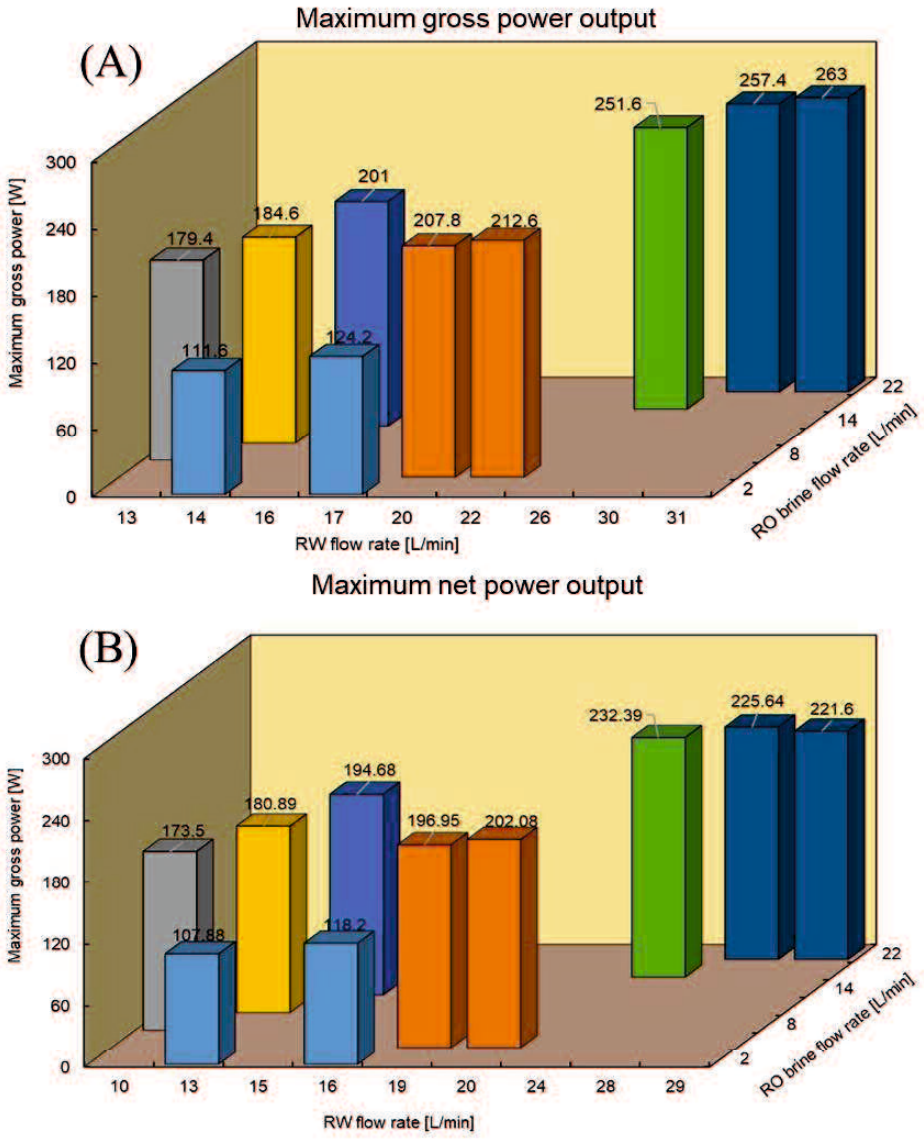

Figure 7. The RED stack performance using model RO brine/RW feed solutions. A: The maximum gross power output, B: The maximum net power output

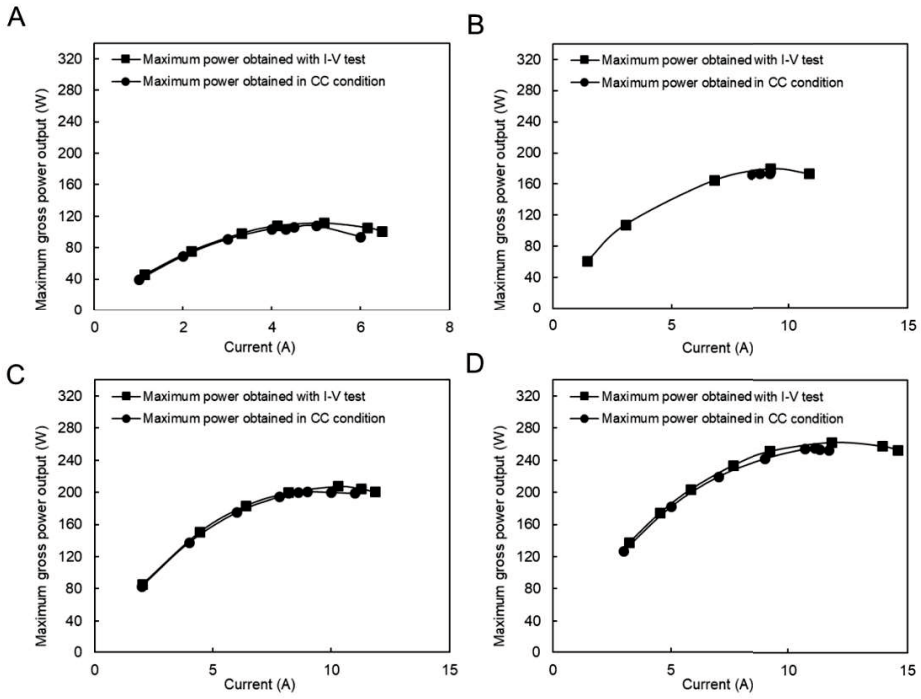

Figure 8. Constant current measurement with model RO brine and RW feed solution, A: RO brine/RW; 2/14 (L/min), B: RO brine/RW; 8/13 (L/min), C: RO brine/RW; 7/20 (L/min), D: RO brine/RW; 22/31 (L/min)

6.4.5 RED performance with natural SW and RW

RED tests using SW and RW have performed due to the availability of seawater close to the project place and in order to comparing the performance The RED pilot-scale using RO brine/RW as the feed solutions. The RED stack performance using different flow rate of RW and SW are shown in Fig. 9. The maximum power output increased from 68.6 W (0.38 W/m^2) into 110.6 W (0.62 W/m^2) by increasing the both SW and RW feed solutions flow rate. In this case, the maximum obtained gross power density was higher than even the RED performance using natural SW/RW in lab-scale which was around 0.2-0.43 W/m^2 [19,23,24]. The RED power output increased faster by increasing the RW flow

rate than increasing the SW flow rate which would be due to the more significant effect of LCC conductivity than HCC. In fact, increasing the RW flow rate keep the conductivity of low concentrate solution in lower value by flushing fresh feed solution in LCC and so keep salinity ratio higher. The maximum obtained power decreased around 35% compare with the RED performance using natural RO brine/RW due to decreasing the salinity ratio between the feed solutions combination.

Same as before, the pumping energy consuming enhanced by increasing the feed flow rate from 4.7 W into 30.7 W which was unexpectedly slightly higher than that in the same condition using natural RO brine/ RW feed solutions. This would be because of the higher natural organic materials as well as foulants that would be exist in SW compare with RO brine. Although RO brine has higher concentration than SW and supposed to show more pressure drop in RED stack channel, but in this study, it has passed three times pre-treatment and filtration steps before using in RED process. These steps include pre-treatment before fed into RO process, during RO process by membrane, and finally sand and cartridge filtration before RED process while the applied SW in RED process just passed sand and cartridge filtration before RED process. Therefore, the amount of natural organic materials and foulants in SW must be higher than that in RO brine and so make more pressure drop and fouling. Among the trade of between gross power output and pumping energy, the maximum net power was obtained using SW/RW: 14/24 L/min with the value of 91.5 W (0.51 W/m^2).

In addition, same with the previous measurements, RED tests in CC condition have performed in 6 feed flow rates condition as shown in Fig. 10. The difference between maximum power obtained by I-V measurement compare with maximum power obtained

in CC condition decreased from 31% (Fig. 10A) into 10% (Fig. 10F) by increasing the feed flow rates. Aa mentioned before, this difference partially would be due to reaching the concentration equilibrium in CC condition and decreasing the respective salinity ratio, OCV, and power generation. The rest of reduction is mainly based on concentration polarization and boundary layer which decrease in high feed flow rate. In addition, the average amount of this difference was higher than that when using natural RO brine and RW as feed solution due to the more filtration and pre-treatment steps on RO brine than SW as mentioned.

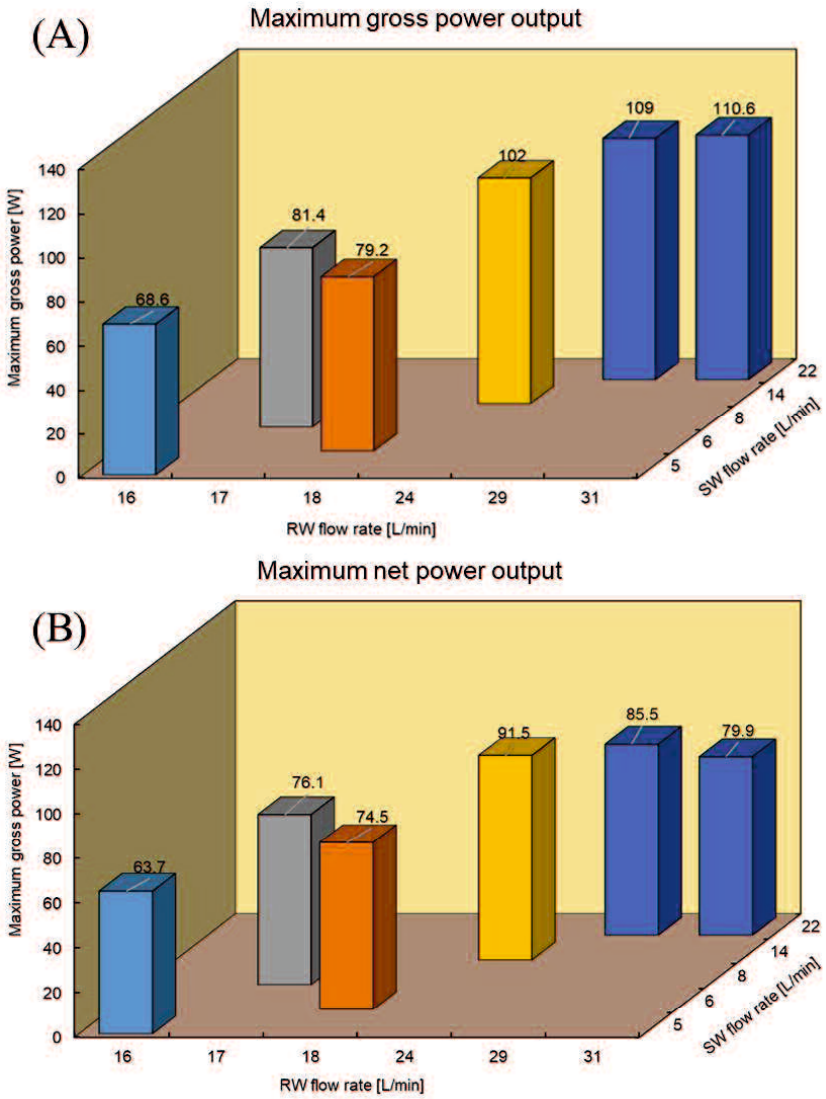

Figure 9. The RED stack performance using natural SW/RW feed solutions. A: The maximum gross power output, B: The maximum net power output

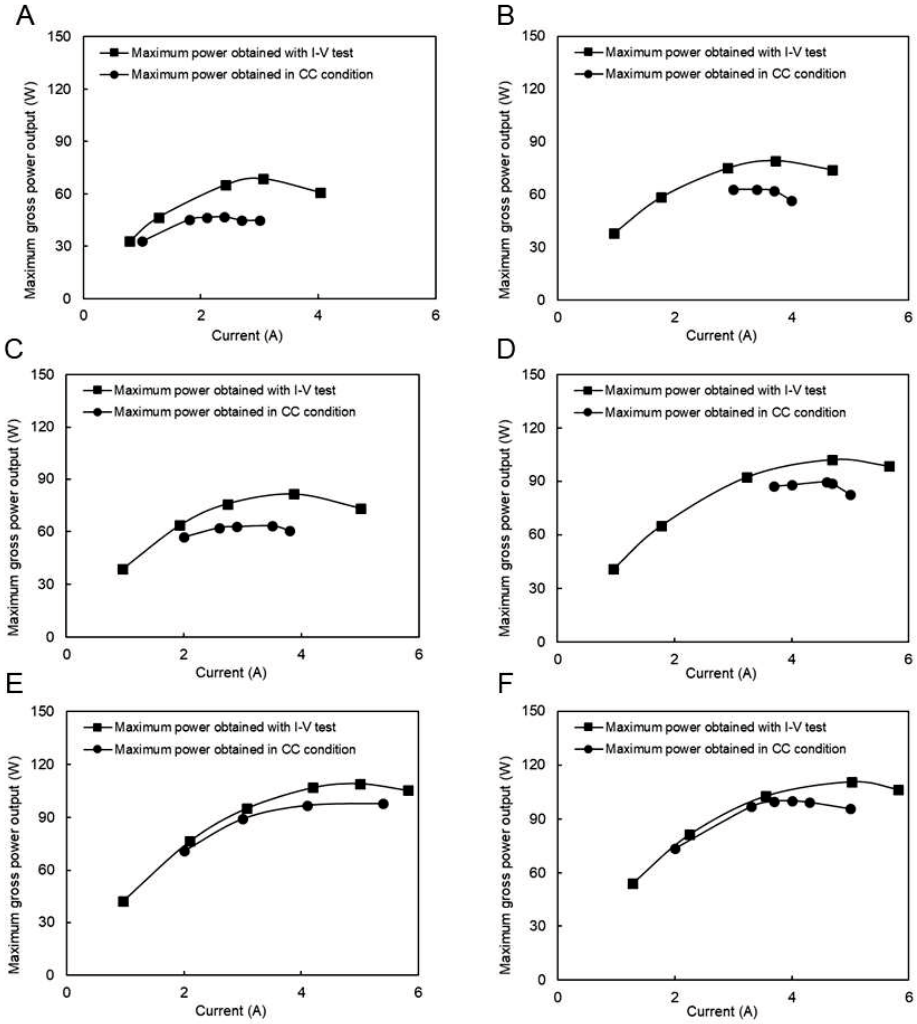

Figure 10. Constant current measurement with natural RO brine and RW feed solution, A: SW/RW; 5/16 (L/min), B: SW/RW; 6/18 (L/min), C: SW/RW; 8/17 (L/min), D: SW/RW; 14/24 (L/min), E: SW/RW; 22/29 (L/min), F: SW/RW; 22/31 (L/min).

6.4.6 RED performance with model SW and RW

The RED tests with model SW and RW were performed at three different feed flow rates during I-V test as shown in Fig. 11. The maximum power output reach to 174.2 W (0.91 W/m^2) which is 37% higher than that with natural SW and RW feed solution by increasing both feeds flow rate. This difference was higher than the difference of the RED

performance using model and natural RO brine/RW as the feed solutions which was around 35%. As mentioned, this would be due to three times treatment of RO brine while it was just one time for natural sea water. In addition, the pumping energy was an expected values of 4.8 W and 13.4 W using SW/RW: 8/10 and 13/20 L/min feed flow rate, while it significantly increased into 44.4 W at the highest feed flow rate condition (SW/RW: 21/29 L/min). Same jumping in pumping energy was also observed using model RO brine/RW: 22/32 L/min feed solution. it seems this feed flow rates are critical flow rate for this stack which caused high amount of pressure drop. By subtraction the pumping energy from the RED stack maximum gross power at different feed flow rates, the maximum net power of have obtained. Although the pumping energy significantly increased at the highest feed flow rate, but the maximum net power output of 129.8 W/m^2 still obtained at this condition.

In addition, Fig. 12A-C shows the RED power output in CC condition using model SW /RW at the same flowrate of RED tests during I-V tests. In all cases, the maximum power obtained in CC condition was closed to the maximum power obtained by I-V tests. The difference in maximum power between I-V test and CC condition decreased by increasing the flowrate from 2.7% into 10%. These values were much lower than the same situation with natural SW and RW which would be due the presence of divalent ions as well as natural organic material and foulants in natural feed solutions as discussed before.

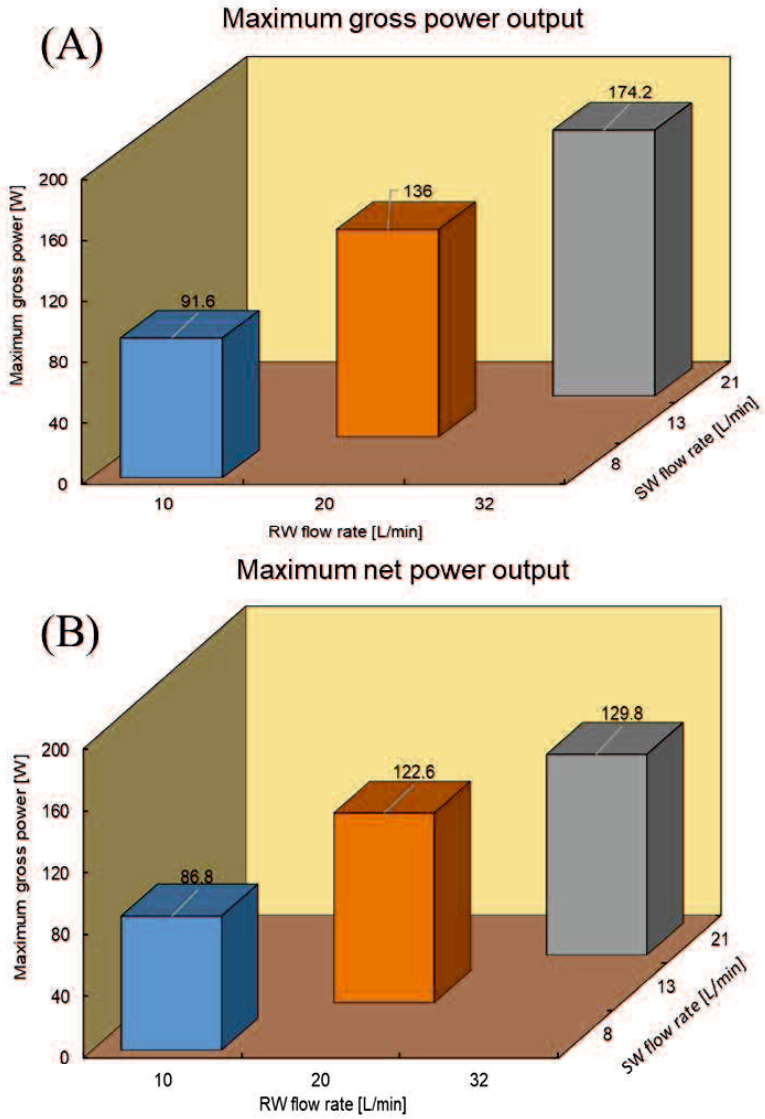

Figure 11. The RED stack performance using model SW/RW feed solutions. A: the maximum gross power output, B: the maximum net power output

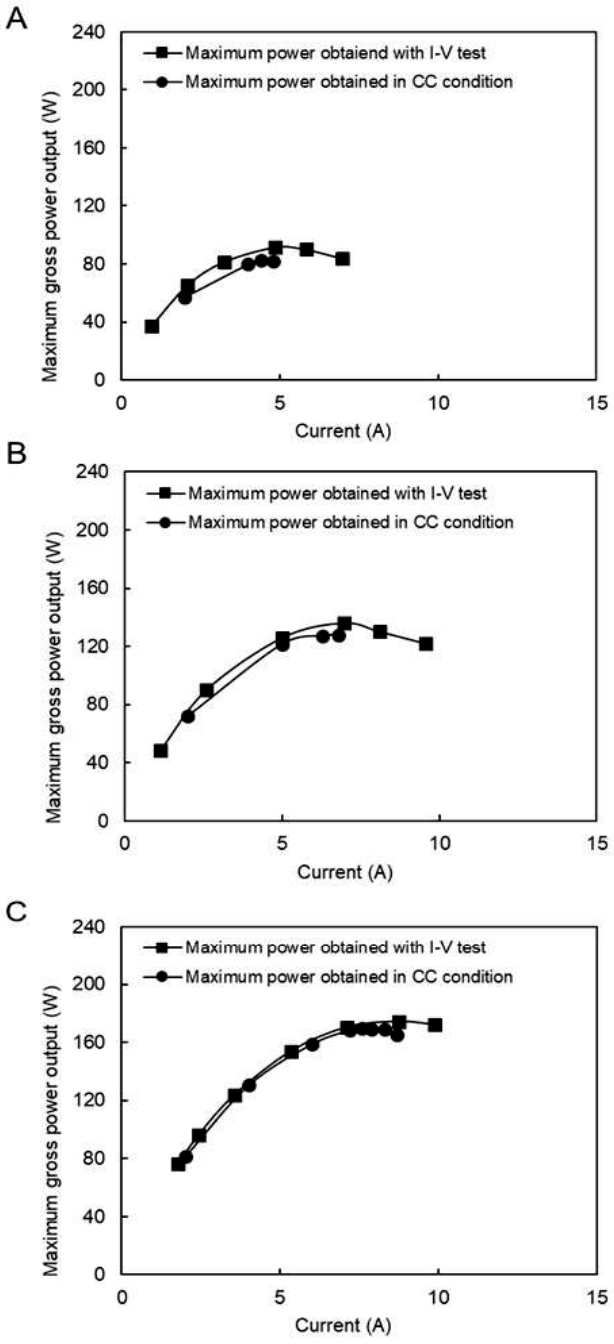

Figure 12. Constant current measurement with model RO brine and RW feed solution A: SW/RW; 8/10 (L/min), B: SW/RW; 13/20 (L/min), C: SW/RW; 21/32 (L/min).

6.4.7 SGE and energy efficiency

The SGE between inlet and outlet of RED feed solution in maximum energy production (reach equilibrium) condition was calculated using model RO brine/RW and SW/RW at the highest and lowest feed flowrates situation as shown in Fig.13. Generally, the energy efficiency of RED stack increased by decreasing the feed flow rate due to having more residence time of feed solutions in the RED stack compartments and respective more ion transportation. In the case of using high feed flow rate condition, around 5% higher energy efficiency was obtained using the SW/RW feed solutions combination in comparison with applying the RO brine/RW feed solutions. Actually, higher salinity ratio and concentration of RO brine/RW feed combination as well as lower changing of salinity ratio at higher feed flow rate condition contributed to the more reduction in membrane permselectivity using this feed solutions compare with SW/RW and respective lower energy efficiency. In addition, the energy efficiency for both type of feed solutions reasonably increased into the same value around 30% by decreasing the feed flow rates since solution have more time for ion transportation. As mentioned, salinity gradient through feed solutions and membrane permselectivity are two important parameters that have significant effect on the amount of ion transportation between the compartments of RED stack per time. Higher salinity gradient as well as membrane permselectivity would make ion transportation faster. In this case (low flow rate), RO brine/RW feed combination have higher salinity gradient as well as lower membrane permselectivity which is vice versa in the case of SW/RW feed solution. Therefore, it seems a trade-off happened through salinity gradient and permselectivity of membrane at low flow rate condition and so the efficiency became almost in the same range.

The amount of gross power has also shown in Fig. 13 to compare the produced ΔSGE_{RED} with the obtained power which has showed by RED efficiency (η_{RED}). In fact, the difference between gross power output with SGE_{RED} would be due to the energy wasting by resistance and heat. The obtained η_{RED} was around 40% at high feed flow rate which increased into 55% by decreasing the flow rate and increasing the respective energy efficiency. This means that from 60% to 45% of SGE_{RED} wasted by decreasing the temperature. It is worth noting that, although the obtained ΔSGE_{RED} stack using RO brine/RW were around 1.7-2 times higher than that using SW/RW, but at the same time the wasting energy of the RED stack using RO brine/RW was also increased with the same ratio.

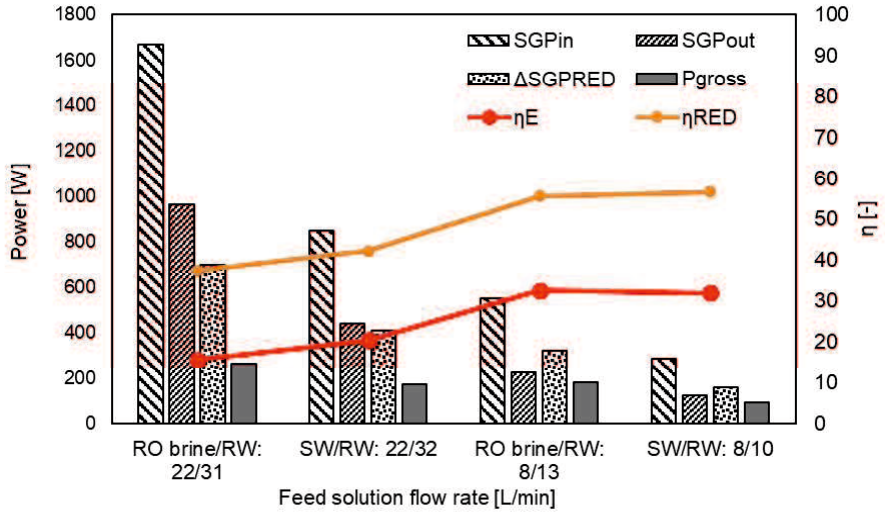

Figure 13. SGE efficiency of RED stack using model feed solution

6.4.8 Available energy in Okinawa water desalination plant

Scaling up the RED process into pilot can be the effective step for commercialization this process. However, commercialization this process should perform in a place with

economic justification. Therefore, by considering the results of the pilot-scale experiments, we could have an appropriate estimation whether improving the RED process into commercial scale or not. In this study, the sea water desalination plant in Okinawa, Japan, has 60,000 m^3/day RO brine production capacity. By considering the maximum power production condition (natural RO brine/RW: 22/31) and pumping energy, around 437KW/day power can be produce. To make it more sense, we need almost 900 m^2 of solar panel with 18.7% efficiency to produce this amount of energy. However, solar panel affect by whether condition (sunny or cloudy) and have limitation in energy production (day and night) which make it unstable in energy production. In addition, using RO brine, which purge into sea or ocean, in RED process could also have one more environmental issue. In fact, RO brine has much higher concentration that sea water and could change the ecosystem of the purging area in the sea or ocean. Therefore, applying RO brine in RED process would leads to reducing the concentration of RO brine by mixing with river water or waste water.

6.5 Conclusion

The power generation performance of a pilot-scale RED stack called RED stack and located in seawater desalination process by RO process presented in this study. The RED stack consisted of 299 cell pairs one side monovalent selective membrane with the selective layer face into low concentrate compartment and totally 179.4 m^2 membrane effective area. Seawater (SW) as well as RO brine (concentrated seawater) which supplied from desalination plant were used as concentrate feed solution. River water (RW) water also considered as low concentered feed solution. The maximum gross power output of

171.6 W (0.96 W/m^2) and 263 W (1.47 W/m^2) were generated using natural and model RO brine/RW feed solution, respectively. The power generation decreased around 34 % using natural RO brine/RW feed solution compare with model feed solution due to the presence of divalent ions in natural solution. In addition, RED stack produced the maximum gross power of 110.6 W (0.63 W/m^2) and 174.2 W (0.99 W/m^2) using natural and model SW/RW feed solution where the difference of the RED stack performance was around 36 % because of the presence of multivalent ions in natural feed solution. The RED performance difference in both cases of using natural and model feed solution were observed lower than literature due to applying one side monovalent selective membrane which diminished the uphill transport. In addition, RED performance was evaluated in constant current condition. In the case of applying model feed solution, the difference of RED stack performance between current-voltage test and constant current condition was low, while this became higher when using natural feed solution. This would be due to the more polarization and fouling of natural feed solution due to natural organic materials

The sweater desalination plant can produce the significant amount of 60,000 m^3 RO brine during 24 hours. Therefore, 437 kW/day power would be available to generate using RO brine/RW feed solution by considering the net power output. 900 m^2 of solar panel with 18.7% efficiency would be needed to produce this amount of energy in 24 hours stable production which is not possible.

6.6 References

[1] E. Güler, W. van Baak, M. Saakes, K. Nijmeijer, Monovalent-ion-selective membranes for reverse electrodialysis, J. Memb. Sci. 455 (2014) 254–270. doi:10.1016/j.memsci.2013.12.054.

[2] R. Long, B. Li, Z. Liu, W. Liu, Performance analysis of reverse electrodialysis stacks: channel geometry and flow rate optimization, Energy. 158 (2018) 427–436. doi:10.1016/j.energy.2018.06.067.

[3] H. Kim, Y.E. Kim, N.J. Jeong, K.S. Hwang, J.H. Han, J.Y. Nam, E. Jwa, S.C. Nam, S.Y. Park, Y. Il Yoon, C.S. Kim, Innovative reverse-electrodialysis power generation system for carbon capture and utilization, J. CO2 Util. 20 (2017) 312–317. doi:10.1016/j.jcou.2017.05.025.

[4] S. Mehdizadeh, M. Yasukawa, T. Abo, Y. Kakihana, M. Higa, Effect of spacer geometry on membrane and solution compartment resistances in reverse electrodialysis, J. Memb. Sci. 572 (2019) 271–280. doi:10.1016/j.memsci.2018.09.051.

[5] R.E. Pattle, Production of electric power by mixing fresh and salt water in the hydroelectric pile, Nature. 174.4431 (1954) 660.

[6] B. Zhang, H. Gao, Y. Chen, Enhanced ionic conductivity and power generation using ion-exchange resin beads in a reverse-electrodialysis stack, Environ. Sci. Technol. 49 (2015) 14717–14724. doi:10.1021/acs.est.5b03864.

[7] D.A. Vermaas, M. Saakes, K. Nijmeijer, Doubled power density from salinity gradients at reduced intermembrane distance, Environ. Sci. Technol. 45 (2011) 7089–7095. doi:10.1021/es2012758.

[8] X. Lin, E. Shamsaei, B. Kong, J.Z. Liu, Y. Hu, T. Xu, H. Wang, Porous diffusion dialysis membranes for rapid acid recovery, J. Memb. Sci. 502 (2016) 76–83. doi:10.1016/j.memsci.2015.12.027.

[9] T. Takahashi, M. Yasukawa, H. Matsuyama, Highly condensed polyvinyl chloride latex production by forward osmosis: Performance and characteristics, J. Memb. Sci. 514 (2016) 547–555. doi:10.1016/j.memsci.2016.04.012.

[10] L. Karimi, A. Ghassemi, H. Zamani Sabzi, Quantitative studies of electrodialysis performance, Desalination. 445 (2018) 159–169. doi:10.1016/j.desal.2018.07.034.

[11] M. Higa, S. Feng, N. Endo, Y. Kakihana, Characteristics and direct methanol fuel cell performance of polymer electrolyte membranes prepared from poly(vinyl alcohol-b-styrene sulfonic acid), Electrochim. Acta. 153 (2015) 83–89. doi:10.1016/j.electacta.2014.11.155.

[12] R. Long, B. Li, Z. Liu, W. Liu, Reverse electrodialysis: Modelling and performance analysis based on multi-objective optimization, Energy. 151 (2018) 1–10. doi:10.1016/j.energy.2018.03.003.

[13] K. Kwon, J. Han, B.H. Park, Y. Shin, D. Kim, Brine recovery using reverse electrodialysis in membrane-based desalination processes, Desalination. 362 (2015) 1–10. doi:10.1016/j.desal.2015.01.047.

[14] Y. Mei, C.Y. Tang, Recent developments and future perspectives of reverse electrodialysis technology: A review, Desalination. 425 (2017) 156–174. doi:10.1016/j.desal.2017.10.021.

[15] S. Pawlowski, J.G. Crespo, S. Velizarov, Pressure drop in reverse electrodialysis: Experimental and modeling studies for stacks with variable number of cell pairs, J. Memb. Sci. 462 (2014) 96–111. doi:10.1016/j.memsci.2014.03.020.

[16] X. Tong, B. Zhang, Y. Chen, Fouling resistant nanocomposite cation exchange membrane with enhanced power generation for reverse electrodialysis, J. Memb. Sci. 516 (2016) 162–171. doi:10.1016/j.memsci.2016.05.060.

[17] X. Zhu, W. He, B.E. Logan, Influence of solution concentration and salt types on the performance of reverse electrodialysis cells, J. Memb. Sci. 494 (2015) 154–160. doi:10.1016/j.memsci.2015.07.053.

[18] M. Tedesco, E. Brauns, A. Cipollina, G. Micale, P. Modica, G. Russo, J. Helsen, Reverse electrodialysis with saline waters and concentrated brines: a laboratory investigation towards technology scale-up, J. Memb. Sci. 492 (2015) 9–20. doi:10.1016/j.memsci.2015.05.020.

[19] A.H. Avci, P. Sarkar, R.A. Tufa, D. Messana, P. Argurio, E. Fontananova, G. Di Profio, E. Curcio, Effect of Mg^{2+}ions on energy generation by Reverse Electrodialysis, J. Memb. Sci. 520 (2016) 499–506. doi:10.1016/j.memsci.2016.08.007.

[20] M. Turek, B. Bandura, Renewable energy by reverse electrodialysis, Desalination. 205 (2007) 67–74. doi:10.1016/j.desal.2006.04.041.

[21] M. Turek, B. Bandura, P. Dydo, Power production from coal-mine brine utilizing reversed electrodialysis, Desalination. 221 (2008) 462–466. doi:10.1016/j.desal.2007.01.106.

[22] J. Veerman, M. Saakes, S.J. Metz, G.J. Harmsen, Reverse electrodialysis: performance of a stack with 50 cells on the mixing of sea and river water, J. Memb. Sci. 327 (2009) 136–144. doi:10.1016/j.memsci.2008.11.015.

[23] R.S. Kingsbury, F. Liu, S. Zhu, C. Boggs, M.D. Armstrong, D.F. Call, O. Coronell, Impact of natural organic matter and inorganic solutes on energy recovery from five real salinity gradients using reverse electrodialysis, J. Memb. Sci. 541 (2017) 621–632. doi:10.1016/j.memsci.2017.07.038.

[24] J. Moreno, V. Díez, M. Saakes, K. Nijmeijer, Mitigation of the effects of multivalent ion transport in reverse electrodialysis, J. Memb. Sci. 550 (2018) 155–162. doi:10.1016/j.memsci.2017.12.069.

[25] Z. Y. Guo, Z. Y. Ji, Y. G. Zhang, F. J. Yang, J. Liu, Y. Y. Zhao, J. S. Yuan, Effect of ions (K^+, Mg^{2+}, Ca^{2+} and SO_4^{2-}) and temperature on energy generation performance of reverse electrodialysis stack, Electrochim. Acta. 290 (2018) 282–290. doi:10.1016/j.electacta.2018.09.015.

[26] D.A. Vermaas, J. Veerman, M. Saakes, K. Nijmeijer, Influence of multivalent ions on renewable energy generation in reverse electrodialysis, Energy Environ. Sci. 7 (2014) 1434–1445. doi:10.1039/c3ee43501f.

[27] J.W. Post, H.V.M. Hamelers, C.J.N. Buisman, Influence of multivalent ions on power production from mixing salt and fresh water with a reverse electrodialysis system, J. Memb. Sci. 330 (2009) 65–72. doi:10.1016/j.memsci.2008.12.042.

[28] T. Rijnaarts, E. Huerta, W. van Baak, K. Nijmeijer, Effect of divalent cations on RED performance and cation exchange membrane selection to enhance power sensities, Environ. Sci. Technol. 51 (2017) 13028–13035. doi:10.1021/acs.est.7b03858.

[29] M. Tedesco, A. Cipollina, A. Tamburini, G. Micale, Towards 1 kW power production in a reverse electrodialysis pilot plant with saline waters and concentrated brines, J. Memb. Sci. 522 (2017) 226–236. doi:10.1016/j.memsci.2016.09.015.

[30] M. Tedesco, C. Scalici, D. Vaccari, A. Cipollina, A. Tamburini, G. Micale, Performance of the first reverse electrodialysis pilot plant for power production from saline waters and concentrated brines, J. Memb. Sci. 500 (2016) 33–45. doi:10.1016/j.memsci.2015.10.057.

[31] Y. Mei, C.Y. Tang, Co-locating reverse electrodialysis with reverse osmosis desalination: Synergies and implications, J. Memb. Sci. 539 (2017) 305–312. doi:10.1016/j.memsci.2017.06.014.

[32] Seawater desalination plant, Enterp. Bur. Okinawa Prefect. (2004).

[33] V.A. Online, R.A. Tufa, E. Curcio, W. Van Baak, J. Veerman, S. Grasman, E. Fontananova, Potential of brackish water and brine for energy generation by salinity gradient power-reverse electrodialysis (SGP-RE), RSC Adv. 4 (2014) 42617–42623. doi:10.1039/c4ra05968a.

[34] J. Nam, K. Hwang, H. Kim, H. Jeong, H. Kim, E. Jwa, S. Yang, J. Choi, C. Kim, J. Han, N. Jeong, Assessing the behavior of the feed-water constituents of a pilot-scale 1000-cell-pair reverse electrodialysis with seawater and municipal wastewater ef fl uent, Water Res. 148 (2019) 261–271. doi:10.1016/j.watres.2018.10.054.

[35] N.Y. Yip, M. Elimelech, Thermodynamic and energy efficiency analysis of power generation from natural salinity gradients by pressure retarded osmosis, Environ. Sci. Technol. 46 (2012) 5230–5239. doi:10.1021/es300060m.

6.7 Supplementary information

6.7.1 Appendix A. Ion activity and solution concentration estimation

The ion activity coefficient of NaCl (γ_{NaCl}) solution at different concentration were calculated using the following equations [35]:

(i) $0.000 < C_{NaCl} \leq 0.024$ $\gamma_{NaCl} = 257.97\ C_{NaCl}^2 - 11.368\ C_{NaCl} + 0.9864$ [A.1]

(ii) $0.0241 < C_{NaCl} \leq 0.190$ $\gamma_{NaCl} = 4.4627\ C_{NaCl}^2 - 1.6864\ C_{NaCl} + 0.8947$ [A-2]

(iii) $0.190 < C_{NaCl}$ $\gamma_{NaCl} = 0.2461\ C_{NaCl}^2 - 0.3472\ C_{NaCl} + 0.8947$ [A-3]

In addition, the equivalent conductivity of different NaCl solution can be estimate using following equations [35]:

(i) $0.000 < C_{NaCl} \leq 0.00856$, $0 < k \leq 1.0295$

$k = 3.9485\ C_{NaCl}^2 - 119.94\ C_{NaCl} + 0.0026$ [A.4]

(ii) $0.00856 < C_{NaCl} \leq 0.172844$, $1.029576 < k \leq 22.720034$

$$k = 85.827\ C_{NaCl}^2 - 116.6\ C_{NaCl} + 0.0113 \quad \text{[A-5]}$$

(iii) 0.190<C_{NaCl}, 22.720034< k

$$k = -15.857\ C_{NaCl}^2 - 104.13\ C_{NaCl} - 0.542 \quad \text{[A-6]}$$

6.7.2 Appendix B. The conductivity of the inlet and outlet

The conductivity of the inlet and outlet solutions in all feed flow rates conditions have shown in Fig. B1-B4. These data were considered in order to calculation the theoretical OCV and leakage.

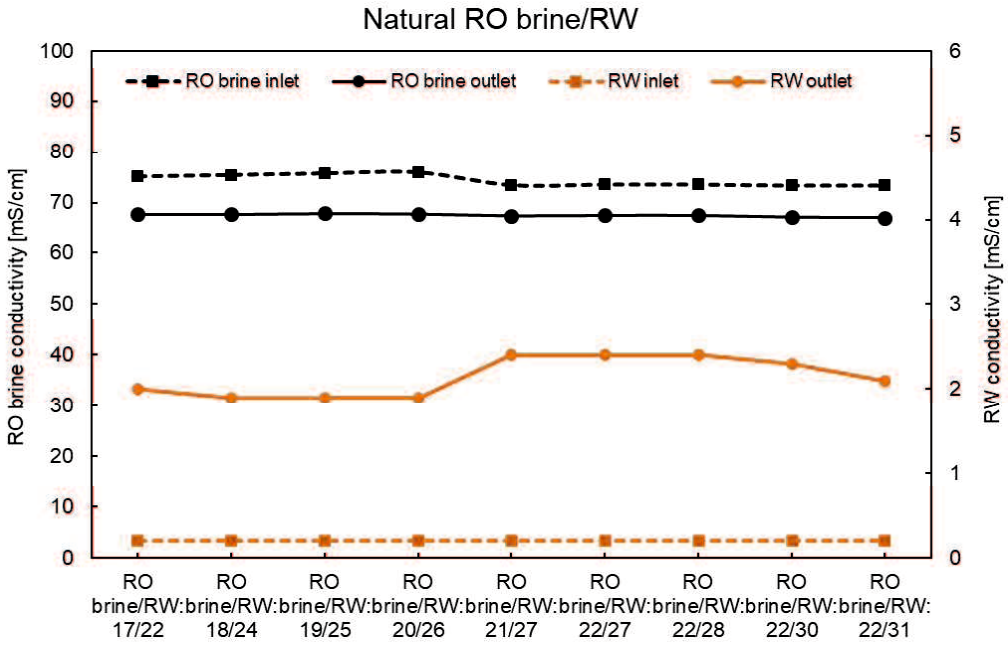

Fig. B1. The conductivity of inlet and outlet solution using natural RO brine/RW at zero current

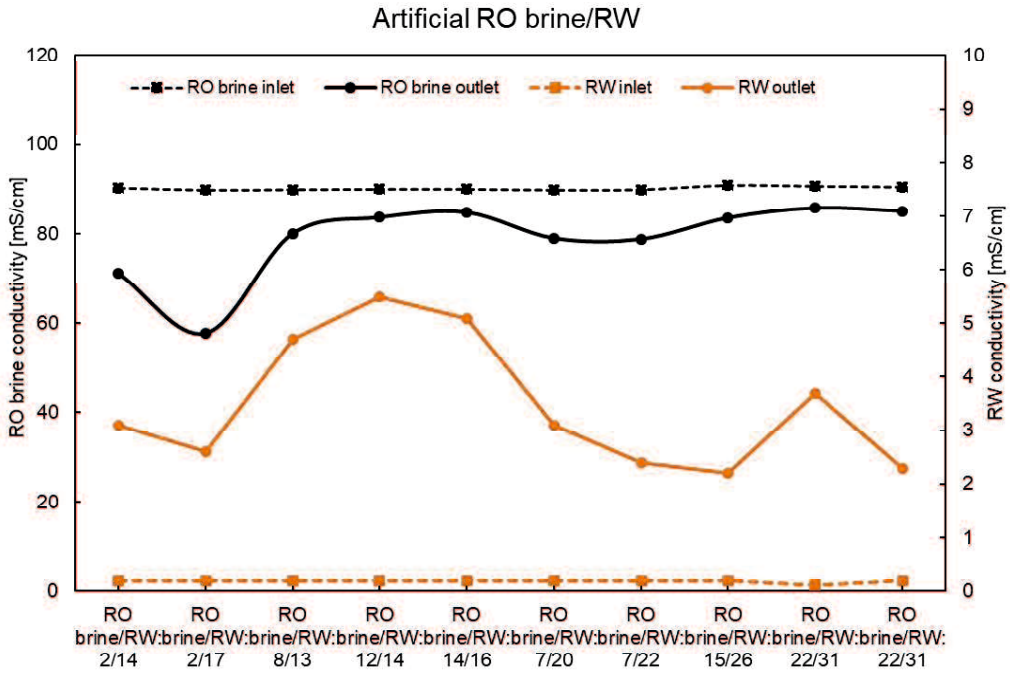

Fig. B2. The conductivity of inlet and outlet solution using model RO brine/RW at zero current

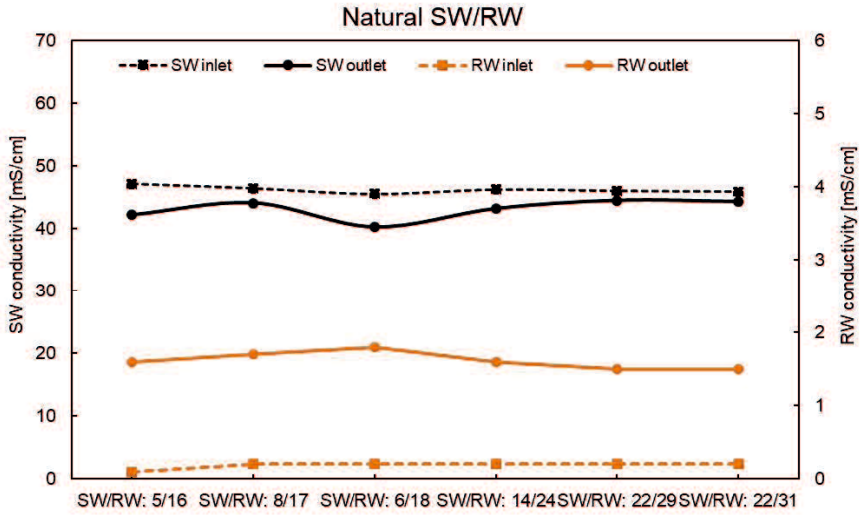

Fig. B3. The conductivity of inlet and outlet solution using natural SW/RW at zero current

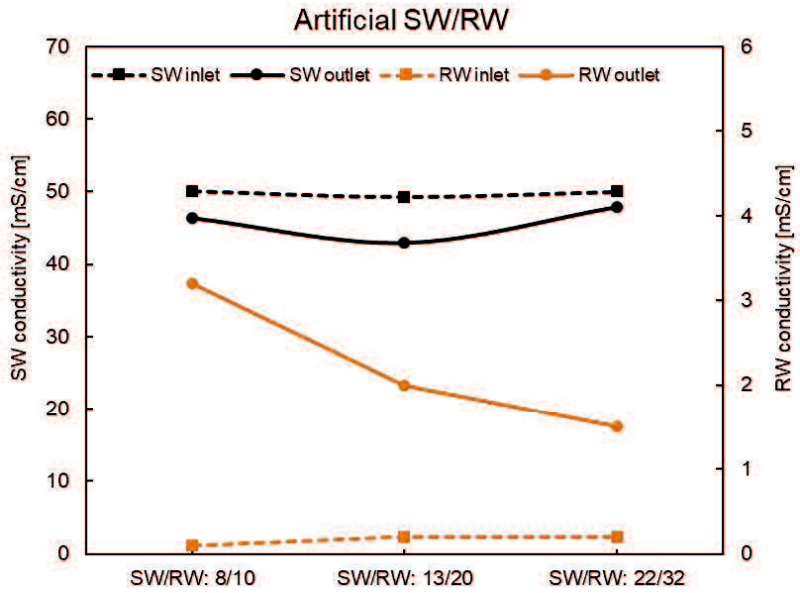

Fig. B4. The conductivity of inlet and outlet solution using natural RO brine/RW at zero current

The actual OCV of all RED tests using natural and model feed solution at different flow rate have shown as Fig. B5-B8. Generally, the OCVs showed increasing behavior by increasing the feed flow rate as discussed.

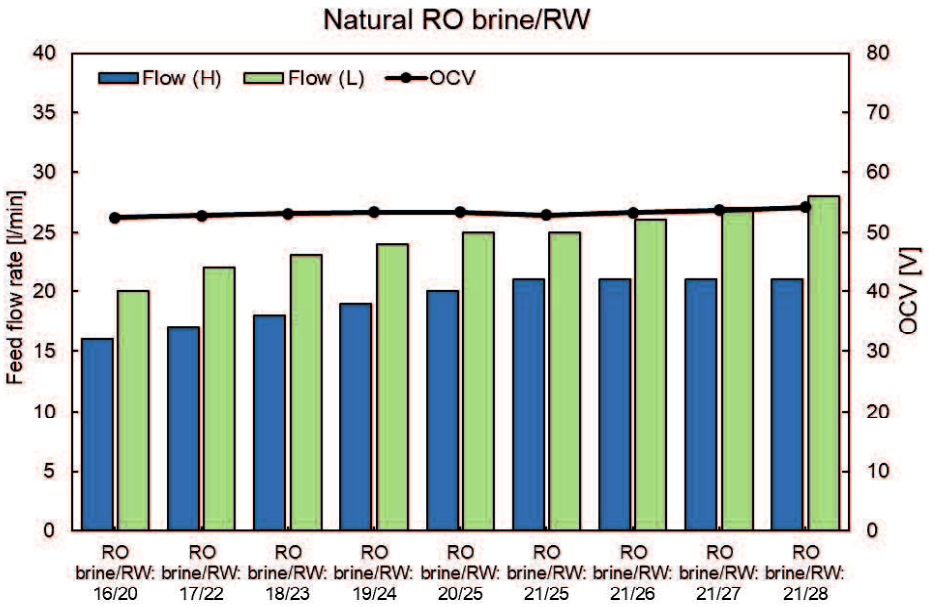

Figure B5. The OCVs of RED stack using natural RO brine and RW feed solution at different feed flow rate

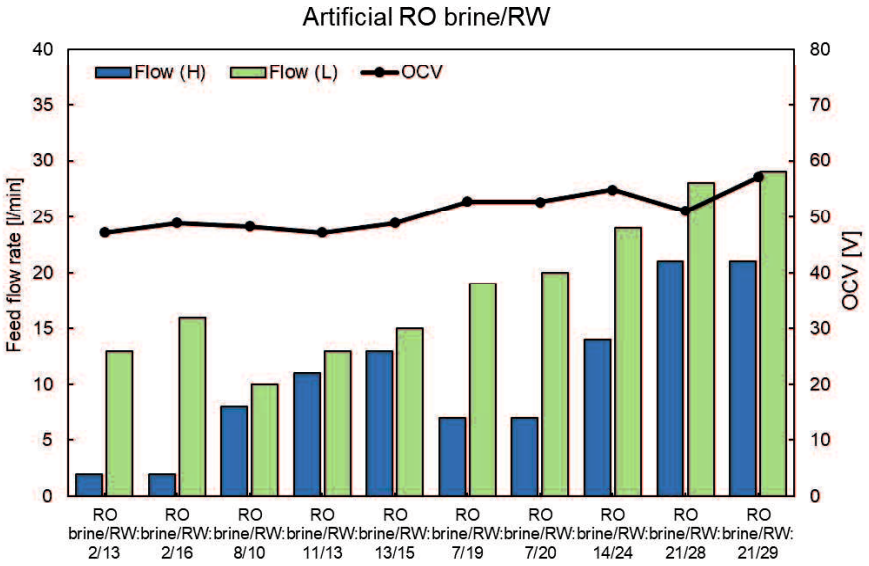

Figure B6. The OCVs of RED stack using model RO brine and RW feed solution at different feed flow rate

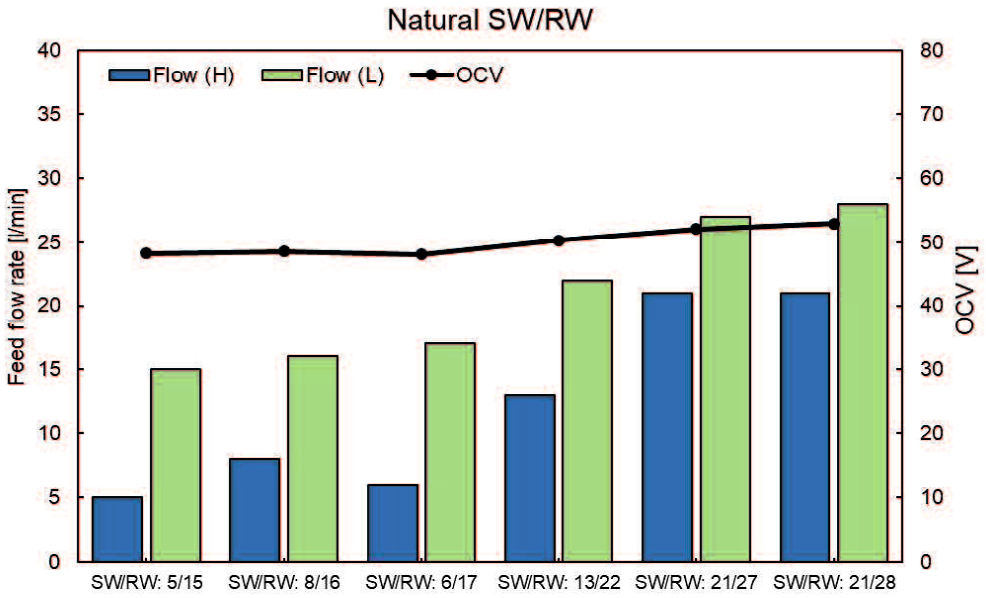

Figure B7. The OCVs of RED stack using natural SW and RW feed solution at different feed flow rate

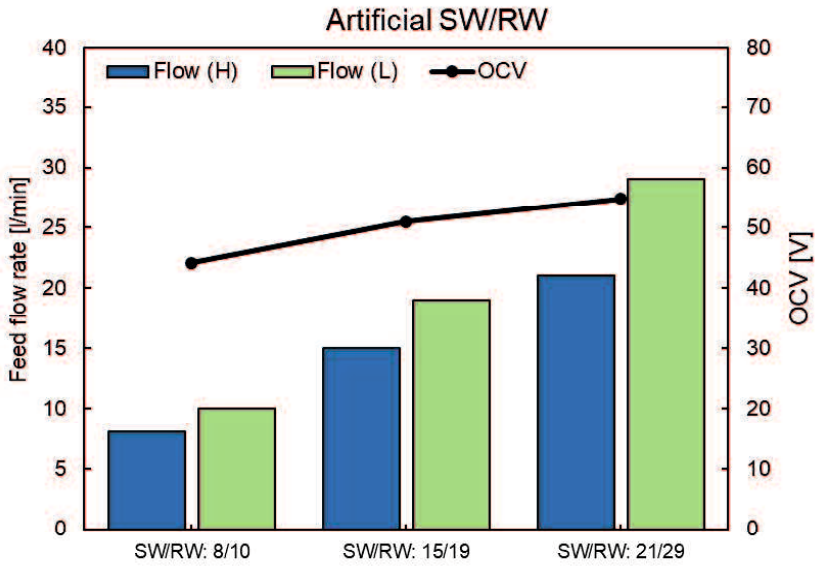

Figure B8. The OCVs of RED stack using model SW and RW feed solution at different feed flow rate

6.7.3 Appendix C. Pressure drop of RED stack

The value of pressure drop during RED performance measurement has shown in Fig. C1-C4. The pressure values are the accumulation of the pressure drop at both high and low concentrate compartments. Pressure drop used to calculate the net power value of RED stack as discussed before.

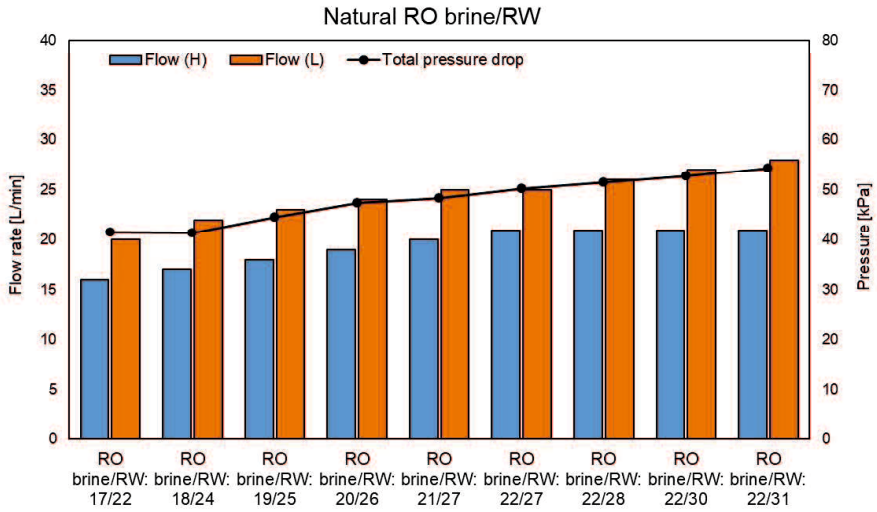

Figure C1. The pressure drop of RED stack as a function of feed flow rate using natural RO brine/RW

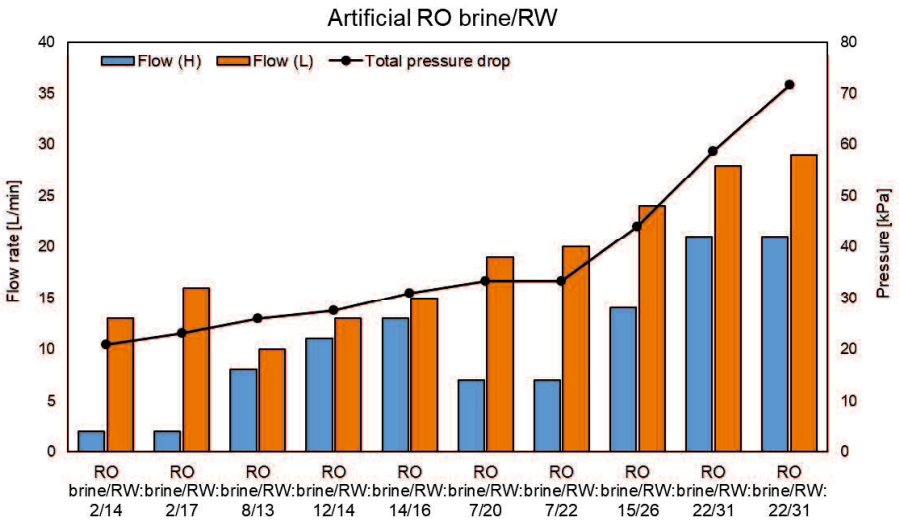

Figure C2. The pressure drop of RED stack as a function of feed flow rate using model RO brine/RW

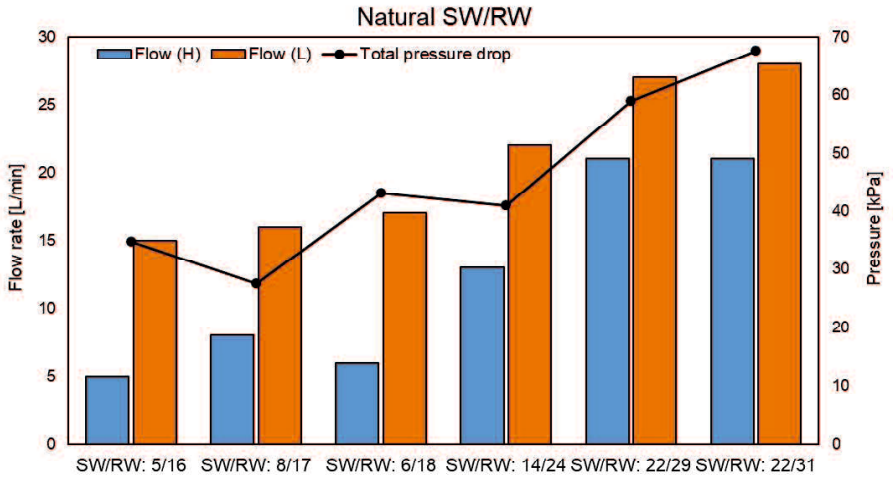

Figure C3. The pressure drop of RED stack as a function of feed flow rate using natural SW/RW

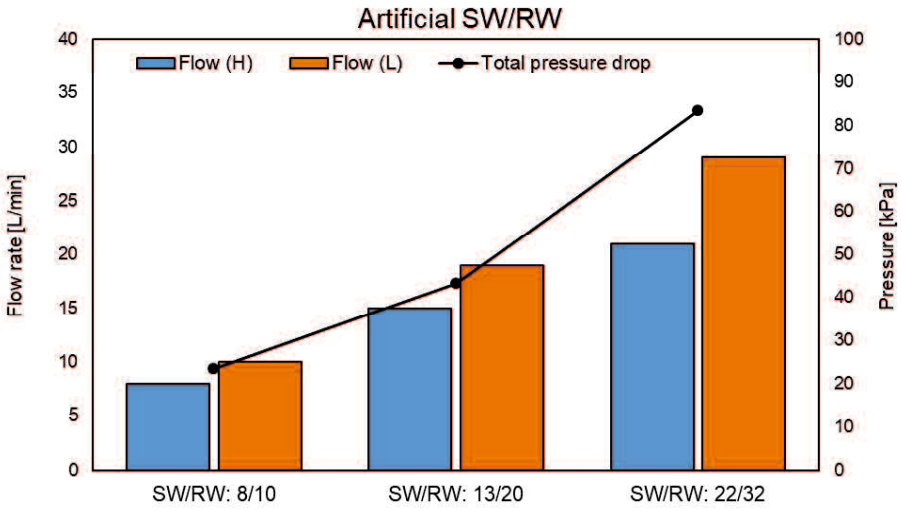

Figure C4. The pressure drop of RED stack as a function of feed flow rate using model SW/RW

Chapter 7

Summary

Salinity gradient energy (SGE) is well known as a renewable source of energy and defined as an electrochemical potential between two solutions with different salinities. SGE can be convert into practical electric power utilizing reverse electrodialysis (RED) process. In RED, the high and low concentrate solutions flow alternatively through stack anion and cation exchange membranes (AEMs and CEMs) which are anion and cation selective, respectively. Cations and anions migrate from high concentrate into low concentrate solution compartment through CEM and AEM, respectively, due to concentration gradient. The ions transportation in opposite direction convert into electric current by redox reaction at suitable electrodes. As a renewable source of energy, the main target of developing RED process is to commercialize this process for energy production. Although many studies have been done on different aspect of RED process, but more investigation is clearly still needed. Therefore, in this Dr. thesis, membrane-based reverse electrodialysis (RED) technique is studied toward its future's implementation of RED total system. The specific target of this thesis was to reach the maximum power density of around 1.5 W/m^2 using one of the biggest pilot-scale RED stack. This thesis consists of 5 experimental chapters (chapters 2~6) expect introduction and summary (chapter 1 and 2). The respective experimental chapters focused on the important research topics such as to improve **"RED stack design" (Chapter 2)**, to optimize the **"RED operation condition" (Chapter 3)**, to find out suitable **"RED applications" (Chapter 4)**, and to find out suitable **"pre-treatment method for RED" (Chapter 5)**, and to estimate **"scale-up of RED stack" (Chapter 6)** using high number of stacked IEMs with large effective membrane area, respectively. The followings are brief summaries of the experimental chapters including motivation and new finding through my comprehensive study.

In this regard, in **Chapter 2**, the spacer shadow effects on both membrane and solution compartment resistances are investigated by using 16 spacers having different geometries with 56-84 % porosity and 0.100-0.564 mm thickness. In addition, we search and propose the suitable spacer geometric parameter for estimating these spacer shadow effects. The results indicate that the spacer shadow effect on membrane has a good correlation with a parameter consisting of area fraction and diameter of spacer filaments, whereas, a parameter consisting of both area and volume fractions of the spacer agreed well with those on solution compartment in a wide range of spacer geometric condition. These results are useful for not only estimating the spacer shadow effect on both membrane and solution resistances for enhancing the subsequent RED power output performance, but also designing a suitable spacer geometry specified for RED. Through this study, we successfully chose a best spacer among them and used it as a first choice for bench- and pilot-scale RED stacks (Chapter 3 and 7, respectively).

In **chapter 3**, we have evaluated the effect of the feed solution temperature on the resulting RED performance using two types of pilot-scale RED stacks consisting of 200 cell pairs having a total effective membrane area of 40 m^2 with different intermediate distances (200 μm and 600 μm). The temperature dependence of the resistance of the solution compartment and membrane, open circuit voltage (OCV), maximum gross power output, pumping energy, and subsequent net power output of the system was individually evaluated. Increasing the temperature shows a positive influence on all the factors studied, and interesting linear relationships were obtained in all the cases, which allowed us to provide simple empirical equations to predict the resulting performance. Furthermore, the temperature dependence was strongly affected by the experimental conditions, such as the

flow rate and type of stack, especially in the case of the pilot-scale stack. This result led to suggest that a suitable location for setting a pilot-scale RED stack was Okinawa (Chapter 6) in Japan because of high temperature.

In **chapter 4**, a typical salt production plant equipped with electrodialysis (ED) and an evaporation system was evaluated for harvesting energy by a RED process. This salt plant has five solutions at different flow rates, ion compositions and concentrations. Both standard CMX/AMX membranes as well as one-sided monovalent selective CIMS/ACS-8T membranes were applied to investigate the effect of divalent ions on RED performance. In this study, we propose the best feed solution combination for producing the maximum possible power from a salt production plant by means of RED. Hence, different membrane potentials, resistance measurement, and RED tests were performed. Generally, the standard membranes showed better RED performance when low amounts of divalent ion were present (< 10%) in the RED feed solutions. In addition, one-sided monovalent selective membrane with the selective layer facing the HCC showed 30% higher performance than that with selective layer facing into the LCC. We also concluded that the properties of low concentrate solution are one of the most important factors in RED performance. Due to this results, we proposed using one side monovalent selective membrane to use in pilot scale RED stack in chapter 6.

In **chapter 5**, the effect of pre-treatment using Polyaluminum chloride (PAC) as a coagulant on the RED performance was investigated using model and real municipal wastewater and seawater samples. The results revealed that the presence of PAC residue after coagulation had a negative impact on the subsequent RED process, especially because of the increased cation exchange membrane resistance, resulting in a 40% reduction in

power generation performance. However, the optimum PAC dosage (and consequent lower amount of PAC residue) enabled a 20% improvement in RED power generation performance because of the removal of 50% of the organic compound content of the wastewater. Our results indicate that the coagulation pre-treatment with the optimized dosage of PAC is useful before RED power generation using municipal wastewater.

In **chapter 6**, a pilot-scale RED stack with 299 cell pairs and 179.4 m^2 effective membrane area was set in a seawater reverse osmosis (SWRO) desalination plant in Okinawa, Japan. For the first time, one-side monovalent selective membranes were installed into the stack, especially in a pilot-scale. Both natural and model RO brine as well as SW were used as high concentrate feed solution, and natural river water (RW) was used as low concentrate feed solution. Consequently, the maximum gross power density using natural and model RO brine/RW reached to 0.96 W/m^2 and 1.46 W/m^2, respectively. The RED stack also produced the maximum gross power of 0.62 W/m^2 and 0.91 W/m^2 using natural and model SW/RW, respectively. In addition, power generation of RED stack was tested under constant current (CC) condition in order to identify the effect of concentration polarization on the RED stack performance which was reasonably lower in the case of using model feed solutions compare with natural feed solutions due to the presence of multivalent ions. The power generation using pilot-scale was the highest reported gross power density in the world. This results proved that our previous studies were truly reliable in order to scale up the RED process as one of the biggest step for commercializing this process.

Publications, Conferences and achievements

8.1 Publications

[1] **Soroush Mehdizadeh *(1st author)***, Masahiro Yasukawa, Takakazu Abo, Yuriko Kakihana and Mitsuru Higa, **"**Effect of Spacer Geometry on Membrane and Solution Compartment Resistances in Reverse Electrodialysis.," *Journal of Membrane Science*, **572,** 271-280 (2019). DOI: https://doi.org/10.1016/j.memsci.2018.09.051 ***(peer reviewed)***

[2] **Soroush Mehdizadeh *(1st author)***, Masahiro Yasukawa, Masaya Kuno, Yoshihiro Kawabata and Mitsuru Higa, **"**Evaluation of Energy Harvesting from Discharged Solutions in Salt Production Plant by Reverse Electrodialysis (RED)," *Desalination,* **467,** 95-102 (2019). DOI: https://doi.org/10.1016/j.desal.2019.04.007. ***(peer reviewed)***

[3] **Soroush Mehdizadeh *(1st author)***, Masahiro Yasukawa, Takakazu Abo, Masaya Kuno, Yuki Noguchi and Mitsuru Higa, **"**The Effect of Feed Solution Temperature on the Power Output Performance of a Pilot-Scale Reverse Electrodialysis (RED) System with Different Intermediate Distance," *Membranes,* **9(6),** 73, (2019). DOI: https://doi.org/10.3390/membranes9060073. ***(peer reviewed)***

[4] **Soroush Mehdizadeh *(1st author)***, Masahiro Yasukawa, Tasuma Suzuki, and Mitsuru Higa, **"**Reverse electrodialysis for power generation using seawater/municipal wastewater: Effect of coagulation pre-treatment," *Journal of Membrane Science, Under review.*

[5] Takakazu Abo, **Soroush Mehdizadeh**, Yuriko Kakihana, Masahiro Yasukawa, Mitsuru Higa, **"**Power generation performance of a pilot-scale reverse electrodialysis

(RED) stack.," *Bulletin of the Society of Sea Water Science, Japan*, **73,** 96-97 (2019) ***(peer reviewed)***

[6] Mitsuru Higa, **Soroush Mehdizadeh**, Shiyan Feng, Nobutaka Endo and Yuriko Kakihana, "Cell Performance of Direct Methanol Alkaline Fuel Cell (DMAFC) Using Anion Exchange Membranes Prepared from PVA-Based Block Copolymer.," *Journal of Membrane Science.* ***(peer reviewed)***

[7] Masahiro Yasukawa, **Soroush Mehdizadeh,** Tomoyuki Sakurada, Takakazu Abo, Masaya Kuno and Mitsuru Higa, "Power generation performance of a bench-scale reverse electrodialysis stack using real wastewaters discharged from seawater reverse osmosis and sewage treatment plants.", *Desalination, Under review.*

8.2 Conferences

[1] **Soroush Mehdizadeh *(presentator)***, "Reverse Electrodialysis (RED) power generation by mixing seawater and river water", *4th Program of International Platform on Ocean Energy for Young Researcher 2017, Institute of Ocean Energy, Saga University (IOES)*, November 2017, Japan. ***(International, Oral)***

[2] **Soroush Mehdizadeh *(presentator)***, Masahiro Yasukawa, Yuriko Kakihana and Mitsuru Higa, "Effect of Spacer Geometry on Reverse Electrodialysis (RED) resistance", *The Fiber Society's Spring 2018 Conference*, June 2018, Japan ***(International, Poster)***

[3] **Soroush Mehdizadeh *(presentator)***, Masahiro Yasukawa, Yuriko Kakihana and Mitsuru Higa, "Effect of Spacer Geometry on Stack Resistance in Reverse

Electrodialysis", *The 11th conference of the Aseanian Membrane Society*, AMS 11, July 2018, Australia. ***(International, Poster)***

[4] **Soroush Mehdizadeh *(presentator)***, Masahiro Yasukawa, Masaya Kuno, Mitsuru Higa, "Applying reverse electrodialysis (RED) to harvest energy from discharge solution of salt plant", *The 5th Seawater-Life-Chemical Cooperation Symposium*, October 2018, Ishinomaki Senshu University, Japan. ***(Domestic, Poster)***

[5] **Soroush Mehdizadeh *(presentator)***, Masahiro Yasukawa, Mitsuru Higa, "Reverse electrodialysis (RED) system using wastewater from salt production plant", *Program of Membrane Symposium 2018,* November 2018*,* Kobe University, Japan. ***(Domestic, Poster)***

[6] **Soroush Mehdizadeh *(presentator)***, Masaya Kuno, Masahiro Yasukawa, Mitsuru Higa, "Energy Harvesting from Discharged Solutions in Salt Production Plant by Reverse Electrodialysis (RED)", *28th Annual Meeting of MRS-J,* December 2018, Kokura, Japan. ***(Domestic, Oral)***

[7] **Soroush Mehdizadeh *(presentator)***, Takakazu Abo, Masahiro Yasukawa, Yuriko Kakihana and Mitsuru Higa, "Power generation performance of a 299 cell pairs pilot-scale RED stack with the highest gross power density in the world", Japan Society of Sea Water Science Young Member, 10th Student Research Presentation, March 2019, Nagasaki, Japan. ***(Domestic, Poster)***

[8] **Soroush Mehdizadeh *(presentator)***, Masahiro Yasukawa, Yuriko Kakihana, Mitsuru Higa "Reverse electrodialysis using seawater/municipal waste water: the effect of municipal waste water chemical pre-treatment by coagulant on RED power

generation", *The 12th conference of the Aseanian Membrane Society*, AMS 12, July 2019, South Korea. ***(International, Oral)***

8.3 Awards

[1] **Soroush Mehdizadeh,** ***"Best presentation award"***

4th Program of International Platform on Ocean Energy for Young Researcher 2017", Institute of Ocean Energy, Saga University (IOES).

[2] **Soroush Mehdizadeh,** ***"Outstanding poster award",***

The Fiber Society Spring 2018 Conference co-organized with The Society of Fiber Science and Technology, Japan

[3] **Soroush Mehdizadeh,** ***"Award for Encouragement of Research"***

The 28th Annual Meeting of MRS-Japan Symposium.

[4] **Soroush Mehdizadeh,** ***"Outstanding performance award"***

Japan Society of Sea Water Science Young Member, 10th Student Research Presentation, March 2019, Nagasaki, Japan.